UNIVERSITY OF SOUTHAMPTON

THERMAL VERTICAL BIMORPH ACTUATORS AND THEIR APPLICATIONS

by

Harald Johann Sehr

A thesis submitted for the degree of
Doctor of Philosophy

FACULTY OF ENGINEERING AND APPLIED SCIENCES
DEPARTMENT OF ELECTRONICS AND COMPUTER SCIENCE

November 2002

UNIVERSITY OF SOUTHAMPTON

ABSTRACT

FACULTY OF ENGINEERING AND APPLIED SCIENCES
DEPARTMENT OF ELECTRONICS AND COMPUTER SCIENCE

Doctor of Philosophy

THERMAL VERTICAL BIMORPH ACTUATORS AND THEIR APPLICATIONS

by Harald Johann Sehr

In this thesis, a novel concept for lateral actuators based on vertical bimorphs is presented. Vertical bimorphs consist of silicon beams side-coated with aluminium, which bend when heated due to the different thermal expansion coefficients of the two materials causing a displacement in the wafer plane. The heating of the actuator is provided by an electrical current through the silicon beam. The simplest implementation of a vertical bimorph actuator is a clamped-clamped beam. To obtain higher deflections, a meander shaped actuator has been designed. By combining four meander actuators, a two-dimensional positioning stage has been realised. The meander actuator has also been applied for normally closed and normally open micro-relays.

Analytical calculations and ANSYS simulations have been carried out to predict the physical behaviour of the bimorph devices, including temperature distribution, static deflection, vertical stiffness, thermal time constant and lateral resonances. For both the clamped-clamped beam actuator and the one-dimensional meander actuator the above parameters have been measured on actual devices showing reasonable to good agreement with the theoretical results. The measurements have been carried out in an SEM, which provided a vacuum environment and enabled measurements using a cursor.

The fabrication required development of non-standard processes, including aluminium deposition onto the sidewalls of silicon beams by angled evaporation and wet-etching, chrome/gold sidewall deposition into contact gaps for micro-relays, photolithography on wafers with 30 μm deep trenches, and a release etch process based on dry-etching. The batch fabrication for the vertical bimorph actuators uses silicon on insulator substrates, deep reactive ion etching for the definition of the silicon beams, gold deposition for the contacts, the aluminium sidewall deposition process for the bimorphs and a release etch based on dry-etching of silicon.

Contents

List of Figures

List of Tables

List of Symbols

a	-	distance of the neutral surface from material interface $[m]$
A	-	area $[m^2]$
A_0	-	constant $[m]$
A_1	-	constant [1]
A_2	-	constant $[m^{-1}]$
α	-	thermal expansion coefficient $[K^{-1}]$
α_a	-	thermal expansion coefficient of material a $[K^{-1}]$
α_b	-	thermal expansion coefficient of material b $[K^{-1}]$
α_{Al}	-	thermal expansion coefficient of aluminium $[K^{-1}]$
α_{Si}	-	thermal expansion coefficient of silicon $[K^{-1}]$
B	-	constant $[K^{-1}m^{-1}]$
C	-	constant $[Km^{-1}]$
C	-	capacitance $[F]$
C_1	-	constant $[m]$
C_2	-	constant $[m]$
c_p	-	specific heat at constant pressure $[NmK^{-1}kg^{-1}]$
d	-	plate separation $[m]$
d	-	amount of aluminium mask overhang, seen from the back
	-	of the wafer $[m]$
d_{ij}	-	tensor of the piezoelectric coefficients $[AsN^(-1)]$
e	-	amount of aluminium mask overhang, seen from the front
	-	of the wafer $[m]$
E_a	-	elastic modulus of material a $[Nm^{-2}]$
E_b	-	elastic modulus of material b $[Nm^{-2}]$
E_{Al}	-	elastic modulus of aluminium $[Nm^{-2}]$
E_{Si}	-	elastic modulus of silicon $[Nm^{-2}]$
EI	-	flexural rigidity $[Nm^2]$
E_j	-	electric field tensor $[Vm^{-1}]$
ϵ_o	-	relative permittivity $[AsV^{-1}m^{-1}]$
ϵ_r	-	relative permittivity [1]
ϵ_T	-	thermal strain [1]
f_i	-	natural frequency, mode number $_i$ $[Hz]$
f_o	-	maximum frequency of full thermal response $[Hz]$
F_x	-	force in x-direction $[N]$
F_y	-	force in y-direction $[N]$
F_z	-	force in z-direction $[N]$
I_a	-	second moment of area for material a $[m^4]$
I_b	-	second moment of area for material b $[m^4]$

I_{Al}	-	second moment of area for aluminium $[m^4]$
I_{Si}	-	second moment of area for silicon $[m^4]$
I_{Aly}	-	second moment of area in y-direction for aluminium $[m^4]$
I_{Siy}	-	second moment of area in y-direction for silicon $[m^4]$
I_{Alz}	-	second moment of area in z-direction for aluminium $[m^4]$
I_{Siz}	-	second moment of area in z-direction for silicon $[m^4]$
k	-	thermal conductivity $[Wm^{-1}K^{-1}]$
k_{Al}	-	thermal conductivity of aluminium $[Wm^{-1}K^{-1}]$
k_{Si}	-	thermal conductivity of silicon $[Wm^{-1}K^{-1}]$
k_{ij}	-	tensor of the inverse piezoelectric coefficients $[AsN^{-1}]$
k_y	-	spring constant in y-direction $[Nm^{-1}]$
k_z	-	spring constant in z-direction $[Nm^{-1}]$
l	-	plate length $[m]$
l_b	-	length of bimorph $[m]$
l_p	-	width and length of contact pad $[m]$
l_1	-	design dimension for meander actuators $[m]$
l_2	-	design dimension for meander actuators $[m]$
l_3	-	design dimension for meander actuators $[m]$
l_4	-	design dimension for meander actuators $[m]$
Δl_i	-	elongation due to the shape of the deflection curve $[m]$
Δl_t	-	elongation due to thermal expansion $[m]$
λ_i	-	parameter reflecting boundary conditions [1]
m	-	mass $[kg]$
M_A	-	reaction couple at point A $[Nm]$
M_B	-	reaction couple at point B $[Nm]$
N	-	number of modes $[m]$
P	-	power $[W]$
P_i	-	electrical polarisation $[Asm^{-2}]$
$\dot{q}$	-	rate at which energy is generated per unit volume $[Wm^{-3}]$
Φ	-	angle of incidence $[^\circ]$
Φ_i	-	phase angle, mode shape number $-i$ [1]
r	-	radius of curvature $[m]$
R	-	reaction force $[N]$
R_A	-	transversal reaction force at point A $[N]$
R_Aa	-	axial reaction force at point A $[N]$
R_B	-	transversal reaction force at point B $[N]$
R_Ba	-	axial reaction force at point B $[N]$
ρ	-	mass density $[kgm^{-3}]$
S_i	-	mechanical strain [1]
σ_i	-	parameter reflecting boundary conditions [1]
t	-	time $[s]$
T	-	temperature $[K]$
T_0	-	initial temperature, bulk temperature $[K]$
t_a	-	thickness of material a $[m]$
t_b	-	thickness of material b $[m]$
T_j	-	mechanical stress tensor $[Nm^{-2}]$
ΔT	-	temperature difference $[K]$
ΔT_{av}	-	average temperature difference $[K]$

ΔT_c	-	temperature difference at the centre of the beam $[K]$
τ	-	thermal time constant $[s]$
τ_s	-	thermal time constant, simulated $[s]$
V	-	voltage $[V]$
v	-	deflection $[m]$
v_c	-	centre deflection $[m]$
v_h	-	deflection, solution of the homogeneous diff. equation $[m]$
v_p	-	deflection, particular solution of the inhomogeneous
	-	diff. equation $[m]$
W	-	potential energy $[Ws]$
w	-	plate width $[m]$
w_{Al}	-	width of aluminium $[m]$
w_{Si}	-	width of silicon $[m]$
x	-	spatial coordinate $[m]$
y	-	spatial coordinate $[m]$
Y	-	transverse deformation $[m]$
$\tilde{y}_i$	-	function of the mode shape, mode shape number $-i$ $[m]$
z	-	spatial coordinate $[m]$

Acknowledgements

I would like to thank my supervisor, Prof. Alan Evans, for giving me the opportunity to be his PhD student and for his guidance, support and understanding throughout my PhD project. Not to forget about the conferences he allowed and encouraged me to go to and the possibility to be employed as an experimental officer.

Many thanks goes to Dr Arthur Brunnschweiler for his advice and ideas and all the interesting conversations.

Special thanks to Dr Graham Ensell for his advice and guidance throughout my PhD project, especially in fabrication related questions and for proofreading of this thesis, but most of all for his friendship and our Sunday morning tennis matches (although I only managed to win once).

A very special thank you goes to Dr Christian Schabmüller, who welcomed me on my very first day in Southampton (both when I started my PhD and when I came to have a look at the place before). Although Niederbayerisch only ranks second on the scale of linguistic sophistication I almost felt like home in our Bavarian corner. 'Cheers mate' for the company at several conferences and for the honour to be best-man for your wedding.

I really appreciated the friendly atmosphere at our group. Many thanks to my fellow PhD students: Dr Trevor Niblock, Dr Nele D'Halleweyn, Graham Leach, Craig Easson, Dr Ahmad Abdul-Rahim, Dr Iain Anteney, Dr Majid Zoorob, Tim Pease, Dr Urs Straube, Dr Stefanos Stefanou, Kharil Osman, Huda El-Mubarek, Minqiang Bu, Deaw Iamraksa, Aris Papakostas, Wen Zhang, Op Pengpad, Lit Ho Chong, Ben Husband and Enrico Gili.

My appreciation to all the researchers: Dr Jochen Schiz, Dr Geoff Nash, Dr Martin Charlton, Dr Yue Tang, Dr Andrew Waite, Dr Janet Bonar, Dr Farrukh Alavi, Dr Neil Lloyd, Mateen Farooqui, Dr Raghied Atta, Dr Tony Zijlstra, Dr Bifeng Rong, Dr Gabriella Dilliway, Peter Ayliffe, Dr Takashi Uchino, Dr Bayram Unal.

Not to forget about our academics: Dr Kees de Groot, Dr Darren Bagnall, Dr Tracey Melvin , Prof. Greg Parker, Prof. Bill Redman-White and Ian McNally. My appreciation for Prof Henri Kemhadjian, Prof. Alan Evans (again) and Prof. Peter Ashburn for 'steering' our research group.

A special mention goes to Dominik Kunz for getting me started with Latex and for the nice chats while cycling home from work, to Mircea Gindila for the chess and tennis games, to my charming colleagues from 2033, Dr Elena Koukharenko and Dr Luminita Grigore, to Mir Mokhtari, Becky Neal, Ruth Houlihan, Luca Plattner and Ketan Mistry for their contribution to the friendly atmosphere in our group and to

Jim Benson for being a great volleyball manager. Many thanks also to Stephanie Lins and Oliver Rückle.

My gratitude to Dr Michele and Dr Paul Routley for their friendship and for Paul's support with my cleanroom work. Thanks to Dr Steve Beeby for his advice and our weekly squash matches. Many thanks to Dr Stephan Weiss for his friendship, the night-shift coffee breaks and all the gourmet dinners at his place. A special thank you to Dr Michael Kraft for his friendship, his advice, for organising parties and walks in the New Forest as well as for his patience in our tennis matches (I better save me the embarrassment of mentioning how many of them I won).

My project involved a lot of fabrication work. I really got great support from the people in and around the cleanroom: Paul Marchese, Corry Kratochvila ('may I ask you a big favour'), Mike Josey (many thanks for the perfect dry-etch training), Brian Ault (always ready to help), Jean Humphry, Richard Bayly (not only master of angled evaporations but, to my surprise, also of squash), Brian Davidson, Tim Hartley (thanks for having an eye on the orange box), Lynn Prowting, Naomi Townsend, Elaine Bayly, Angela Macmanus, Robin Williams, Uma Bhattathiripad, Sally Croucher, Dr Nasser Afshar-Hanaee. Also to the men from behind the scenes: Alan Walker, Alan Purdy, John Amy, Pinder Sant, Dave Dawkins (even in England there are a few fans of Germany), Ted Meech, Tom Fielder, Denny Jack. Not to forget about Ken Frampton and his team at the mechanical workshop. Special mention goes to Tony Blackburn for his advice concerning the aluminium sidewall deposition ('it was a pleasure dealing with you'). Appreciation to Derek Jenkins from Rutherford Laboratories for doing the DRIE on my wafers.

Many thanks to my project students, Ian Tomlin and Biyun Huang, for their contribution to the vertical bimorph project. A special thank you to Dr Ovidiu Grigore for his advice on solving differential equations.

I certainly do not want to miss the opportunity to thank our secretaries: Glenys Howe, Jilly Searle, Lucia Hewett, Christine Foster, Audrey Ashford-Smith and Angie Mo.

I really enjoyed working in the Microelectronics Research Group. I tried hard not to forget anybody. In case I did, it most certainly was not on purpose.

Lastly, but most importantly a very special thank you goes to my parents and my two brothers for their continuous support and motivation. Ein besonders herzliches Dankeschön gilt meinen Eltern und meinen beiden Brüdern, die mich während meiner vierjährigen Zeit als PhD-Student stets unterstützt und motiviert haben. Vergelt's Gott.

Chapter 1

Introduction

1.1 Micromachining and Microelectromechanical Systems

In the 1960s, the idea of using silicon not only as a substrate for micro-electronic devices but also as a material for micro-mechanical components and applying batch fabrication techniques from micro-electronics to obtain micro-structures meant the birth of micromachining. Since the majority of micro-mechanical components can only perform useful applications in combination with electronic control circuitry, a system approach is required, which naturally leads to the term 'Microelectromechanical Systems' (MEMS). MEMS generally describes systems made of very small components, including electrical or electronic as well as mechanical components. Today, the MEMS concept includes a wide range of systems including thermal, magnetic, fluidic and optical components, with or without moving parts [1]. Note, the 'MEMS' term originated in the USA but is now widely used all over the world. The European term 'Microsystems' or 'Microsystem Technology' seems a more general description and puts more emphasis on the system idea. However, today 'MEMS' and 'Microsystems' are used as synonyms.

Although micromachining came from microelectronic processing techniques it is by no means limited to those. However, the batch processing method based on UV photolithography with its potential for cost efficient mass production plays an important part in micromachining. For silicon micromachining, many new processes have been added to enlarge the portfolio of achievable structures. Anisotropic wet etching, deep reactive ion etching and different wafer bonding techniques are but a few examples of specific MEMS processes. To fabricate metallic micro-components, high aspect ratio photolithography and electroplating techniques are combined. The LIGA process is based on X-ray lithography and electroplating. Embossing and moulding

of plastics extends these techniques to fabrication of plastic micro-parts. [2] and [3] give a comprehensive overview on micromaching techniques.

The first microsystems were membrane pressure sensors [4]. Many more sensors followed: accelerometers, gyroscopes, magnetic sensors, gas sensors, chemical sensors, biosensors and optical sensors. Their use is widespread, mainly in automotive, communication and pharmaceutical applications. Not only sensing systems were designed but also micro actuators using electrostatic, piezoelectric, magnetic, thermal and other mechanisms to produce either linear (translational) or rotary movement. They have been applied in micropositioning, relays, microfluidic devices, mechanical resonators, micro grippers and actuated micro mirrors. Printheads for inkjet printers are another important application of MEMS.

1.2 Thermal Vertical Bimorph Actuators and Their Role in MEMS

The initial idea behind this work was to design an integrated micropositioning stage that can be used for integrated scanning probe devices. Scanning probe devices such as a scanning tunnelling microscope and an atomic force microscope scan a tip of molecular size across the surface of the sample to obtain a topographic image. Traditionally, they use macroscopic piezo actuators with very precise resolution.

Soon after the invention of scanning probe microscopes, it was recognised that they are not only suitable for imaging samples but also for modifying their surface. Different methods of this so-called proximal probe lithography have been applied to create surface features of submicron dimensions. However, the serial character of operation leads to a very slow operation speed, which limits the application of proximal probe lithography. In order to overcome this limitation, parallel operation of a large number of probes is required. To use arrays of independent micro probes, integrated two- or three-dimensional positioning stages are required. Fast actuation, wide range of movement and precise actuation control are the main demands for such actuators. At this point innovative MEMS solutions are desirable.

Several approaches of integrated micro positioning stages have been implemented by different research groups, including piezoelectric [5] and electrostatic actuators [6]. The piezoelectric approach suffers from a very limited range of movement, whereas the electrostatic scanner requires very high driving voltages. Micro-positioning actuators that enable large displacements with no need for very high driving voltages and actuation power are required.

In this work, we introduce the concept of micro positioning stages based on ther-

mally actuated bimorphs. Up to now, micro actuators based on the bimetal effect [7] have only been used as planar actuators achieving movement out of the wafer plane [8]. To obtain movement in the horizontal plane, we devise vertical bimorphs consisting of silicon side-coated with aluminium. They perform displacement in the wafer plane and enable the design of one- and two-dimensional positioning actuators.

The application of thermal vertical bimorph actuators is by no means limited to micro scanning probe devices or micropositioning tasks. They are also suitable for micro-switches, micro fluidic applications such as micro valves and pumps, micro grippers, ciliary actuators and other micro robots. To demonstrate the working principle of thermal vertical bimorph actuators, we present different designs including a simple one-dimensional actuator based on a double clamped beam as well as a one- and two-dimensional meander shape actuator. Normally open and normally closed micro-switches have been implemented as an example of a practical application of vertical bimorph actuators.

1.3 Aims of this Thesis

The aims of this thesis were:

- To design and fabricate vertical bimorph actuators that can be used for two- and three-dimensional positioning stages.
- To model the physical behaviour of vertical bimorph actuators.
- To compare the theoretical model with experimental results.

1.4 Structure of the Thesis

Chapter 2 gives a literature review on the field of micro-actuators. Actuation principles including electrostatic, piezoelectric and thermal effects as well as other actuation principles are discussed. Applications of micro-actuators in scanning probe devices, micro-switches, micro fluidics, actuated mirrors, mechanical resonators and micro-grippers are described.

In chapter 3, the concept of thermal vertical bimorph actuators is introduced. The working principle is explained, using the example of a cantilever and a clamped clamped beam actuator. An advanced actuator design based on a meander shaped silicon beam is presented, which enables application in one- and two-dimensional micro positioners as well as normally open and normally closed micro-relays.

Theoretical analyses are discussed in chapter 4. For the clamped clamped beam actuator, an analytical model was developed to predict the temperature distribution, static deflection, vertical stiffness and lateral resonances. An ANSYS simulation was used to verify the analyses on the temperature distribution as well as the static deflection and to obtain the thermal time constant of the system. For the one- and two-dimensional meander type actuator, all the above parameters were investigated using ANSYS simulations.

Due to their novelty and geometric complexity, a significant amount of process development work was necessary to devise a fabrication process for vertical bimorph actuators, discussed in chapter 5. A process for aluminium sidewall deposition was developed. The micro-switches required a process for the deposition of chrome/gold sidewall contacts. Thick photoresist patterning was optimised to be used on wafers with a topography of 30 μm. Lastly, different methods of releasing the actuators by silicon and oxide etching from the back of the wafer were investigated.

In chapter 6, the fabrication processes for the clamped-clamped beam actuator, the meander type actuators as well as the micro-relays are described and relevant details of the mask design are pointed out.

Chapter 7 describes test and measurement of the devices. For both the clamped-clamped beam actuator and the one-dimensional meander actuator, the static deflection, the thermal time constant and lateral resonant modes were measured. For the two-dimensional meander actuator and the micro-relays, preliminary measurements are presented.

Chapter 8 is the conclusion and gives an outlook on further work.

Chapter 2

Micro Actuators and Their Applications - A Review

2.1 Introduction

Mechanical actuators convert another form of energy, which can be electrical, chemical, thermal, magnetic or radiation energy, into mechanical energy or mechanical work. In the macroscopic world, combustion engines, electro motors and muscles are typical examples of actuators. Recent advances in micro fabrication processes have enabled industry and researchers to develop actuators of sub-millimetre dimensions, commonly referred to as microactuators.

This chapter gives an overview of the field of microactuators. Microactuators can be split into rotation actuators performing rotary movement and translation actuators, which perform movement along a straight line (therefore, also linear actuators). We limit the discussion to translation actuators. First, the actuation principles are discussed. The main focus is on thermal actuators since they are the most relevant to the work presented here. Secondly, applications of microactuators are reviewed.

2.2 Actuation Principles

2.2.1 Electrostatic Actuators

Electrostatic actuation is based on the attractive force between two opposite electrical charges. In the following subsection fundamental theory as well as the most important practical concepts of electrostatic actuation are discussed.

Fundamental Theory on Electrostatic Actuation

The following considerations are based on [9]. The basic element for electrostatic actuation is a parallel plate capacitor, the capacitance C of which is given by

$$C = \epsilon_r \, \epsilon_0 \, \frac{l \, w}{d} \tag{2.1}$$

where ϵ_0 is the permittivity in vacuum, ϵ_r the relative permittivity, w the plate width, l the length of a plate and d the separation between the two plates as shown in figure 2.1a.

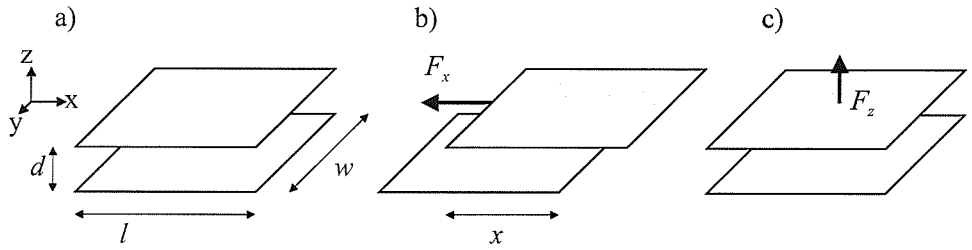

Figure 2.1: Parallel plate capacitor

If a voltage V is applied across the two plates, the potential energy W of the capacitor is

$$W = -\frac{1}{2}CV^2 = -\frac{\epsilon_r \epsilon_0 l w V^2}{2d} \tag{2.2}$$

To calculate the lateral force, we consider the two plates offset with an overlap x. Then the potential energy becomes

$$W = -\frac{\epsilon_r \epsilon_0 x w V^2}{2d} \tag{2.3}$$

The negative first derivative of equation 2.3 with respect to x yields the lateral force F_x (figure 2.1b).

$$F_x = -\frac{\partial W}{\partial x} = \frac{\epsilon_r \epsilon_0 w V^2}{2d} \tag{2.4}$$

The vertical force F_z (figure 2.1c) is obtained by differentiating equation 2.2 with respect to d.

$$F_z = -\frac{\partial W}{\partial d} = -\frac{\epsilon_r \epsilon_0 w l V^2}{2d^2} \tag{2.5}$$

While the lateral force F_x is a constant with respect to the displacement in the

x-direction, the vertical force F_z is highly nonlinear with respect to the displacement in the z-direction.

The above derivation is based on parallel plate capacitors neglecting the energy associated with fringing effects. If the overlap of the two plates is significant the fringing areas remain almost constant when the plates move and the parallel plate assumption is reasonable. When the plates do not overlap the fringing effects become important and equation 2.4 becomes invalid.

Parallel Plate Actuators

Parallel plate actuators rely on the vertical force between two oppositely charged electrodes. As pointed out above, this involves the disadvantage of utilising nonlinear forces. Therefore, only small displacements can be achieved in practice, which limits their suitability for translation actuation. However, in general higher forces than with a comb drive actuator can be obtained.

Electrostatic Comb Actuator

The constant lateral force F_x (equation 2.4) is utilised in comb drive actuators, which are the most commonly used electrostatic actuators. The core part of the actuator is an interdigitated capacitor (electrostatic comb), which consists of a fixed electrode and a movable electrode suspended by a spring as shown in figure 2.2. When a voltage is applied across the electrodes, the suspended electrode moves towards the fixed electrode due to the attractive force described by equation 2.4.

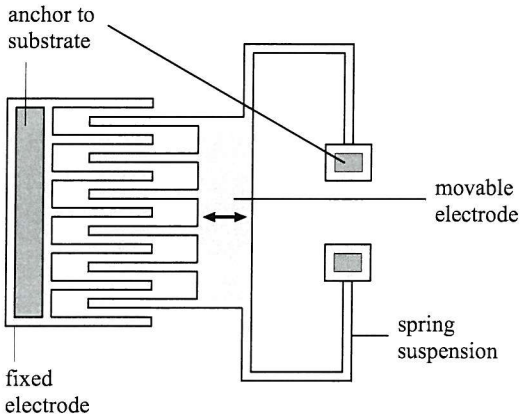

Figure 2.2: Comb drive actuator

Comb drive actuators have been fabricated from polysilicon by surface micromachining techniques [10], [11] and from single crystal silicon employing the so-called SCREAM process [12].

2.2.2 Piezoelectric Actuators

Piezoelectric actuation is based on the inverse piezoelectric effect. The piezoelectric effect means that mechanical stress (represented by the stress tensor T_j) applied to a piezoelectric material causes an electrical polarisation P_i [13].

$$P_i = d_{ij} T_j \tag{2.6}$$

where d_{ij} is the tensor of the piezoelectric coefficients. Reciprocally, an electric field (tensor E_k) produces a mechanical strain S_i, which is given by

$$S_i = k_{ij} E_j \tag{2.7}$$

where k_{ij} is the tensor of the inverse piezoelectric coefficients.

The most common piezoelectric materials in micro-devices are ZnO (zinc oxide), PZT (lead zirconate titanate) and $BaTiO_3$ (barium titanate). ZnO can be sputtered as a polycrystalline film. PZT and $BaTiO_3$ are ceramics and are difficult to deposit as a thin film [2]. Piezoelectric actuators are capable of producing high forces with short reaction times. Their disadvantage is the relatively small movement on the order of several nm/V [14]. However, several implementations of piezoelectric actuators aim at overcoming this issue as discussed below.

Stack Actuator

Several piezoelectric ceramic layers sandwiched between metal electrodes are placed on top of one another to form a stack or multi-layer actuator as shown in figure 2.3. This means the layers are mechanically placed in series and the strains add up to the overall displacement of the stack [15]. Electrically, the electrodes are in parallel, which significantly reduces the voltage compared to single layer actuators. Note that the polarisation of the piezo-layers is alternating between the positive and negative z-direction [16]. Fabrication methods are discussed in [17].

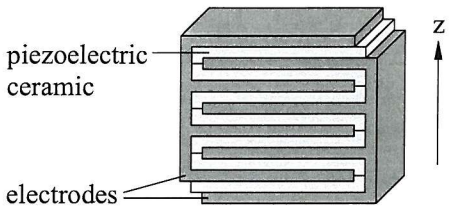

Figure 2.3: Piezoelectric stack actuator

Piezoelectric bimorph

Figure 2.4 shows the working principle of a piezoelectric bimorph [14]. Two piezoelectric ceramic plates, covered by electrodes on the bottom and top are mounted on a supporting plate. The direction of the polarisation of the piezoelectric ceramic is perpendicular to the cantilever. Applying a voltage to the electrodes as shown in figure 2.4 means that there is an electric field parallel to the polarisation in the upper ceramic layer causing it to expand in the x-direction. The electric field in the lower ceramic layer is opposite to the polarisation resulting in a contraction in the x-dimension. The overall result is the bimorph bending with the convex face uppermost. Note that the stack actuator shown in figures 2.3 uses the longitudinal piezo effect whereas the bimorph in figure 2.4 is based on the transversal effect.

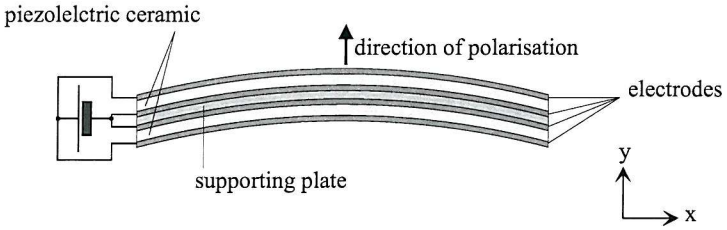

Figure 2.4: Piezoelectric bimorph

2.2.3 Thermal Actuators

Thermal actuation relies on the fact that matter expands when its temperature is increased and contracts when the temperature is decreased. For most materials, the thermal strain ϵ_T is proportional to the temperature change ΔT.

$$\epsilon_T = \alpha \Delta T \tag{2.8}$$

where α is the thermal expansion coefficient, which is specific to each material [18].

Since α is in the range of $2 \cdot 10^{-6}\ K^{-1}$ to $25 \cdot 10^{-6}\ K^{-1}$, only very small displacements can be obtained using linear thermal expansion. A 1000 μm long silicon beam ($\alpha = 2.6 \cdot 10^{-6}\ K^{-1}$) only expands by 0.26 μm when heated up 100 K. Therefore, practical implementations of thermal actuators include an amplification mechanism to increase the displacement range. According to the amplification mechanism used, thermal actuators can be split into two groups [19]. The first uses two materials, which have different thermal expansion coefficients. These are referred to as bimetallic or bimorph actuators. The second mechanism uses only one material and applies constraints or asymmetrical design to amplify the movement. Buckling actuators,

bent beam actuators, hot arm actuators and compliant structures are examples for one-material implementations of thermal actuators.

Thermal Bimorph Actuators

Thermal bimorph actuators consist of two materials (a and b) of different thermal expansion coefficients α_a and α_b. When heated from temperature T_0 to T, they bend towards material b, if α_a is greater than α_b, as illustrated in figure 2.5.

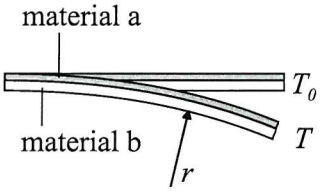

Figure 2.5: Bimorph actuator at temperature T_0 and T.

The inverse radius of curvature $\frac{1}{r}$ is given by

$$\frac{1}{r} = \frac{(\alpha_a - \alpha_b)(T - T_0)}{\frac{t_a+t_b}{2} + \frac{2(E_a I_a + E_b I_b)}{t_a+t_b}\left(\frac{1}{E_a t_a} + \frac{1}{E_b t_b}\right)} \tag{2.9}$$

where t_a and t_b are the thicknesses of material a and b respectively, E_a and E_b their elastic moduli and I_a and I_b their second moments of area [7]. Riethmueller and Benecke fabricated planar bimorph actuators consisting of epitaxial silicon and electroplated gold heated by a polysilicon heater [8]. With a 500 μm long bimorph cantilever, deflections of about 50 μm at an input power of 130 mW have been achieved. Doering et al. [20] used a bimorph actuator made from epitaxial silicon and aluminium for fluid deflection. Sun and coworkers [21] fabricated a bistable micro-relay based on surface micromachined bimorph actuators. Bimorph actuators have also been used for tilting micromirrors [22, 23]. Note that all bimorph microactuators realised so far have a planar arrangement of the two layers and therefore only allow movement out of the wafer plane.

Hot Arm Actuators

Hot arm actuators or pseudobimorhs are fabricated from one material. They consist of two adjacent arms arranged in a U-shape as shown in figure 2.6 [24]. A current through the arms causes heat dissipation. Since the hot arm is narrower its electrical resistance is greater and it reaches a higher temperature. Therefore, it also expands more than the wider cold arm, resulting in a bending motion similar to that of a bimorph.

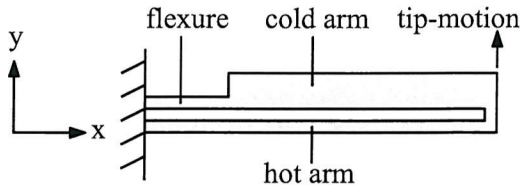

Figure 2.6: Bent beam actuator

Comtois et al. fabricated hot arm actuators from polysilicon [25]. With a 300 μm long arm a tip deflection of 17 μm at an input power of 30 mW was achieved.

Pan and Hsu demonstrated a similar actuator exploiting asymmetrical thermal expansion of two adjacent polysilicon beams of different length [26]. This design increases the asymmetric thermal effect and can also be driven by uniform heating of the whole structure. Allen et al. use a double hot-arm design to increase the efficiency of the electrothermal actuator [27]. The driving current passes through two adjacent hot arms only. The opposite cold arm and the flexure of the cold arm are not included in the electrical circuit and hence no power is dissipated there.

Compliant structures

Similar to hot arm actuators, electrothermal actuation of compliant structures utilises non-uniform heating to obtain movement [28]. An uneven current distribution causes non-uniform heat-dissipation and hence non-uniform temperature distribution. The structure is designed to convert the unevenly distributed thermal expansion into the required displacement.

Keller and Howe fabricated thermally actuated tweezers making use of a compliant actuating mechanism [29] as shown in figure 2.7. The nonuniform current distribution is obtained by beam structures of different electrical conductivity realised with the HEXSIL process [30]. At an input power of about 1 mW, a tip displacement of 25 μm has been achieved.

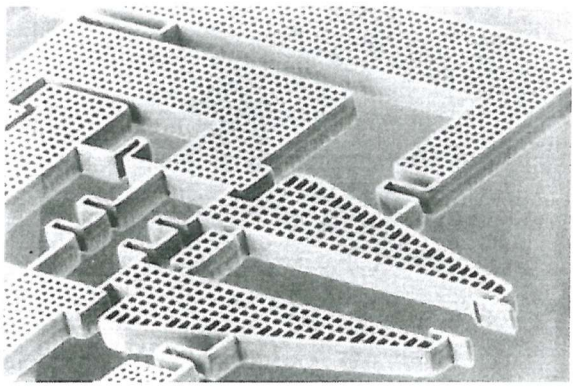

Figure 2.7: HEXSIL tweezers [29].

Figure 2.8 shows a typical example of a simple electrothermal compliant actuator [31]. A driving voltage applied between the two contact pads causes a current flow. The resulting Joule-heating leads to a non-uniform temperature distribution. Since the structure is anchored to the substrate, the constrained thermal heating results in the desired deformation pattern.

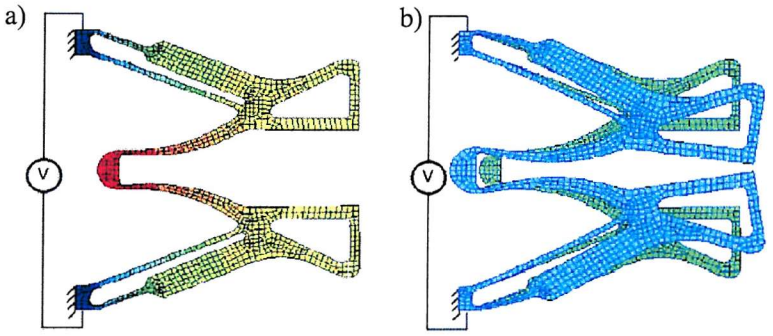

Figure 2.8: Electro-thermal compliant micro-gripper [31], a) temperature distribution, b) deformation.

For more complicated structures and optimised performance, systematic design of compliant actuators is required. Jonsmann et al. [32] utilise an iterative sequence of finite element analysis and material redistribution. More details on topological synthesis for compliant structures aiming at "design for required deflection" can be found in [33–35].

Buckling Actuators

When a straight clamped-clamped beam is heated from temperature T_0 to T_1, thermal stress is generated in the beam since it is not free to expand. When the corresponding axial force exceeds the critical load, buckling occurs and the beam assumes a curved shape as illustrated in figure 2.9 [18]. This deformation is exploited in buckling actuators. If the width of the beam is smaller than the height, the beam moves laterally. If the height is smaller than the width, vertical movement is obtained. A drawback of buckling actuators the uncertainty in which direction the beam will move. Note that buckling in this sense does not mean mechanical failure but lateral displacement of a slender beam caused by compressive axial stress.

Chiao and Lin demonstrated buckling actuators fabricated from doped polysilicon [36]. With a beam of 100 μm in length and an input current of 6 mA, a displacement of 2.7 μm [37] was achieved.

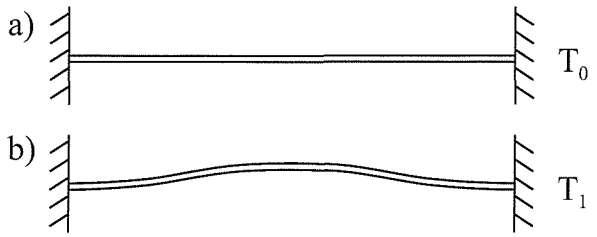

Figure 2.9: Buckling actuator at temperature T_0 and T_1.

Bent-Beam Actuators

Similar to buckling actuators, bent-beam actuators convert axial stress into transverse motion. They consist of a V-shaped beam with fixed ends which is heated by a current flow. The thermal expansion of the beam causes the apex to move in the y-direction as shown in figure 2.10.

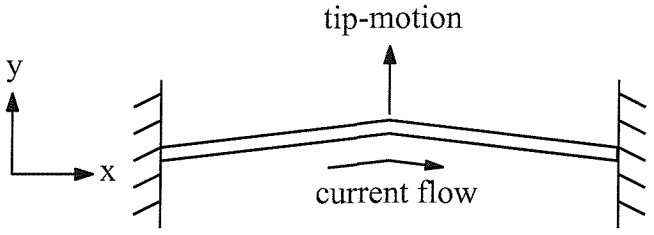

Figure 2.10: Bent beam actuator

Que and coworkers [38] fabricated bent-beam actuators from silicon and nickel. With an 800 μm long beam, a tip displacement of 5 μm at an input power of 180 mW was achieved. A 410 μm long nickel beam yields a displacement of 10 μm at an input power of 80 mW. They also report cascaded bent beam devices and used the actuators to drive rotary microengines and linear stepper motors [39]. A theoretical analysis is given in [40].

2.2.4 Other Actuation Principles

Shape Memory Alloy Actuators

When shape memory alloys (SMA), mainly titanium and nickel alloys, are mechanically deformed they return to their original state when heated beyond a certain critical temperature [2, 14]. The reason for this behaviour is a change from one crystal phase (martensite phase) at lower temperature to another crystal phase at elevated temperature (austensite). The effect is reversible and shows a hysteresis. Easy control, high stress and large deflection are the main advantages of SMA actuators. The most significant disadvantages are low power efficiency and problems in fabricating

microactuators.

Buetelfisch et al. [41] fabricated a microactuator that combines SMA actuation with a silicon microstructure. The silicon structure for a gripper tool is defined using deep reactive ion etching (DRIE). A NiTi foil is laser-machined to form the SMA actuator. It is clipped onto the silicon structure and additionally glued on with epoxy resin.

Magnetostrictive Actuators

Magnetostrictive materials are ferromagnetic materials, which undergo an expansion or contraction when a magnetic field is applied. The reason for the change in length is the alignment of the Weiss' domains parallel to the magnetic field [14]. The magnetostrictive effect was first discovered in nickel. For actuator applications terbium-iron and dysprosium-iron alloys (e. g. Terfenol-D) are used, since they produce considerably higher strains (in the region of $1 \cdot 10^{-3}$ to $2 \cdot 10^{-3}$) [2].

A Terfenol-D actuator usually consists of a rod inserted into a coil, which generates the magnetic field. Since the tensile strength of Terfenol-D is very low, the actuator is designed to be under permanent tension [42]. Sputtering of magnetostrictive materials allows integration into silicon devices. Flik et al. [43] fabricated a fluidic switch actuated by a magnetostrictive bimorph structure, which is shown in figure 2.11.

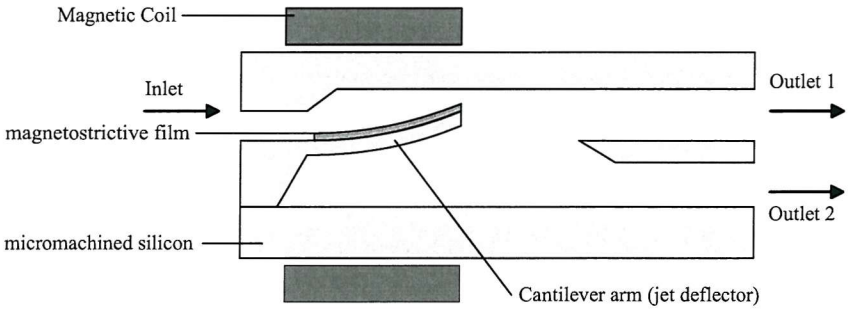

Figure 2.11: Magnetostrictive fluidic switch [43].

Electromagnetic Actuators

Electromagnetic actuators in the form of electro-motors play a very important part in the macro world. But also in the micro-regime electromagnetic actuators have been implemented. Improving the magnetic properties of materials and fabrication techniques for micro-coils remain challenges researchers are faced with [14].

Figure 2.12 shows a reluctance stepping motor [44]. The rotor with three inde-

pendent electro-magnets tends to take a position with regard to the serrated stator such that the magnetic resistance (reluctance) reaches a minimum. If the coils are excited with a phase-shifted current, a sliding motion can be obtained.

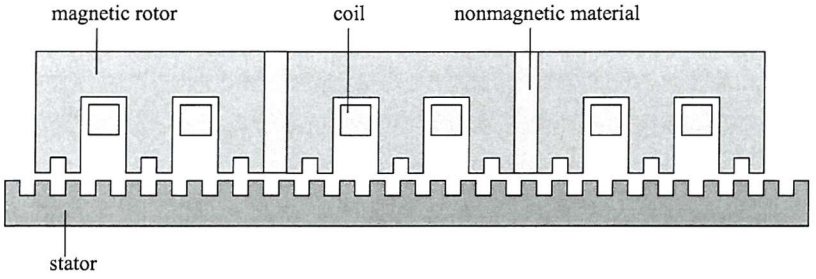

Figure 2.12: Electromagnetic stepper drive [44].

Ahn and Allen [45] presented a process to fabricate coils for magnetic actuators. It is based on polyimide molds (4 layers), electroplating of a permalloy core and sputtering of an aluminium conductor. Figure 2.13 shows the coil with its planar aluminium conductor and the two-level magnetic core.

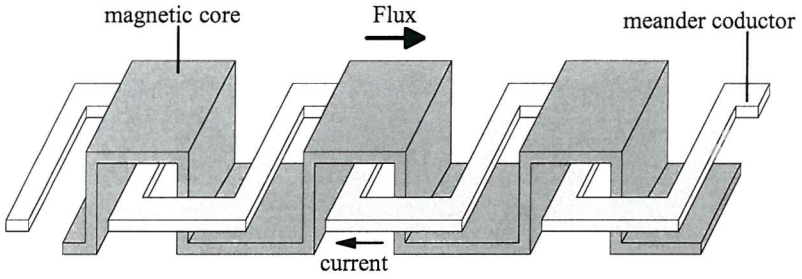

Figure 2.13: Meander-type magnetic coil [45].

Further Actuation Principles

It should be noted at this point that further actuation principles have been used for microactuation, including hydraulic, pneumatic, electrorheological, biological and chemical actuators. More details can be found in [2] and [14].

2.3 Applications of Microactuators

2.3.1 Integrated Scanning Probe Devices

The invention of the scanning tunnelling microscope (STM) in 1982 provided scientists and industry with an instrument capable of imaging and measuring the surface

topology of conducting samples with unprecedented resolution and accuracy. A tunnelling current between the conductive tip and the surface is utilised to track and measure the topology of the sample [46]. The atomic force microscope (AFM) followed in 1986 expanding the range of samples to nonconductive materials. Pressing the probe against the surface, maintaining a constant force allows tracking of the surface to acquire topological data [47].

The excellent resolution of scanning probes has been combined with fabrication techniques to produce nanoscale structures and devices. This so-called nanolithography or nanofabrication includes anodic oxidation [48–52], resist patterning [53–55], chemical vapour deposition [56, 57], field evaporation [58, 59], and single atom positioning [60].

The serial character of scanning probe microscopy and proximal probe lithography means the throughput of those techniques is very limited. To overcome this problem, development work is being done towards parallel probe devices, which increase the working speed significantly. Parallel probes require integrated translation microactuators, which allow for a wide actuation range without occupying a large area and without consuming a lot of energy. Different approaches have been applied to fulfill these requirements comprising piezoelectric, electrostatic and electro-thermal systems. In the following subsections, these approaches are reviewed.

Piezoelectric Bimorph STM

Akamine and coworkers [5] implemented a microfabricated STM consisting of a piezoelectric bimorph cantilever allowing motion in three dimensions. The cantilever consists of 2 layers of piezoelectric ZnO films, embedded into 3 electrode layers of aluminum and 4 dielectric layers. The upper and lower metal layer is divided into 2 independently addressable electrodes. Thus, there are 4 piezoelectric sections that can be controlled by the surrounding 5 electrodes. Figure 2.14 shows a cross section of the bimorph.

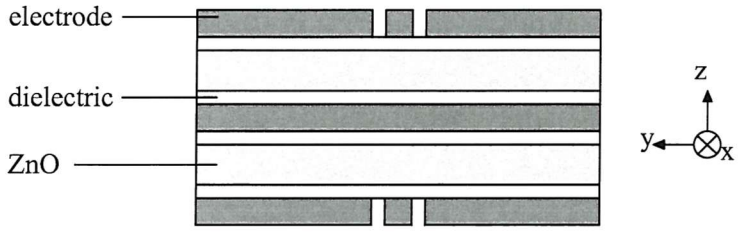

Figure 2.14: Cross section of the piezoelectric bimorph [5].

Figure 2.15 illustrates the movements achievable. When the same electric field is applied to all four piezoelectric sections, they all contract in the same way resulting

in motion in the x-direction (figure 2.15a). Bending in the the y-direction is achieved when applying opposite fields to the left and right electrodes (figure 2.15b). Opposite electric fields on the top and the bottom electrodes cause bending in the z-direction. (figure 2.15c). Opposite fields on diagonal pairs of electrodes cause twisting of the cantilever (figure 2.15d). While in the z-direction a deflection of 250 nm/V is achievable, the movement in the x- (1.4 nm/V) and y-direction (10 nm/V) is very limited.

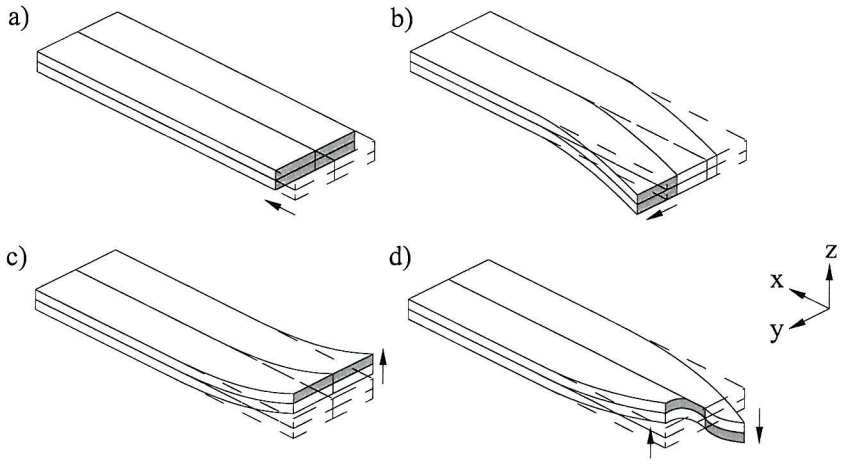

Figure 2.15: Working principle of a piezoelectric bimorph [5].

The piezoelectric bimorphs are fabricated by repeated deposition of Al, PECVD-nitride and ZnO layers (3 μm thick) onto a silicon bulk micromachined membrane. When the layers for the bimorph are deposited and structured, the silicon membrane is removed, revealing the freestanding cantilever.

Electrostatic SPMs

Indermuehle et al. [6] fabricated and operated an AFM based on electrostatic actuation. Four electrostatic comb actuators enable a table to be scanned in the xy-plane. An AFM tip is integrated onto this table to perform topographic measurements. The movement of the tip and the table in the z-direction is detected by a laser beam deflection system from the back. Fabrication involves silicon fusion bonding of two structured wafers and subsequent definition of the tip and beams by RIE processes. A maximum displacement of 12 μm with an applied voltage of 300 V has been observed. Figure 2.16 shows the integrated AFM device.

Employing the SCREAM process [61], two integrated STMs based on comb actuators have been implemented by Xu et al. [62]. The small STM measures 200 μm by 200 μm and allows movements of 50 nm with an applied voltage of 40 V. The large device, 2 mm by 2 mm, has an actuation range of up to 2.9 μm with a driving voltage

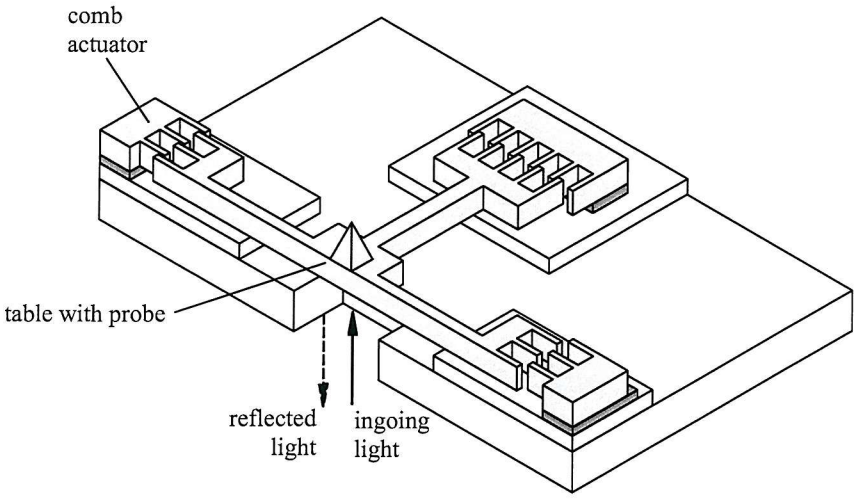

Figure 2.16: Integrated electrostatic AFM [6].

of 40 V. This STM has been used to obtain a topographic image of a silicon sample. Using a similar fabrication process, Yao and coworkers fabricated an xy-translation actuator measuring only 40 μm by 40 μm [63]. It incorporates four parallel plate actuators, which allow movements of up to 200 nm for a driving voltage of 55 V.

Thermally Actuated Micro Scanning Probe

Trevor Niblock [64] fabricated a three-dimensional actuator based on planar bimorphs. It consists of two perpendicular silicon bridges with 4 independently addressable heating resistors. On the back of the silicon bridges aluminium is deposited to obtain the bimorph structure. Figure 2.17 shows the quadrapod actuator.

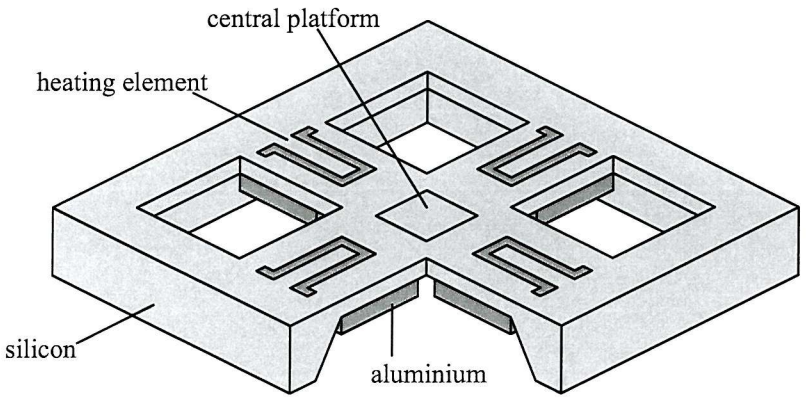

Figure 2.17: Thermally actuated quadrapod structure [64].

The quadrapod design is a robust 3-dimensional actuator. It delivers a wide actuation range for the out of plane movement (up to 100 μm). However, the in-plane movement is limited to approximately 500 nm in each direction. Another disadvantage lies in the high power consumption (0.5 W for 100 μm).

2.3.2 Micro-Switches

Miniaturisation of relays has been an important application of MEMS technology since its infancy [65]. Compared to transistors and other solid state devices, mechanical switches offer the advantage of lower on-resistance and higher off-resistance as well as a separation of the control and load circuit. Miniaturisation of mechanical switches helps increase their operational speed and decrease fabrication costs. Application areas of micro relays are wide including automotive applications, test equipment and telecommunications [66]. Whereas standard relays use electromagnetic actuation only, micro-relays also employ electrostatic and thermal principles.

To be of practical use, micromachined relays have to meet the following requirements: The switching gap should be large to withstand reasonable load voltages. For load voltages in the kV range, approximately 250 μm is required. With MEMS-actuators the gap is typically limited to roughly 5 to 20 μm allowing a load voltage of up to approximately 300 to 600 V [67]. Another important aspect is that a sufficient contact force is needed to obtain a low and stable contact resistance. The contact forces of conventional relays are typically tens of mN, whereas suitable MEMS actuators only provide up to a few mN. However, a suitable selection of the contact metallurgy can significantly reduce the contact force to about 1 mN [68]. The ability to carry large currents is inherently restricted in MEMS-relays, since planar metallisation techniques only allow limited crossectional areas for conductors. Electroplating of conductors is a way to overcome this disadvantage [66].

Electrostatically Driven Micro-Switches

Electrostatic micro relays mainly use parallel plate actuators to close or open electrical contacts (section 2.2.1). Schiele et al. [69] fabricated electrostatic relays using a surface micromachining process with two metal layers. Figure 2.18 shows a schematic view of the relay. A contacting bar at the end of a cantilever electrode connects the two fixed contacts, when the actuation voltage is supplied between the two actuation contacts. Further examples of electrostatically actuated relays can be found in [70–73].

Magnetic Micro-Relays

Taylor and Allen implemented an integrated magnetic micro-relay, where a single layer coil is used as the actuator [74]. The design is a double-pole single-throw relay, which means one coil is used as the actuator for two independent contact pairs. The relay is fabricated by polyimide mold electroplating techniques [75].

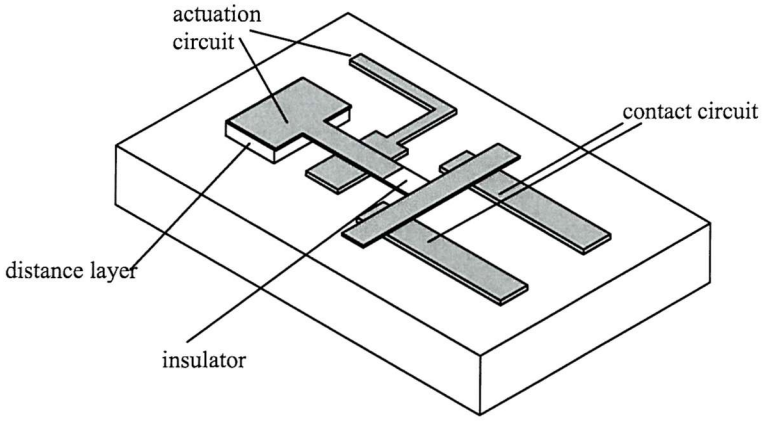

Figure 2.18: Electrostatic micro-relay [69].

Thermal Micro-Relays

Seki et al. [76] demonstrated a thermally driven micro-relay based on a buckling actuator. A thin silicon clamped-clamped beam has a polysilicon heater on top. When heated the silicon beam buckles upwards and closes contacts attached to a glass plate. The fabrication process is based on direct bonding of a handle silicon wafer to the device wafer. Sun et al. [21] fabricated a bistable micro-relay based on thermally actuated planar bimorphs.

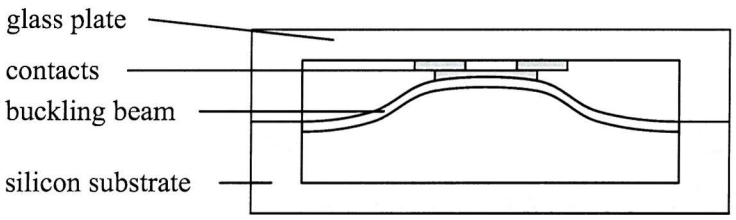

Figure 2.19: Thermal buckling micro-relay [76].

2.3.3 Other Applications of Micro-Actuators

The following subsection gives an overview of further applications of translation actuators.

Microfluidics

The field of microfluidics has become an important part of MEMS with applications in ink-jet printing and medicine. General reviews of the field are given in [2] and [77]. The main application of actuators is in membrane micropumps. These have been implemented based on electrostatic [78, 79], piezoelectric [80–82], electromagnetic [83]

and thermal bimorph actuators [84]. Schabmueller [85] et al. demonstrated a gas-liquid micropump tolerant to air bubbles based on piezoelectric actuation. Two bulk micromachined silicon wafers are glued together. One of them houses the valves, the other one forms the membrane on top of which a PZT actuator is glued. Figure 2.20 shows the micropump.

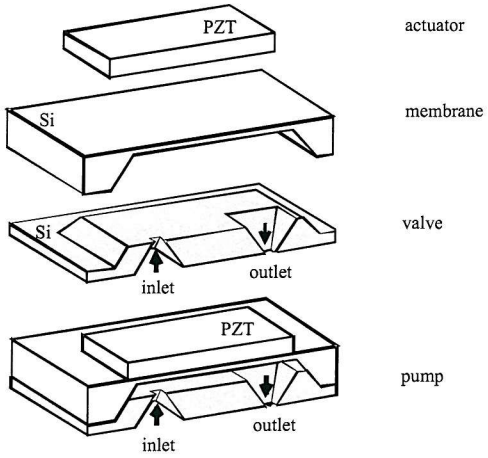

Figure 2.20: Piezoelectric micropump [86].

Mechanical Resonators

Vibrating micro structures can be used for a wide range of sensing applications. The dependence of the resonant frequency on physical parameters which effect the vibration energy is exploited for precise measurements [87]. A theoretical review on the use of resonators for sensing applications is given in [88]. The vibrations have been excited by electrostatic [10, 89], piezoelectric [90, 91] and thermal actuation [92]. Typical applications are accelerometers [91], gyroscopes [93], pressure sensors [94], chemical and biological sensors [95].

Figure 2.21 shows a pressure sensor based on a resonant microbeam [94]. The microbeam is inside a vacuum-cavity and is electrostatically excited. It sits on a silicon diaphragm which is subjected to the pressure to be measured. The resonant frequency of the beam shifts with the applied axial strain. The fabrication combines surface and bulk micromachining.

Actuated Micromirrors

Micro-scanners based on actuated mirrors are used for optical signal processing [96], raster scanning projection [97] and bar code scanning [98]. A review is given by [99]. The basic structure is a suspended micromirror, which tilts along one or two axes as

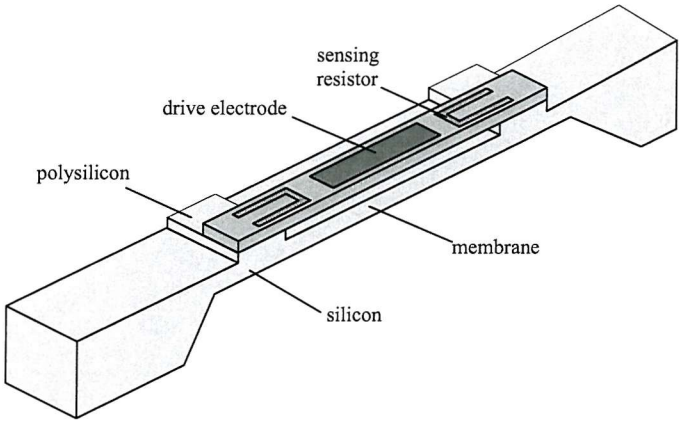

Figure 2.21: Pressure sensor based on a resonant micro-beam [94].

seen in figure 2.22. Micromirrors are driven electrostatically [100, 101], piezoelectrically [102], electromagnetically [103] and thermally [22, 23, 104, 105].

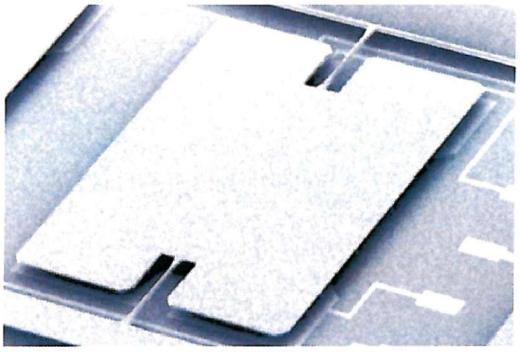

Figure 2.22: SEM-view of an electrostatically driven micromirror [99].

Microgrippers

Assembling microparts requires gripping tools exceeding the precision of conventional manipulators. Since grippers that pick parts using adhesive substances [106], magnetism [107], vacuum or electrostatics [99] are limited in their application, mechanical tweezer-like tools are gaining importance. They need to be designed to suit the parts to be picked in terms of the tweezer gap and the gripping force.

For opening and closing the tweezers, microgrippers use electrostatic [108], piezoelectric [109, 110], thermal (bimorph) [111, 112], thermal (compliant structures) [29, 35], and shape memory alloy actuators [41, 113, 114]. Figure 2.23 shows a piezoelectrically actuated microgripper made from glass [110].

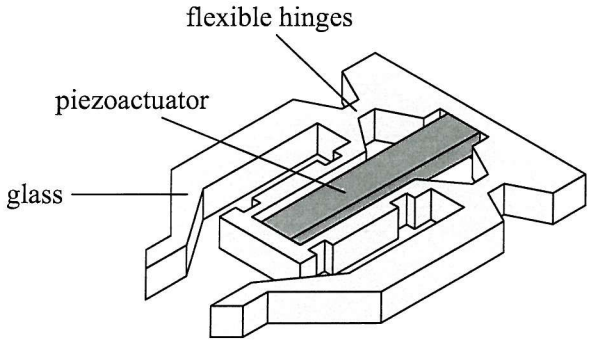

Figure 2.23: Piezoelectrically driven microgripper [110].

2.4 Conclusion

Besides sensors and control circuitry, microactuators are necessary components in many microsystems. Different actuation principles have been used depending on the application. Electrostatic actuators have been implemented as parallel plate actuators and comb-drives. They are rather easy in fabrication but suffer from high operational voltages and fairly low forces. Piezoelectric actuators provide high forces, but with a very limited actuation range. Thermal actuators have been demonstrated based on the bimetal effect, buckling and unevenly distributed power dissipation (hot arm actuators and compliant structures). While thermal actuators are generally easy to fabricate, they have the disadvantages of comparably high power consumption and difficulty in control. Electromagnetic actuators are feasible, however they are complicated in fabrication. Besides these classic actuation principles, micro actuators have also been demonstrated based on the magnetostrictive effect, shape memory alloys, hydraulics, pneumatics, electrorheological, biological and chemical effects. Applications of microactuators are widespread and include micro-relays, micro-positioning systems, micropumps, resonant drives and micromirrors.

2.5 Overview on Actuator Principles

The following listing gives an overview on the advantages and disadvantages as well as applications of the most important actuator principles. Quantitative figures are given where appropriate.

2.5.1 Electrostatic Actuators

- Advantages: easy fabrication, high speed, low power consumption.
- Disadvantages: high voltage required (50 to 300 V, [14]), low forces.

- Applications: micro positioning [6], micro mirrors [100], micro grippers [108], micro-switches [69] , resonant sensors [10], micro pumps [79].

2.5.2 Piezoelectric Actuators

- Advantages: high forces, good resolution, low power consumption.
- Disadvantages: high voltages required (50 to 1000 V, [14]), limited actuation range (few μm)
- Applications: micro positioning [5], micro mirrors [102], micro grippers [68], resonant sensors [90], micro pumps [80].

2.5.3 Thermal Actuators

- Advantages: high forces, large actuation range, easy fabrication, low voltages.
- Disadvantages: high power consumption, slow reaction speed.
- Applications: micro positioning [64], micro mirrors [104], micro grippers [29], micro-switches [76], resonant sensors [92], micro pumps [84].

2.5.4 Electromagnetic Actuators

- Advantages: high forces.
- Disadvantages: difficult fabrication.
- Applications: micro mirrors [103], micro-switches [74], micro pumps [83].

Chapter 3

Concept of Vertical Bimorph Actuators

3.1 Introduction

In chapter 2, a wide range of translation actuators have been reviewed. Silicon micromachined translation actuators perform movement either parallel or normal to the wafer plane and are classified as in-plane or out-of-plane actuators respectively. As far as thermal actuators are concerned, in-plane motion was only achieved with approaches based on one material including hot arm actuators, compliant structures, bent-beam and buckling actuators. Bimorph actuators were restricted to out of plane-deflection, because all standard metal deposition techniques are planar processes in nature and hence only planar bimorphs were implemented.

Since bimorph designs offer the highest actuation range at a comparably low temperature, it would also be desirable to have in-plane bimorph devices. To achieve in-plane movement, fabrication of vertical bimorphs is proposed, the concept of which is presented in this chapter. These use the bimetal effect to perform large in-plane displacements with low power consumption at low operating temperatures (up to about 120 $^{\circ}$ C). Vertical bimorphs are an entirely novel concept and have only been implemented by Southampton University [115–117]. However, the fabrication requires aluminium deposition onto the sidewalls of silicon trenches - a new process, which is discussed in chapter 5.2.

First, the basic concept is presented. Then, a prototype one-dimensional actuator based on a clamped-clamped beam is discussed. The disadvantages of the clamped-clamped approach lead to the design of a meander-shaped beam, which can be used for an advanced one-dimensional actuator. A combination of four meander-beams enables two-dimensional translation movement. The meander-beam design is also

applied to normally open and normally closed micro-switches. Lastly, an actuated cantilever is presented.

3.2 Thermally Actuated Vertical Bimorph Beams

Thermally actuated bimorphs use two materials with significantly different thermal expansion coefficients. In planar bimorphs, the two materials are sandwiched on top of one another, whereas in vertical bimorphs the two materials are next to each other. In our implementation based on silicon micromachining processes, a vertical bimorph consists of a silicon beam side-coated with aluminium. When heated, the beam bends towards the silicon side due to the larger thermal expansion coefficient of aluminium as illustrated in figure 3.1.

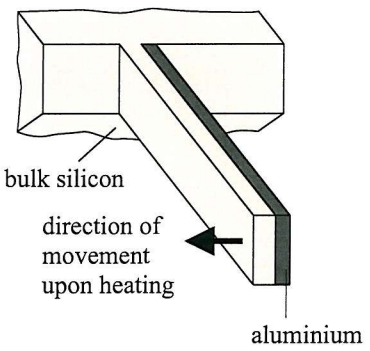

Figure 3.1: Vertical bimorph beam.

3.3 Clamped-Clamped One-Dimensional Actuator

Figure 3.2 depicts a one-dimensional actuator based on a double clamped beam. This design is the most straightforward approach for an internally heated vertical bimorph. The implementation of the actuator uses a silicon on insulator (SOI) substrate. The contact pads are in electrical contact with the silicon underneath and hence with the silicon of the beam. The aluminium fillets are electrically insulated from the silicon beams by a thin oxide layer. Thereby it is ensured, that the bimorphs are the parts of the highest electrical resistance in the circuit and therefore have the highest voltage drop. Trenches around the bondpads provide electrical insulation of the circuit from the bulk silicon. When a driving voltage is applied at the two contact pads, a current flows through the silicon beam causing heat dissipation. Since the thermal expansion coefficient of aluminium is significantly higher than that of silicon, the bimorph bends to the left as indicated by the arrow in figure 3.2.

A disadvantage of the clamped-clamped design is that only small displacements can be achieved as compared to a cantilever beam. Furthermore, buckling effects can occur causing difficulties in the prediction of the displacement and direction of movement. Buckling describes the phenomenon of lateral displacement of a slender beam loaded by axial compressive forces [18]. Buckling does not necessarily mean failure of the beam. It is a different mechanism from the bimetal effect, which is based on a bending moment due to the different thermal expansion coefficients of aluminium and silicon.

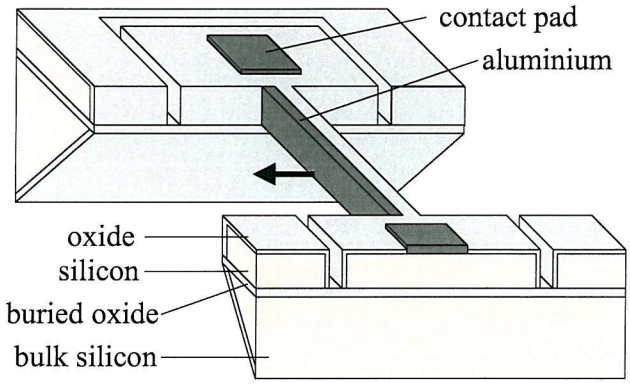

Figure 3.2: One-dimensional clamped-clamped beam actuator.

3.4 One-Dimensional Meander Type Actuator

For improved displacement range, an advanced one-dimensional actuator is devised. It consists of a meander-shaped silicon beam with sidewalls partly covered by aluminium as shown in figure 3.3. The fabrication requires two aluminium sidewall deposition stages. The working principle is almost identical to the clamped-clamped actuator. A current through the silicon of the bimorph causes heat dissipation and hence bending of the bimorphs. This results in a displacement of the front plate as indicated by the arrow. The symmetrical design ensures a linear motion. Isolation trenches around the contact pads and a thin oxide layer provide the necessary electrical insulation. A gold conductor (that is in contact to the silicon beam) keeps the heat dissipation at the front plate to a minimum. There is no aluminium on the sidewall of the hinge, which therefore does not contribute to the actuation.

3.5 Two-Dimensional Meander Type Actuator

Combining four basic meander type actuators enables two-dimensional actuation, as required for a positioning system. Figure 3.4 shows a two-dimensional actuator. To

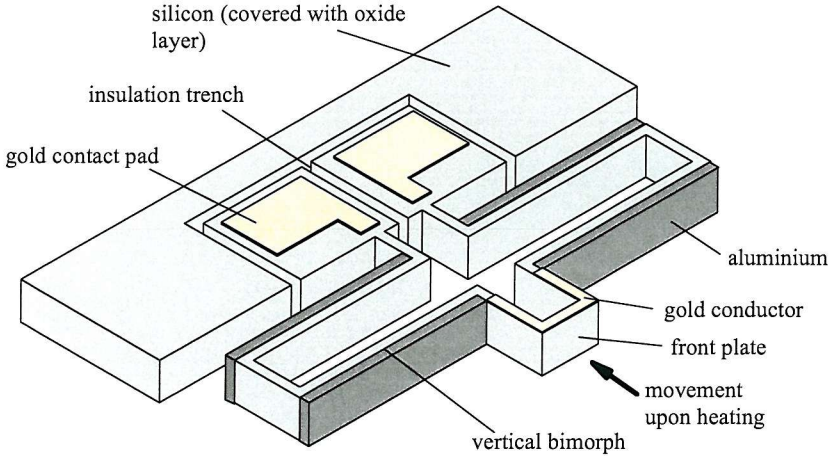

Figure 3.3: One-dimensional meander type actuator.

move the central table in the positive x-direction, a symmetrical voltage is applied to the contact pair labelled +x. An electrical current flows through the corresponding meander beam, heating up the beam and causing the bimorphs to bend. The bimorphs are arranged such that they pull the central table in the positive x-direction. All other beams are inactive and act merely as a compliant suspension of the table. Again, the symmetrical design assures that the table moves along a straight line. To avoid unwanted current flow, the unused contacts are kept at ground potential. Movement in the -x, +y and -y direction is obtained similarly by applying a voltage to the corresponding contacts.

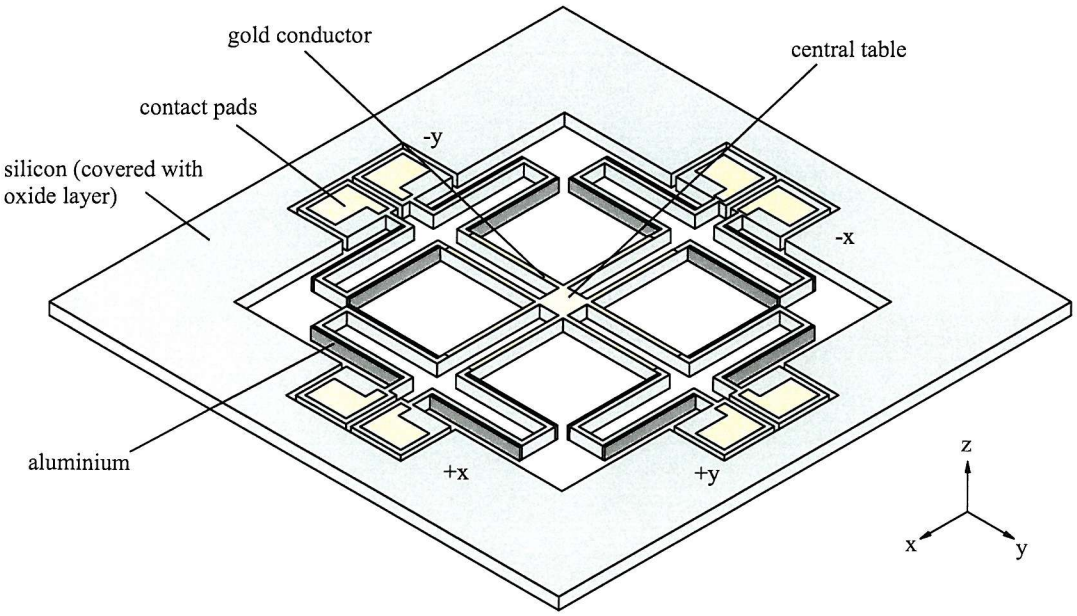

Figure 3.4: Two-dimensional meander type actuator.

3.6 Micro-Relays

A one-dimensional meander actuator moves a gold conductor situated at the front plate, which opens and closes the contact between a fixed gold contact pair. In the case of a normally open micro-switch, the actuator is designed to close the contact gap when the actuation voltage is applied, as depicted in figure 3.5. In the case of a normally closed switch the actuator opens the contact when powered as illustrated in figure 3.6.

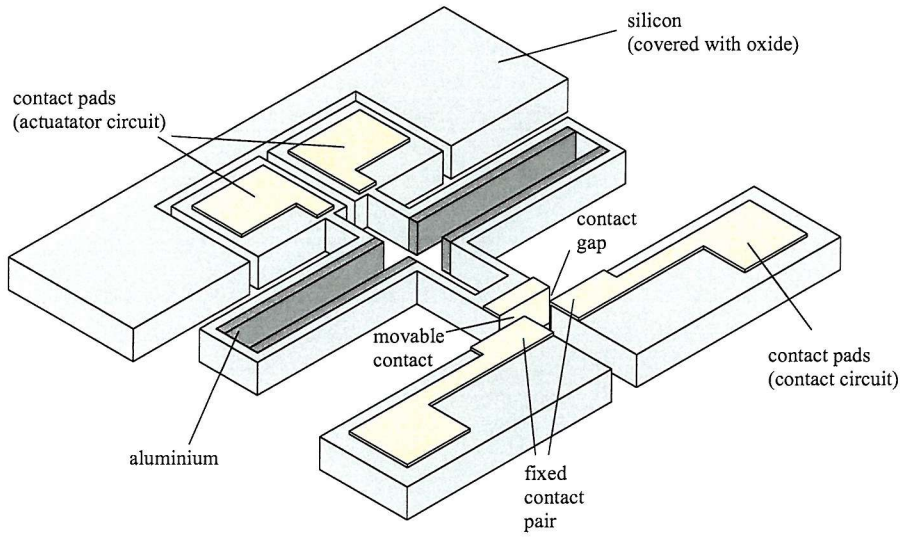

Figure 3.5: Normally open micro-switch based on the meander type actuator.

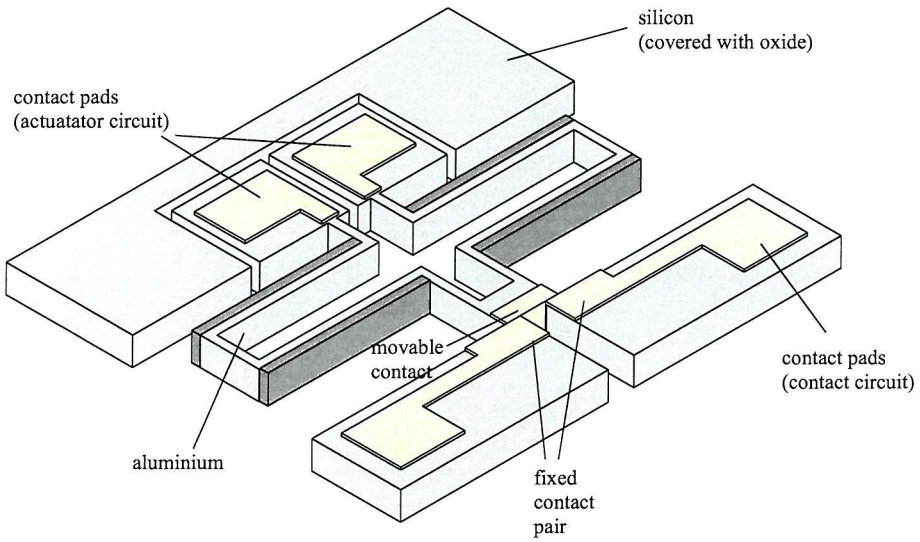

Figure 3.6: Normally closed micro-switch based on the meander type actuator.

3.7 Actuated Bimorph Cantilever

It is possible to perform large displacements with a bimorph cantilever beam. Due to the asymmetrical design the tip motion does not follow a straight line. Figure 3.7 shows the actuated cantilever. Contact pad A is in contact to the underlying silicon and hence in contact to the silicon beam. Pad B is insulated from the silicon by a thin oxide layer, but is in contact to the aluminium of the bimorph. A gold conductor at the tip of the beam is in contact to both the aluminium and the silicon of the beam. This arrangement enables an electrical current to pass from pad A through the silicon beam and back through the aluminium sidewall coating to pad B. Since the resistivity of silicon is significantly higher than that of aluminium, the voltage drop across the silicon beam and hence its power dissipation is higher than in the aluminium. Thus, the bimorph can be heated by applying a driving voltage across the two contact pads. The tip of the cantilever moves as indicated by the arrow in figure 3.7.

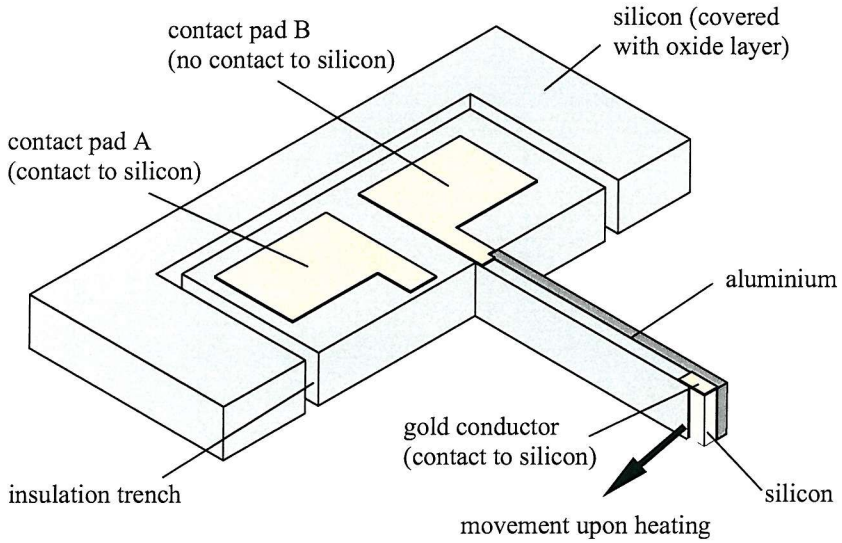

Figure 3.7: Actuated bimorph cantilever.

3.8 Conclusion

Besides electrostatic comb drives and thermally excited compliant structures, vertical bimorphs are efficient integrated in-plane actuators. They only consume moderate input power, enable large deflections, can be operated at convenient voltages and are rather straightforward in fabrication. They are compatible to other MEMS and microelectronics processes. The concept allows a large amount of freedom in design, since deep reactive ion etching (DRIE) is used for the pattern definition.

The simplest design for linear motion is based on a double clamped beam. Better performance can be achieved with a meander-shaped actuator. This is also the basic building block for a two-dimensional positioning stage and micro-switches. An actuated cantilever has been presented, which offers large deflections. However, the movement is not along a straight line. Other actuator designs and applications are conceivable.

Chapter 4

Theoretical Analyses

4.1 Introduction

In this chapter analyses are carried out to predict the physical behaviour of vertical bimorph actuators. The analyses are concerned with temperature distribution, beam deflection, vertical stiffness, thermal time constants and resonant modes. Both analytical and numerical methods are applied.

In section 4.2 an analytical model for the clamped-clamped beam actuator is developed and used to obtain the temperature distribution curve (4.2.1) and the deflection curve (4.2.2). Based on the equation for the deflection curve, design guidelines are derived (4.2.3). To get an idea about the vertical stiffness of the actuator, the vertical spring constant is derived (4.2.4). In section 4.2.5 vertical resonant modes are calculated analytically.

In section 4.3, ANSYS simulations are carried out on the clamped-clamped beam actuator including temperature distribution (4.3.2), static deflection (4.3.3), thermal time constant (4.3.4) and resonant frequencies (4.3.5). Section 4.4 is concerned with ANSYS simulations on the one-dimensional meander type actuator, section 4.5 describes ANSYS simulations of the two-dimensional meander actuator.

4.2 Analytical Analyses on the Clamped-Clamped Beam Actuator

Figure 4.1 shows the critical dimensions of the bimorph actuator. We have fabricated actuators varying in these dimensions. The height h is 6 μm, the length l ranges from 400 μm to 1400 μm. The width w_{Si} of the silicon part of the bimorph is between 3 μm and 5 μm, the width w_{Al} of the aluminium part of the bimorph is between 1 μm

and 2.5 μm.

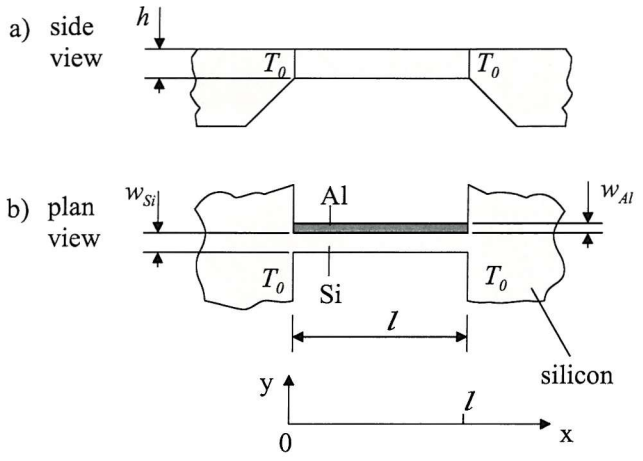

Figure 4.1: Critical dimensions of the clamped-clamped actuator.

4.2.1 Temperature Distribution

The model is based on the following simplifying assumptions: The electrical resistivity is constant along the beam. The electrical power dissipated by the current flow is entirely converted into heat and evenly distributed along the beam. The ends of the bimorph remain at a constant temperature T_0, and all the heat generated in the bimorph is conducted to the ends of the beam, which results in a temperature distribution along the bimorph. The thin oxide layer has been neglected in the calculations.

The heat diffusion equation according to Incropera and de Witt [118] is given by

$$\frac{\partial}{\partial x}\left(k\frac{\partial T}{\partial x}\right)+\frac{\partial}{\partial y}\left(k\frac{\partial T}{\partial y}\right)+\frac{\partial}{\partial z}\left(k\frac{\partial T}{\partial z}\right)+\dot{q}=\rho c_p\frac{\partial T}{\partial t} \tag{4.1}$$

where T is the temperature, x, y, z are the spatial coordinates, k the thermal conductivity, $\dot{q}$ is the rate at which energy is generated per unit volume (Wm^{-3}) and ρ the mass density, c_p the specific heat at constant pressure and t the time. The heat diffusion equation describes the condition of conservation of energy for a control volume. It is based on the fact that the sum of the heat transfer rates through the boundary areas of the control volume and the energy generation rate within the control volume equals the change of thermal energy stored in the control volume. Solving the heat distribution equation considering the boundary conditions yields the temperature distribution of the structure concerned. In the case of our bimorph beam, it is assumed that the electrical power due to the current through the silicon part of the bimorph is entirely converted into heat. We only take steady-state

heat conduction along the bimorph beam into account. Convection and radiation are neglected. The thermal conductivity k is constant. Thus, the heat diffusion equation simplifies to

$$\frac{d^2T}{dx^2} + \frac{\dot{q}}{k} = 0 \tag{4.2}$$

The energy generation rate $\dot{q}$ equals the electrical input power P divided by the volume of the bimorph:

$$\dot{q} = \frac{P}{lh(w_{Si} + w_{Al})} \tag{4.3}$$

The thermal conductivity k is given by the weighted mean value of the thermal conductivity for aluminium k_{Al} and silicon k_{Si} [118]:

$$k = \frac{w_{Si}k_{Si} + w_{Al}k_{Al}}{w_{Si} + w_{Al}} \tag{4.4}$$

To solve the differential equation, the boundary condition that the temperature on both ends of the beam equals T_0 is used:

$$T(x = 0) = T(x = l) = T_0 \tag{4.5}$$

Substituting equations 4.3 and 4.4 into equation 4.2 and solving the differential equation yields the equation of the temperature distribution curve:

$$\Delta T(x) = -\frac{C}{l}x^2 + Cx \tag{4.6}$$

$$C = \frac{P}{2h(w_{Si}k_{Si} + w_{Al}k_{Al})} \tag{4.7}$$

where $\Delta T(x) = T(x) - T_0$ is the temperature difference between location x at the bimorph and the bulk silicon. The constant C has been introduced for simplification of the equation. Figure 4 shows the calculated temperature distribution curve for a 1000 μm long bimorph beam at an input power of $P = 2\ mW$. This power would be produced using a voltage of 9 V across the silicon beam used in the experimental work (see chapter 7).

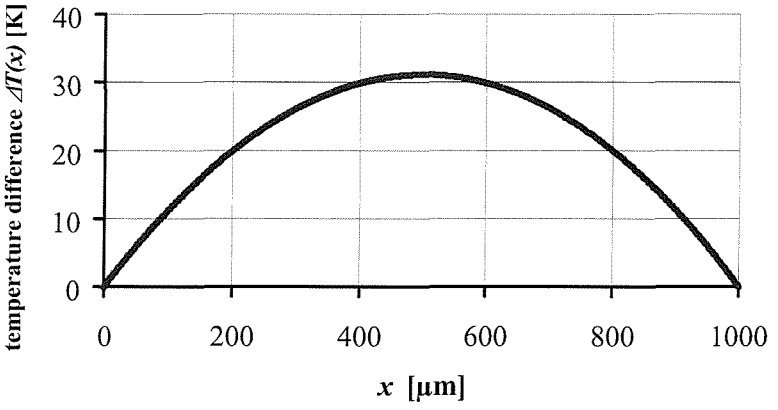

Figure 4.2: Temperature distribution curve $\Delta T(x)$ ($P = 2\ mW$, $l = 1000\ \mu m$, $w_{Si} = 5\ \mu m$, $w_{Al} = 2.5\ \mu m$, $h = 6\ \mu m$).

4.2.2 Deflection Curve

Our bimorphs have rectangular cross-sections. Hence the second moment of area for the silicon part I_{Si} and for the aluminium part I_{Al} can be expressed by [18]:

$$I_{Si} = \frac{1}{12} h w_{Si}^3 \tag{4.8}$$

$$I_{Al} = \frac{1}{12} h w_{Al}^3 \tag{4.9}$$

According to Timoshenko [7], the inverse radius of curvature $\frac{1}{r}$ for a bimorph beam not subjected to external forces is given by

$$\frac{1}{r} = B\Delta T(x) \tag{4.10}$$

$$B = \frac{2(\alpha_{Al} - \alpha_{Si})}{(w_{Si} + w_{Al}) + \frac{h(E_{Si} w_{Si}^3 + E_{Al} w_{Al}^3)}{3(w_{Si} + w_{Al})} \left(\frac{1}{E_{Si} w_{Si} h} + \frac{1}{E_{Al} w_{Al} h} \right)} \tag{4.11}$$

where α_{Si} and α_{Al} are the thermal expansion coefficients , E_{Si} and E_{Al} the Young's moduli of silicon (< 100 >direction) and aluminium respectively. The constant B has been introduced for simplification.

As illustrated in Figure 4.3a, for a clamped-clamped beam, the reaction forces R_A and R_B at the end-points A and B, and the reaction couples M_A and M_B have to be taken into account. From the free body diagram in Figure 4.3b we obtain the equilibrium of moments:

$$M = M_A - R_A x \tag{4.12}$$

where M is the bending moment at the cross-section of the beam at location x.

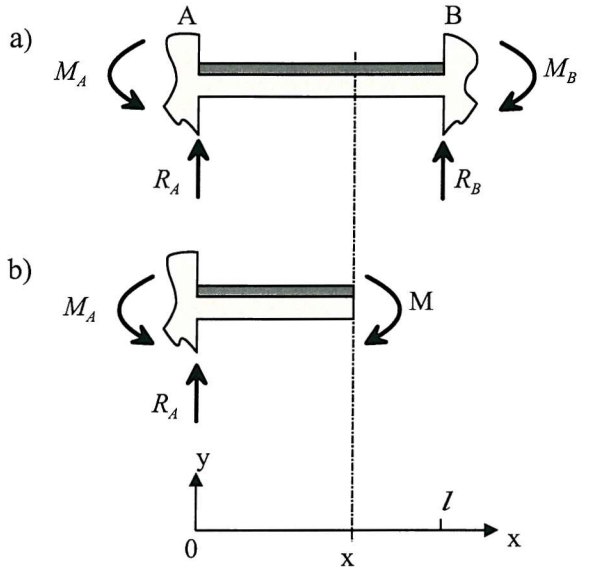

Figure 4.3: a) Reaction forces and reaction couples at the supports of the beam, b) free body diagram.

For small slopes of deflection and materials that follow Hooke's law, the second derivative of the deflection $\frac{d^2v}{dx^2}$ equals the inverse radius of curvature $\frac{1}{r}$. Taking that into account and considering the reactions at the ends of the beam, we obtain the differential equation of the deflection curve from equation 4.10 [18]:

$$\frac{d^2v}{dx^2} = -\frac{R_A}{EI}x + \frac{M_A}{EI} + B\Delta T(x) \tag{4.13}$$

where EI is the flexural rigidity of the beam.

To solve the differential equation, the temperature distribution (equations 4.6, 4.7) is substituted, equation 4.13 is integrated twice and the boundary conditions are accounted for: The slope $\frac{dv}{dx}$ and the deflection v at both ends of the beam equal zero.

$$\frac{dv}{dx}|_{(x=0)} = \frac{dv}{dx}|_{(x=l)} = 0 \tag{4.14}$$

$$v(x=0) = v(x=l) = 0 \tag{4.15}$$

From equations 4.14 and 4.15, we get the unknown reaction couple M_A and the unknown reaction force R_A.

$$R_A = 0 \tag{4.16}$$

$$\frac{M_A}{EI} = -\frac{1}{6}BCl \tag{4.17}$$

Using equations 4.16 and A.17, the deflection curve is found to be

$$v(x) = -\frac{1}{12}\frac{BC}{l}x^4 + \frac{1}{6}BCx^3 - \frac{1}{12}BClx^2 \tag{4.18}$$

Solving the differential equation also showed that the lateral reactions R_A and R_B are 0 which agrees with similar calculations carried out in [18] and a structural ANSYS simulations described in section 4.3.3. Figure 4.4 depicts the calculated deflection curve $v(x)$ for a 1000 μm long bimorph beam at an input power of 2 mW (9 V) based on the temperature distribution curve depicted in Figure 4.2. The centre deflection is about 2.2 μm. Note that the calculation carried out here does not account for axial reaction forces at the ends of the beam. An analysis accounting for those is given in appendix A.

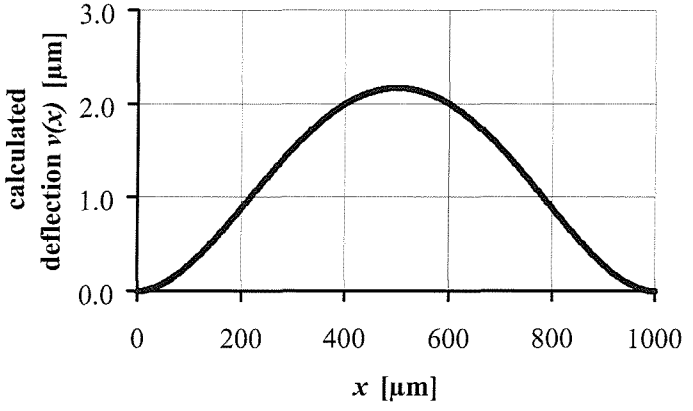

Figure 4.4: Deflection curve $v(x)$ ($P = 2\ mW$, $l = 1000\ \mu m$, $w_{Si} = 5\ \mu m$, $w_{Al} = 2.5\ \mu m$, $h = 6\ \mu m$).

4.2.3 Design Considerations

The analytical model from sections 4.2.1 and 4.2.2 can be used to obtain guidelines for performance optimised design. The maximum deflection v_c of the bimorph always occurs at the centre of the beam. For the operation of the actuator, this centre deflection is of particular interest. It can be expressed as follows

$$v_c = v\left(x = \frac{l}{2}\right) = -\frac{1}{192}BCl^3 \tag{4.19}$$

Considering equation 4.7 and 4.11, v_c can be expressed as a function of the input power P the length of the bimorph l, the width of the silicon w_{Si} and the width of the aluminium w_{Al}.

$$v_c = v_c(P, l, w_{Si}, w_{Al}) \tag{4.20}$$

The maximum temperature difference also occurs at the centre of the bimorph ΔT_c and is given by

$$\Delta T_c = \Delta T_c\left(x = \frac{l}{2}\right) = \frac{1}{2}Cl \tag{4.21}$$

ΔT_c can also be expressed as a function of the same parameters as v_c.

$$\Delta T_c = \Delta T_c(P, l, w_{Si}, w_{Al}) \tag{4.22}$$

Length of the bimorph

From equations 4.19, 4.11 and 4.7 it can be seen that the centre defelction v_c rises with the third power of the length l. Therefore one should design long beams for large displacements. However, increasing the length of the beam also means

- an increase in the centre temperature difference ΔT_c, which can be a disadvantage for some applications, such as BioMEMS.
- an increase in the time constant τ (see section 4.3.4) which is a drawback for positioning and switching applications.
- a decrease of the vertical spring constant k_z, leading to decreased vertical stiffness (see section 4.2.4), increasing the risk of unintended movement in the z-direction.
- a decrease of the resonant frequencies (see section 4.2.5) which is a drawback for micro positioners.

Therefore, the length should stay within reasonable limits. In our clamped-clamped beam design, the length l ranges from 400 μm to 1400 μm.

Electrical Input power

The centre deflection v_c is directly proportional to the electrical input power P (see equations 4.19, 4.11 and 4.7). This linear relation should ensure good actuation control. The centre temperature difference ΔT_c also rises linearly with P (see equations 4.7, 4.11 and 4.21).

Width of the Aluminium Part of the Bimorph

Figure 4.5 shows a plot of the centre deflection v_c as a function of the width w_{Al} of the aluminium part of the bimorph at constant P, w_{Si}, l, h. The plot is based on equation 4.19. It shows that for a given w_{Si} there is a maximum v_c, which is approx. at $w_{Al} = 1.2\ \mu m$ for $w_{Si} = 3\ \mu m$, $w_{Al} = 1.6\ \mu m$ for $w_{Si} = 4\ \mu m$ and $w_{Al} = 2.0\ \mu m$ for $w_{Si} = 5\ \mu m$. These values for w_{Al} can be easily achieved with the aluminium sidewall evaporation process presented in chapter 5.2. The blunt peaks of the curves suggest that fabrication tolerances for w_{Al} will not have a big influence on the actuator performance.

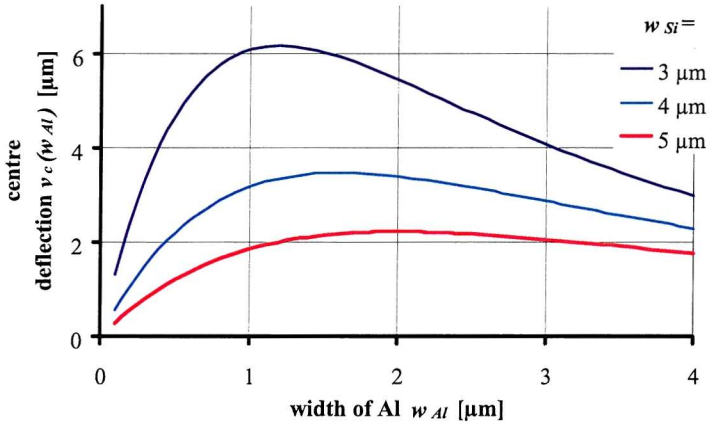

Figure 4.5: Centre deflection v_c as a function of the width of the aluminium part w_{Al} for $w_{Si} = 3, 4, 5\ \mu m$ ($P = 2\ mW$, $l = 1000\ \mu m$, $h = 6\ \mu m$).

4.2.4 Vertical Stiffness

Vertical bimorphs are designed for movement in the wafer plane (x- and y-direction). To avoid unwanted displacement out of the wafer plane (z-direction), it is desirable to have a high rigidity in z-direction. The spring constant in z-direction k_z is an indicator for the rigidity. In the following section, k_z is derived. Figure 4.6 shows a vertical bimorph subjected to a load F_z acting in the (negative) z-direction.

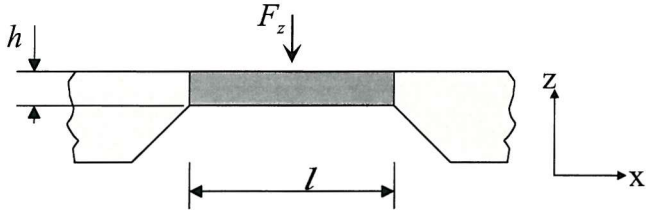

Figure 4.6: Bimorph beam subjected to out of plane load F_z

The out of plane deflection of the centre (z-direction) v_z is given by [18]

$$v_z = -\frac{F_z l^3}{192 E I_z} \tag{4.23}$$

where EI_z is the flexural rigidity of the bimorph in the z-direction. Since our bimorphs are composite beams, the flexural rigidity needs to be evaluated separately for aluminium and silicon. The second moment of area for the silicon part I_{Siz} and the aluminium part I_{Alz} are given by [18] (see also equations 4.33, 4.35).

$$I_{Siz} = \frac{1}{12} w_{Si} h^3 \tag{4.24}$$

$$I_{Alz} = \frac{1}{12} w_{Si} h^3 \tag{4.25}$$

With equations 4.24 and 4.25, 4.23 becomes

$$v_z = -\frac{F_z l^3}{16 h^3 (E_{Si} w_{Si} + E_{Al} w_{Al})} \tag{4.26}$$

The spring constant k_z is the load F divided by the deflection v_z

$$k_z = \frac{-F_z}{v_z} = -\frac{16 h^3 (E_{Si} w_{Si} + E_{Al} w_{Al})}{l^3} \tag{4.27}$$

For comparison, the lateral spring constant k_y for a load F_y acting on the centre of the bimorph in the negative y-direction is derived. Analogously to equation 4.27, k_y is given by

$$k_y = -\frac{-F_y}{v_y} = \frac{192 (E_{Si} I_{Siy} + E_{Al} I_{Aly})}{l^3} \tag{4.28}$$

For a 1000 μm long bimorph beam ($w_{Si} = 5\ \mu m$, $w_{Al} = 2.5\ \mu m$, $h = 6\ \mu m$), k_z is $2.8\frac{N}{m}$. With equations 4.32, 4.34 and 4.34, k_y is calculated to be $8.7\frac{N}{m}$. In order to avoid displacement in the z-direction, k_z should be significantly larger than k_y. Therefore, the height h of the bimorphs needs to be increased. That is the reason, why a 30 μm thick device silicon layer was chosen for the meander type actuators.

4.2.5 Lateral Resonances

When external forces excite vibrations we have the case of forced vibration. The system vibrates at the frequency of the excitation. If the frequency of the excitation

coincides with the natural frequency of the system, large vibrations occur, which are only limited by damping [119]. Large oscillations at resonant frequencies can interfere with the operation of micro-actuators. Therefore, their operational frequency needs to be kept well below the natural frequency. On the other hand, resonances can be exploited in precision sensor applications as described in chapter 2.3.3.

If the vibration takes place in the wafer plane they are called lateral vibrations or lateral resonances. With vertical bimorphs, lateral resonances can be excited thermally, a novel approach for lateral vibrations (see chapter 2.3.3). In this section we develop an analytic expression for the natural frequency of the bimorph structure. In section 4.3.5 we use a modal analysis in ANSYS which accounts for further aspects of the vibration.

According to Blevins [120] the natural frequency of a straight beam is given by

$$f_i = \frac{\lambda_i^2}{2\pi l^2}\sqrt{\frac{EI}{m}} \tag{4.29}$$

where the index $_i$ denotes the mode number. λ_i is a dimensionless parameter reflecting the boundary conditions of the beam, l is the length of the beam, E the Young's modulus, I the second moment of area, and m the mass of the beam per unit length.

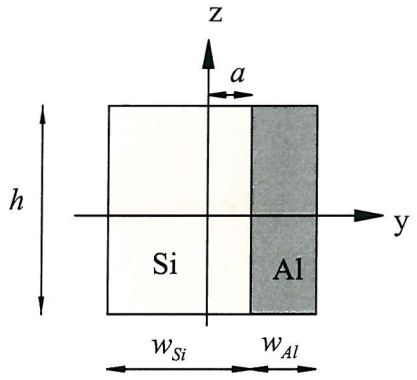

Figure 4.7: Cross section of the bimorph, the z-axis denotes the neutral surface for bending in the wafer plane.

Our bimorphs are composite beams which require equation 4.29 to be adjusted accordingly. To express the second moment of area for the silicon part I_{Siy} and the aluminium part I_{Aly}, we need to find the location of the neutral surface. Figure 4.7 shows a cross section of the bimorph. The neutral surface for bending in the wafer plane is given by the z-axes. The distance of the neutral surface from the material interface is a. In equilibrium the total axial force in x-direction acting on the cross section of the beam must be zero. This is expressed by [18]

$$E_{SI} \int_{Si} ydA + E_{Al} \int_{Al} ydA = 0 \tag{4.30}$$

Since the height h of the bimorph is constant, the differential element of area dA can be replaced with hdy. Inserting the integration limits, which denote the width of the silicon and aluminium part, respectively, results in

$$E_{Si}h \int_{a-w_{Si}}^{a} ydy + E_{Al}h \int_{a}^{a+w_{Al}} ydy = 0 \tag{4.31}$$

Solving the integrals, and rearranging for a, we get

$$a = \frac{E_{Si}w_{Si}^2 - E_{Al}w_{Al}^2}{2(E_{Si}w_{Si} + E_{Al}w_{Al})} \tag{4.32}$$

The second moment of area for the silicon part is given by

$$I_{Siy} = \int_{Si} ydA = h \int_{a-w_{Si}}^{a} ydy \tag{4.33}$$

which is evaluated to be

$$I_{Siy} = h\left(a^2 w_{Si} - a w_{Si}^2 - \frac{1}{3}w_{Si}^3\right) \tag{4.34}$$

Analogously, the second moment of area for the aluminium part is

$$I_{Aly} = \int_{Al} ydA = \int_{a}^{a+w_{Al}} ydy \tag{4.35}$$

which is evaluated to be

$$I_{Aly} = h\left(a^2 w_{Al} + a w_{Al}^2 + \frac{1}{3}w_{Al}^3\right) \tag{4.36}$$

The flexural rigidity EI of the bimorph is given by the sum of the flexural rigidities of both parts

$$EI = E_{Si}I_{Siy} + E_{Al}I_{Aly} \tag{4.37}$$

The mass per unit length is the sum of the masses per unit length of both parts of the bimorph

$$m = hw_{Si}\rho_{Si} + hw_{Al}\rho_{Al} \tag{4.38}$$

where ρ_{Si} and ρ_{Al} are the mass densities of aluminium and silicon respectively.

With equations 4.32, 4.34, 4.36, 4.37 and 4.38, the resonant frequency for the composite bimorph beam can be calculated from equation 4.29. For a 1000 μm long bimorph beam ($w_{Si} = 5\ \mu m$, $w_{Al} = 2.5\ \mu m$, $h = 6\ \mu m$) the first lateral mode f_1 is $47.46khz$ ($\lambda_1 = 4.7300$), the second lateral mode f_2 is $130.8kHz$ ($\lambda_2 = 7.8532$).

Mode Shape

For a freely vibrating beam, the total transverse deformation $Y(x,t)$ can be written as the sum of the modal deformations of the different natural modes [120]

$$Y(x,t) = \sum_{i=1}^{N} A_i \tilde{y}_i(x) \sin(2\pi f_i t + \phi_i) \tag{4.39}$$

where the index $_i$ denotes the mode number, N is the total number of modes, A_i is the amplitude, ϕ_i the phase angle and $\tilde{y}_i(x)$ is the function of the mode shape. The mode shape describes the deformation pattern associated with a certain natural mode and becomes important for resonance measurements. It is given by [120]

$$\tilde{y}_i(x) = \cosh\frac{\lambda_i x}{l} - \cos\frac{\lambda_i x}{l} - \sigma_i\left(\sinh\frac{\lambda_i x}{l} - \sin\frac{\lambda_i x}{l}\right) \tag{4.40}$$

Figure 4.8 shows normalised plots of the mode shapes for the first and second mode of a clamped-clamped beam. The first mode has one half wave, the second mode has two ($\sigma_1 = 0.982502215$, $\sigma_2 = 1.000777312$).

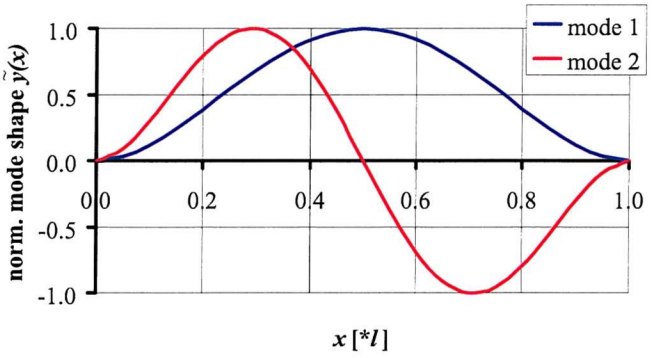

Figure 4.8: Normalised mode shapes for a clamped-clamped beam, mode 1 and 2.

4.3 ANSYS Simulations on the Clamped-Clamped Beam Actuator

To confirm the analytical results and to extend our analyses to areas where analytical models are impractical to apply, we used ANSYS/Multiphysics [121] to carry out simulations based on the finite element method (FEM) and the finite difference method (FDM). Appendix D.1 lists the corresponding ANSYS log files.

4.3.1 Model for the Clamped-Clamped Actuator

All ANSYS simulations on clamped-clamped actuators are based on the same FEM-model. The three-dimensional model consists of two rectangular blocks one of which represents the silicon bridge of the bimorph, the other one the aluminium sidewall deposition. The blocks were split into finite elements as shown in figure 4.9. Three-dimensional solid elements with eight nodes were used as depicted in figure 4.10. There are 80 elements along the length of the beam, both for the silicon and the aluminium part of the bimorph. For thermal simulations we used an element type with temperature as a degree of freedom (solid70), for structural simulations, an element type with three-dimensional translation as degrees of freedom (solid45) is used. Constant material properties were used as shown in table 4.1.

	Silicon (< 100 >direction)	Aluminium
Elastic modulus [Pa]	$1.3 \cdot 10^{11}$	$6.5 \cdot 10^{10}$
Thermal expansion Coefficent [K^{-1}]	$2.6 \cdot 10^{-6}$	$2.5 \cdot 10^{-5}$
Thermal conductivity [$Wm^{-1}K^{-1}$]	$1.49 \cdot 10^{2}$	$2.37 \cdot 10^{2}$
Mass density [kgm^{-3}]	$2.38 \cdot 10^{3}$	$2.7 \cdot 10^{3}$
Specific Heat [$Jkg^{-1}K^{-1}$]	702.2	897.7

Table 4.1: Material Properties

4.3.2 Temperature Distribution

This simulation is to check the analytical analysis on the temperature distribution curve. It is based on the above model (see 4.3.1) and uses the thermal element type (solid70). A heat generation of input power P is applied to the silicon part of the bimorph. The ends of the bimorph are kept at a constant temperature T_0.

Figure 4.11 gives the simulated temperature distribution curve for a 1000 μm long bimorph beam at an input power of $P = 2\ mW$. The curve is literally identical with

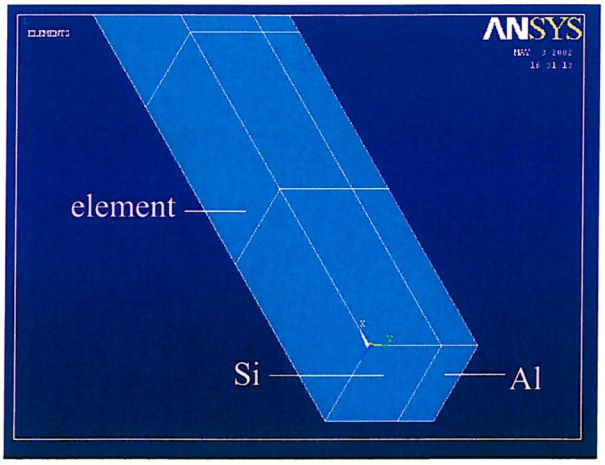

Figure 4.9: ANSYS model of the clamped-clamped actuator.

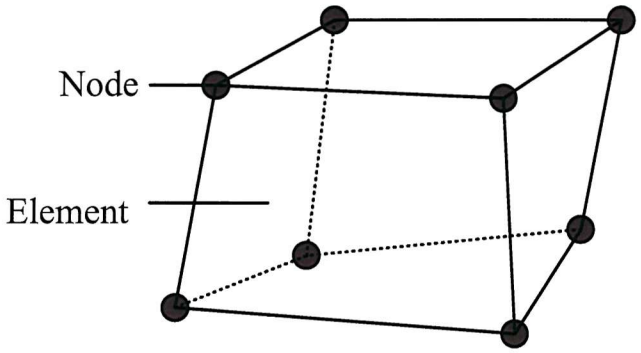

Figure 4.10: Solid element used for ANSYS simulation.

the analytically calculated temperature distribution (figure 4.2). This confirms the validity of our thermal model.

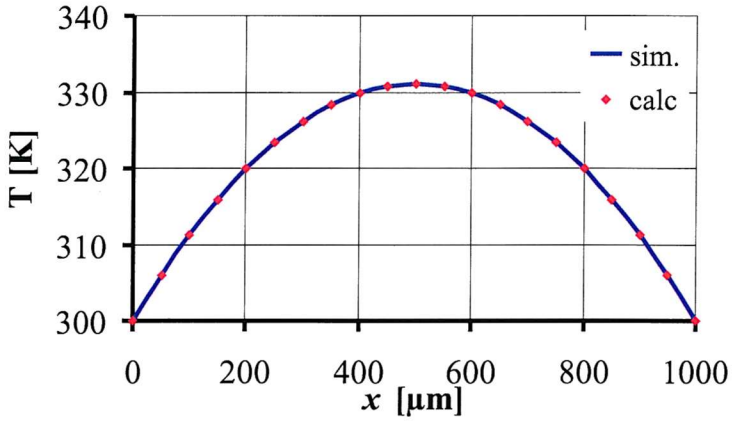

Figure 4.11: Simulated temperature distribution curve compared with analytically calculated curve ($P = 2\ mW$, $l = 1000\ \mu m$, $w_{Si} = 5\ \mu m$, $w_{Al} = 2.5\ \mu m$, $h = 6\ \mu m$, $T_0 = 300K$).

4.3.3 Static Deflection Curve

The simulated temperature distribution is used as input for a structural analysis (element type: solid45). Both ends of the bimorph are fixed against translation in any direction. Figure 4.12 shows the simulated deflection curve for a 1000 μm long bimorph beam at an input power of $P = 2\ mW$. Again, it is identical with the analytical deflection curve (figure 4.4) confirming the validity of the model.

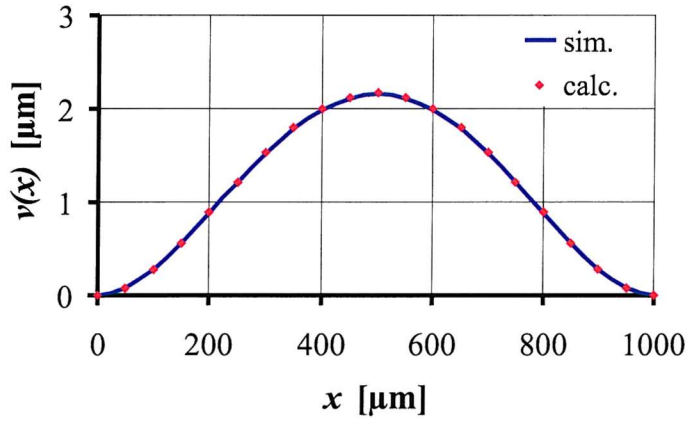

Figure 4.12: Simulated deflection curve compared with analytically calculated curve ($P = 2\ mW$, $l = 1000\ \mu m$, $w_{Si} = 5\ \mu m$, $w_{Al} = 2.5\ \mu m$, $h = 6\ \mu m$, $T_0 = 300K$).

In figure 4.13, the centre deflection v_c is plotted against the input power. Our model yields a linear rise of the deflection with power, which agrees with the analytical model (section 4.2.2).

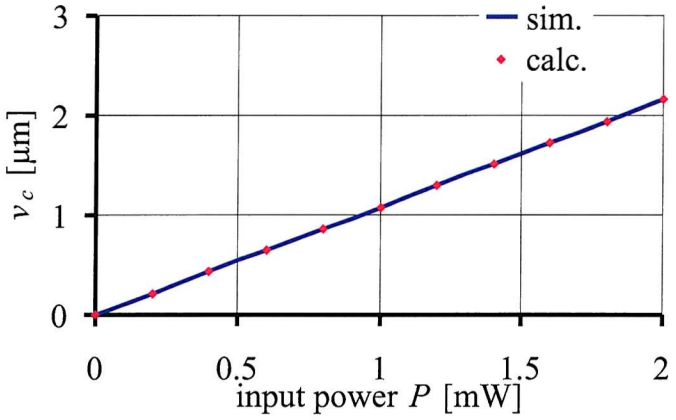

Figure 4.13: Centre deflection v_c as a function of the input power P ($l = 1000\ \mu m$, $w_{Si} = 5\ \mu m$, $w_{Al} = 2.5\ \mu m$, $h = 6\ \mu m$, $T_0 = 300K$).

The axial reaction forces at the supports were found to be compressive with a value of $7.1 \cdot 10^{-4}$ N. The lateral reaction forces R_A and R_B were simulated to be

$3.6 \cdot 10^{-12}$ N. This is 8 orders of magnitude lower than the axial reactions confirming that the lateral reactions are zero in practical considerations.

4.3.4 Thermal Time Constant

The operational speed of vertical bimorph actuators is limited by the thermal time constant of the system. The time constant describes the rate at which the actuator reaches its static state temperature distribution (see 4.2.1) and hence its maximum lateral deflection at a given input power. From the time constant, the maximum frequency f_o of the full thermal response can be calculated. f_o is also the maximum frequency at which the full deflection is reached. It is an important criterion in actuator applications such as micro-positioning and switching.

To find the thermal time constant, a transient thermal analysis is required. The most widely used analytical approach is the lumped capacity method described in [118] and [122]. This method is based on the assumption that the temperature gradient along the object investigated is negligible. This condition, however, is not met by our bimorph actuators, since their operation is based on a temperature distribution (see 4.2.1). Therefore, we used a transient thermal simulation in ANSYS to determine the time constant of the actuators.

We utilise the above model (see section 4.3.1) with the thermal element type (solid70). Initially, the whole beam is at a constant temperature T_0. At the time $t = t_0$, the input power P is switched on and the transient thermal analysis option in ANSYS simulates the temperature as a function of time $T(t)$. Figure 4.14 shows a temperature versus time plot for a 1000 μm long bimorph beam at a pulse input power of $P = 2\ mW$ for a location at the centre of the beam $T = T(t, x = l/2)$ for an interval of 10 ms.

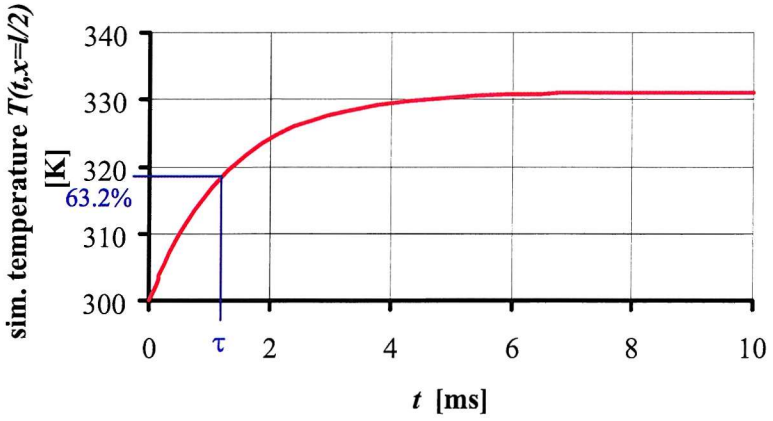

Figure 4.14: Simulated temperature versus time plot $T(t, x = l/2)$ ($P = 2\ mW$, $l = 1000\ \mu m$, $w_{Si} = 5\ \mu m$, $w_{Al} = 2.5\ \mu m$, $h = 6\ \mu m$, $T_0 = 300K$).

The shape of the temperature versus time plot $T(t)$ (figure 4.14) suggests that it can be fitted to an exponential rise function

$$T(t) = T_1 \cdot (1 - e^{-\frac{t}{\tau}}) \tag{4.41}$$

where T_1 is the static temperature of the centre of the bimorph for a given input power and τ is the thermal time constant of the system. To verify this assumption we rephrase equation 4.41

$$ln(1 - \frac{T(t)}{T_1}) = -\frac{t}{\tau} \tag{4.42}$$

Therefore, plotting $1 - \frac{T(t)}{T_1}$ on a logarithmic scale versus the time t should give a linear graph where the slope is equal to $-\frac{1}{\tau}$. We used the data points of the transient ANSYS simulations to obtain the graph shown in figure 4.15. The linear graph confirms our hypothesis that the temperature versus time plot is an exponential rise function. Furthermore, from the slope, we found τ to be 1.27 ms. This value can be verified on the temperature versus time plot by taking the time at the point where 63.2 % of the static temperature T_1 is reached as illustrated in figure 4.14.

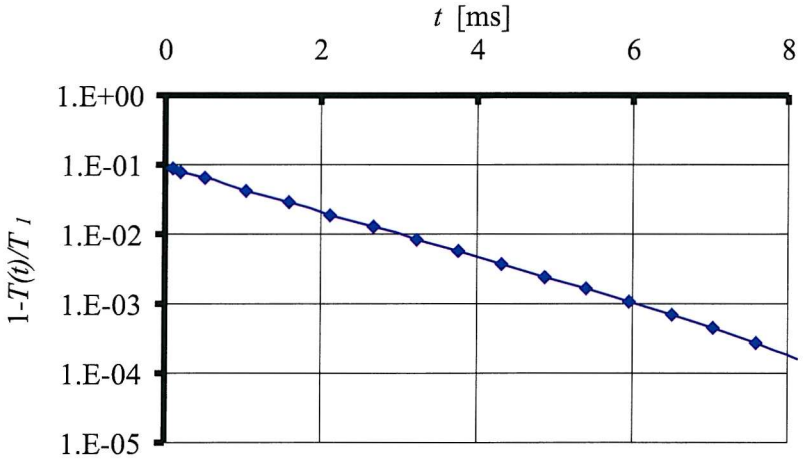

Figure 4.15: Plot of $1 - \frac{T(t,x=l/2)}{T_1}$ versus time t ($P = 2\ mW$, $l = 1000\ \mu m$, $w_{Si} = 5\ \mu m$, $w_{Al} = 2.5\ \mu m$, $h = 6\ \mu m$, $T_0 = 300K$).

Assuming that a time of 5 τ is necessary to reach the full deflection after the positive edge of an input signal (after 5τ, 99.3 % of the full deflection is reached for an exponentially rising waveform) and the rest position after the negative edge, the highest frequency f_o at which the full deflection amplitude is reached is calculated to be 78.7 Hz. Note that vibrations of higher frequency can also be thermally excited with vertical bimorph actuators. However, there is not enough time for the beam

to cool down to the bulk temperature T_0 before the next heating pulse occurs. This results in a static deflection upon which a vibration is superimposed.

4.3.5 Lateral resonances

In order to check the validity of our ANSYS model (section 4.3.1) for modal analysis and the validity of the analytical calculations, an ANSYS modal simulation for the straight clamped-clamped bimorph was carried out. A modal analyses in ANSYS determines the resonant frequencies and mode shapes of structures. The above model (section 4.3.1) was used. Both ends of the beam are fixed against any translation movement. For a 1000 μm long bimorph beam (w_{Si} = 5 μm, w_{Al} = 2.5 μm, h = 6 μm) the first lateral mode f_1 is 47.27 kHz, the second lateral mode f_2 is 130.4 kHz. These values agree very well with the results of the analytical calculation above (section 4.2.5).

Figure 4.16 shows the simulated mode shapes for the same beam for the first and second mode. They are in good agreement with the calculated mode shape functions (see section 4.2.5).

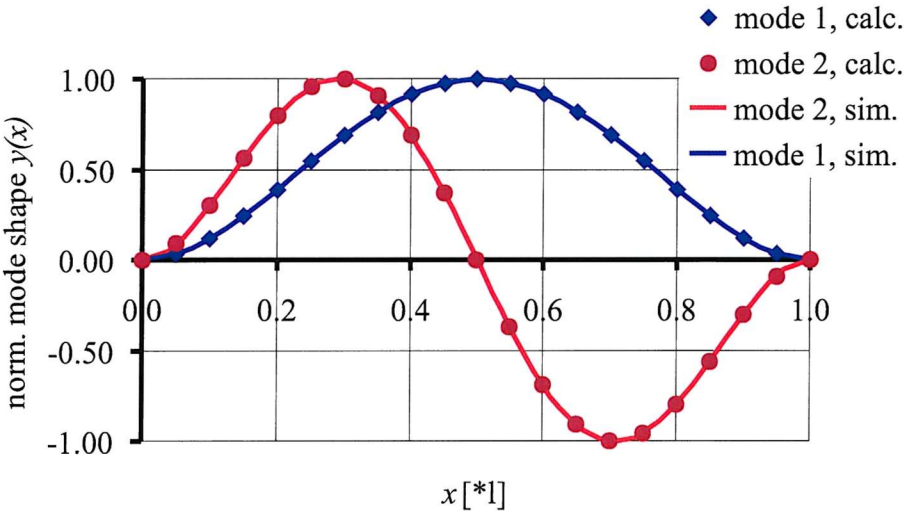

Figure 4.16: Simulated and calculated mode shapes for a clamped-clamped beam, mode 1 and 2.

For the real bimorph beams, there are two additional phenomena, which have a great influence on the resonant frequency. These phenomena are discussed below.

Tensile Stress in the Aluminium Layer

There is a tensile stress in the aluminium sidewall deposits resulting from the evaporation process, where the aluminium in the crucible is heated up by an electron beam

and is still at a temperature above room temperature when it reaches the wafer where it is deposited. The tensile stress tends to increase the resonant frequency [120]. From a simulation point of view this stress is accounted for by an aluminium reference temperature T_{refAl} higher than room temperature. T_{refAl} is the temperature at which there is no stress in the aluminium. The exact value for T_{refAl} is not known, therefore simulations are carried out over a range of reference temperatures.

We carried out a modal analysis as described above. The aluminium reference temperature T_{refAl} was varied from 300 K to 340 K in 10 steps and for each step a solution was obtained. The lateral resonant frequency for the first mode f_1 and second mode f_2 was then plotted against the reference temperature. Figure 4.17 shows the plots for a 1000 μm long bimorph beam.

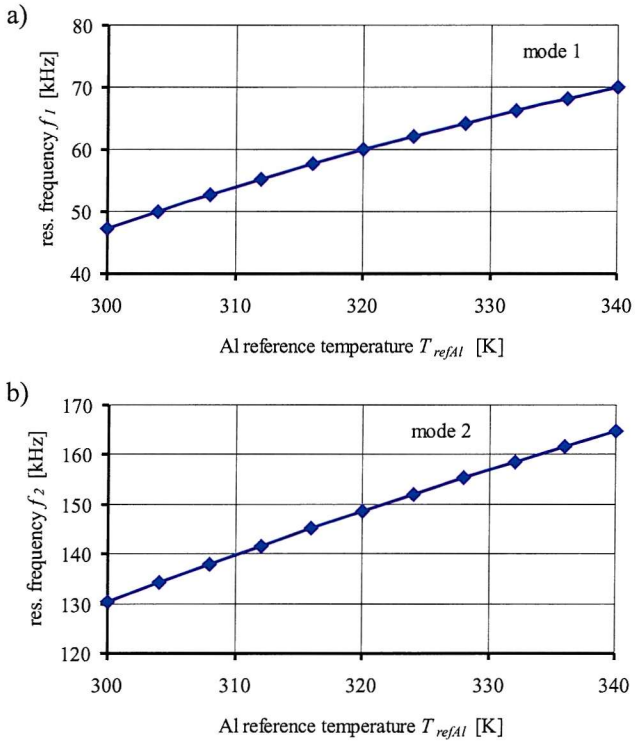

Figure 4.17: Resonant frequencies f_1 and f_2 plotted against the aluminium reference temperature T_{refAl}, a) mode 1, b) mode 2 ($l = 1000\ \mu m$, $w_{Si} = 5\ \mu m$, $w_{Al} = 2.5\ \mu m$, $h = 6\ \mu m$, $T_0 = 300K$).

Static deflection

When an AC-power beyond the maximum frequency of full thermal response f_o is applied to the actuator, a static deflection of the bimorph is caused (4.3.4). This static displacement causes a curvature of the beam, which tends to decrease the lateral resonant frequency [120].

To quantify the influence of this static deflection on the resonant frequency, the results of the static analysis were used as a prestress input for the modal analysis. The resonant frequencies were determined for different values of static input power resulting in different static deflections v_c. Figure 4.18 shows plots of resonant frequencies f_1 and f_2 for a 1000 μm long bimorph beam . The static deflections result from input power values ranging from 0 to 2 mW.

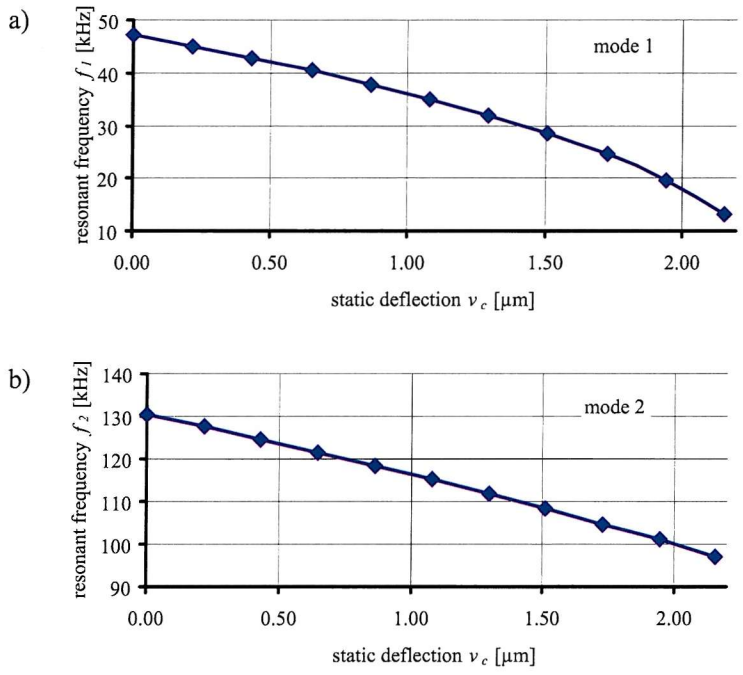

Figure 4.18: Resonant frequency f_1 and f_2 plotted against static deflection v_c, a) mode 1, b) mode 2 ($l = 1000\ \mu m$, $w_{Si} = 5\ \mu m$, $w_{Al} = 2.5\ \mu m$, $h = 6\ \mu m$, $T_0 = 300K$, $T_{refAl} = 300K$).

Since the aluminium reference temperature T_{refAl} cannot easily be measured for the actual devices it is useful to plot an array of curves for different T_{refAl}. Measuring the resonant frequency for a certain static deflection then allows to determine T_{refAl}. Figure 4.19 gives an array of curves by plotting the resonant frequency as a function of the static displacement v_c for different aluminium reference temperatures T_{refAl}.

4.4 ANSYS Simulations on the One-Dimensional Meander Type Actuator

Due to the complexity of the geometry, numeric simulations in ANSYS were carried out to investigate the behaviour of the one-dimensional meander type actuator.

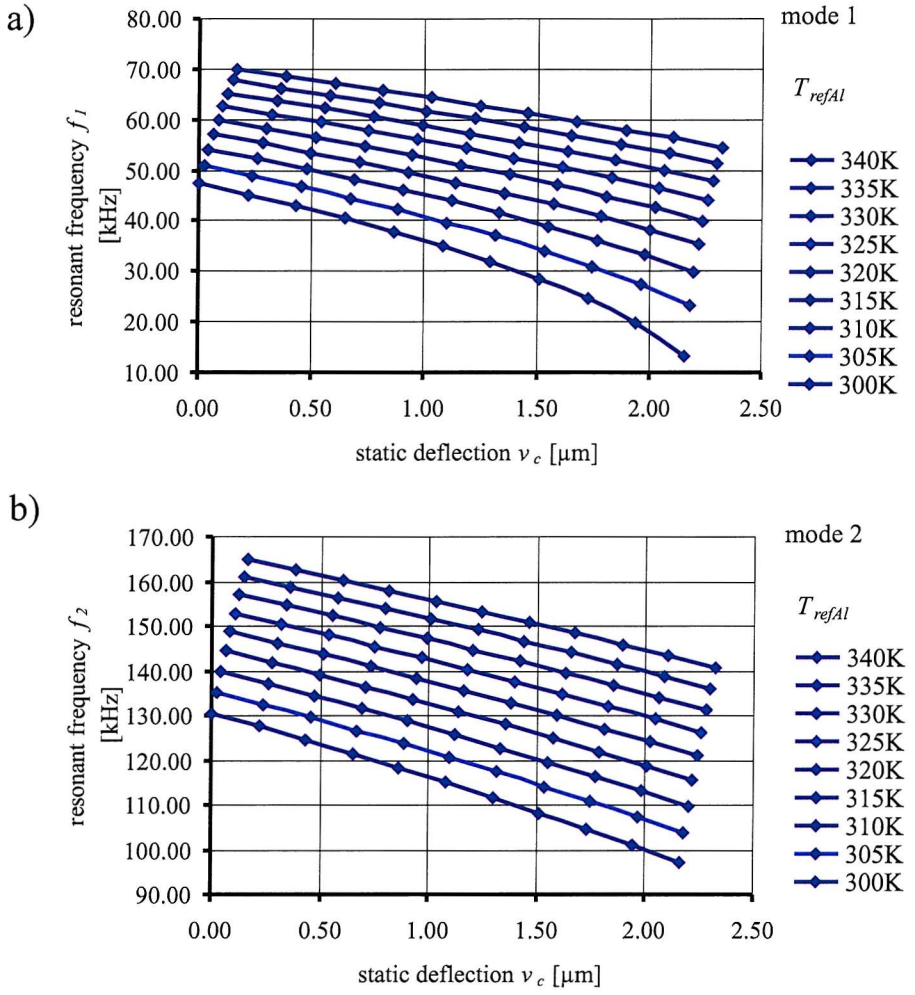

Figure 4.19: Resonant frequencies f_1 and f_2 plotted against static deflection v_c for different aluminium reference temperatures T_{refAl}, a) mode 1, b) mode 2 ($l = 1000\ \mu m$, $w_{Si} = 5\ \mu m$, $w_{Al} = 2.5\ \mu m$, $h = 6\ \mu m$, $T_0 = 300K$).

Appendix D.2 lists the corresponding ANSYS log files.

4.4.1 ANSYS-Model

Figure 4.20 depicts the model for the one-dimensional meander actuator. The same three dimensional elements as in section 4.3 were used. There are 80 elements along the length of each of the four bimorphs, both for the silicon and the aluminium part. For thermal simulations we used an element type with temperature as a degree of freedom (solid70). For structural simulations an element with three-dimensional translation as degree of freedom was used. Constant material properties were used as shown in table 4.1.

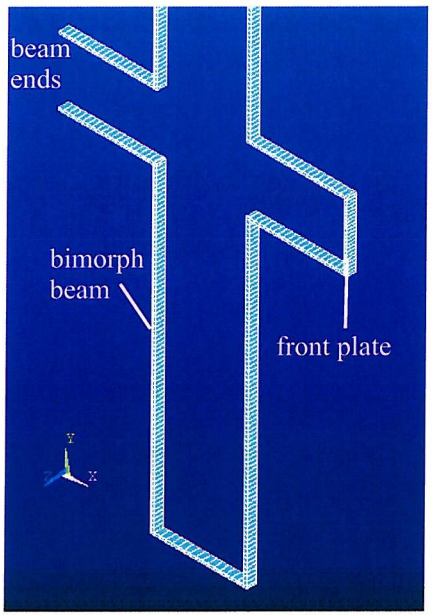

Figure 4.20: Model for the one-dimensional meander actuator.

4.4.2 Temperature Distribution

A heat generation of power P was applied to the silicon beams apart from the front plate region, where a gold conductor on the actual device will reduce the resistance so that virtually no heat dissipation takes place. The ends of the silicon beam (top left corner of the diagram) are kept at a constant temperature T_0. The thermal element type (solid70) was used for the heat transfer analysis. Figure 4.21 shows the resulting temperature distribution along the meander geometry. At an input power P of 6 mW, the maximum temperature at the front plate, 401 K, is reached.

4.4.3 Static Deflection

The temperature distribution was used as the input for a structural analysis. The ends of the beam were fixed against translation movements in any direction. Figure 4.22 depicts the deflection for an input power of 6 mW.

To obtain a deflection versus power plot, consecutive simulations were carried out with different input power P. The deflection of the front plate was written to a file and plotted against the input power. Figure 4.23 shows the deflection plot. A linear rise is observed.

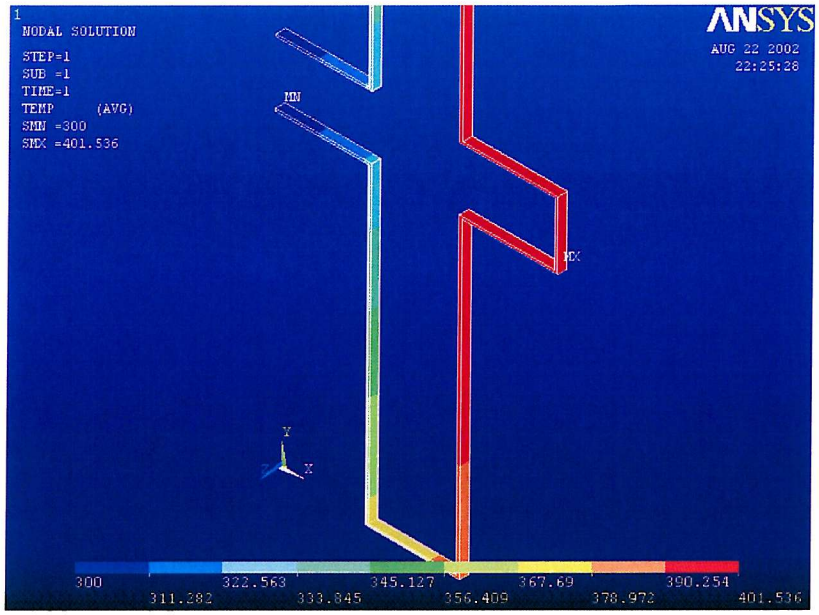

Figure 4.21: Temperature distribution for the one-dimensional meander actuator, P = 6 mW, T_0 = 300 K, l_b = 1000 μm, w_{Si} = 8 μm, w_{Al} = 1.5 μm, l_1 = 300 μm, l_2 = 300 μm, l_3 = 300 μm, l_4 = 200 μm.

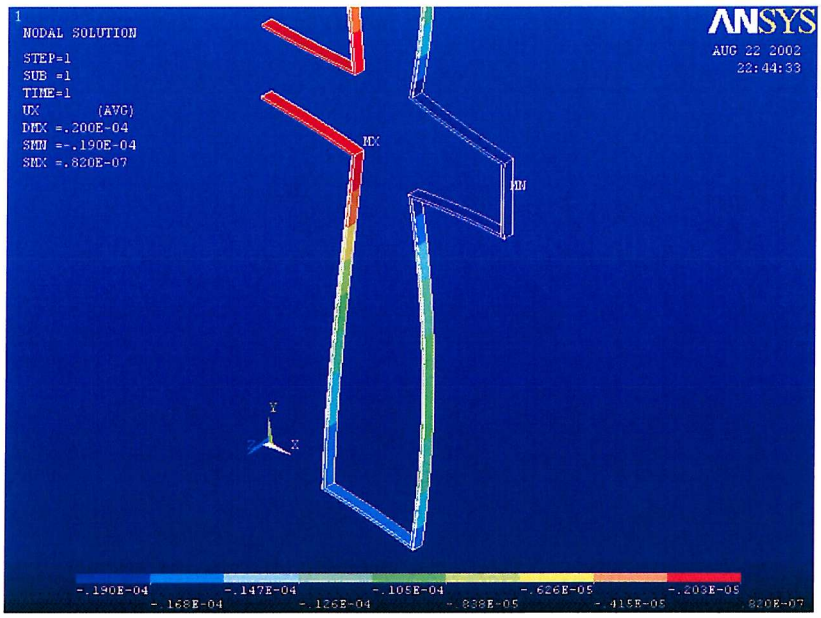

Figure 4.22: Static deflection of the one-dimensional meander actuator, displacement in x-direction is colour-mapped, dimensions see figure 4.21.

4.4.4 Thermal Time Constant

A transient thermal analysis was carried out utilising the above model with the thermal element type (solid70). Initially, the whole actuator was kept at temperature T_0 and at the time $t = t_0$ the electrical input power was switched on. A temperature versus time plot was simulated. Figure 4.24 shows the temperature versus time plot

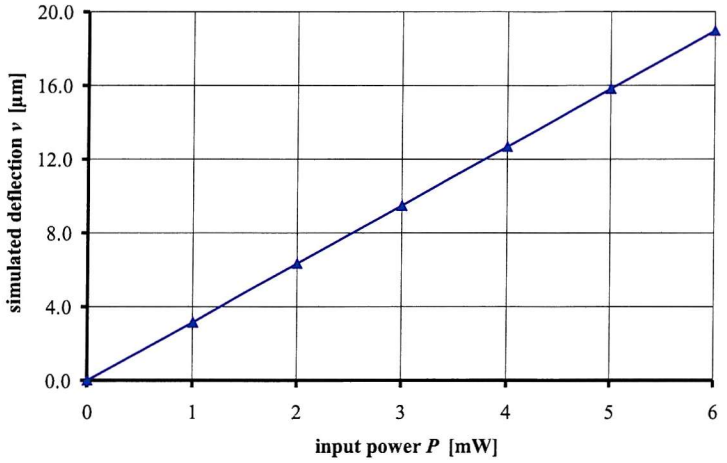

Figure 4.23: Deflection of the front plate against input power, dimensions see figure 4.21.

for a point at the front plate, where the highest temperature occurs.

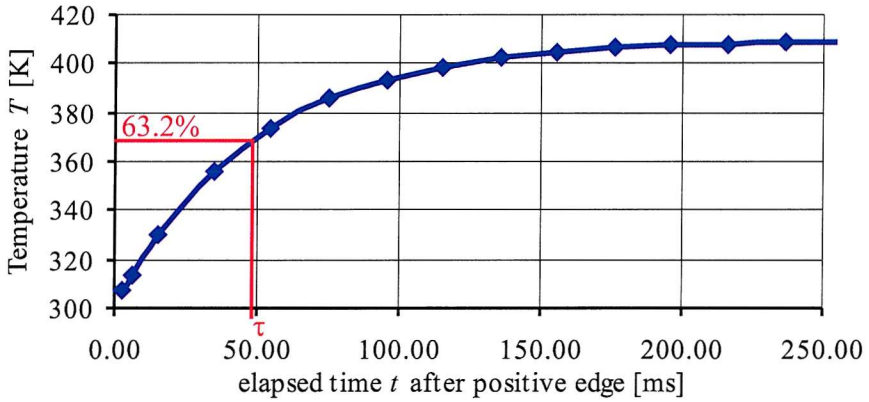

Figure 4.24: Temperature versus time, $P = 6$ mW, dimensions see figure 4.21.

The shape of the temperature versus time plot $T(t)$ in figure 4.24 suggests that it can be fitted to an exponential rise function. This assumption was confirmed using the method described in section 4.3.4. The time constant τ was found to be 48 ms. It could also be confirmed from the temperature versus time plot at the point, where 63.2 % of the maximum temperature is reached. Based on the assumption that 5τ are necessary for reaching the maximum temperature after the input power has been applied and that another 5τ are needed to cool down to T_0 after the power has been switched off, a maximum frequency for the full thermal response of 2.1 Hz is calculated. This is the highest frequency, at which the maximum temperature and hence the maximum displacement of the actuator is reached. Faster operation is possible, but will mean that the actuator does not reach the maximum temperature

and does not cool down to T_0.

4.4.5 Lateral Resonances

A modal analysis was carried out based on the above model of the one-dimensional meander actuator. The ends of the beam were fixed against translation movement. We have extracted the first 10 modes. The second mode is a vibration where the front plate moves back and forth in the x-direction. This mode is the only one that could be excited in resonant measurements (see chapter 7.3.4). For an actuator of the above dimensions (see figure 4.21) it was simulated to be at 3.89 kHz. Figure 4.25 depicts the mode shape for the second mode.

Note, as described in section 4.2.5, there is a tensile stress in the aluminium layer of the actual devices. Also, there is a static deflection upon which the vibrations are superimposed. Simulations, where the static deflection and the tensile stress in the aluminium layer (increased aluminium reference temperature) were accounted for showed that both parameters do not have a significant influence on the resonant frequency of the meander geometry. The resonant frequency only changed by a few Hz.

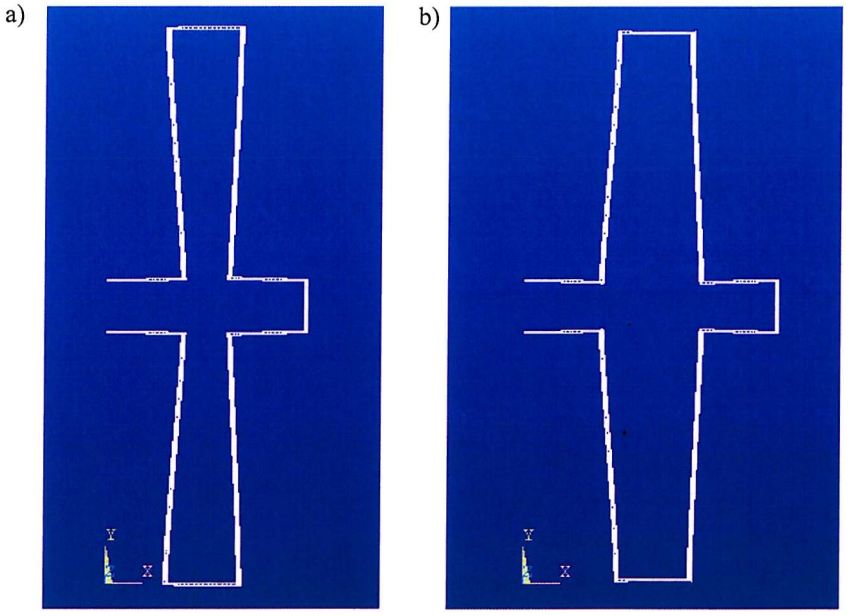

Figure 4.25: Mode shape for the second mode of the one-dimensional meander actuator.

4.5 ANSYS Simulations on the Two-Dimensional Meander Type Actuator

Since the analyses carried out here are very similar two those on the one-dimensional meander type actuator, only a brief description is given. Appendix D.3 lists the corresponding ANSYS log files.

4.5.1 Model

In figure 4.26, the model for the two-dimensional meander actuator is shown. The same three-dimensional elements as in section 4.3 were used. There are 40 elements along the length of each bimorph, both for the silicon and aluminium part.

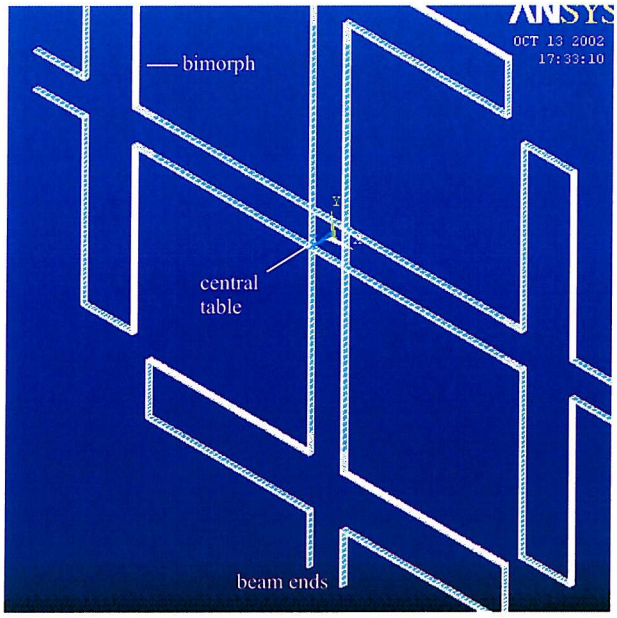

Figure 4.26: Model for the two-dimensional meander actuator.

4.5.2 Temperature Distribution

Except for the beams connecting the bimorphs with the central table, where a gold conductor on the beams of the actual device will reduce the resistance so that virtually no heat dissipation would take place, a heat generation of power P was applied to the silicon beams of the -x actuator. The ends of all four actuators were kept at a constant temperature T_0. The thermal element type (solid70) was used for the heat transfer analysis. Figure 4.27 shows the temperature distribution. At an input power P of 6 mW, the maximum temperature at the bimorph, 354 K, is reached.

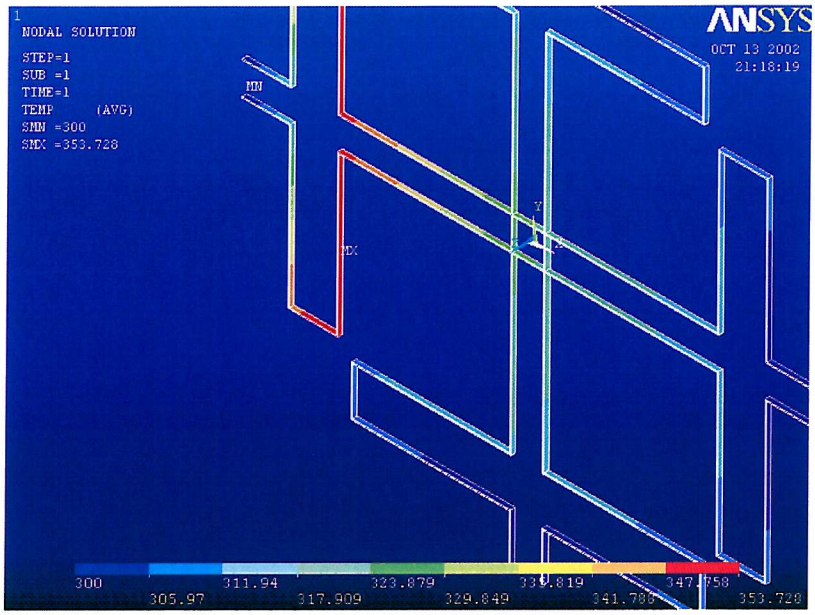

Figure 4.27: Temperature distribution for the two-dimensional meander actuator, P = 6 mW (-x actuator), T_0 = 300 K, l_b = 1000 μm, w_{Si} = 8 μm, w_{Al} = 1.5 μm, l_1 = 1100 μm, l_2 = 300 μm, l_3 = 300 μm, l_4 = 200 μm.

4.5.3 Static Deflection

The temperature distribution was used as the input for a structural analysis. All ends of the beams were fixed against translation movements in any direction. Figure 4.28 depicts the deflection for an input power of 6 mW.

Figure 4.28: Static deflection of the two-dimensional meander actuator, displacement in x-direction is colour-mapped, dimensions see figure 4.27.

To obtain a deflection versus power plot, consecutive simulations were carried out

with different input power P. The deflection of the central table was written to a file and plotted against the input power (positive values for deflection in the -x direction). Figure 4.29 shows the deflection plot. A linear rise is observed.

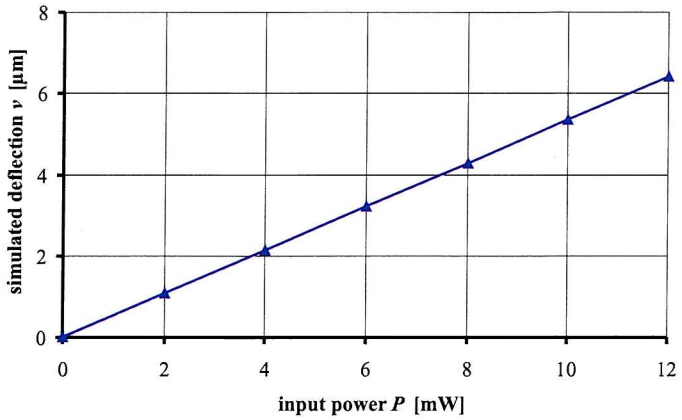

Figure 4.29: Deflection of the central table against input power, dimensions see figure 4.27.

4.5.4 Thermal Time Constant

A transient thermal analysis was carried out utilising the above model with the thermal element type (solid70). Initially, the whole device was kept at temperature T_0 and at the time $t = t_0$ the electrical input power for the -x direction actuator was switched on. A temperature versus time plot was simulated. Figure 4.30 shows the temperature versus time plot for the point of maximum temperature (inner bimorph) of the -x direction actuator.

The temperature versus time plot (figure 4.30 again is an exponential rise function, which could be confirmed using the method described in section 4.3.4. The time constant τ was found to be 31 ms. It can also be obtained from the graph at the point, where 63.2 % of the maximum temperature is reached. Based on the assumption that 5τ is necessary for reaching the maximum temperature after the input power has been applied and that another 5τ is needed to cool down to T_0 after the power has been switched off, a maximum frequency for the full thermal response of 3.2 Hz is calculated. This is the highest frequency, at which the maximum displacement of the actuator can be reached.

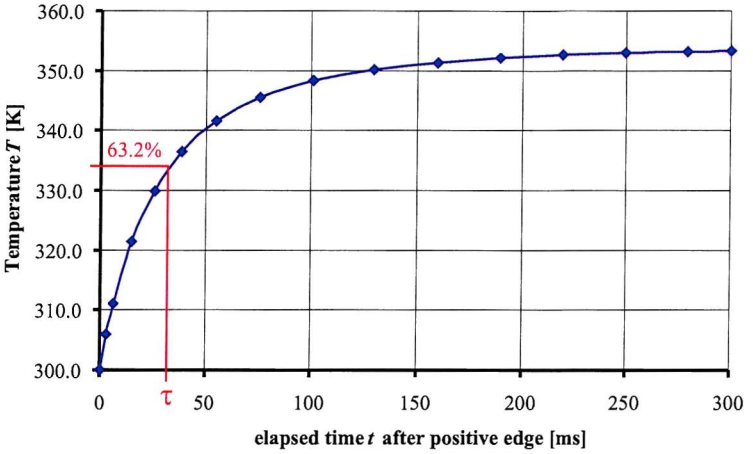

Figure 4.30: Temperature versus time, $P = 6$ mW, dimensions see figure 4.27.

4.5.5 Lateral Resonances

A modal analysis was carried out based on the above model of the two-dimensional meander actuator. All the ends of the actuator were fixed against translation movement. We have extracted the first 10 modes. The first mode is a vibration where the central table moves back and forth in the x-direction. For an actuator of the above dimensions (see figure 4.27) it was simulated to be at 2.926 kHz. Figure 4.31 depicts the mode shape for the first mode. Note, the aluminium reference temperature and the static deflection have not been accounted for in the simulations.

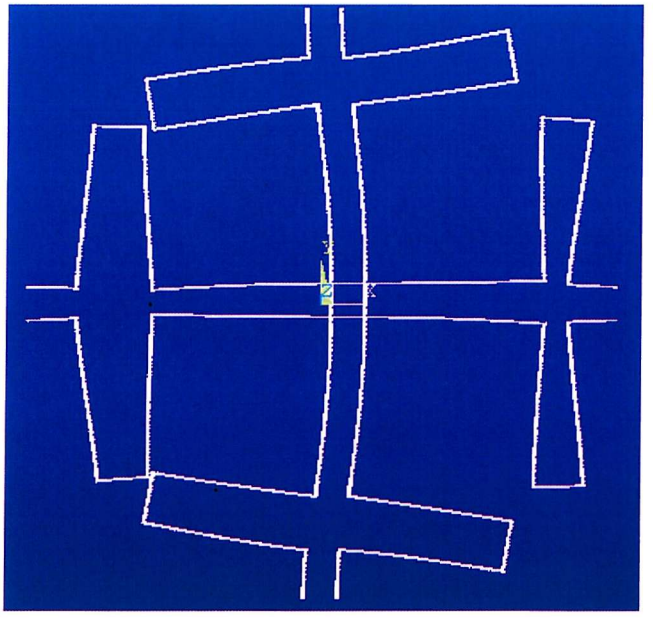

Figure 4.31: Mode shape for the first mode of the two-dimensional meander actuator.

4.6 Conclusion

We have carried out analytical and numerical analysis to predict the physical behaviour of vertical bimorph actuators. The simple geometry of the clamped-clamped beam actuators allowed us to develop an analytical model for investigating the temperature distribution, static deflection, vertical stiffness and lateral resonant frequencies. The thermal time constant was simulated using ANSYS Multiphysics based on the finite element method. For both the one- and the two-dimensional meander type actuators, ANSYS simulations where used for analysing the above aspects. In general, good agreement with measurements on the actual devices and between different analyses has been achieved.

Chapter 5

Process Development

5.1 Introduction

Thermally excited vertical bimorphs are a novel approach for lateral actuation. The geometrical structures required present a serious challenge for micro fabrication techniques, with the need for new processes as well as non-standard processes.

Aluminium deposits are needed on the sidewalls of silicon beams for the bimorph elements. This requires a new metal deposition approach (section 5.2). The microrelays require gold contacts, which cover both the sidewalls and the horizontal wafer surface (section 5.3). Working with 30 μm deep trenches is a challenge for the photolithography (section 5.4). Lastly, the bimorph beams need to be free to move, which requires removal of the handle silicon and the buried oxide layer in a so-called release etch (section 5.4). These process steps have required a considerable amount of process development work, which is presented in this chapter.

5.2 Aluminium Sidewall Deposition

In order to fabricate planar bimorphs, a metal layer is deposited onto silicon by evaporation, sputtering or electroplating, which are all planar deposition processes. The fabrication of vertical bimorphs requires a process capable of depositing aluminium onto the sidewalls of silicon beams. As there is no single-stage sidewall deposition process for metals, a multi-step process had to be developed. Test processes were carried out combining sputtering as well as evaporation with wet- and dry-etching techniques. In this section, we describe the concepts of combining the single processes in multi-step process sequences and present the results obtained [123].

5.2.1 Involved Processes

An overview is given of the processes needed for our aluminium sidewall deposition experiments. Further details can be found in [3, 124, 125].

Electron Beam Evaporation

Electron beam evaporation takes place in an evacuated process chamber. The aluminium in a crucible is heated by an electron beam, which is forced onto a circular track by crossed electric and magnetic fields. The aluminium vaporises. Due to the long mean free path at the very low pressure (about 10^{-5} Pa), there are only very few collisions of aluminium particles with gas particles. Therefore, the aluminium particles move in straight lines towards the substrate wafers, where they condense from the vapour phase and form an aluminium film. Figure 5.1 illustrates the process of electron beam evaporation. Due to the fact that the aluminium particles reach the wafers from a certain angle, the step coverage is inherently poor, but can be improved by rotation of the wafers during the evaporation. Rotation of the wafers also improves the thickness uniformity of the deposited metal layer over the wafer.

Deposition onto sidewalls can only be achieved, if the substrate is orientated at a shallow angle with respect to the aluminium crucible. A thickness monitor, based on a resonant sensor, allows in situ control of the deposition thickness. When coated with aluminium, its mass increases and hence its resonant frequency decreases. The change in the resonant frequency is detected and can be calibrated to monitor the film thickness.

Due to the fact that aluminium condenses from the vapour phase, it is deposited at an elevated temperature. Since aluminium has a larger thermal expansion coefficient than silicon, there is a thermally induced tensile stress in the aluminium deposit and a compressive stress in the silicon substrate.

Aluminium Sputtering

In aluminium sputtering, an aluminium target mounted on the cathode is bombarded with energetic argon ions from a DC generated plasma. This ion bombardment removes aluminium particles from the target by momentum transfer and these condense on the substrate forming an aluminium film. As sputtering is carried out at a higher pressure than evaporation (about 1 Pa), the mean free path is much shorter and the aluminium particles undergo many scattering collisions and arrive at the substrate from all different angles. Consequently, the step coverage is significantly better than that obtained by evaporation and aluminium is also deposited onto sidewalls. Figure

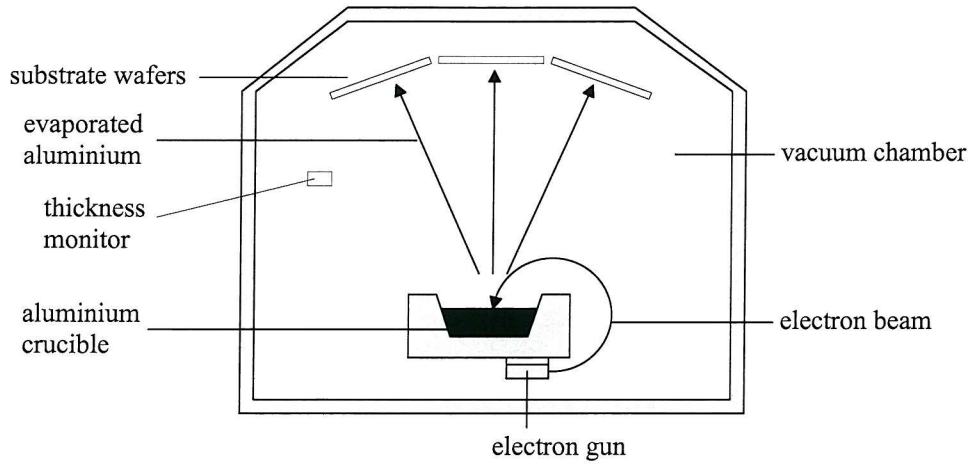

Figure 5.1: Electron beam evaporation.

5.2 illustrates aluminium sputtering.

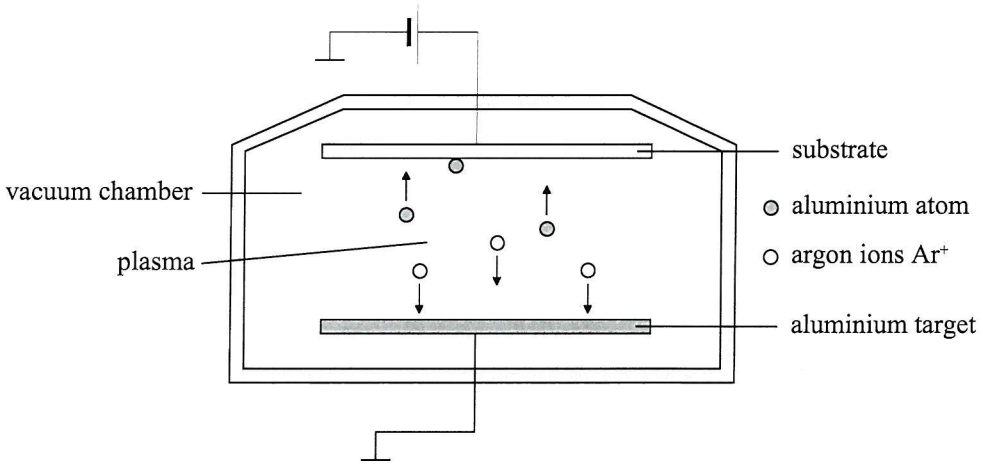

Figure 5.2: Aluminium sputtering.

Aluminium Etching

Aluminium can be wet-etched in orthophosphoric acid. This wet-etching process etches in an isotropic manner. For structuring aluminium layers, a photolithography step is carried out to provide a patterned resist mask. The aluminium wet-etch is done by immersing the wafers into the etching solution until the aluminium has disappeared from the areas exposed by the photolithography. Due to the isotropic character, a large under-etch can be observed as depicted in figure 5.3.

Anisotropic etching of aluminium is achieved employing a dry-etch process in chlorine (Cl_2)- and silicon tetrachloride ($SiCl_4$)-plasma (figure 5.4). An oxide layer is needed as an etch stop, since this aluminium etch process lacks selectivity to silicon. Due to the mainly anisotropic character of the etch, hardly any undercut is observed.

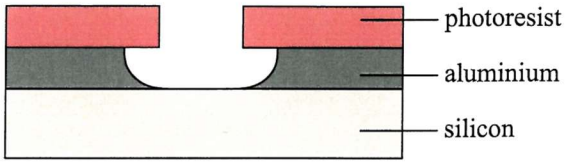

Figure 5.3: Profile view after aluminium wet-etch. Undercut due to isotropic character.

The etch end-point is determined by a rise of the pressure in the process chamber, which indicates that the aluminium layer has been etched through. To make sure that aluminium has been removed over the whole exposed area, a short over etch time is given to the process. A disadvantage of the dry-etch process is the fact that the etch rate is higher at the edges of the wafer compared to the centre of the wafer resulting in a radial nonuniformity.

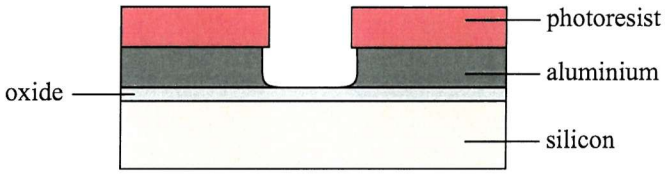

Figure 5.4: Profile view after aluminium dry-etch. Only small under-cut due to the anisotropic character.

5.2.2 Fabrication Techniques

This section describes the processes carried out for the investigation into aluminium deposition onto sidewalls of silicon beams. The corresponding LMS-process listing is given in appendix B.1.1.

Substrate Preparation

All experiments carried out use standard (100) silicon substrates. 6 μm deep trenches of 5 μm to 500 μm width are etched into the substrate using an anisotropic dry-etch in hydrogen bromide (HBr) and silicon tetrachloride ($SiCl_4$). An oxide is grown providing the etch stop layer required for the aluminium dry-etch. This oxide layer also serves as electrical insulation in the actual bimorph devices. Figure 5.5 shows the substrate prepared for aluminium sidewall deposition tests.

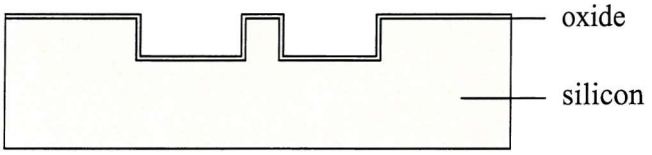

Figure 5.5: Substrate with trenches for aluminium sidewall deposition.

Aluminium Sidewall Deposition Based on Sputtering and Dry-Etching

One approach to depositing aluminium onto sidewalls involves the sputtering of aluminium and subsequent aluminium blanket dry-etching. The sputtering process deposits aluminium onto both the horizontal surfaces and the sidewalls. The aluminium thickness obtained on the sidewalls is about half the thickness of the layer on the horizontal wafer surface as shown in Figure 5.6a. Blanket dry-etching means that the etch process is carried out without a resist mask, thus exposing the entire aluminium surface to the reactive species. Due to the anisotropic character of the dry-etch, some aluminium remains on the sidewalls, if the etch process is stopped immediately after all the aluminium has been removed from the horizontal wafer surface. Figure 5.6b sketches the result.

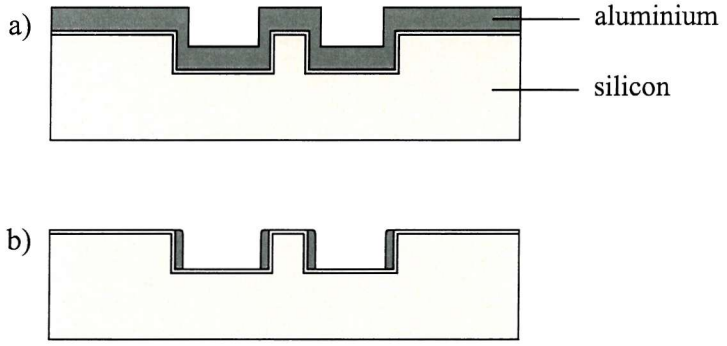

Figure 5.6: Sketch of aluminium sidewall deposition based on a) sputtering and b) subsequent dry-etching.

Aluminium Sidewall Deposition based on Angled Evaporation and Dry-Etching

The second approach for aluminium sidewall deposition utilises angled evaporation and a subsequent aluminium blanket dry-etch. To deposit aluminium onto sidewalls, a shallow angle Φ of the substrate wafer with respect to the aluminium crucible has to be chosen as illustrated in figure 5.7. A problem that arises from this setup is that the aluminium thickness varies across the wafer both on the horizontal faces and on the sidewalls. This is due to different distances and angles between the crucible and the different areas of the wafer surface. To realise this setup in practice, a special

jig is used to hold the wafer above the crucible at a predetermined angle. To ensure reproducibility of the results, the flat of the wafer is always placed at the lowest position of the jig.

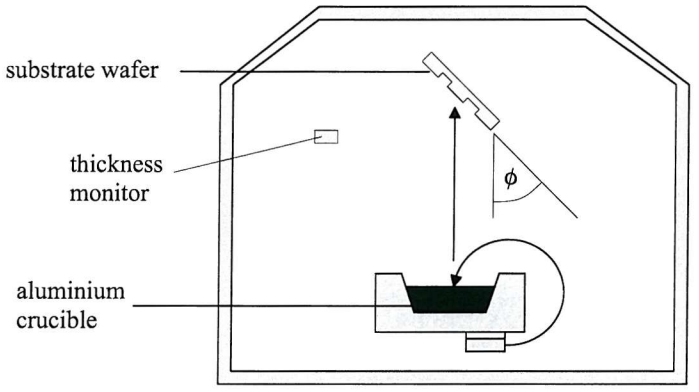

Figure 5.7: Evaporation at a shallow angle Φ between the wafer and the aluminium crucible for aluminium deposition onto sidewalls.

As a result of the line-of-sight of the angled evaporation, aluminium is deposited on the top horizontal wafer surface, the right-hand side sidewalls and the non-shadowed parts of the horizontal faces in the trenches (figure 5.8a). After the anisotropic blanket dry-etch, aluminium fillets on the right-hand side sidewalls remain (figure 5.8b).

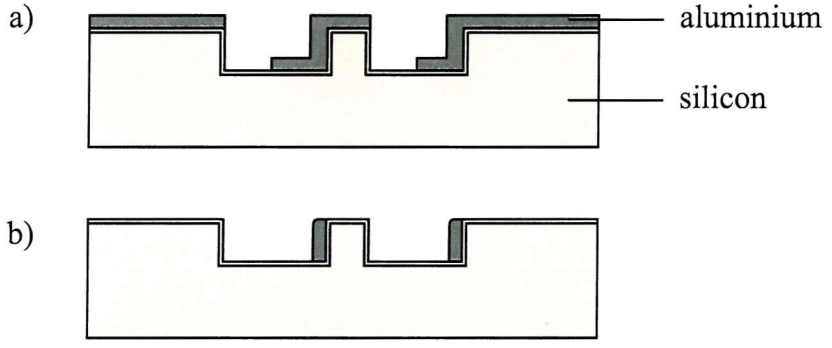

Figure 5.8: Sketch of aluminium sidewall deposition based on a) angled evaporation and b) subsequent dry-etching.

Aluminium Sidewall Deposition Based on Angled Evaporation and Wet-Etching

This approach combines angled evaporation and subsequent wet-etching of aluminium. The evaporation is carried out at a very shallow angle Φ ($\Phi < 45$). This ensures that the deposition on the right-hand side sidewall is thicker than that on the horizontal surfaces (figure 5.9a). The isotropic wet-etch of aluminium is stopped immediately after all aluminium on the top wafer surface has been etched away. Consequently,

the aluminium on the sidewalls is thinned by approximately the thickness of the original aluminium film on the horizontal face, but is not removed completely. Thus, aluminium fillets remain on the right-hand side sidewalls (figure 5.9b).

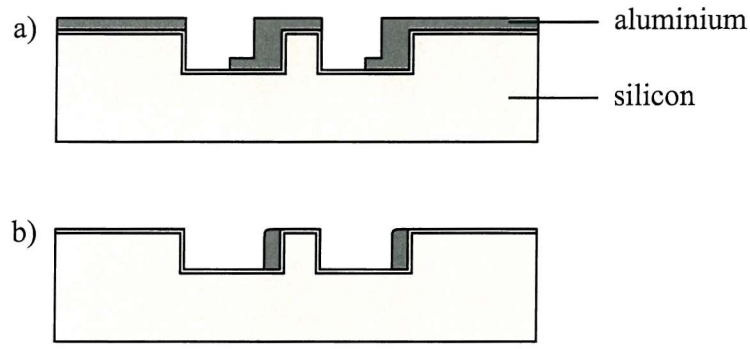

Figure 5.9: Sketch of aluminium sidewall deposition based on a) angled evaporation and b) subsequent wet-etching.

5.2.3 Experimental Results

In this section, the results of the experiments are presented, using SEM-pictures. In order to take pictures of profile views, the wafers were cleaved before taking SEM-pictures. Both angled evaporation and aluminium dry-etching introduce nonuniformities across the wafer. Therefore, the position along the cleave-line, referred to as 'picture position', becomes an important parameter. It ranges from 0 (wafer flat) to 100 (wafer curve) as illustrated in figure 5.10.

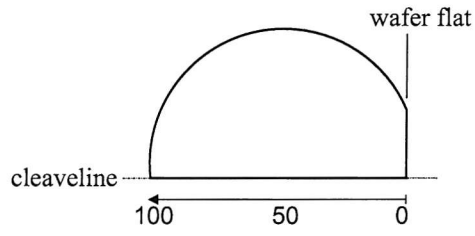

Figure 5.10: Sketch of a cleaved wafer, illustrating 'picture position' in numbers from 0 to 100.

Sputtering and Dry-Etching

Figure 5.11 shows a sputtered aluminium layer covering silicon trenches. The thickness measured in the SEM picture is about 1.7 μm on the horizontal plane and about 0.7 μm on the sidewall. Good sidewall coverage can be observed.

Figure 5.12 shows aluminium fillets remaining after the dry-etching process. Before the dry-etch, an aluminium layer of 1 μm thickness on the horizontal surface was

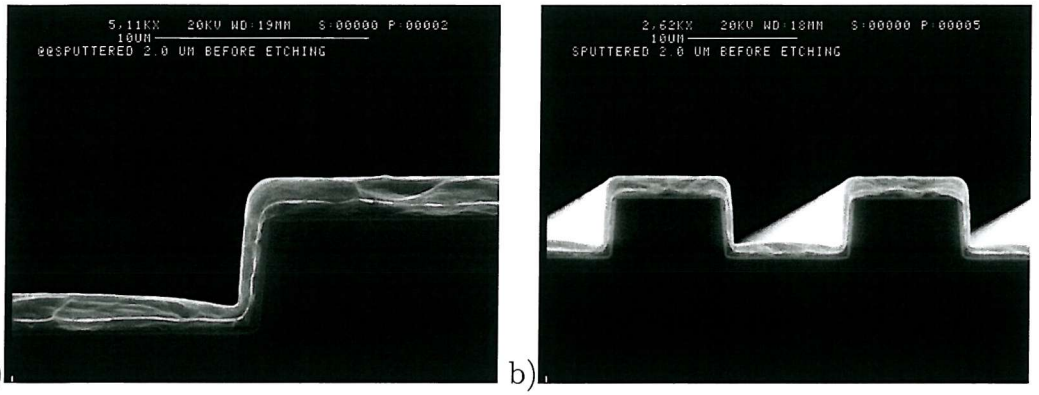

a) b)

Figure 5.11: Silicon trenches, sputter-coated with a 1.7 μm thick aluminium layer on horizontal faces, 0.7 μm on sidewalls (before dry-etch), a) one step, b) several trenches (picture position: 30).

sputtered onto the wafer. The thickness of the fillets after the dry-etch is about 0.25 μm. Figure 5.12a shows a profile view of the aluminium fillet. A significant notch in the aluminium can be observed at the bottom of the trench. At the top of the fillet, an an over-etch can be seen. The reason for this over-etch lies in the higher dry-etch rate at the edge of the wafer. Stopping the dry-etch when the aluminium on the horizontal surface is removed at the centre of the wafer means that areas closer to the edges are subject to a deeper etch visible as an over-etch. Figure 5.12b shows a three-dimensional view of an aluminium fillet. The surface of the aluminium fillet looks very rough. This might be a consequence of the relatively long dry-etch time for the comparably thin deposit on the sidewall. Both the over-etch at the top of the sidewall fillet and a notch at the foot of the fillet can be seen in this picture.

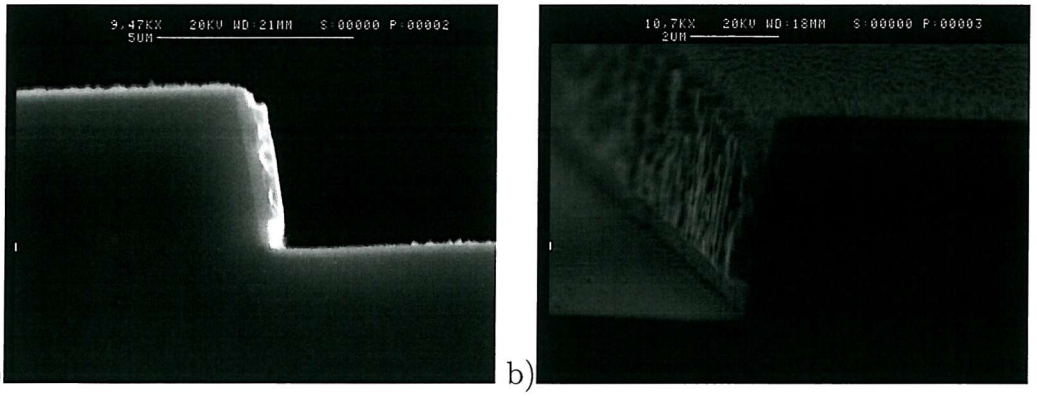

a) b)

Figure 5.12: Aluminium fillets on silicon sidewalls obtained by sputtering and subsequent dry-etching a) profile view b) 3-dimensional view (aluminium thickness on sidewalls: 0.25 μm, picture position: a) 61, b) 77).

Angled evaporation and dry-etching

Figure 5.13 shows silicon trenches covered with an evaporated aluminium layer, 1 μm thick. In Figure 5.13a, the shadowing effect can be seen. Good step coverage can be observed on the left-hand side edges where there is no shadowing.

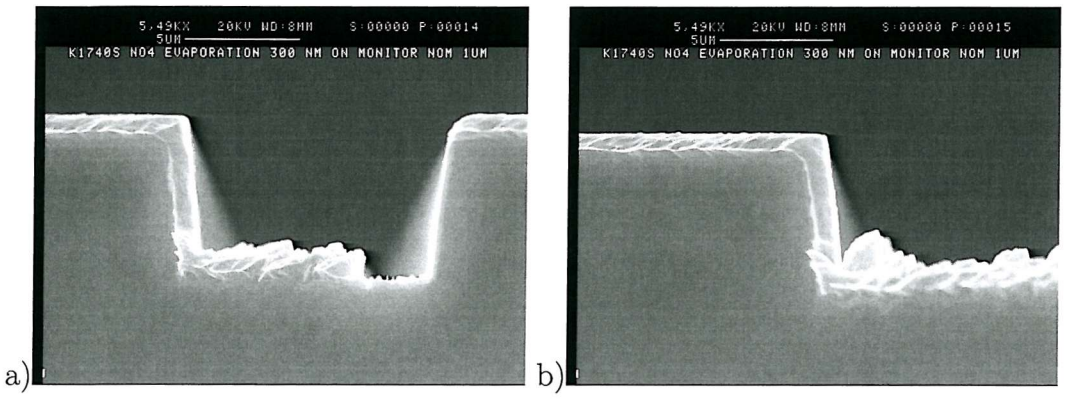

a) b)

Figure 5.13: Silicon trenches, coated with a 1 μm thick (horizontal surfaces and sidewalls) evaporated aluminium layer (before dry-etch), a) profile view of a 10 μm wide trench b) profile view of a wide trench (evaporation angle $\Phi = 60\,^{\circ}$, picture position: 48).

Figure 5.14 shows aluminium fillets obtained by angled evaporation and subsequent dry-etching. The fillet shown in figure 5.14a has a significant over-etch and notch. This is because it is located close to the edge of the wafer, where the etch rate of the aluminium dry-etch is highest. The fillet shown in figure 5.14b is located at the centre of the wafer. Consequently, hardly any over-etch is observed and the notch is smaller than that in figure 5.14a.

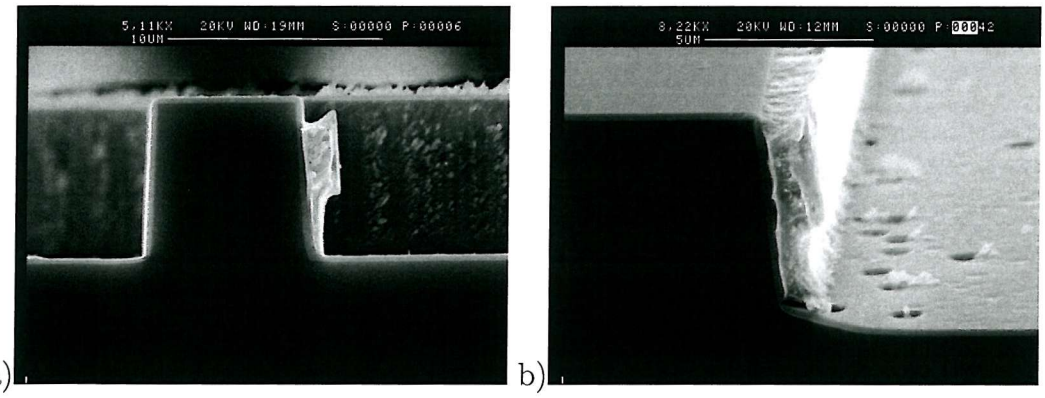

a) b)

Figure 5.14: Aluminium fillets on sidewalls obtained by angled evaporation and subsequent dry-etch, a) profile view of an aluminium fillet, b) 3-dimensional view of another aluminium fillet (aluminium thickness on sidewalls: 1.6 μm, evaporation angle $\Phi = 60\,^{\circ}$, picture position: a) 88, b) 53).

Angled Evaporation and Wet-Etching

Figure 5.15 shows silicon steps covered with a fairly thick layer of evaporated aluminium (2.8 μm on the sidewalls, 1.2 μm on horizontal faces) deposited at a shallow angle of $\Phi = 24^\circ$. Since the sidewall-deposit is 1.6 μm thicker than the deposit on the horizontal surfaces, isotropic wet-etching of the aluminium results in a sidewall thickness of approximately 1.6 μm.

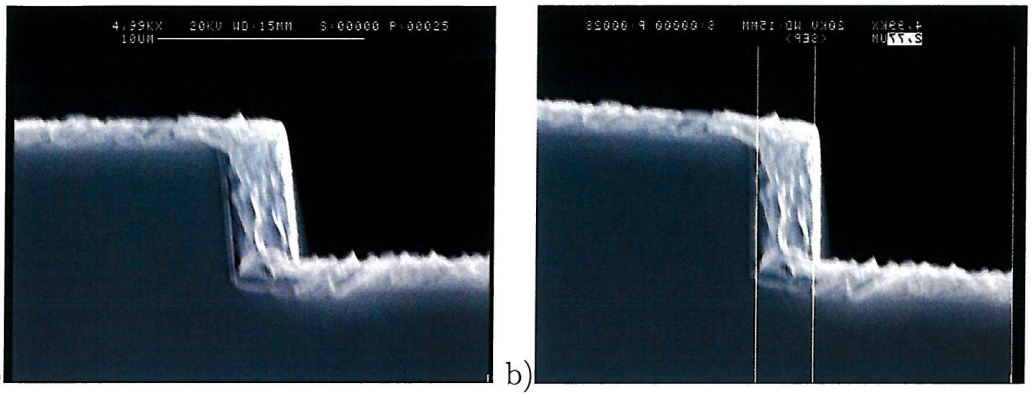

a) b)

Figure 5.15: Silicon trenches, coated with an evaporated aluminium layer (before dry-etch), a) profile view of one step b) the same step, slightly rotated to allow thickness measurement (aluminium thickness on sidewalls: 2.8 μm, aluminium thickness on horizontal surfaces: 1.2 μm, evaporation angle Φ= 24 $^\circ$, picture position: 60).

In figure 5.16, the thickness of the aluminium deposit obtained by angled evaporation (before wet-etching) on both the sidewall and on the horizontal surfaces is plotted versus the position on the wafer. The deposits are thicker towards the flat as the flat was placed closer to the aluminium crucible in the evaporation jig. The thickness varies by about 25 % across the wafer. The thicknesses have been measured from profile views in the SEM.

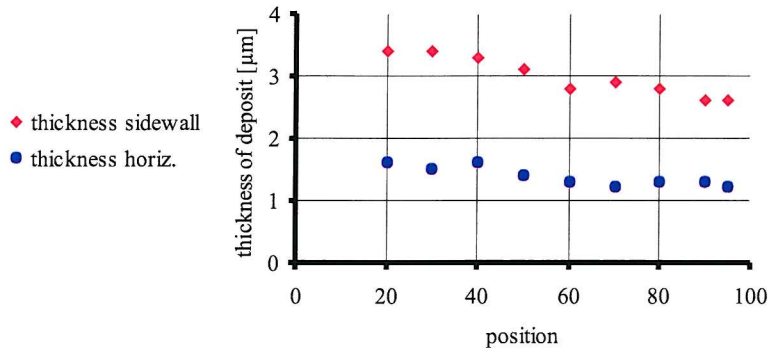

Figure 5.16: Thickness of the aluminum deposit on the sidewall and on horizontal faces plotted against the position along the cleave-line for aluminium deposition obtained by angled evaporation (before wet-etch).

Figure 5.17 shows aluminium fillets obtained by angled evaporation and subsequent wet-etching. The wet-etch is stopped after the aluminium has been removed from the horizontal wafer surface. Figure 5.17a shows a fillet close to the flat of the wafer, where the thickest aluminium deposits could be observed before etching. Consequently, a fairly thick fillet (2.3 μm) is still left after the isotropic wet-etch. The over-etch and the notch at the foot of the fillet are within an acceptable range. The fillet in figure 5.17b, which is located at the centre of the wafer, is noticeably thinner (1.7 μm) as the original deposit was thinner. The over-etch and the notch are slightly increased due to the relatively longer etch-time after the aluminium on the horizontal surface has been removed in the vicinity.

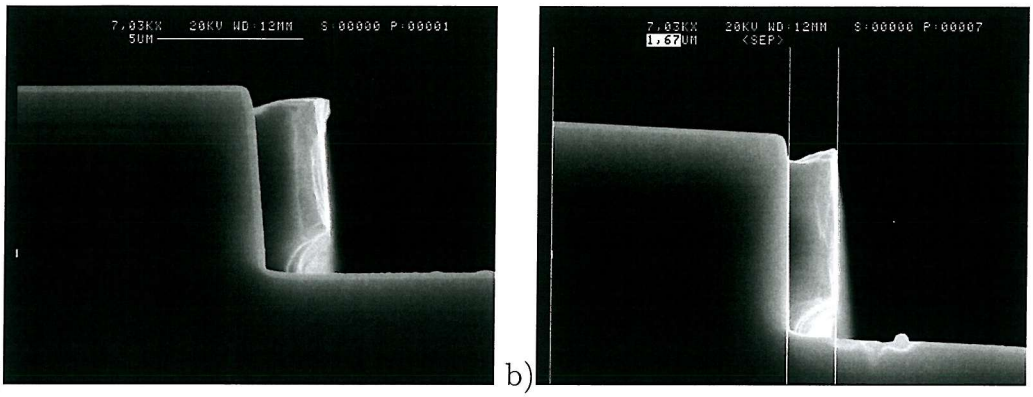

Figure 5.17: Aluminium fillets on sidewalls obtained by angled evaporation and subsequent wet-etch, a) profile view of an aluminium fillet in an area near the flat, b) profile-view of an aluminium fillet in the centre area of the wafer (aluminium thickness on sidewalls: a) 2.3 μm, b) 1.7 μm , evaporation angle $\Phi = 24^\circ$, picture position: a) 20, b) 60).

Figure 5.18 shows the thickness of the fillets obtained by angled evaporation and subsequent aluminium wet-etch plotted against the position along the cleave-line. The fillets are thicker closer to the flat where the original aluminium deposit was thicker. The thickness of the aluminium fillets varies by about 45 % across the wafer, measured from profile views in the SEM.

The results of the wet-etch can be optimised in terms of the over-etch and notch by varying the etch-time across the wafer. Initially, the whole wafer is immersed into the etching solution. As soon as the aluminium at the curve (thinnest deposit) has been removed from the horizontal surface this part of the wafer is retracted from the etching bath. As the etching progresses, the wafer is gradually retracted further from the etching solution with an optimised etching time for the different aluminium thicknesses across the wafer (figure 5.19). Figure 5.20 shows aluminium fillets obtained by angled evaporation and the improved wet-etching technique described above. Hardly any notch and a significantly reduced over-etch can be observed.

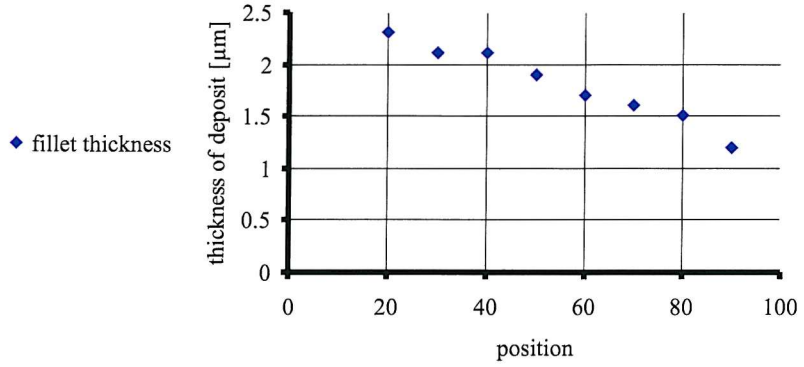

Figure 5.18: Thickness of the aluminum fillets plotted against the position along the cleave-line for aluminium deposition obtained by angled evaporation and subsequent wet-etch.

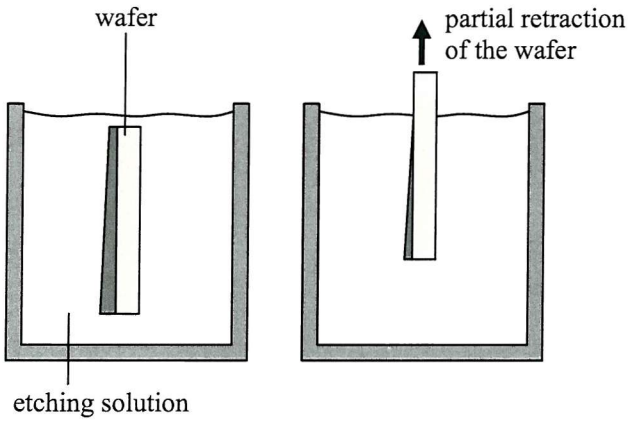

Figure 5.19: Optimised aluminium wet-etch, a) wafer immersed completely, b) gradual retraction of the wafer.

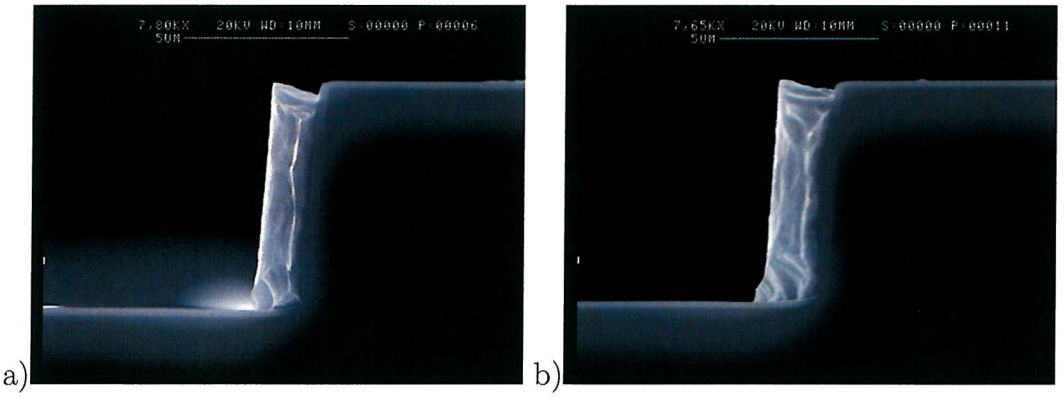

Figure 5.20: Aluminium fillets on sidewalls obtained by angled evaporation and subsequent wet-etch with gradual retraction of the wafer, a) profile view of an aluminium fillet in the centre area of the wafer, b) profile-view of an aluminium fillet in an area near the flat (aluminium thickness on sidewalls: a) 1.4 μm, b) 1.7 μm, evaporation angle $\Phi = 24^\circ$, picture position: a) 50, b) 30).

5.2.4 Summary

Three different multi-step process sequences to obtain aluminium deposits onto sidewalls of silicon trenches have been investigated: Aluminium sputtering and subsequent dry-etching, angled evaporation of aluminium and subsequent dry-etching and angled evaporation of aluminium and subsequent wet-etching.

The sputter process has the disadvantage that sidewall deposits are thinner than deposits on the horizontal surfaces, which leads to very long dry-etch times resulting in damage to the inherently thin sidewall fillets. Angled evaporation offers the advantage that the thickness ratio between sidewalls and horizontal surfaces can be controlled to a certain extent. This allows the dry-etch times to be reduced and the thickness of the aluminium fillets to be increased. To avoid the non-uniformity of the dry-etching process, wet-etching can be employed, provided that the deposits on the sidewalls are thicker than those on the horizontal surfaces.

The overall result of the investigation showed that combining angled evaporation and wet-etching yields the best sidewall deposits and is the easiest to control as well as the most reproducible process. Over-etch and notching can be minimised by gradually retracting the wafer from the etching bath.

5.3 Chrome/Gold Sidewall Contact Deposition

The micro-relays introduced in chapter 3.6 use gold contacts for the contact circuit. As the adhesion of gold is very poor on silicon or oxide, a chrome adhesion layer is necessary. Since the moving contact moves laterally in the wafer plane, the chrome/gold contacts are required on the opposite sidewalls of the trench etched into the device silicon layer which forms the contact gap. In this section, the requirements for the chrome/gold contact deposition are discussed and the results for evaporations at different angles are given. The LMS-process file is listed in appendix B.1.3.

5.3.1 Requirements for the Chrome/Gold Contacts

The chrome/gold contacts have to cover opposite sidewalls of the trenches in the silicon. They also need to be connected to chrome/gold conductors on the horizontal wafer surface. Hence, a good step coverage for the chrome/gold deposition is required. Additionally the gold coating on the sidewalls should reach down to the bottom of the trench to maximise contact area. Figure 5.21 shows a cross-section of the contact gap illustrating the ideal chrome/gold contact.

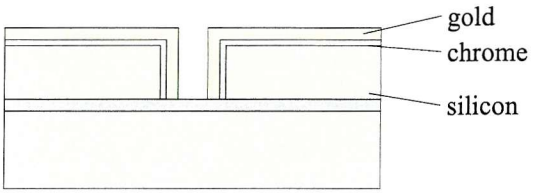

Figure 5.21: Contact trench with ideal chrome/gold contact.

5.3.2 Implementation of the Chrome/Gold Deposition

Two consecutive chrome/gold evaporations at a rather steep angle of incidence Φ (definition see figure 5.7) are carried out to cover the steps both on the right- and the left-hand side of the trench using the jig for angled evaporation. The first evaporation deposits a chrome/gold layer onto the right-hand side sidewall and the horizontal surface of the wafer (figure 5.22a), the second evaporation deposits chrome/gold onto the left-hand side sidewall and the horizontal surface (figure 5.22b). The rather steep angle is chosen because the trenches for the contacts are quite narrow (6 μm to 24 μm) and deep (30 μm). Ideally, the gold coating on the sidewall should reach down to the bottom of the trench, but not extend along the bottom of the trench. However, it is impossible to achieve this with different aspect ratio trenches. In wide trenches, the chrome gold deposition extends along the bottom of the trench (see figure 5.22I). These horizonal chrome/gold areas need to be removed at the release etch stage in order to ensure the functionality of the contacts. A standard chrome/gold wet-etch is used. In narrow trenches, the chrome gold sidewall coating does not reach to the bottom of the trench (figure 5.22II). Hence, the contact area is reduced.

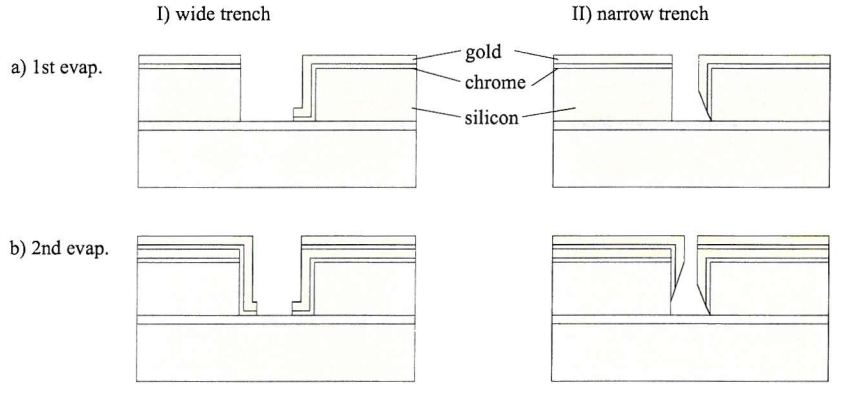

Figure 5.22: Two-stage chrome/gold contact evaporation.

To optimise the angle of incidence Φ for the contact evaporation, experiments were carried out on silicon testwafers with 6 μm deep trenches (HBr-process). Three different angles of incidence Φ were used. Figure 5.23 shows SEM images of section views taken from the test wafers with the three different angles Φ. Table 5.1 gives the process parameters and the results for the different angles Φ.

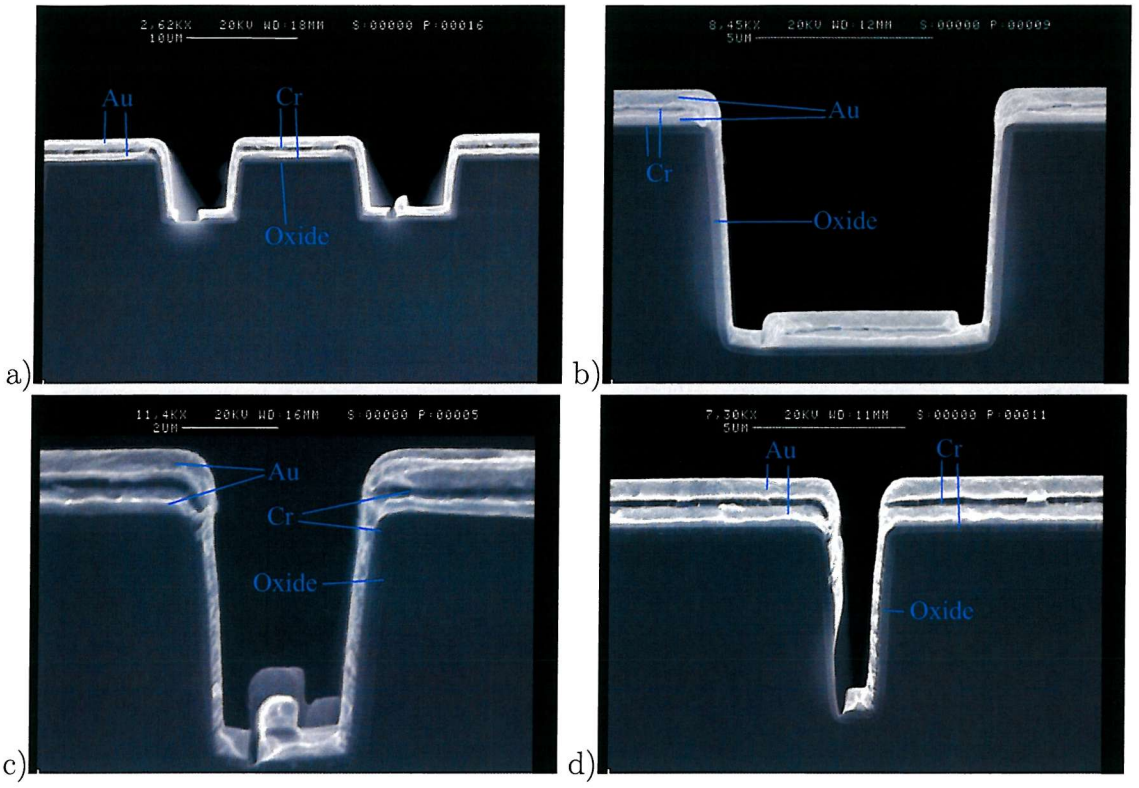

Figure 5.23: SEM section images of chrome/gold contact evaporation, a) $\Phi = 57^\circ$, b) $\Phi = 80^\circ$, c) $\Phi = 75^\circ$, d) $\Phi = 75^\circ$.

	figure 5.23a	figure 5.23b	figure 5.23c,d
Φ [$^\circ$]	57	80	75
Cr evaporation time [s]	40	20	20
Cr evaporation em. current [A]	0.05	0.05	0.05
Cr thickness, sidewall, right [nm]	320	n/a	120
Cr thickness, sidewall, left [nm]	280	n/a	130
Cr thickness, horizontal, 1 [nm]	320	n/a	200
Cr thickness, horizontal, 2 [nm]	340	50	180
Au evaporation time [s]	180	120	120
Au evaporation em. current [A]	0.4	0.4	0.4
Au thickness, sidewall, right [nm]	770	250	270
Au thickness, sidewall, left [nm]	820	200	270
Au thickness, horizontal, 1 [nm]	680	450	400
Au thickness, horizontal, 2 [nm]	1100	500	650

Table 5.1: Contact evaporation results (see figure 5.23).

5.3.3 Summary

For the fabrication, an angle Φ of 75 $^\circ$ is chosen because it gives good thicknesses for both chrome and gold on the horizontal surface as well as on the sidewalls. It also

ensures that the sidewall depositions reach far down the trench even at high aspect ratio.

5.4 Thick Photoresist Patterning

The vertical bimorph actuators of the second generation (see chapter 3.4 and 3.5) are based on SOI-substrates with a 30 μm thick device silicon layer. At the beginning of the process sequence, trenches reaching down to the buried oxide layer, are etched into the device silicon layer to define the geometry of the actuators. This leaves the challenge that all subsequent photolithography stages have to be carried out on a wafer with 30 μm steps with an almost vertical sidewall angle. For better understanding a review of basic photolithography is given below.

5.4.1 Photolithography Basics

Photolithography is used to transfer patterns from a mask into a photosensitive film, called photoresist, which is used as a mask for the subsequent etching or deposition process. Good references are [3, 124, 125]. Lithography follows this basic sequence:

- Coating: The substrate is prepared by a dehydration bake to remove moisture on the surface and then a priming stage to improve the adhesion of the resist. Then, the photoresist is dispensed onto the wafer and spread by spinning. The viscosity of the resist and the spin speed determine the resist thickness.
- Softbake: The softbake is performed either on a hotplate or in a convection oven and removes solvents from the resist layer and hardens it.
- Exposure: The hardened photoresist is illuminated with UV light through a mask, which starts a photochemical process in the exposed resist. In the case of a positive resist, the exposed portions undergo a chemical change that makes them soluble in the developer. In the case of a negative resist, the exposed portions become insoluble in the developer, whereas the unexposed parts retain their solubility. In this work, merely positive photoresists are used, therefore any reference to resist always means a positive resist. Some photoresists need a post exposure bake on a hotplate or in an oven to enhance the chemical reaction.
- Development: The wafer is immersed into a solvent, the developer, which dissolves the soluble portions of the photoresist. A hardbake on a hotplate or in an oven gives the resist the required chemical or thermal robustness to withstand the following etching or deposition process. Figure 5.24 depicts the basic photolithography sequence.

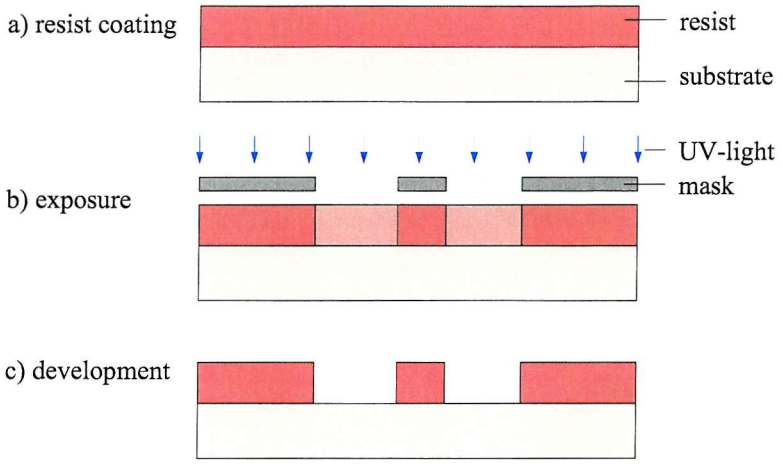

Figure 5.24: Basic photolithography sequence.

5.4.2 Requirements for Thick Photoresist Patterning

Figure 5.25 illustrates the requirements for the thick-resist patterning. The remarks in brackets refer to the location on the wafer as marked in figure 5.25. The photolithography for the following process stages requires thick photoresist patterning:

- Contact window etch: A dark-field pattern is etched into the insulation oxide to define the contact windows for the gold contact pads. The areas of the contact windows on the wafer surface (a1) and the silicon beams (a2) need to be opened (development) in order to reveal the oxide to the etching solution whereas the other beams (a3) and the wafer surface(a4) have to be properly covered with resist.

- Gold Etch: A light-field mask defines the areas of the gold contacts. The contact areas at the wafer surface (b1) and the silicon beams (b2) have to be covered with resist, whereas the other resist on the wafer surface (b3), the beams (b4) and in the trenches (b5) has to be removed completely in the developer.

- Aluminium sidewall evaporation: A light-field pattern protects areas in the trenches (c1) and some of the beams (c2) from the aluminium evaporation. Again, the rest of the resist on the wafer surface (c3), the beams (c4) and in the trenches (c5) has to be removed completely.

For the thick resist photolithography, the following practical requirements can be concluded.

- The photoresist needs to be thicker than 30 μm in order to cover the silicon beams. This is considerably thicker than standard photoresist at 2.2 μm. A more viscous resist and multiple coatings were tested.

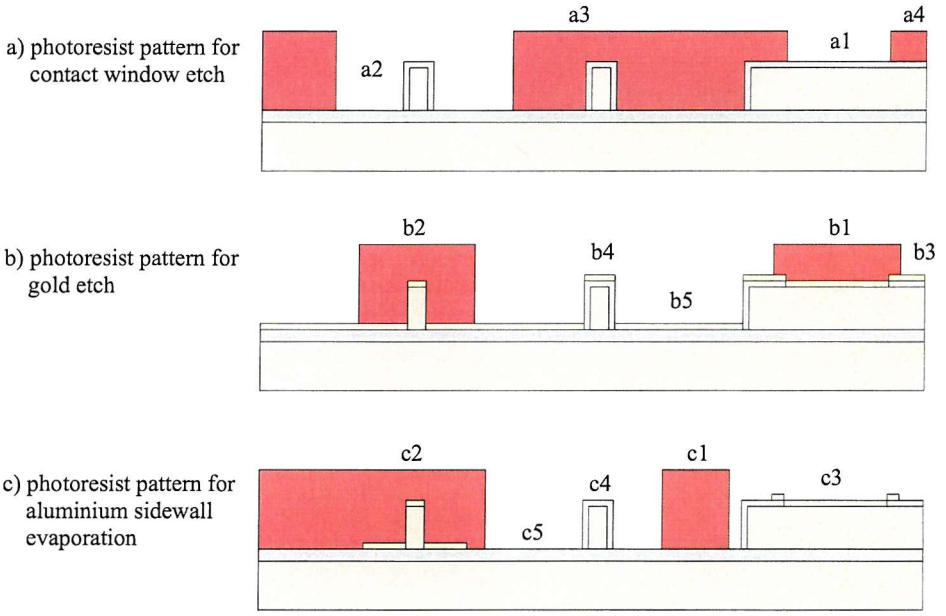

Figure 5.25: Illustration of the requirement for thick-resist patterning.

- The exposure dose has to be chosen such that even the resist in the trenches (highest overall resist thickness) becomes soluble in the developer. However, the exposure dose should not be too high in order to ensure that the masked areas of the resist retain their insolubility.
- Similar to the exposure dose, the development time has to be optimised for complete removal of exposed resist without attacking unexposed resist.
- The soft bake and hard bake procedure has to make sure that the solvents evaporate from the resist to make it suitable for the subsequent etch or evaporation process. Especially for the aluminium evaporation, the wafer is at an elevated temperature. A careful removal of the solvents is required.

5.4.3 Process Details

In the order of the basic sequence described above, the process details are given below. Appendix B.1.2 lists the LMS-process file.

Resist Coating

To obtain a thick coating, a viscous positive resist, Shipley Megaposit SPR220-7 [126], is used. Figure 5.26 shows a spin speed curve. We have measured the thickness for single-spin coatings to be 9.5 μm for 2000 rpm and 11 μm for 1500 rpm, which is in good agreement with the provider's curve. To obtain a 35 μm thick coating two spins with a spin speed of less than 1500 rpm are required.

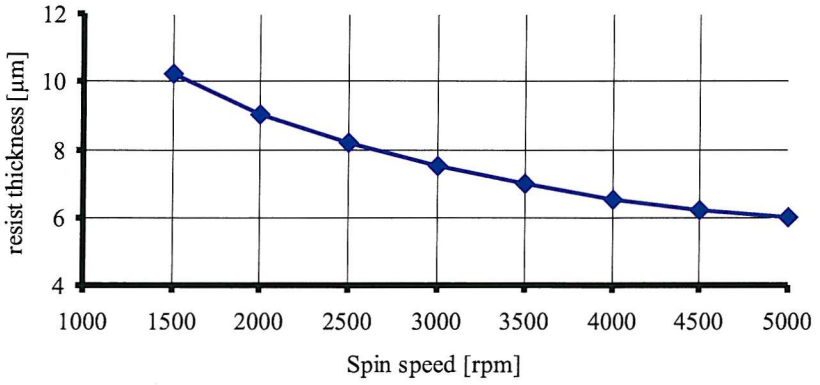

Figure 5.26: Spin speed curve for Megaposit SPR220-7 resist [126].

With coatings thicker than 10 μm, a thick edge bead is observed as sketched in figure 5.27. The edge bead prevents the mask from getting into proper contact with the wafer at the exposure stage and hence reduces the imaging quality significantly. Furthermore, the thick edge bead means a problem for baking, since the risk of solvent bubble formation increases with resist thickness. A way to reduce the edge bead effect is to add a second spin stage at a high speed for a short time. We found, that a double coating with the following two stages gives an approximately 35 μm thick resist layer on a flat wafer or a coating that reasonably covers steps and beams on a wafer with trench topography.

- Stage 1: Spin speed: 750 rpm, time: 120 s
- Stage 2: Spin speed: 4000 rpm, time: 20 s

The disadvantages of a fast second spin stage are:

- The fast spin stage significantly reduces the resist thickness.
- On a wafer with topography, the step coverage is reduced.
- On wafers with topography, air bubble formation increases in the corners of the trenches.
- The edge bead is only reduced, but not completely removed.

Due to these drawbacks, an additional exposure and development step is used for edge bead removal (see below).

For the coating we found that a double spin at a spin speed of 800 rpm for 40 s yields a resist thickness of roughly 38 μm with good step coverage.

We also investigated single spin coatings to get a resist thickness of more than 30 μm. A spin speed as slow as 300 rpm is required. However, during the softbake, the resist retreats from areas close to the edge of the wafer and close to to edges of trenches, resulting in an unreliable step coverage.

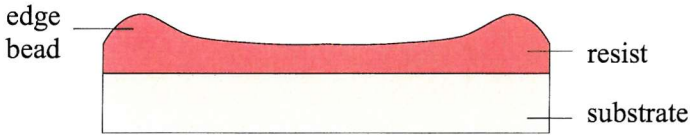

Figure 5.27: Edge bead.

Softbake

Hot plate and oven bakes and combinations of the two have been investigated. Even though hot plate baking is more time efficient it tends to cause a more pronounced solvent bubble formation and can lead to unreliable step coverage as mentioned above. Therefore, the standard softbake procedure only consists of oven baking:

- After the first spin: Bake in oven at 90 ° C for 15 minutes.
- After the second spin: Bake in oven at 90 ° C for 90 minutes.

This recipe for softbake (combined with an appropriate hardbake, see below) makes the resist suitable for all etch and evaporation processes applied.

Edge Bead Removal

To remove the edge bead, we expose the wafer after the softbake through a mask of circular shape that only exposes the edge bead to the UV light and protects the other photo resist. The edge bead can then be dissolved in the developer. This approach removes the edge bead completely and allows the simple spinning process described above. Figure 5.28 illustrates the edge bead removal. The following process details are used:

- Exposure: 800 s (HTG).
- Development: 7 minutes, tank development.

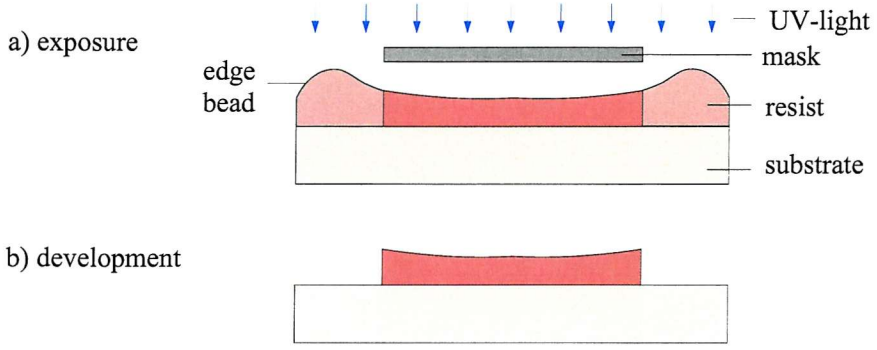

Figure 5.28: Edge bead removal process.

Exposure

We use contact printing on an HTG mask aligner. Different exposure times have been used on test wafers with the original topography (30 μm deep trenches):

- exposure time: 400 s. The pattern definition on the wafer surface is good but there are resist residues in the trenches (after development).
- exposure time: 550 s. The pattern definition on the wafer surface is still good, and there are no residues in the trenches (after development).
- exposure time: 650 s. The quality of the pattern definition on the wafer surface is decreasing, and there are no residues in the trenches (after development).

An exposure time of 550 s is be used for the standard processing.

Development

A development time of 5 to 7 min in a dunk tank with manual agitation is sufficient for good pattern definition and to remove the resist from the trench areas.

Hardbake

The hardbake is carried out in a convection oven at 90 $^\circ$ C for 4 hours. The sidewalls of the resist get rounded during the hardbake. However, for all etching and evaporation processes applied, rounded sidewalls do not have any influence on the functionality of the resist. Table 5.2 gives a comprehensive overview on the process parameters.

Coating	Spin SPR220-7 at 800 rpm for 40 s, twice
Soft bake	Bake in convection oven at 90 ° C for 15 minutes after the first spin and for 90 min after the second spin
Edge Bead Removal	Expose for 800 s (circular mask,HTG), develop for 7 min
Exposure	Contact Print, exposure time 550 s (HTG)
Development	Dunk Tank Development, 5 to 7 min
Hark bake	Bake in oven at 90 ° C for 4 hours

Table 5.2: Overview on process parameters for thick resist patterning.

5.4.4 Summary

Applying the viscous SPR220-7 photoresist in two coatings, baking in a convection oven, optimised exposure and development times and an edge-bead removal stage using an additional exposure and development stage enables photolithography on wafers with 30 μm deep trenches, where areas in the trenches, on the silicon surface and on the top of narrow silicon beams are covered or revealed as desired.

5.5 Release Etch

To obtain freely moving actuators, the handle silicon and the buried oxide layer need to be removed in the bimorph areas of the actuators. Even though this may appear to be a straightforward process, many problems occurred in this process, resulting in a significant amount of process development work. Several approaches for the release etch have been tested. In this section, we describe the different methods and highlight their problems and advantages as well as their disadvantages.

5.5.1 KOH-etching

Anisotropic wet-etching in potassium hydroxide (KOH) is used to etch a recess from the back of the SOI wafer reaching almost to the buried oxide layer. Deep KOH-etching requires an oxide/nitride mask, since the selectivity to oxide is too low for long etch processes. Furthermore, KOH rapidly etches aluminium. Therefore, the KOH etching needs to be done as the first major process step in the fabrication sequence. Figure 5.29 shows the relevant parts of the process sequence.

An oxide layer of 300 nm in thickness is grown (wet oxidation) and a 160 nm thick nitride layer is deposited in an LPCVD furnace. The two layers are patterned by dry-etching on the backside of the wafer to form the mask for wet-etching of the handle silicon. The wet-etch is carried out in a KOH-solution at 70 ° C (figure 5.29b). The

etch depth is measured with an optical microscope by focussing on the wafer surface and the horizontal surface of the etch pit and measuring the difference between the two focal points. The etch is stopped, when roughly 10 μm of handle silicon still remains. This leaves a reasonably strong membrane for the subsequent process steps. The oxide/nitride mask is then stripped in hydrofluoric acid and orthophosphoric at 160 $^\circ$ C acid respectively.

After KOH-etching, the front side processing is carried out, including contact gold deposition and aluminium sidewall deposition (figure 5.29c).

Before the release etch, a protection photoresist is spun onto the front of the wafer and baked (figure 5.29d). A double coating with SPR220-7 is used as described in section 5.4. It fulfills the following tasks:

- It prevents reactive species of the SF_6-plasma from attacking silicon on the front side of the wafer (see section 5.5.2).
- It reinforces the buried oxide membrane, when the handle silicon is completely removed.
- It protects the beams from mechanical damage from the cooling water and from contamination with sawdust during the sawing stage.

The remaining handle silicon is etched using an RIE blanket dry-etch in an SF_6 plasma (figure 5.29e, RF-power: 100 W). With a generous overetch, this process takes about 20 minutes. Due to the vacuum in the etching chamber and the elevated temperature during the plasma-reaction, solvent bubble formation and cracks can occur in the photoresist layer, especially if baked in a convection oven. More details are given in section 5.5.2.

The buried oxide is removed in an RIE-process in a trifluoromethane (CHF_3) and Argon plasma (figure 5.29f). Solvent bubble formation and cracks in the resist are an even bigger problem here, since an RF-power of 200 W is used and the process takes roughly 100 minutes to completely etch the 2 μm of buried oxide.

The wafer is sawn into chips with a standard rotary dicing saw (figure 5.29g). The protection resist prevents the actuators from contamination with sawdust and from mechanical damage through the cooling water. The photoresist is then removed in acetone, the chips are cleaned in fuming nitric acid, rinsed in water and dried in a laminar air flow. A dip in isopropyl-alcohol (IPA) removes stains and residues left due to the air drying. IPA is significantly more volatile than water and hence leaves less residues on the wafer.

The main disadvantage of etching recesses with KOH is that the whole front side processing has to be carried out on the thin oxide/silicon membranes. A high number

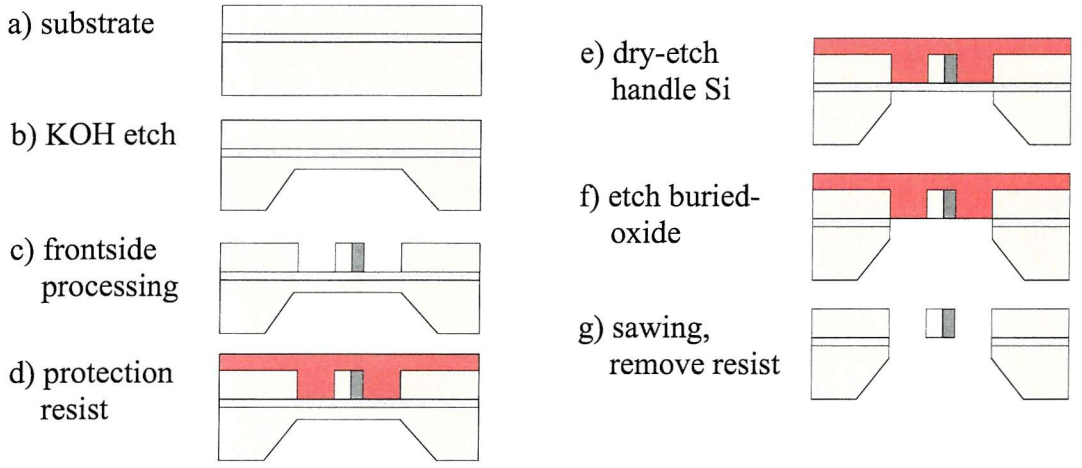

Figure 5.29: Sequence for KOH release-etch.

of devices are lost due to breakage of the membrane. The vacuum chucks on the resist spinner and the mask aligner are the most significant threat. Furthermore, there is still a need for silicon as well as buried oxide dry-etching. Even though the silicon dry-etching is significantly shorter than in all the other approaches, the disadvantages (see the following sections) of this stage cannot completely be eliminated.

5.5.2 Silicon Dry-Etching with Protection Resist

The disadvantages of the KOH release etch lead to the idea of using the SF_6 process for etching the handle silicon all the way to the buried oxide layer. This allows for the release etch to be carried out after the front side processing is completed and will produce a significant advantage for the expected yield. As mentioned in the preceding section, a protection resist is required for this etching stage, mainly to protect the silicon structures on the front from being etched by stray SF_6 species. Figure 5.30 gives the relevant process sequence.

As mentioned above, the front side processing is carried out before the release etch (figure 5.30b). A 1000 nm thick aluminium layer is evaporated and patterned on the back of the wafer to form the mask for the SF_6 silicon etch (figure 5.30c). The metal mask is required because neither oxide nor photoresist would withstand the long dry-etch process.

On the front of the wafer, a photoresist layer for protection is spun (figure 5.30d). Protection of the silicon beams on the front from being etched by reactive SF_6 species is very important during the long dry-etch process. In initial etching tests without protection resist, an etch attack could be noticed at the silicon beams already after about 90 minutes of etching, thinning the beams by approximately 1 μm on either side, making them very fragile. After the spin, a softbake is carried out. More details

are discussed below.

The handle silicon wafer is etched in a semi-anisotropic SF_6 process, at an RF-power of 100 W and a pressure of 150 mT (figure 5.30e). The etch rate is approximately 1 $\frac{\mu m}{min}$, resulting in an etching time of 7.5 hours for the 450 μm thick handle wafer. In practice, the etch rate can be as low as 0.5 $\frac{\mu m}{min}$ resulting in an etching time of 15 hours. This slow etch rate results from increased temperatures, because the protection resist forms a thermal insulation layer, reducing the cooling effect of the cover plate in the plasma reactor.

The semi-anisotropic character of the etch means that the aluminium mask is significantly undercut. This undercut needs to be accounted for in the mask design. Once the etch has reached the buried oxide it cannot progress further in depth, but only widens the recess due to the partly isotropic character. This fact is exploited to adjust the size of the recess at the buried oxide layer by carrying on the etch until the length and the width of the recess in the handle wafer is slightly larger than the dimensions of the trenches on the front of the wafer.

Figure 5.31 shows a profile view of a test wafer after the SF_6 through wafer etch. The aluminium mask got undercut and overhangs the silicon by an amount e. On the bottom of the wafer, the width of the recess is an amount d wider than the aluminium mask. We have measured the two amounts along the cleaveline of the wafer and found that e ranges from 370 μm to 410 μm, and d ranges from 80 μm to 140 μm for the 525 μm thick test wafer. These figures were used to optimise the size of the openings of the aluminium mask. Appendix B.1.4 lists the LMS-process file of the corresponding test batch.

To cover cracks in the protection photoresist a second resist layer is applied and baked in a convection oven. The aluminium mask is removed in orthophosphoric acid. Then, the buried oxide layer is etched in 7:1 buffered hydrofluoric acid (figure 5.30f). The protection resist prevents the insulation oxide layer on the front of the wafer as well as the aluminium sidewall deposits from being etched. However, it is difficult to remove the buried oxide layer without leaving residues and without the aluminium sidewall deposits being attacked. Just a short exposure of the aluminium sidewall deposits to HF can remove them completely from the silicon beams. The unwanted chrome/gold patches, which were deposited onto the buried oxide layer during contact evaporation are removed in standard chrome and gold wet-etch solutions.

Wafer sawing, resist removal and cleaning is carried out as described above (figure 5.30g).

For initial tests, a double coating of SPR220-7 resist was used for the protection layer as described in section 5.4 with a 90 min oven bake at 90 $^\circ$ C. An enormous solvent bubble formation was observed after about 60 min of dry-etching. The resist

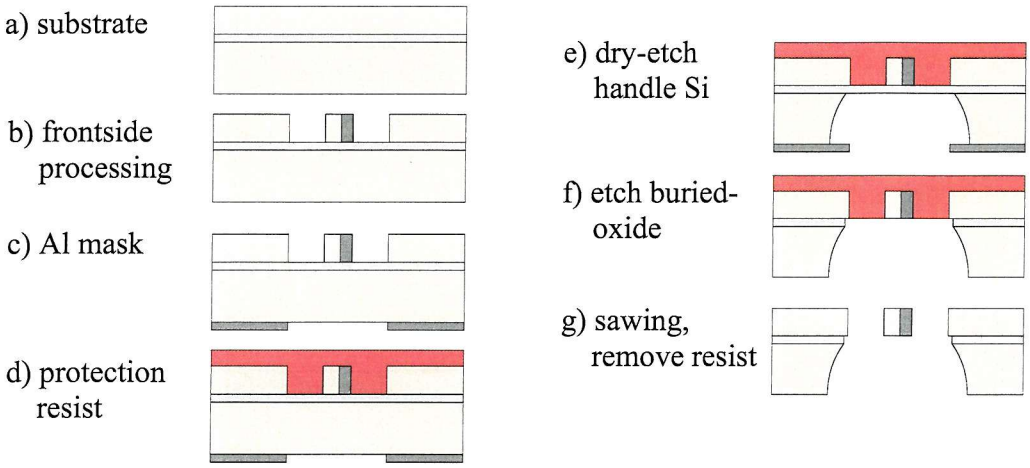

Figure 5.30: Sequence for SF_6 release-etch with protection resist.

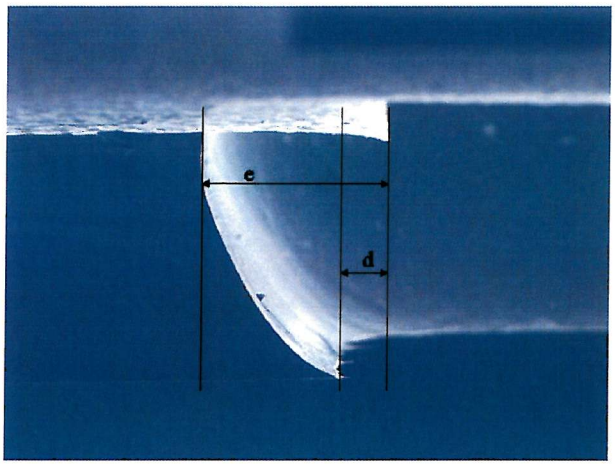

Figure 5.31: SEM profile view of a test wafer after SF_6 through wafer etch.

peeled off in large flakes. This phenomenon indicates that the solvent concentration in the photo resist was not reduced to a limit acceptable for the RIE process.

An improved protection resist technique uses a single spin of SPR220-7 at 500 rpm to cover the beams on the front of the wafer. The bake is carried out on a hotplate, which is ramped from 60 ° C to 90 ° C in 20 min and then left at 90 ° C for 15 min. The edge bead removal as described in section 5.4 is carried out followed by a second hotplate bake, ramping from 60 ° C to 100 ° C in 30 min and then soaking at 100 ° C for 3 hours. The procedure makes the photoresist suitable for etching times in the range of 100 to 200 minutes but it is still insufficient for the through wafer etch process, which takes about 10 to 15 hours. The reason for this is that this long etching time leads to a significant loss of protection resist due to ashing in the plasma reaction.

The problems experienced with SPR220-7 call for a thermally and chemically more stable protection resist. The epoxy based negative resist SU-8 [127–129] has been investigated. Due to its high viscosity (SU-8 100) it covers the beam area on the

front of the wafer with a single coating. It is softbaked on a hotplate that is ramped up to 150 ° C and withstands the dry-etching without noticeable changes. However, it is very difficult to remove. The most common method is to immerse it in hot NMP, which swells the resist and reduces its adhesion to the substrate. This removal procedure however involves very high mechanical stress, which breaks free-standing silicon beams.

Another alternative is PMGI positive photoresist [130]. It has a glass temperature of 190 ° C. Its high viscosity (PMGI-SF23) allows a single spin coating at 1000 rpm to cover the beams. It is baked on a programmable hotplate that is ramped from 20 ° C to 140 ° C at a rate of 40 $\frac{^\circ C}{hour}$, left at 140 ° C for 1 hour and then cooled off slowly. PMGI dissolves in NMP meaning it can be neatly removed from the wafer. However, the adhesion of PMGI deteriorates in the dry-etch process and some solvent bubbles occur. Furthermore, the etch rate of the dry-etch is slowed down significantly to approximately 0.3 $\frac{\mu m}{min}$ because of the low thermal conductivity of the resist layer.

5.5.3 Silicon Dry-Etching with Backing Wafer Glued on with Cool Grease

An alternative to a protection photoresist is to protect the front of the device wafer with another silicon wafer, a so-called backing wafer. This can be glued on in various ways. One approach is to use Cool Grease [131], a heat conductive paste specially developed for application in plasma-etchers. Figure 5.32 gives an overview of the respective release etch process.

The front side processing and the aluminium mask patterning are carried out as described above. Then, Cool Grease is spread onto the backing wafer with a spatula (figure 5.32a). The backing wafer is heated on a hotplate to assist homogeneous spreading of the paste. There is no baking required for curing or hardening of the paste.

The device wafer is glued onto the backing wafer such that the device silicon side lies on the Cool Grease of the backing wafer (figure 5.32b). The two wafers are manually pressed against each other to ensure good adhesion. The etching of the handle silicon wafer (figure 5.32c) and the buried oxide layer (figure 5.32d) is carried out as described in the preceding section.

The sawing is done from the back of the device wafer (figure 5.32e). The saw cut only touches the backing wafer, but does not saw it into pieces. To separate the devices from the backing wafer, the sandwich is immersed into acetone, which slowly dissolves Cool Grease.

The advantage of using a backing wafer glued on with Cool Grease lies in the fact

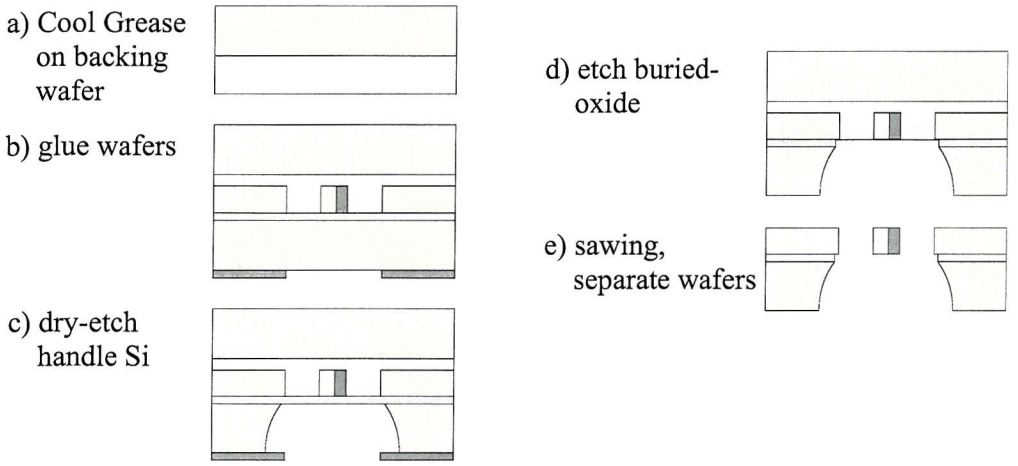

Figure 5.32: Sequence for SF_6 release-etch with backing wafer glued on with Cool Grease.

that the thermal conductivity of the wafer sandwich is very good, resulting in a fast dry-etch rate of approximately 0.9 $\frac{\mu m}{min}$.

However, there are significant disadvantages, making this approach unsuitable for the work discussed here:

- Removing Cool Grease in acetone or NMP always leaves large residues. Cool Grease can be etched in orthophosphoric acid or photoresist developer, however these also attack aluminium, making them incompatible with the bimorph beams.
- Due to the increased temperature during the silicon dry-etch, the Cool Grease expands and applies pressure onto the buried oxide membranes. This causes some of the membranes to break and Cool Grease comes onto the back of the buried oxide layer forming a mask (figure 5.33), which prevents the oxide from being etched later on. Figure 5.34 shows an image taken from the back of the wafer in an optical microscope where Cool Grease has broken through the buried oxide layer, leaving residues on the oxide.

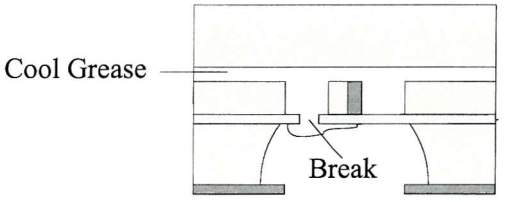

Figure 5.33: Cool Grease breaks through the buried oxide layer.

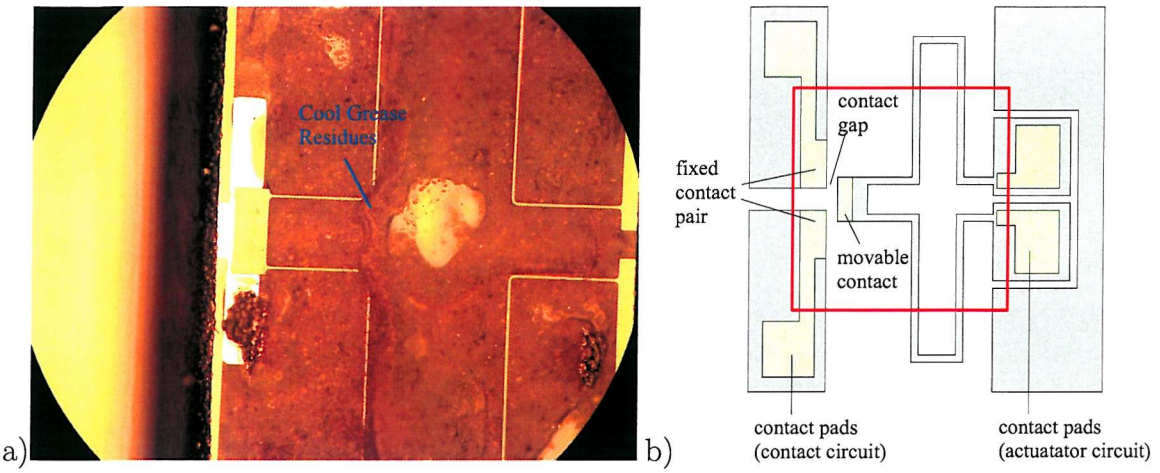

Figure 5.34: a) Image taken in an optical microscope showing Cool Grease broken through the buried oxide layer, leaving masking residues (taken from the back of the wafer), b) sketch of a normally open relay for orientation.

5.5.4 Silicon Dry-Etching with PMGI Resist and Backing Wafer Glued on with Cool Grease

In order to reinforce the buried oxide membrane, a PMGI resist layer is applied onto the device wafer. Figure 5.35 shows the relevant process sequence.

The front side processing and the preparation of the aluminium mask is carried out as given above. A PMGI layer is spun onto the device wafer and baked as described in section 5.5.2. Cool Grease is applied to the backing wafer (see section 5.5.3) as shown in figure 5.35a.

Then, the two wafers are glued together (figure 5.35b). Dry-etching of the handle silicon (figure 5.35c) and the wet-etching of the buried oxide layer (figure 5.35d) are carried out as described in section 5.5.2.

The sawing is carried out from the back of the device wafer and only cuts the device wafer into dices. To separate the devices from the backing wafer, the sandwich is immersed into NMP which dissolves the PMGI layer and also the Cool Grease (figure 5.35e).

The problem with this release etch method is that the PMGI layer prevents good heat conduction and hence leads to high substrate temperatures during the silicon etch, slowing the etch rate to approximately 0.4 $\frac{\mu m}{min}$. The high temperature also leads to increased stress in the Cool Grease which causes breaks even in the reinforced buried oxide layer. Even though the PMGI layer covers the silicon beams initially, after the wafer separation, Cool Grease residues are found on the silicon beams. These drawbacks make this release etch approach unsuitable for bimorph devices.

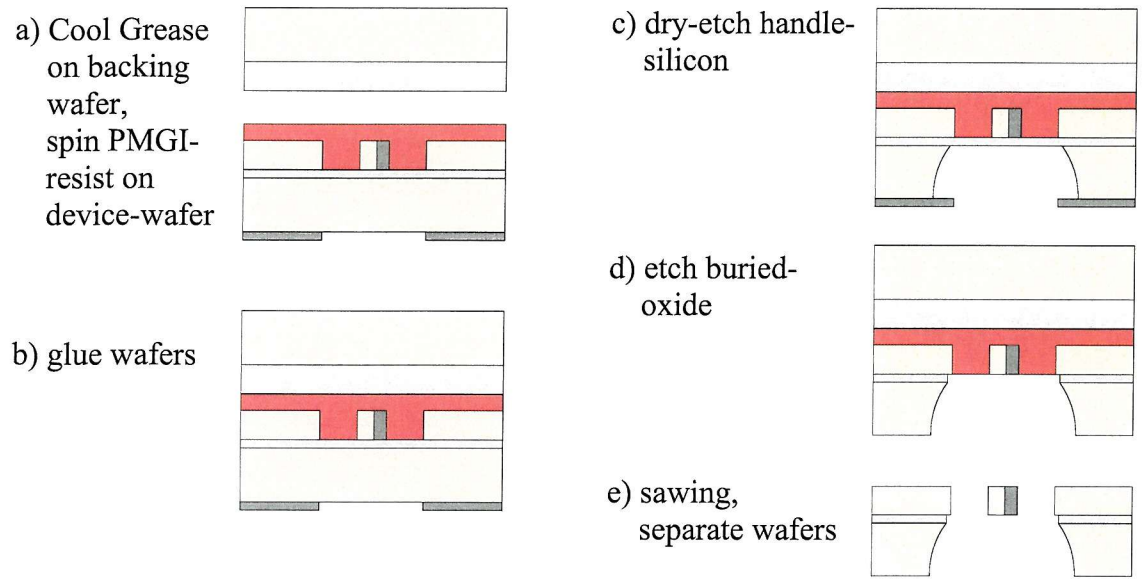

Figure 5.35: Sequence for SF_6 release-etch with PMGI photo-resist and backing wafer glued on with Cool Grease.

5.5.5 Silicon Dry-Etching with Backing Wafer Glued on with SPR220-7 Photoresist

This approach uses SPR220-7 photo resist to glue the backing wafer onto the device wafer. Figure 5.36 gives the relevant process steps.

The front side processing and the preparation of the aluminium mask is carried out as given in section 5.5.2. SPR220-7 photoresist is spun onto the device silicon wafer at 800 rpm for 40 s. The softbake is carried out on a programmable hotplate, which ramps from 20 ° C to 105 ° C at a rate of 60 $\frac{^\circ C}{hour}$, stays at 105 ° C for 2 hours and then cools down to 20 ° C at a rate of 80 $\frac{^\circ C}{hour}$ (figure 5.36a). SPR220-7 is also spun onto the backing wafer at 2000 rpm for 40 s.

Then, the two wafers are glued together such that the two resist layers join together. The above hotplate bake is repeated to harden the resist on the backing wafer (figure 5.36b).

The recess into the handle silicon is etched using the SF_6 process (figure 5.36c). Even though there is a photoresist layer between the device wafer and the backing wafer, there is good heat conduction and hence a quick etch rate of 1.0 $\frac{\mu m}{min}$.

The aluminium mask is removed in orthophosphoric acid. To prepare for the buried oxide etch, the two wafers are separated in acetone (figure 5.36d) and the device wafer is cleaned in fuming nitric acid. The backing wafer and the photoresist are removed before the buried oxide etch because internal stress in the photoresist can damage the silicon beams as soon as the supporting oxide is removed.

Then the buried oxide is etched using an RIE-process in CHF_3 and Ar plasma (RF-power: 200 W, etch time 100 minutes, see figure 5.36e). The dry-etch is preferred to a wet-etch in buffered HF, because the hydrofluoric acid attacks the sidewall aluminium on the bimorphs. No protection resist is required since this RIE process is anisotropic and the insulation oxide on the front of the wafer is not attacked. Most of the chrome/gold patches, which were deposited onto the buried oxide layer during contact evaporation break off when the buried oxide is etched. No special stage for chrome/gold etching is required.

To prepare the device wafer for sawing, a layer of SPR220-7 is spun onto a new backing wafer at 1000 rpm for 40 s (figure 5.36f). Then, the device wafer is glued onto the backing wafer such that the front of the device wafer lies in the photo resist (figure 5.36g). A very thick layer of SPR220-7 is spun onto the back of the device wafer at 200 rpm for 40 s (figure 5.36h). This means that the silicon beams are completely encapsulated in photoresist for protection from mechanical damage by the cooling water and from contamination with sawdust.

The device wafer is sawn from the back (figure 5.36i). The saw cut only touches the backing wafer, but does not saw it into pieces. To separate the devices from the backing wafer, the sandwich is immersed into acetone. The diced devices are then cleaned in fuming nitric acid and dried in a laminar air flow.

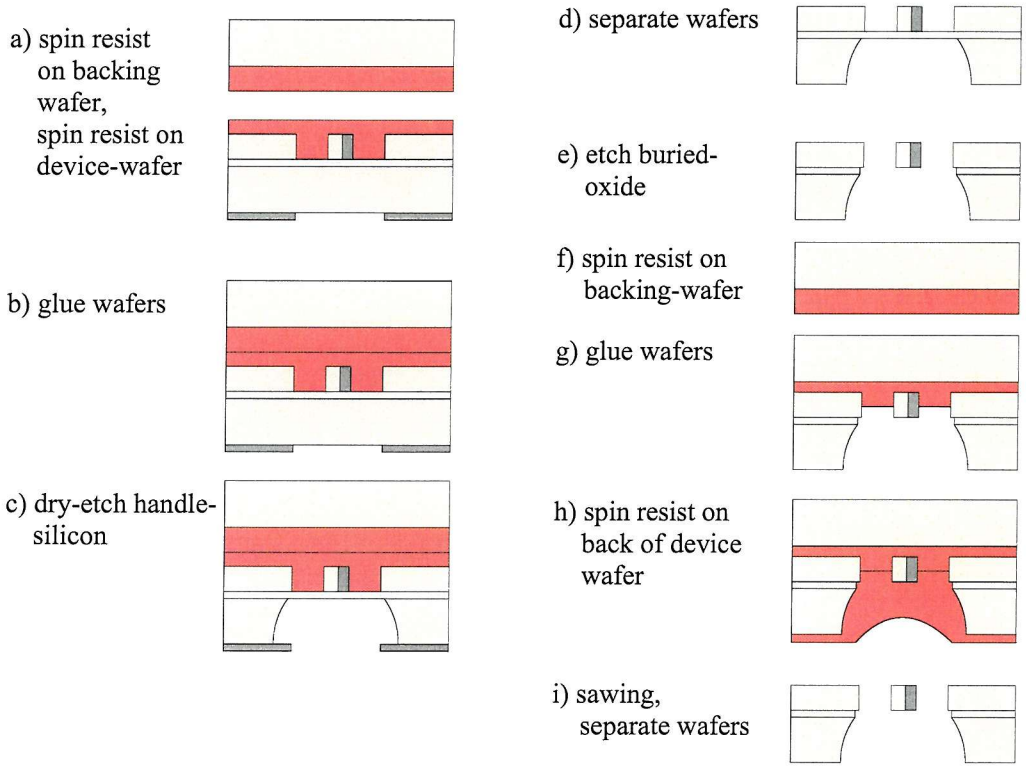

Figure 5.36: Sequence for SF_6 release-etch with backing wafer glued on with SPR220-7 photoresist.

5.5.6 Summary

Releasing the bimorph actuators without breaking the delicate beams and without removing the aluminium sidewall deposits has turned out to be a difficult task. The best solution was that described in section 5.5.5: Gluing a backing wafer with SPR220-7 photoresist for the silicon dry-etch and dry-etching the buried oxide without protection. There are no major drawbacks. However, still plenty of the silicon beams break during the release sequence reducing the yield to rather low figures.

5.6 Conclusion

Several non-standard processes have been developed for the fabrication of vertical bimorph actuators. Aluminium deposition onto sidewalls of silicon trenches has been realised by angled evaporation (shallow angle) and subsequent aluminium wet-etching. Chrome/gold conductors covering both silicon sidewalls and the wafer surface are deposited by angled chrome/gold evaporation at a steep angle of incidence. A photolithography process for the topography of 30 μm deep trenches has been developed, based on two coatings with a viscous positive resist, SPR220-7. Releasing the bimorph actuators is achieved using an SF_6 based silicon dry-etch from the back, with a backing wafer that is glued on the front with SPR220-7 resist.

Chapter 6

Design and Fabrication

6.1 Introduction

In this chapter, the overall process sequences for different implementations of vertical bimorph actuators as well as relevant aspects of the mask design are shown. Based on silicon on insulator substrates (SOI), standard dry-etching and bulk micromachining processes are combined with specially developed fabrication approaches (see chapter 5) to obtain the bimorph actuators. Even though many parts of the fabrication process are the same for the different designs, the full process is described for a clamped-clamped beam actuator (section 6.2.1), one- and two-dimensional meander type actuators (section 6.2.2) and the micro-relays (section 6.2.3).

In section 6.3 the design for the clamped-clamped beam, the one- and two-dimensional meander-type actuators, normally open and normally closed micro-relays as well as an actuated cantilever are discussed.

6.2 Fabrication Process

6.2.1 Clamped-Clamped Beam Actuator

The clamped-clamped beam actuator was the first prototype of a vertical bimorph actuator to be fabricated. The process is based on SOI substrates, RIE, the aluminium sidewall deposition process (chapter 5.2) and the KOH release etch (chapter 5.5.1). It uses aluminium as the contact metal. Figure 6.2 shows the process flow with cross-sections in the bimorph and the contact area as marked in figure 6.1. Appendix B.2.1 lists the corresponding LMS-process file.

The silicon on insulator substrates (SOI) used in the process consist of a device

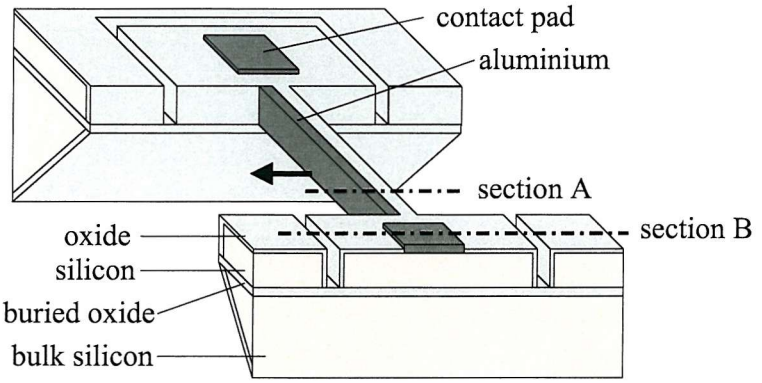

Figure 6.1: Clamped-clamped beam actuator.

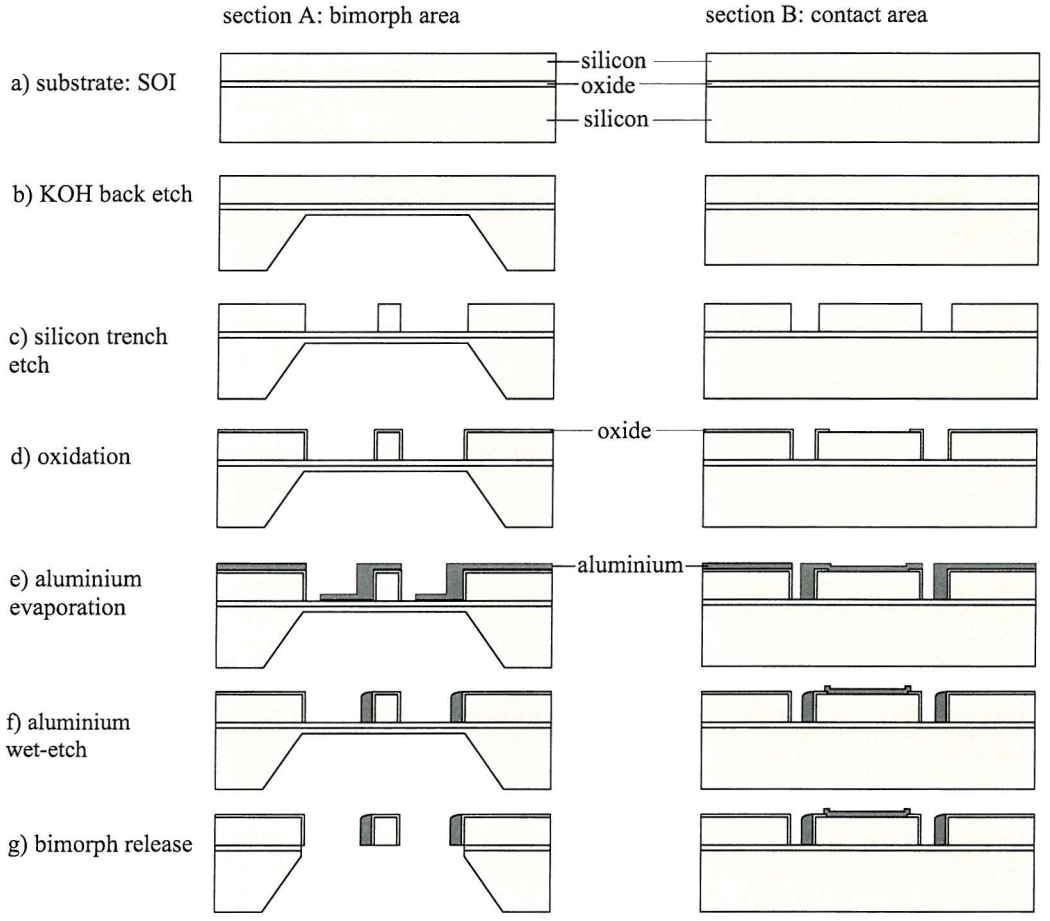

Figure 6.2: Fabrication process for the clamped-clamped beam actuator.

silicon layer on the top, which is 6 μm thick, a buried oxide layer of 2 μm in thickness and a handle silicon layer, 525 μm thick (figure 6.2a). The device silicon layer is p-type with a resistivity of 0.12 Ωcm. The SOI wafers are fabricated by bonding two oxidised wafers together and thinning the upper wafer to the desired thickness of the device layer by applying lapping, polishing and etching techniques. The SOI substrates are provided by a commercial vendor.

Alignment marks for double-sided alignment are etched on the front and the back

of the substrates. Double-sided alignment is necessary to align structures on the back with respect to structures on the front. We first etch 5 μm deep alignment marks on the back of the wafer employing a silicon dry-etch process in a sulphur hexafluoride (SF_6) plasma. Due to the transparency of silicon in infrared light, the alignment marks on the backs can be seen using an infrared camera on the mask aligner. This allows aligning the marks on the front to those on the back. To assist dicing later on, scribe lanes are also etched into the silicon both on the front and on the back. Figure 6.2 does not show the alignment marks or the scribe lanes as they are some distance away from the bimorph devices and the bondpads.

Etching a 500 μm deep recess from the back of the wafer will facilitate the release of the bimorph beams later on. This step is done by anisotropic potassium hydroxide (KOH) etching (figure 6.2b). KOH etching requires an oxide/nitride mask. To provide this mask, an oxide layer of 600 nm is grown in a wet oxidation process and a 160 nm thick nitride layer is deposited in a low-pressure chemical vapour deposition process (LPCVD). Both layers are patterned by photolithography and a dry-etch process in an CHF_3 plasma.

To define the shape of the bimorphs and to insulate the contact pads from the bulk silicon, trenches are etched into the device silicon layer from the front reaching down to the buried oxide layer (figure 6.2c). An anisotropic dry-etch in an $HBr/SiCl_4$-plasma is used. This etch requires an oxide mask. Therefore, a 1.3 μm thick low temperature oxide (LTO) is deposited and structured by photolithography and a dry-etch in an CHF_3 plasma.

In order to electrically insulate the aluminium sidewall deposits from the silicon beams, a thermal wet-oxidation (200 nm) is carried out. To allow contact between the aluminium bond pads and the silicon underneath, contact windows have to be etched into this oxide layer. To do so, an oxide wet-etch in buffered hydrofluoric acid (HF) is carried out as shown in figure 6.2d.

At this stage the angled evaporation of aluminium as described in chapter 5.2 is done at an angle Φ of 24 $^\circ$ aiming at a spacer thickness of 1.5 μm to 2 μm. The evaporation also deposits an approximately 1 μm thick aluminium layer on the horizontal surface of the wafer, which will be used for the aluminium contact pads. Figure 6.2e shows the wafer after the aluminium evaporation. An aluminium wet-etch is carried out in orthophosphoric acid to complete the aluminium sidewall deposition. In order not to remove the aluminium at the bondpad areas, a photolithography step is done providing a resist layer that protects the bondpads from being etched (figure 6.2f).

To release the bimorph beams, the remaining silicon of the handle layer and the buried oxide layer have to be etched (see also chapter 5.5.1). To protect the front-side and to reinforce the bimorph beams for sawing, a photoresist is spun on the front

of the wafer. The release etch is done by two dry-etch stages from the back (figure 6.2g). To separate the chips, the wafer is sawn along the scribe lanes. Removing the resist on a single chip basis completes the fabrication process.

Figure 6.3 shows SEM images of a clamped-clamped beam actuator. The actuator is 400 μm long, the silicon part of the bimorph is 5 μm wide, the aluminium part is 2 μm wide. In figure 6.3b the aluminium sidewall deposition can be seen.

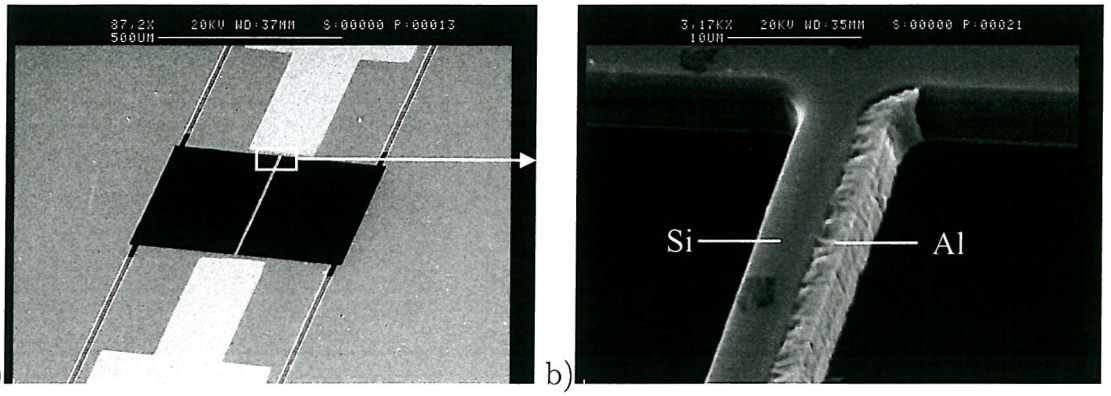

Figure 6.3: SEM images of a clamped-clamped beam actuator, l = 400 μm, w_{Si} =5 μm, w_{Al} = 2 μm, a) whole actuator with contact pad, b) magnified view of the bimorph.

6.2.2 Meander Type Actuators

The fabrication process for both one-dimensional and two-dimensional actuators is an improved and extended version of the process described in section 6.2.1. The most significant differences are that four aluminium side-wall evaporations are necessary, which need to be selective as described below. For the release of the bimorphs we use the dry-etch from the back with a backing wafer glued on with photo resist (see chapter 5.5.5) instead of KOH-etching. Figure 6.4 shows the two-dimensional actuator, where the cross-sections relevant for the fabrication process are marked. In figure 6.5, an overview of the fabrication process is given. Figure 6.6 provides the corresponding layout snapshots during the fabrication process. The numbering for figure 6.6 is adopted from figure 6.5 to improve clarity. Appendix B.2.2 lists the corresponding LMS-process file.

We use a silicon on insulator substrate (SOI) with a 30 μm thick device silicon layer, a buried oxide layer of 2 μm in thickness and a handle silicon layer, 450 μm thick (figure 6.5a). The device silicon layer is p-type with a resistivity of 0.06 to 0.12 Ωcm.

The shape of the bimorphs and the insulation trenches are etched into the device silicon layer from the front by deep reactive ion etching (DRIE, figure 6.5b). The so-

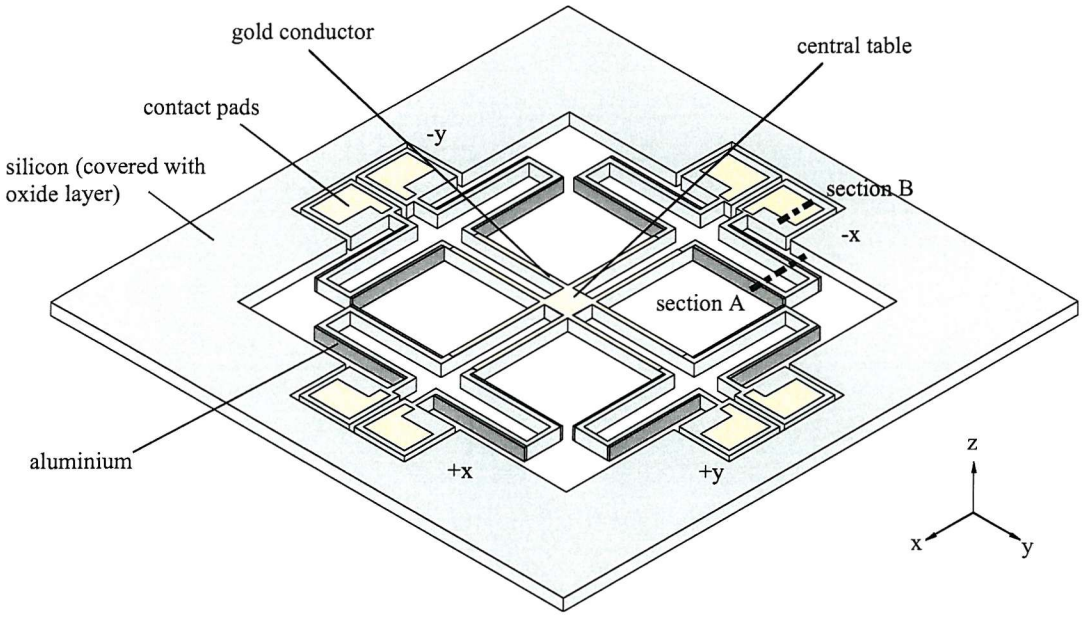

Figure 6.4: Two-dimensional actuator, sections marked.

called Bosch process [132] is applied, which alternates etching and sidewall passivation cycles. The etching is carried out in an inductively coupled plasma (ICP) reactor. The etching cycle is based on SF_6. For the sidewall passivation C_4F_8 is used. A cycle time of 12 s was chosen for the etching cycle, a time of 8 s for the passivation stage. To etch the 30 μm thick device silicon, 30 cycles are required. A standard 2.2 μm thick photoresist layer (Shipley Megaposit SPRT 518) serves as the etching mask. Figure 6.7 shows a silicon beam after the DRIE stage. A corrugated sidewall surface can be observed, which results from the alternation of etching and passivation. The trenches reach down to the buried oxide layer.

In order to electrically insulate the aluminium fillets of the bimorphs from the silicon beams, a thermal wet-oxidation (200 nm) is carried out (figure 6.5c). Contact windows are etched into the oxide layer to allow contact between the gold contact pads and the silicon underneath, which provides the electrical connection to the silicon beams (figure 6.5d). Then, a chrome/gold layer is evaporated and structured to form the gold contact pads (figure 6.5e,f).

At this stage, the aluminium sidewall deposition process as described in chapter 5.2 is carried out. The two-dimensional actuator requires four evaporations. To obtain the aluminium fillets on the sidewall of the silicon beam where required, all other silicon beams need to be covered with photo resist (figure 6.5g). The resist has to be at least 30 μm thick to cover the beams. The thick resist process using SPR220-7 as described in chapter 5.4 is applied.

Then the angled evaporation of aluminium is carried out at a shallow angle of incidence, which means that the aluminium deposits on the sidewalls are thicker than

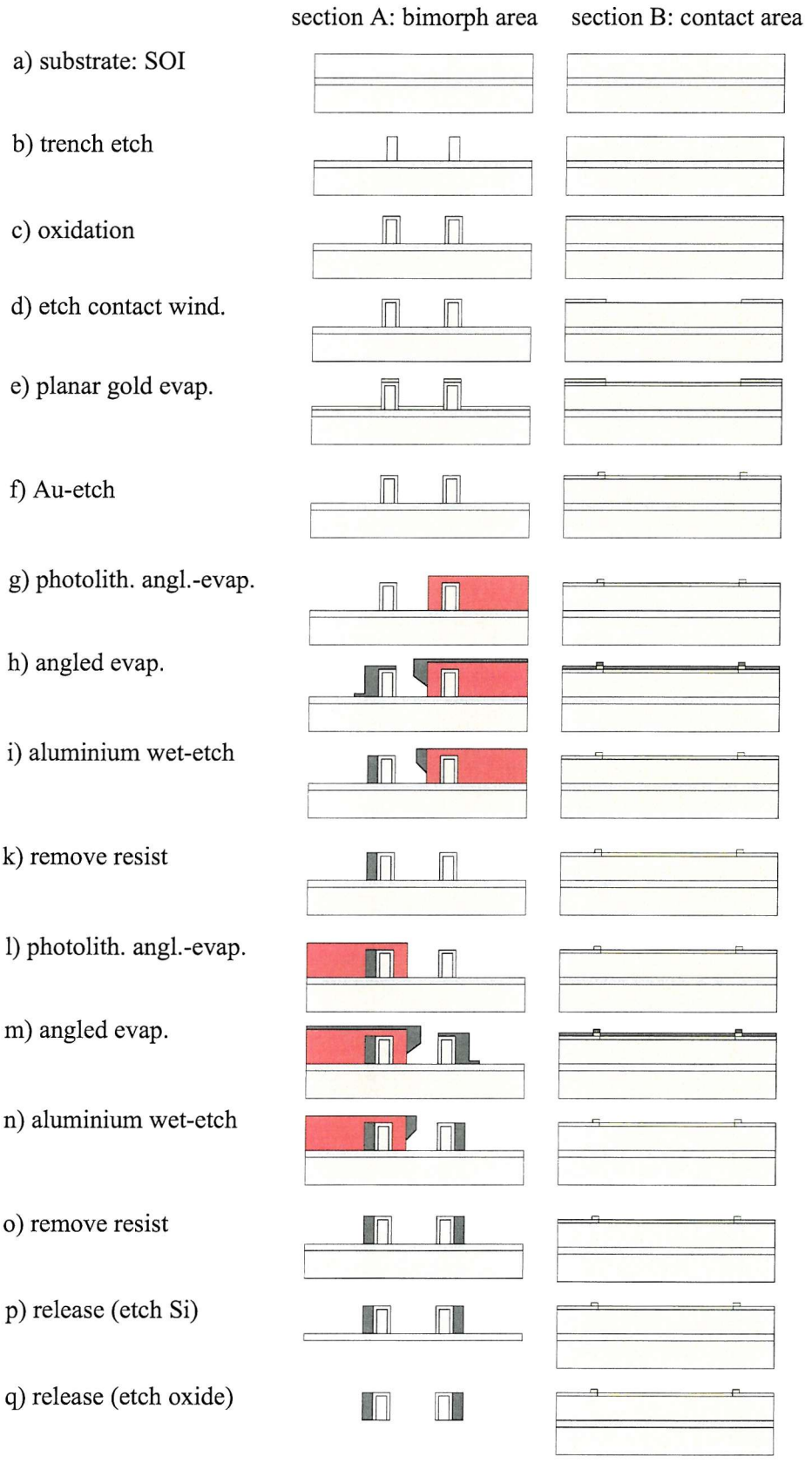

Figure 6.5: Fabrication process for the two-dimensional actuator.

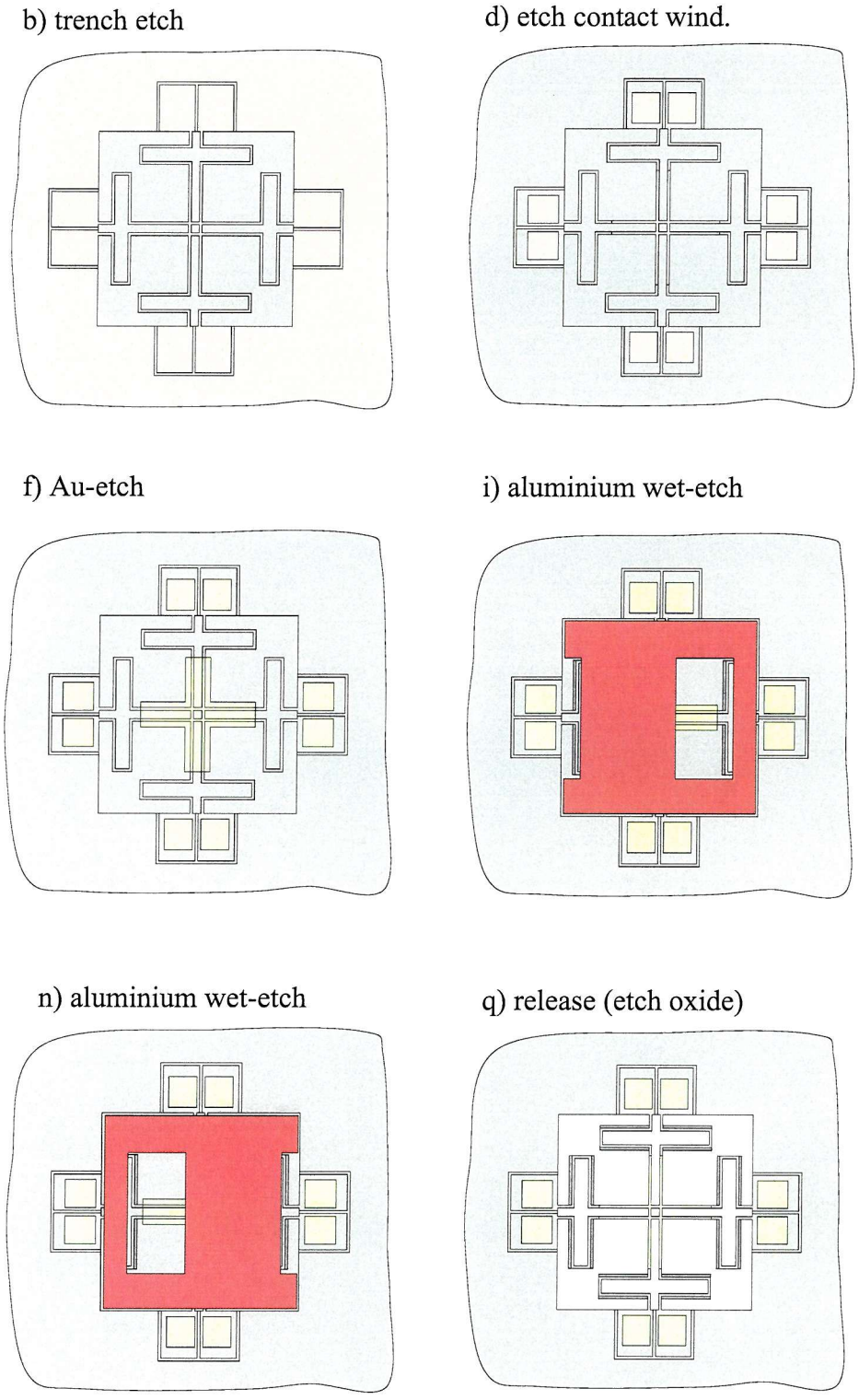

Figure 6.6: Layout sequence for the fabrication of the two-dimensional actuator.

the ones on the horizontal surfaces (figure 6.5h). The aluminium on the horizontal surfaces is then etched away by a standard wet-etch process in orthophosphoric acid (figure 6.5i). The etch is stopped immediately when all the aluminium on the horizontal surfaces is etched away, leaving behind aluminium fillets on the sidewall.

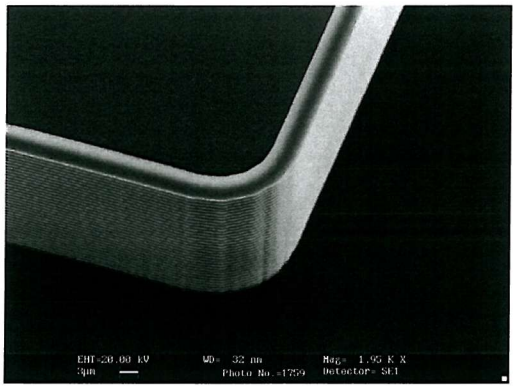

Figure 6.7: SEM image of a silicon beam after DRIE.

Removing the photo resist lifts off the unwanted aluminium fillets and completes the aluminium sidewall evaporation for the left-hand side fillet (figure 6.5k). For the right-hand side fillet, the photolithography, wet-etching and resist removal (figure 6.5l,m,n) are repeated accordingly resulting in the cross section depicted in figure 6.5o. Two more repetitions are required to get the aluminium sidewall deposits not shown in this cross section.

To release the bimorph beams, a recess has to be etched into the handle silicon wafer from the back. This is done using the RIE processes described in chapter 5.5.5 (figure 6.5p). To protect the devices on the front, a backing wafer is glued onto the device wafer with SPR220-7 photo resist. After the silicon etching the wafers are separated and the device wafer is cleaned in fuming nitric acid. Then, the buried oxide is etched away in a dry-etch process (figure 6.5q).

Another backing wafer is glued on to protect the device wafer during the sawing stage. After the dicing, the backing wafer is removed in acetone and the devices are cleaned in fuming nitric acid.

Figure 6.8 shows SEM-images of a one-dimensional meander-type actuator. The bimorphs are 1000 μm long, the silicon is 7 μm wide, the aluminium on the sidewalls is 1.4 μm wide. In figure 6.9, a two-dimensional meander actuator is shown. Its bimorphs are 1000 μm long, the silicon is 7 μm wide, the aluminium on the sidewalls is 1.8 μm wide. Near the central table, there are gold patches remaining, which did not break off completely during the buried oxide etch.

6.2.3 Micro-Relays

The fabrication is similar to the process for the meander actuator described in section 6.2.2. The most significant differences are: There are only two aluminium side-wall evaporations. Two chrome-gold evaporations as described in chapter 5.3 are used for the contact deposition. Appendix B.2.3 lists the corresponding LMS-process file.

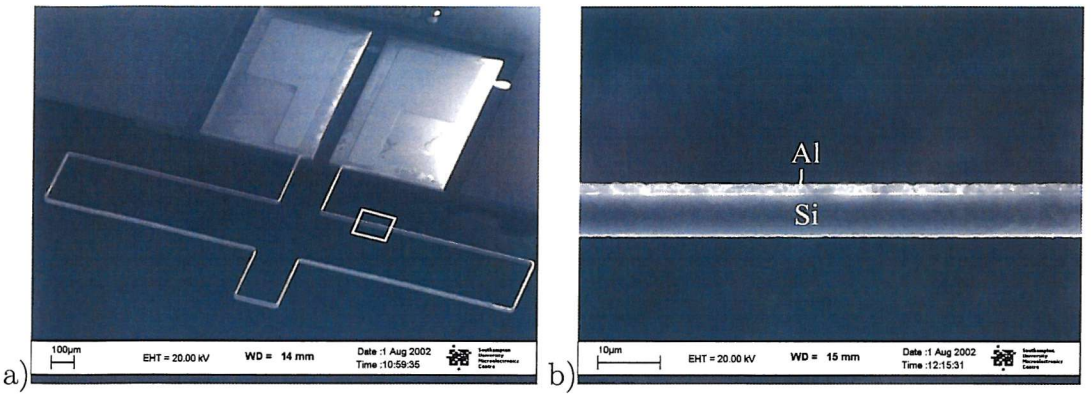

Figure 6.8: SEM images of a one-dimensional meander actuator, bimorph length: $1000\mu m$, $w_{Si} = 7$ μm, $w_{Al} = 1.4$ μm a) whole actuator b) magnified view of a bimorph.

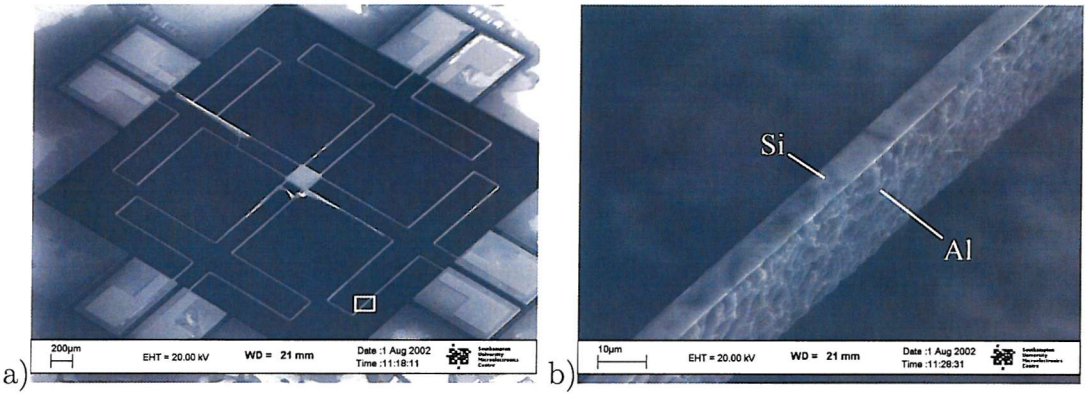

Figure 6.9: SEM images of a two-dimensional meander actuator, bimorph length: 1000 μm, $w_{Si} = 7$ μ m, $w_{Al} = 1.8$ μm a) whole actuator b) magnified view of a bimorph.

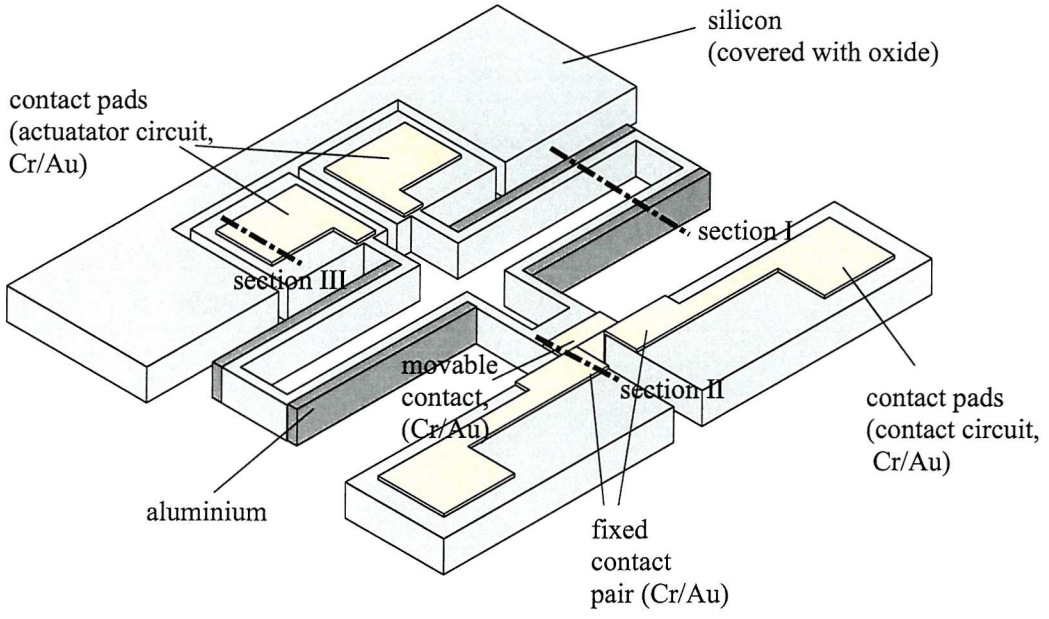

Figure 6.10: Schematic diagram of a normally closed micro-relay.

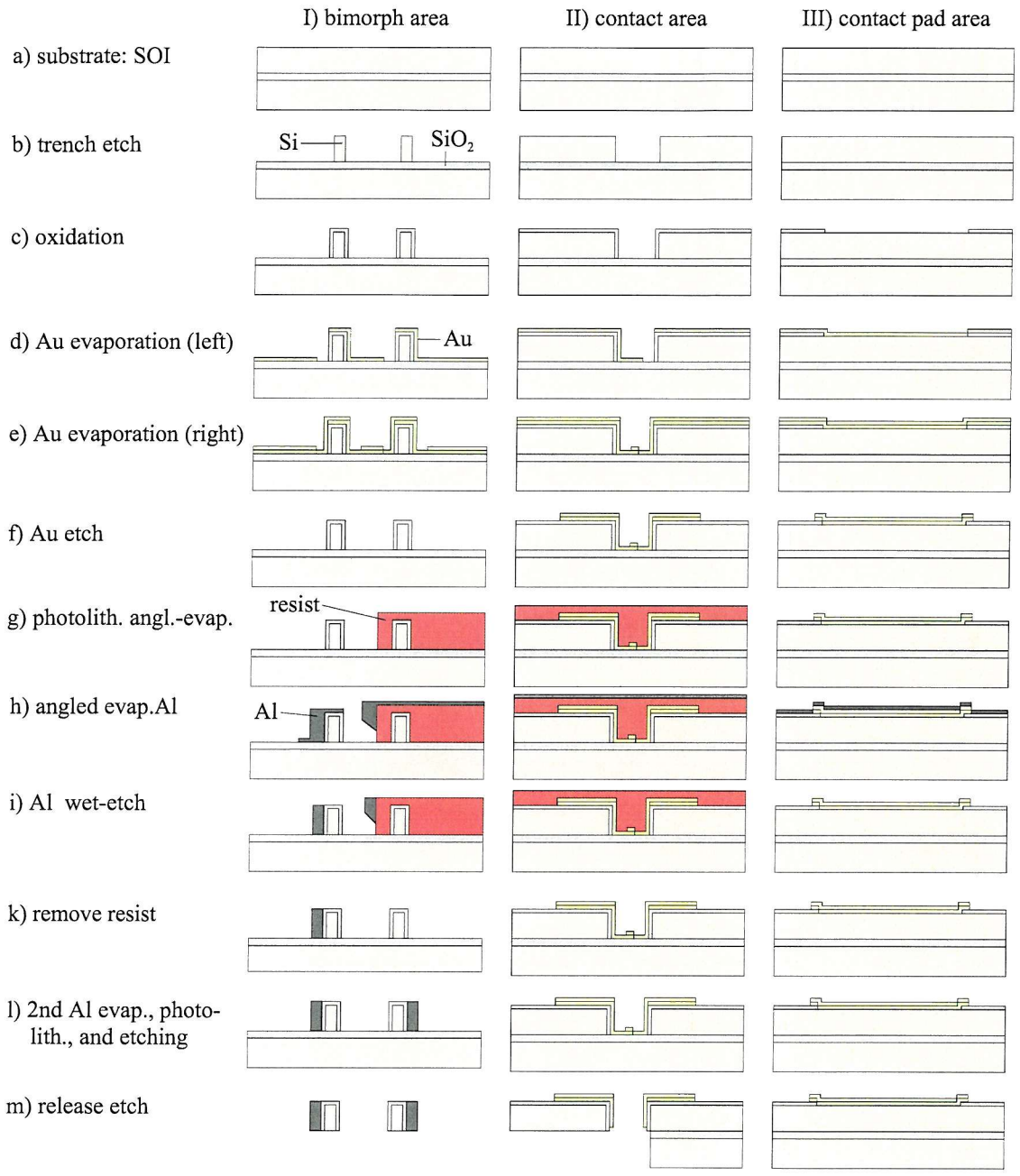

Figure 6.11: Fabrication process for the two-dimensional actuator.

Figure 6.11 shows the process flow at 3 different cross sections of the wafer. Column I depicts the bimorph area, column II the contact electrodes and column III the contact pads of the actuator circuit as marked in figure 6.10.

As for the meander type actuators, we use a silicon on insulator substrate (SOI) with a 30 μm thick device silicon layer, a 2 μm thick buried oxide layer and a 450 μm thick handle silicon layer (figure 6.11a). The device silicon layer is p-type with a resistivity of 0.06 to 0.12 Ωcm.

The shape of the bimorphs and the insulation trenches are etched into the device silicon layer from the front by DRIE as described in section 6.2.2. The trenches reach

down to the buried oxide layer (figure 6.11b).

In order to electrically insulate the silicon from the aluminium of the bimorph and from the contact electrodes, a thermal wet-oxidation (200 nm) is carried out (figure 6.11c). Contact windows are etched into the oxide layer to allow contact between the gold contact pads (actuator circuit) and the silicon underneath, which provides the electrical connection to the silicon beams (figure 6.11c, III).

For the contact pads of both the actuator circuit and the contact circuit as well as the contact electrodes, two chrome/gold evaporations are carried out. The angle of incidence is chosen such, that chrome/gold is deposited both on the horizontal surfaces and on the sidewalls of the contacts as described in chapter 5.3. The first evaporation deposits chrome/gold onto the left contact electrode (moveable contact) as depicted in figure 6.11d, II. The second evaporation deposits chrome/gold onto the right contact electrode (fixed contact) as shown in figure 6.11e, II. The unwanted chrome/gold is etched away in a wet-etch (figure 6.11f).

At this stage the aluminium sidewall deposition process described in chapter 5.2 is carried out. Two aluminium evaporations are required, since aluminium sidewall deposits are needed both on the left- and right- hand side of the silicon beams. To obtain the aluminium spacer on the sidewall of the silicon beam where it is wanted, all the other silicon beams need to be covered with photo resist (figure 6.11g). Then, the angled evaporation of aluminium is carried out at a shallow angle of incidence, which means that the aluminium deposits on the sidewalls are thicker than the ones on the horizontal surfaces (figure 6.11h, I). The aluminium on the horizontal surfaces is removed by a standard wet-etch. The etch is stopped immediately when all the aluminium on the horizontal surfaces is etched away, leaving behind aluminium fillets on the sidewalls (figure 6.11i, I). Removing the photo resist lifts off the unwanted aluminium fillets and completes the aluminium sidewall evaporation for the left-hand side spacer (figure 6.11k). For the right-hand side spacer, the photolithography, wet-etching and resist removal are repeated accordingly resulting in the cross section depicted in figure 6.11l, I.

To release the bimorph beams, a recess has to be etched into the handle silicon wafer from the back (figure 6.11m). This is done by a RIE process from the back (see chapter 5.5.5). To protect the devices on the front, a backing wafer is glued onto the device wafer with SPR220-7 photo resist. After the silicon etching, the wafers are separated and the device wafer is cleaned in fuming nitric acid. Then, the buried oxide is etched away in a dry-etch process.

Another backing wafer is glued on to protect the front of the device wafer and as protection during the sawing stage. Excess chrome/gold are etched away in standard wet-etch stages. The device wafer is diced and the backing wafer is removed in

acetone. The devices are cleaned in fuming nitric acid. Figure 6.12 shows an SEM image of a normally closed micro-relay before the release-etch.

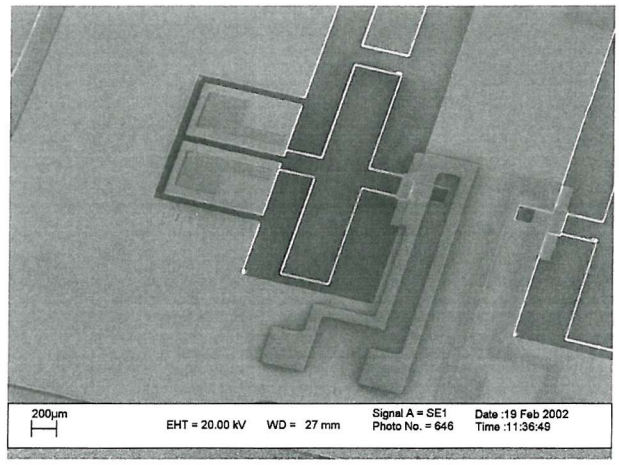

Figure 6.12: SEM image of a normally closed micro-relay before the release etch.

6.3 Design

To point out relevant details of the mask design, important parts of the mask design are shown with sketches based on the original mask design files (L-Edit), focussing on the trench-etch, gold-etch and aluminium-etch layers.

6.3.1 Clamped-Clamped Beam Actuator

The double clamped actuators were the first prototypes for thermally actuated vertical bimorphs. The feasibility of the principle and the fabrication process had to be proven. Hence, many designs of different dimensions were implemented.

Figure 6.13 shows sketches of the layouts of clamped-clamped beam actuators with and without a central platform. The actuator shown in figure 6.13b consists of a divided bimorph beam of length $l_b = 300$ μm for the upper as well as the lower part of the beam. The central platform is a square of length $l_c = 170$ μm. The contact pads are squares of length $l_p = 500$ μm. The width $w_{Si} = 5$ μm of the silicon part of the bimorph can be seen as a narrow white line surrounded by rectangles of the trench etch layer. The layers for the KOH back-etch, the alignment marks and the contact windows (oxide wet-etch) are not shown in the picture. Figure 6.13a shows an actuator element without central platform. The bimorph has a length $l = 1000$ μm. All other dimensions are the same as described above.

The different designs included in our layout set comprise the following:

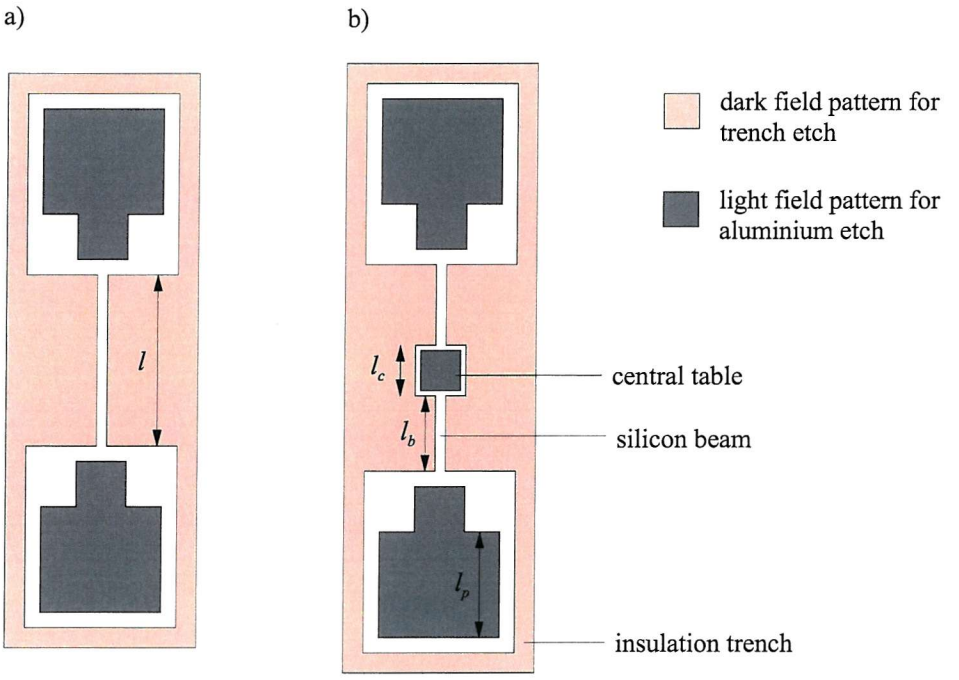

Figure 6.13: Layout of double-clamped actuators, a) without central platform, b) with central platform, trench etch pattern and aluminium etch pattern shown.

- Actuator elements with a central platform (as depicted in figure 6.13b) with a bimorph length of l_b = 200 μm, 300 μm, 500 μm, 700 μm and with a silicon width w_{Si} = 2 μm, 3 μm, 5 μm.
- Actuator elements without a central platform (as depicted in figure 6.13a) with a bimorph length l = 400 μm, 600 μm, 1000 μm, 1400 μm and a silicon width w_{Si} = 2 μm, 3 μm, 5 μm.

This results in 24 different designs, which are distributed across each wafer.

6.3.2 One-Dimensional Meander Type Actuator

Figure 6.14 depicts a part of a one-dimensional meander type actuator. The trench-etch pattern is shown. It is a dark field pattern, which means after the photo lithography, there will be photoresist where the pattern is not drawn, and there will be no photoresist where the pattern is present. The length of the bimorphs l_b is 1000 μm, the width of the silicon w_{Si} is either 5 μm or 8 μm. The other dimensions are: l_1 = 300 μm, l_2 = 300 μm, l_3 = 300 μm, l_4 = 200 μm. The insulation trench is 80 μm wide.

In figure 6.15, the trench etch and the gold etch patterns are shown. The gold etch pattern is a light field pattern, which means there will be resist wherever there is the pattern. The length of the square contact pad l_p is 400 μm. The gold-etch patch

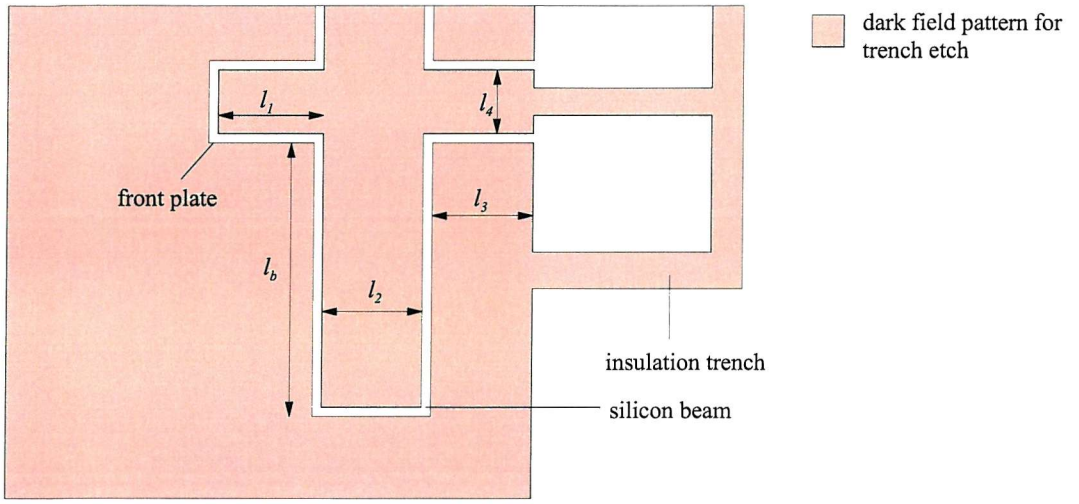

Figure 6.14: Layout of a one-dimensional meander type actuator, trench-etch layer shown.

at the front plate is needed for the gold conductor on top of the silicon beam (chapter 3.4). It overlaps the silicon beams by l_o which is about 80 μm to make sure that the thick resist will cover the silicon beams. This is necessary because the sidewalls of the thick photoresist are not perfectly rectangular but rounded. That means, the beams would protrude from the resist if the patch of the gold etch mask would not overlap the silicon beams as illustrated in figure 6.16.

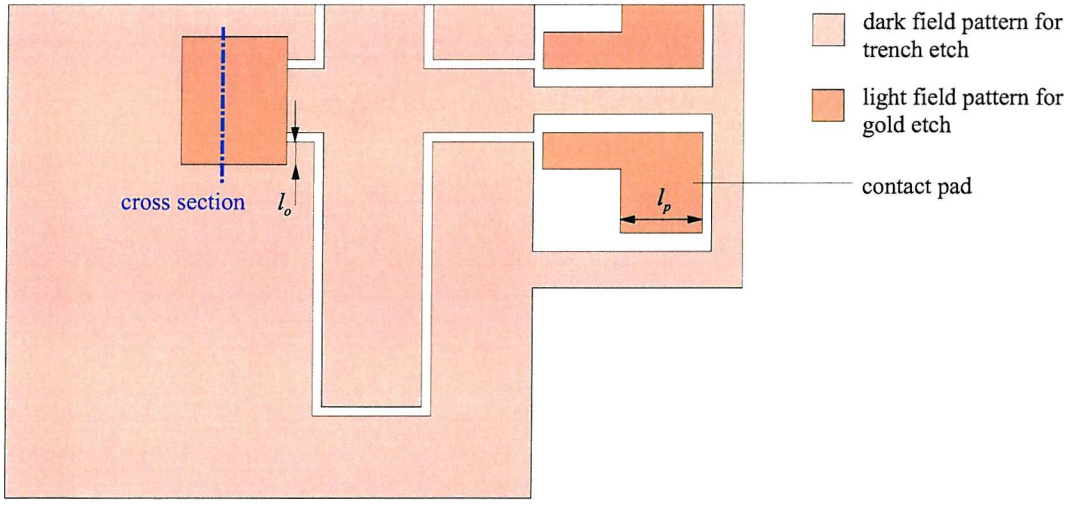

Figure 6.15: Layout of a one-dimensional meander type actuator, trench-etch and gold etch layers shown.

Figure 6.17 shows the trench etch and the first aluminium etch pattern, which is light field tone. The photoresist of the aluminium etch pattern fulfills the task of covering the areas in the trench region, where no aluminium sidewall deposition takes place. Only left-hand side bimorphs and horizontal surfaces are revealed to the aluminium evaporation. A zigzag pattern between the two branches of the silicon

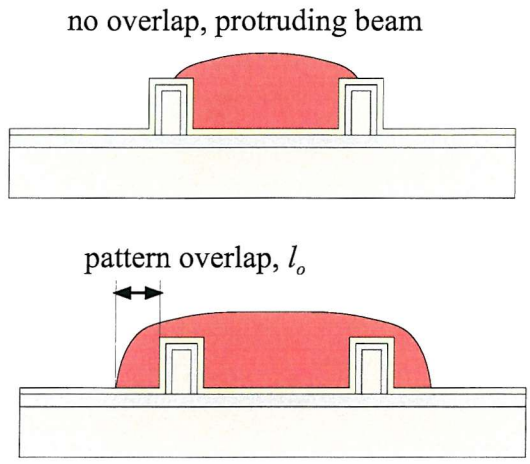

Figure 6.16: Cross section of the front plate area, illustrating the necessity of the gold etch pattern overlap.

beam means that the angle of incidence for the aluminium evaporation onto the photoresist is very shallow. Therefore, the aluminium thickness on the sidewall of this zigzag photoresist pattern does not exceed the aluminium thickness on the horizontal surfaces and hence this sidewall deposit is entirely removed from the photoresist in the aluminium wet-etch.

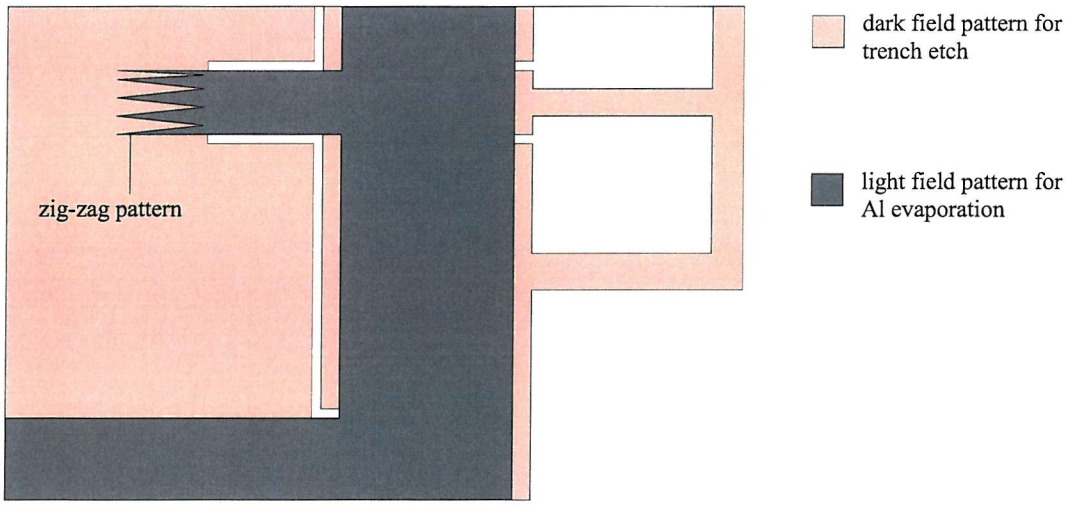

Figure 6.17: Layout of a one-dimensional meander type actuator, trench-etch and first aluminium-etch patterns shown.

In figure 6.18, the trench etch pattern and the second aluminium etch pattern (light field) are shown. Only right-hand side bimorphs and horizontal surfaces are revealed to the aluminium evaporation. To make sure that there are no sidewall deposits on the edge of the photoresist, the aluminium etch pattern goes very close to the rim of the trench, resulting in sidewall deposits that do not reach down to the buried oxide (figure 6.19), which therefore are lifted off in the resist removal stage.

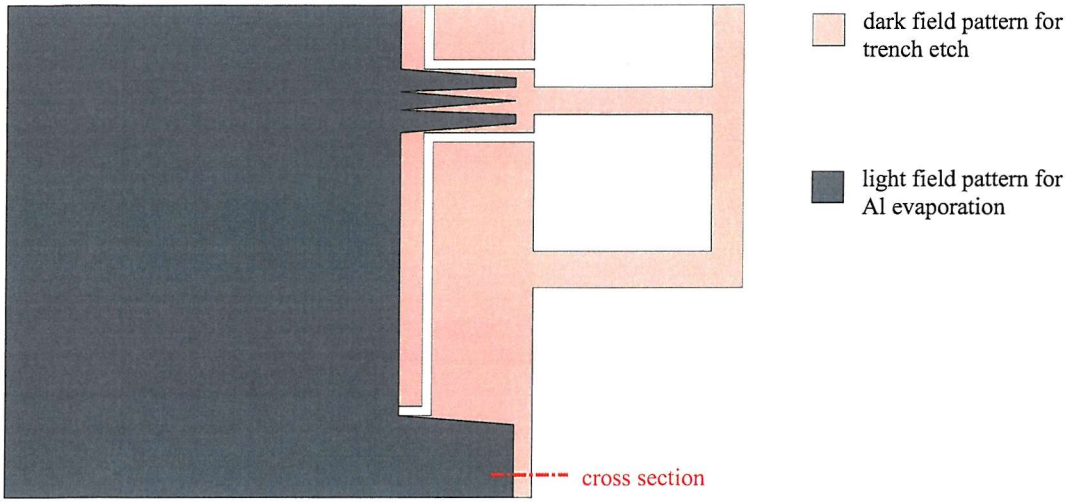

Figure 6.18: Layout of a one-dimensional meander type actuator, trench-etch and second aluminium-etch patterns shown.

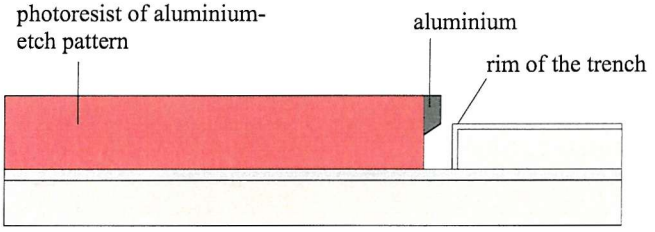

Figure 6.19: Cross section of the rim of the trench with the photoresist of the aluminium etch pattern.

6.3.3 Two-Dimensional Meander Type Actuator

Figure 6.20 depicts a part of a two-dimensional meander type actuator showing the trench-etch pattern (dark field). The length of the bimorphs l_b is either 800 or 1000 μm, the width of the silicon is either 5 μm or 8 μm. The other dimensions are: l_1 = 900 or 1100 μm, $l_2 = 300$ μm, $l_3 = 300$ μm, $l_4 = 200$ μm, $l_c = 255$ μm. The insulation trench is 80 μm wide.

In figure 6.21, the trench etch and the gold etch (light field) patterns are shown. The width of the square contact pad l_p is 400 μm. The cross-shaped gold-etch pattern is for the gold conductors on top of the silicon beams in the central area of the actuator. It overlaps the the beams by l_o which is 80 μm.

Similar to the one-dimensional actuator, the aluminium-etch patterns go very close to the trench-etch rim and zigzag patterns are used to avoid unwanted depositions of aluminium on the sidewalls of the photoresist (figure 6.22).

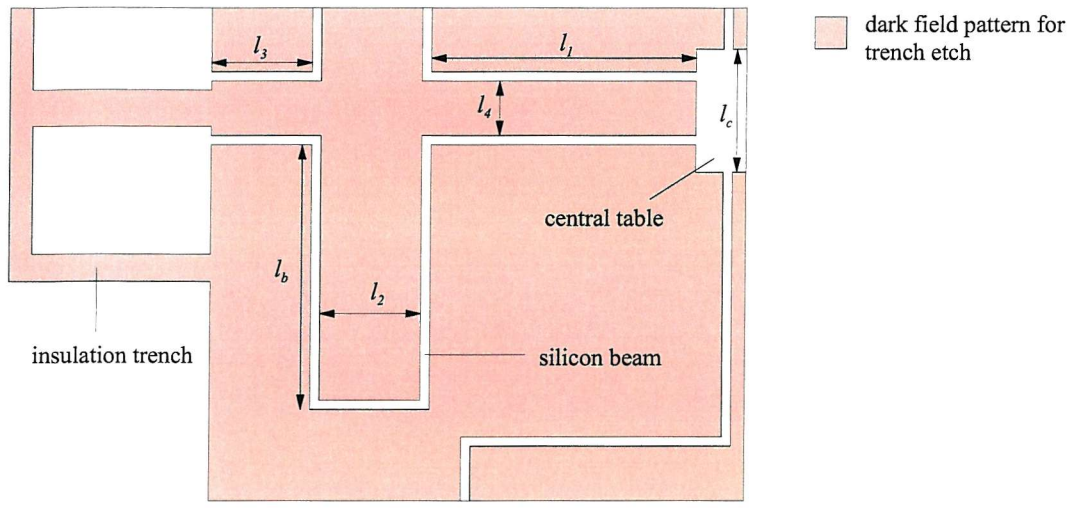

Figure 6.20: Layout of a two-dimensional meander type actuator, trench-etch pattern shown.

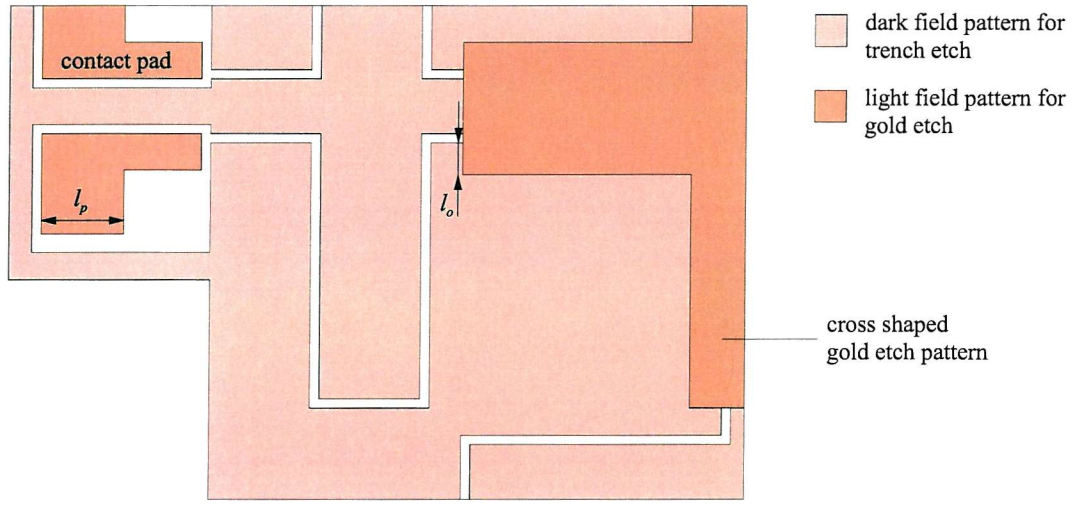

Figure 6.21: Layout of a two-dimensional meander type actuator, trench-etch and gold-etch patterns shown.

6.3.4 Micro-Relays

Figure 6.23 depicts the layout for a normally-closed micro-relay with the trench etch pattern (dark field) shown. The length of the bimorphs l_b is 1000 μm, the width of the silicon w_{Si} is either 5 μm or 8 μm. The other dimensions are: l_1 = 300 μm, l_2 = 300 μm, l_3 = 300 μm, l_4 = 200 μm. The insulation trench is 80 μm wide. The contact gap is either 6 μm, 12 μm or 20 μm wide. The different gap dimensions will result in different opening and closing characteristics. Although initially, there is a contact gap for the normally closed micro-relay, the moving contact moves towards the fixed contact pair (at room temperature) and closes the electrical contact as soon as the buried oxide layer is removed in the release etch process. This results from the elevated temperature at which the aluminium is evaporated (chapters 4.3.5, 5.2).

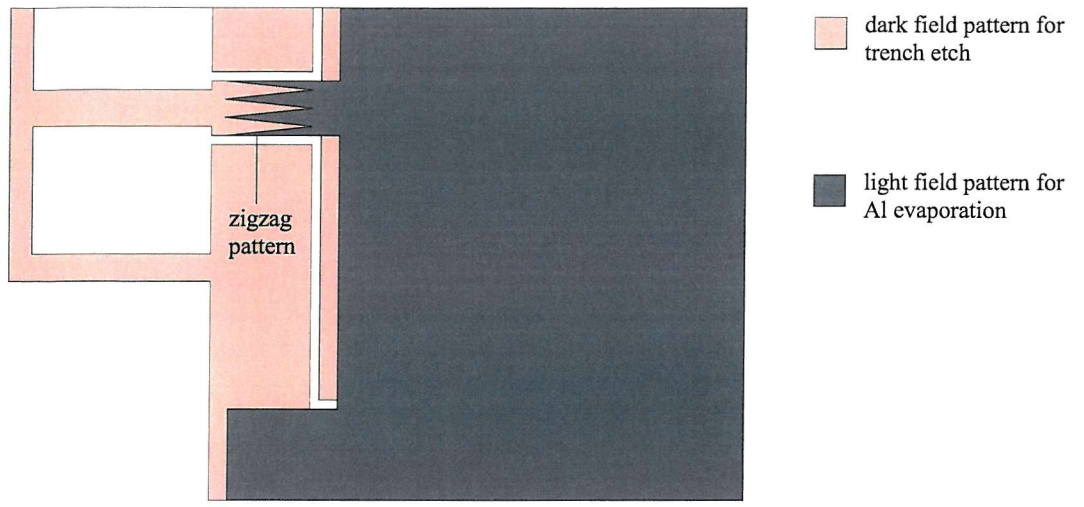

Figure 6.22: Layout of a two-dimensional meander type actuator, trench-etch and first aluminium-etch patterns shown.

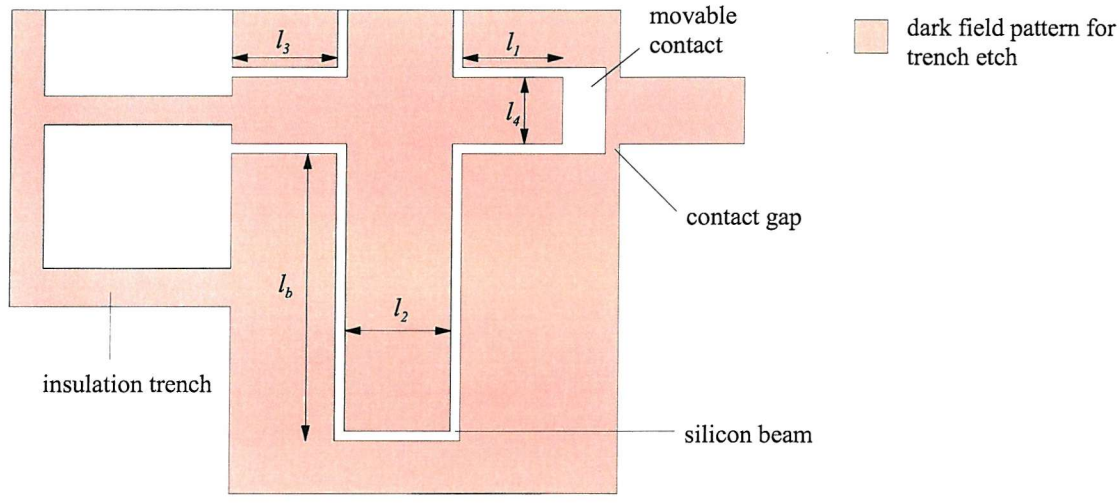

Figure 6.23: Layout of a normally-closed micro-relay, trench-etch pattern shown.

In figure 6.24, the trench etch and the gold etch (light field) patterns are shown. The gold-etch pattern for the contact circuit not only covers areas on the wafer surface but also patches within the trench including the contact gap. This results in a chrome/gold layer on top of the buried oxide remaining after the gold etch step. This chrome/gold layer needs to be removed in the release-etch stage in order to avoid a short-circuit between the two fixed contacts.

Figure 6.25 shows the trench-etch and the first aluminium-etch (light field) patterns for a normally-closed micro-relay. The aluminium etch pattern only reveals the left side of the left-hand side bimorphs. The second aluminium etch pattern will reveal the right side of the right hand side bimorphs. This means that the normally closed relay gets the aluminum deposits on the outside of the bimorphs. The aluminium etch layers go very close to the rim of the trench to avoid unwanted aluminium sidewall fillets.

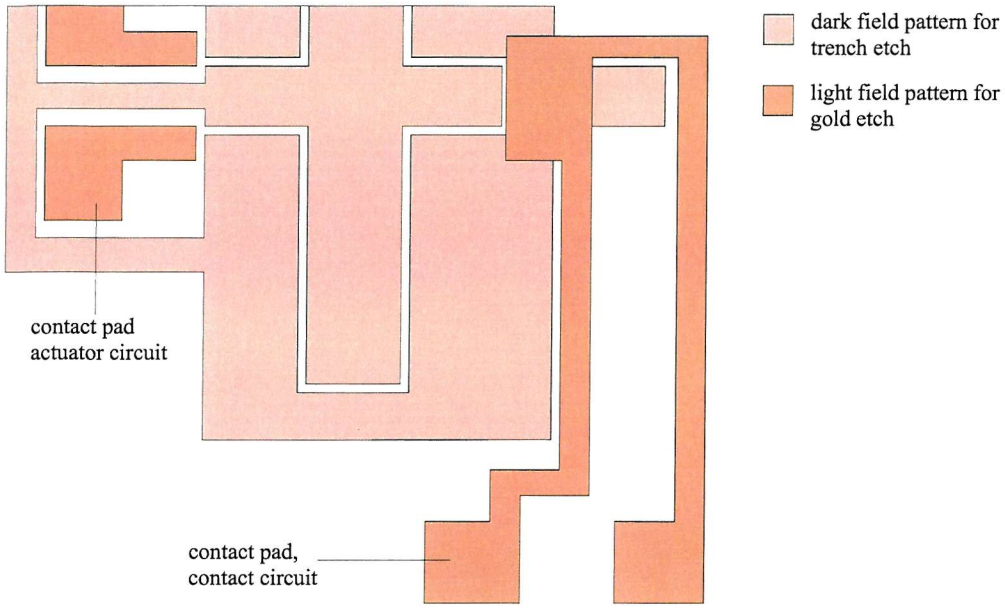

Figure 6.24: Layout of a normally-closed micro-relay, trench-etch and gold-etch patterns shown.

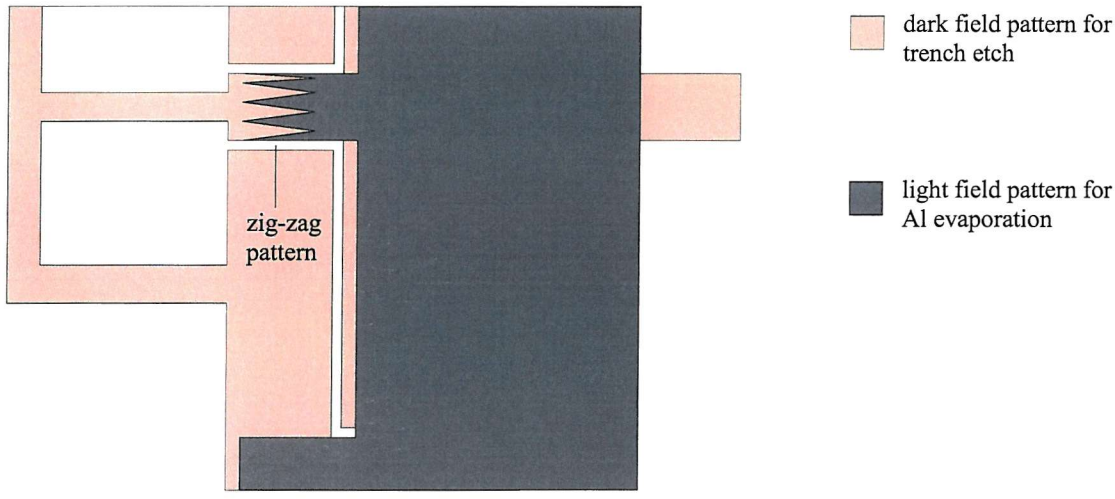

Figure 6.25: Layout of a normally closed micro-relay, trench-etch and first aluminium-etch patterns shown.

In figure 6.26, the trench-etch and the first aluminium-etch (light field) patterns for a normally-open micro-relay are shown. The first aluminium etch pattern only reveals the left side of the right bimorphs. The second aluminium etch pattern will reveal the right side of the left bimorphs. This means the aluminium fillets for the normally open relay are on the inside of the bimorphs, resulting in opposite movement upon heating as compared to the normally-closed micro-relay (see chapter 3.6).

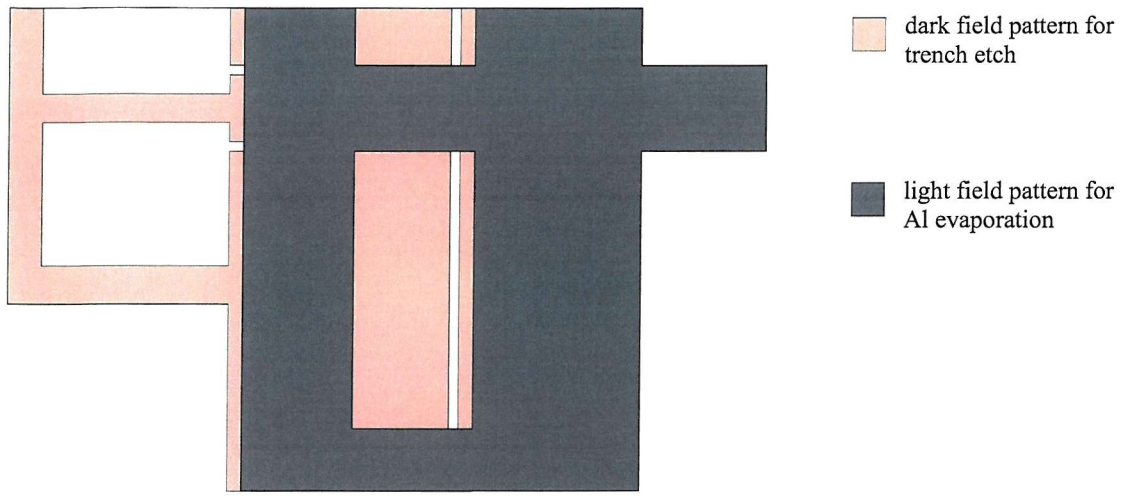

Figure 6.26: Layout of a normally closed micro-relay, trench-etch and first aluminium-etch patterns shown.

6.3.5 Actuated Cantilever

Figure 6.27 depicts the trench-etch and gold-etch layer of an actuated cantilever. The cantilevers are 1000 μm or 1500 μm long (l_b). The silicon width is either 5 μm or 8 μm. The oxide layer underneath contact pad A is removed in the contact window etch (see figure 6.28). Therefore, contact pad A is in electrical contact with the device silicon layer underneath. Contact pad B is insulated from the silicon by the oxide layer, but overlaps with the bimorph, meaning that it is electrically connected to the aluminium of the bimorph. At the tip of the bimorph cantilever, the oxide layer is removed and a chrome/gold contact patch overlaps with the aluminium of the cantilever, providing an electrical connection between the silicon and the aluminium of the bimorph. Thus, there is a path for an electrical current from contact pad A through the silicon and the aluminium of the bimorph to contact pad B (see also chapter 3.7). This current is used for heating the cantilever.

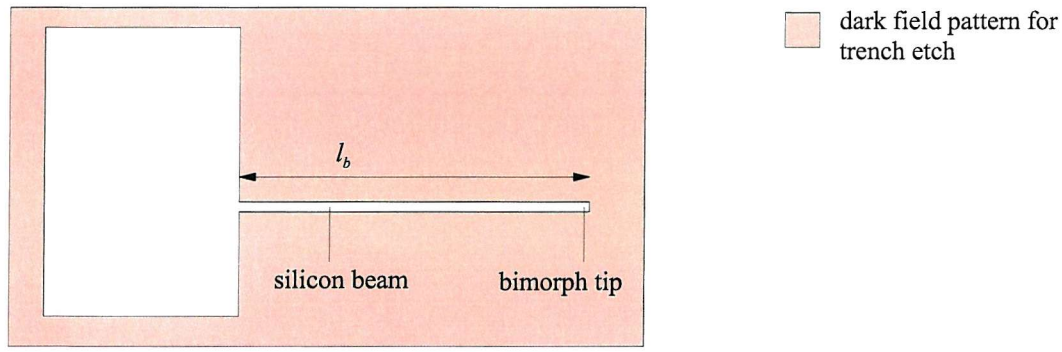

Figure 6.27: Layout of an actuated cantilever, trench-etch pattern shown.

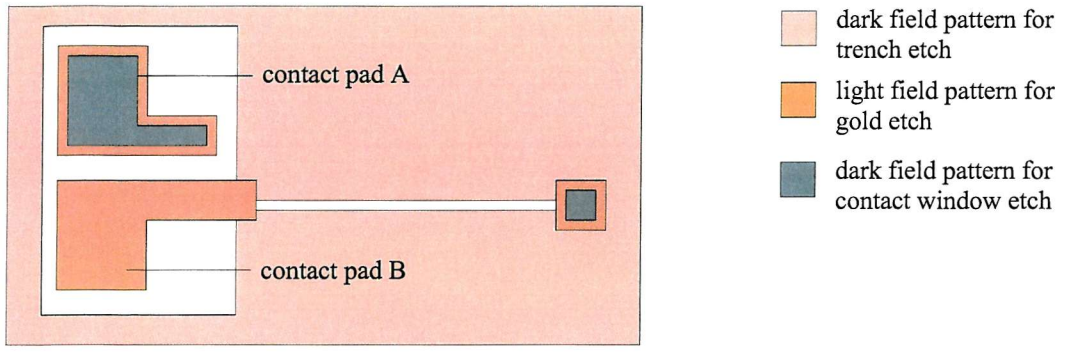

Figure 6.28: Layout of an actuated cantilever, trench-etch, gold-etch contact window etch patterns shown.

6.4 Conclusion

Vertical bimorph actuators require a comparably complicated fabrication process involving many nonstandard stages. Starting with an SOI substrate, the actuator geometry is defined by silicon trench etching. Chrome/gold deposition for the contacts, angled evaporation of aluminium for the sidewall deposits and a release etch based on silicon dry-etching are combined to obtain freely moving actuators.

The mask design includes actuators of different dimensions for each implementation. Especially the clamped-clamped beam, the first prototype of vertical bimorphs, has been designed in a wide range of dimensions. The length of the bimorphs, the width of the silicon beams and the contact gap for the micro-relay are the most important design parameters. Special detailed solutions have been found in designing the aluminium etch patterns to avoid undesired sidewall deposits.

Chapter 7

Test and Measurements

7.1 Introduction

In this chapter, measurements on clamped-clamped beam actuators and one-dimensional meander type actuators are described. The main measurement tool is an SEM that allows precise displacement measurements with its cursor tools and provides a vacuum environment. Static deflection, thermal time constants and lateral resonant modes have been measured and compared to the results of analytical calculations and simulations. The sections on two-dimensional meander actuators and micro-switches discuss preliminary results and problems that have occurred during the fabrication and measurement stages.

7.2 Clamped-Clamped Beam Actuator

The measurement of static deflection, thermal time constant and lateral resonances for clamped-clamped beam actuators is described. The significance of the thermal time constant for the maximum frequency of full thermal response is discussed in chapter 4.3.4. Thermally exciting lateral resonances with vertical bimorph actuators is a novel approach. The theoretical background is documented in chapter 4.2.5.

The measurement results have been published in [117, 133, 134]. More details are found in the project reports of Ian Tomlin [135] and Biyun Huang [136].

7.2.1 Test Setup

Figure 7.1 depicts the setup for testing the bimorph actuators. A power supply provides the input power for heating the bimorphs. The power supply is replaced with

either a pulse generator or a signal generator for time-constant or resonance measurements. The current through the bimorph and the applied voltage is measured in order to obtain the electrical input power. The actuator chip is placed in an SEM-chamber where accurate measurement of the lateral displacement can be performed. Furthermore, the SEM-chamber provides a vacuum environment to eliminate influences of the ambience. Thus, the test conditions are close to the theoretical model discussed in chapter 4.2.1. However, it should be pointed out that the actuators also work in air since conduction is the dominant heat loss mechanism. A peltier-cooler keeps the bulk silicon of the device at a constant temperature.

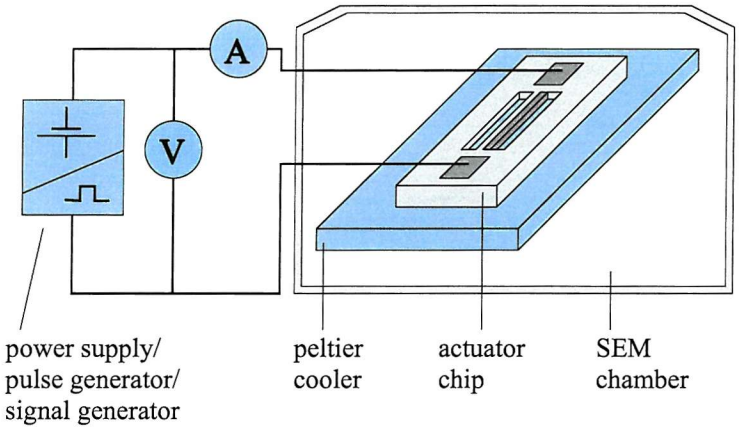

Figure 7.1: Setup for the test of the actuators.

A test-jig has been fabricated to hold and contact the actuator chips during the measurement. It accommodates the peltier-cooler and the contact pins as shown in figure 7.2. The actuator chip is held in place by the springs, clamping it against the surface of the peltier-cooler. The springs also form the electrical connections to the bond pads. It has been fitted with connectors compatible with the feed-throughs of the SEM so that it can be used inside the SEM chamber.

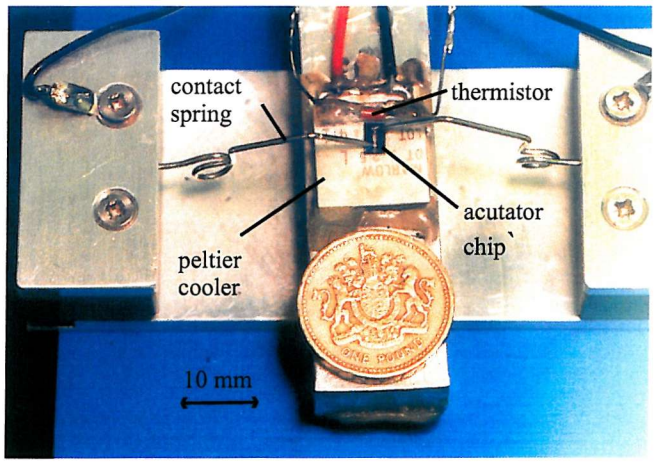

Figure 7.2: Setup for the test of the actuators.

7.2.2 Static Displacement

For measuring static deflection, actuation voltage and current are measured and the electrical input power P is calculated for each measurement point. The corresponding centre deflection v_c is measured with the cursor tools of the SEM. Figure 7.4 depicts a plot of centre deflection versus input power for a bimorph with the following dimensions: Bimorph length l: 1000 μm, width of aluminium w_{Al}: 2.5 μm, width of silicon w_{Si}: 5 μm, bimorph height h: 6 μm. The centre deflection denotes the displacement of the centre of the beam (compare figure 7.3) in the positive y-direction with respect to the unheated state. It should be noted that in the unheated state, the beam is curved with a centre deflection of 1.7 μm in the negative y-direction compared to a straight line through the supports. This initial curvature results from stress within the aluminium coating due to the elevated temperature during the aluminium evaporation. At 3 mW input power, a displacement of about 4.5 μm was obtained. The measured curve shows displacements in the same order of magnitude as a graph obtained by the analytical calculation described in chapter 4.2.2 and the structural ANSYS simulation described in chapter 4.3.3. The direction of the displacement in the positive y-direction is consistent with the simulation. The resistance of the beam was measured to be 45.2 kΩ, which agrees with the calculated value of 45.0 kΩ resulting from the resistivity specification.

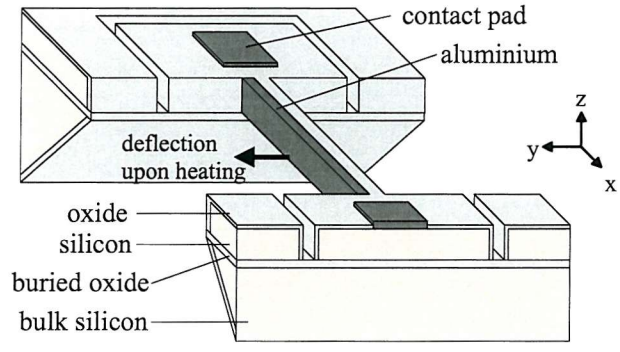

Figure 7.3: Deflection of a clamped-clamped bimorph upon heating.

Figure 7.5 shows displacement versus input power for a beam with the same dimensions (bimorph length: 1000 μm, width of silicon: 5 μm, bimorph height: 6 μm), but without an aluminium coating. The deflection merely results from buckling of the silicon beam under the thermally induced axial compression. There is no bimetal effect. With an input power of 3 mW the displacement is about 0.45 μm, which is an order of magnitude smaller than the bimorph displacement.

Figure 7.6 shows displacement versus input power for the same beam as used in figure 7.4. The input power is increased from 0 mW to about 7 mW and then decreased to 0 mW allowing about 5 minutes for the whole cycle. Hysteresis is observed be-

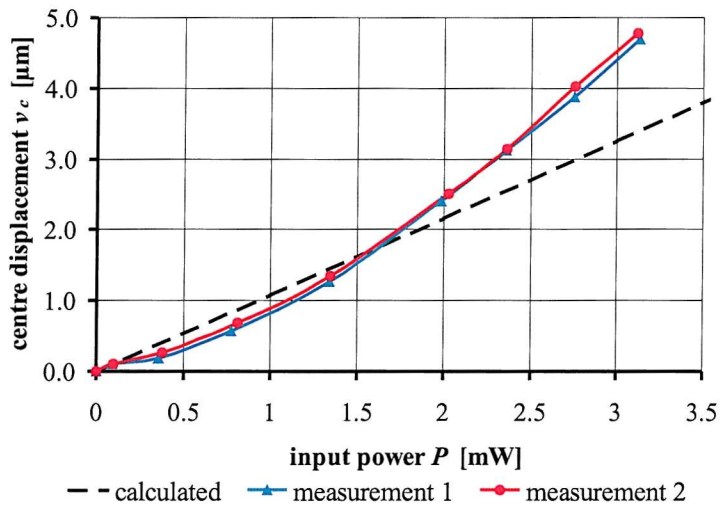

Figure 7.4: Displacement against power, static DC-measurement (l = 1000 μm, w_{Al} = 2.5 μm, w_{Si} = 5 μm, h = 6 μm).

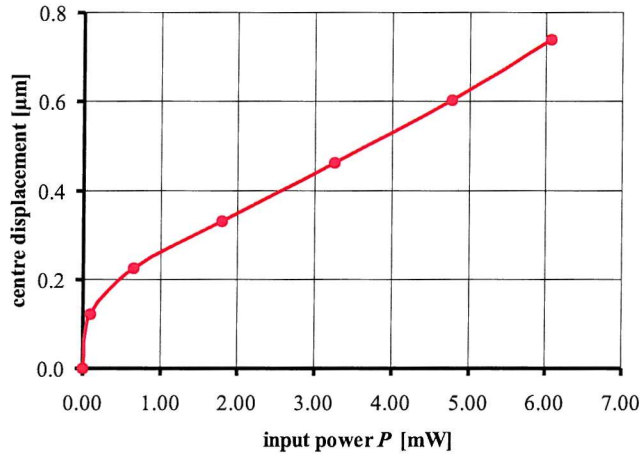

Figure 7.5: Displacement against power for a beam without aluminium sidewall spacers, static dc-measurement (l = 1000 μm, w_{Si} = 5 μm, h = 6 μm).

tween the increasing-power and decreasing-power branches. Repeated measurements show that the hysteresis is repeatable. The exact reason is not understood. It should be pointed out that no hysteresis was observed in the other measurements (figure 7.4, figure 7.7) where a lower input power was applied. This suggests there is a threshold value for the input power or possibly a threshold value for the temperature beyond which a hysteresis occurs. Possible reasons are thermal loading beyond the elastic range of the bimorph materials (aluminium and silicon) or a change in the temperature distribution of the whole chip (possible heating of the bulk silicon).

Figure 7.7 shows another plot of displacement as a function of input power. For these measurements, a pulsed input signal with a pulse time of 20 ms and a pause

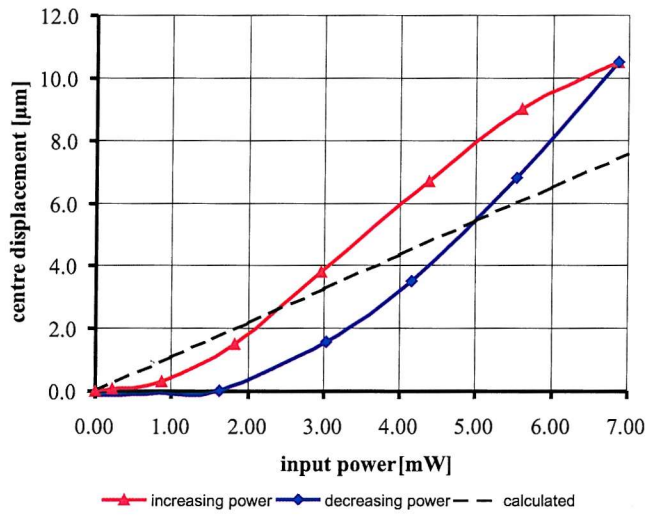

Figure 7.6: Displacement against power, static DC-measurement (l = 1000 μm, w_{Al} = 2.5 μm, w_{Si} = 5 μm, h = 6 μm). A hysteresis effect curve for increasing and decreasing power is observed.

time of 20 ms was applied to a bimorph with the following dimensions: l = 1400 μm, w_{Al} = 2.5 μm, w_{Si} = 5 μm, h = 6 μm. The advantage of using a pulsed input power is that bimorph cools down to the starting temperature during the pause time of the signal. Therefore, possible gradual heating effects of the bulk silicon are eliminated. During the pause time, the centre deflection is measured with the SEM cursor tools. A pulsed input power of 1 mW produced a displacement of around 4 μm. Again, the calculation gives displacement in the same order of magnitude. The resistance of the beam was measured to be 63.6 kΩ, which is close to the calculated value of 63.0 kΩ resulting from the resistivity specification. No twisting of the beams has been observed.

7.2.3 Thermal Time constant

The time constant can be determined by applying a Joule-heating voltage pulse and measuring the deflection amplitude for different pulse and pause widths. To obtain the response to a positive edge (switching on the power), a pulsed input signal, where the pulse time is much shorter than the pause time, is applied to the actuator and the corresponding deflection amplitude is measured. Gradually increasing the pulse width, increases the deflection amplitude until the maximum deflection is reached as illustrated in figure 7.8a. The maximum deflection has the same magnitude as the static deflection obtained by applying a DC input of the same power. Similarly, using an input signal, where the pause time is much shorter than the pulse time, the deflection response for a negative edge (switching off the power) is obtained. The pause width is increased gradually and the corresponding deflection amplitude

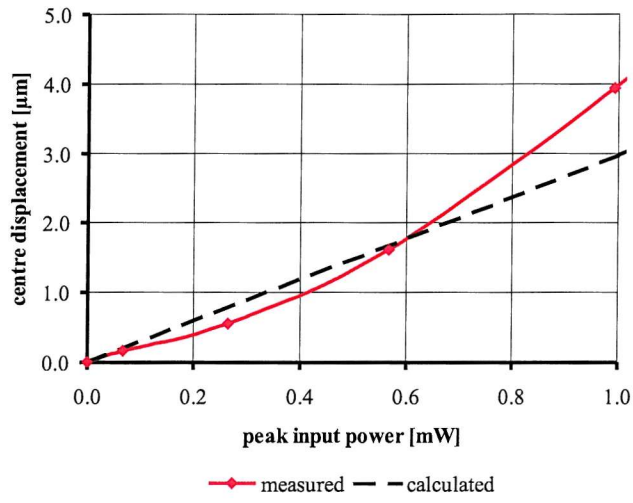

Figure 7.7: Displacement against power, pulsed input signal: pulse time: 10 ms, pause time: 10 ms, (l = 1400 μm, w_{Al} = 2.5 μm, w_{Si} = 5 μm, h = 6 μm).

is measured (figure 7.8b). To facilitate deflection measurements on the SEM screen, the frequency of the pulse generator is synchronised with the scanning frequency of the SEM (50 Hz) to obtain a stationary picture.

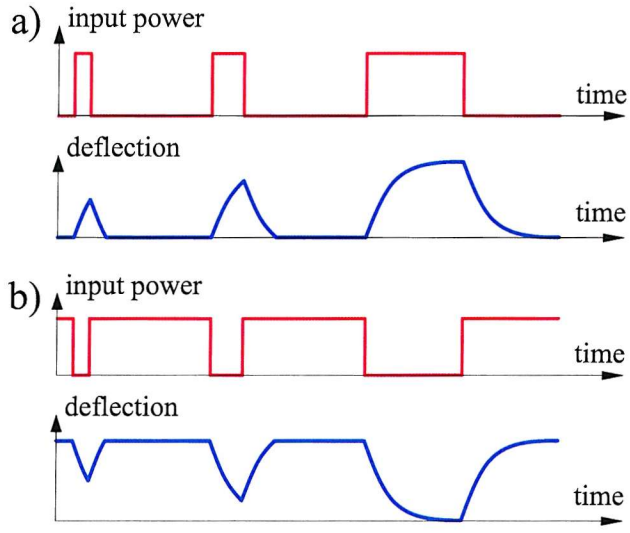

Figure 7.8: Pulsed input signal and deflection response for measurement of the time constant a) to a positive edge, b) to a negative edge.

Using this measurement method, deflection versus elapsed time plots have been obtained. Figure 7.9 shows the plots for a bimorph actuator of the following dimensions: l = 600 μm, h = 6 μm, w_{Si} = 4.3 μm, w_{Al} = 3.1 μm. The input power P is 3.2 mW during the pulse (device resistance R = 28.9 kΩ, current I = 332 μA, voltage V = 9.6 V). Using the method described in chapter 4.3.2, the rise of the deflection curve in figure 7.9 is found to be exponential with a time constant τ of 0.5 ms. Assuming

that a time of 5τ is necessary to reach the full deflection after a positive edge of the input signal (after 5τ, 99.3 of the full deflection is reached for an exponentially rising waveform) and the rest position after a negative edge, the maximum frequency of full thermal response f_o is calculated to be 200 Hz.

Table 7.1 gives the time constants and the operational frequencies for actuators of different dimensions. Larger dimensions increase the time constant due to increased thermal mass. Table 7.1 also gives the simulated time constants τ_s based on a transient thermal simulation in ANSYS (see chapter 4.3.2). The measured and simulated time constants are in good agreement.

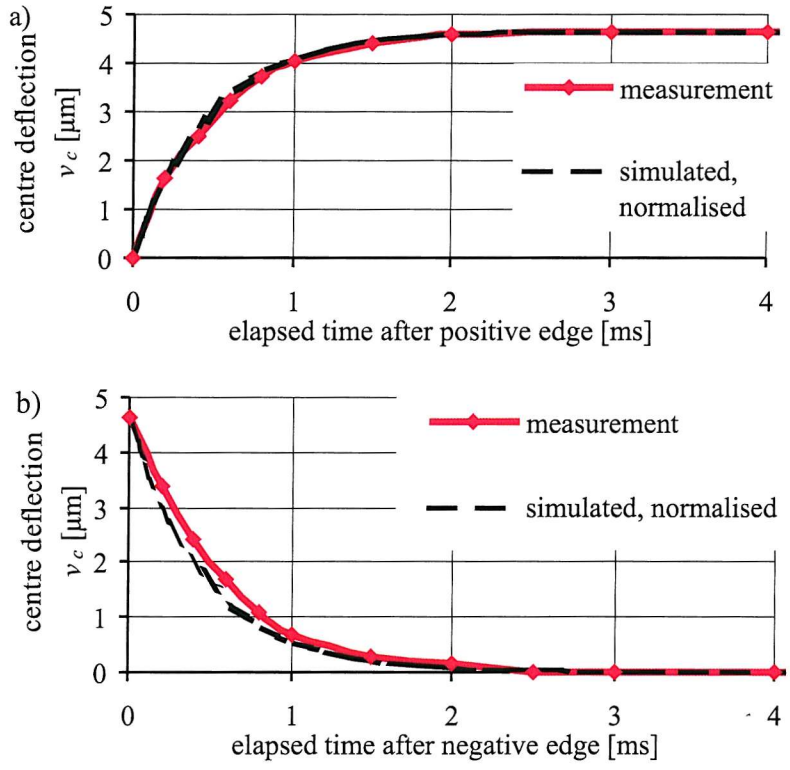

Figure 7.9: Measured deflection versus elapsed time after a) positive edge and b) negative edge (l = 600 μm, h = 6 μm, w_{Si} = 4.3 μm, w_{Al} = 3.1 μm.)

l [μm]	600	1000	1000	1400
w_{Si} [μm]	4.3	2.8	5.1	5.0
w_{Al} [μm]	3.1	3.2	2.8	3.0
τ_s [ms] (simulated)	0.47	1.22	1.33	3.6
τ [ms] (measured)	0.50	1.20	1.48	3.8
f_o [Hz]	200	83	67	26

Table 7.1: Measured time constant τ and maximum frequency of full thermal response f_o for actuators of different dimensions, compared with the simulated time constant τ_s.

7.2.4 Lateral Resonant Frequency

To measure lateral resonances, the actuator is driven with an AC input. Frequencies that significantly exceed the maximum frequency of full thermal response are used, which does not allow the beam to cool down to the bulk temperature. Therefore, the input signal causes a static deflection upon which a vibration is superimposed. This static deflection can be minimised through the application of a low AC input power. However, experiments have shown that a fairly large AC input signal is required (approximately 1 to 2 mW) to excite lateral modes that can be easily detected in the SEM. Since both the positive and the negative half wave of the signal heat up the beam, the frequency of the temperature change and hence the frequency of the vibration is double the frequency of the driving signal. The driving frequency is manually swept from a value below half the calculated resonant frequency to a value above this frequency and then decreased again. The vibration amplitude is measured with the SEM cursor tool at the centre of the bimorph beam for several frequency values to obtain an amplitude versus frequency plot. We found, the most accurate way of measuring the vibration amplitude is to measure the total width of the blurred image of the beam and subtract the width of the static beam. Figure 7.10 depicts SEM-images of the bimorph actuator viewed from above both in its stationary (figure 7.10a) and resonating stage (figure 7.10b). Although the frequency of the resonating beam is significantly higher than the refresh rate of the SEM-screen, the minimum and maximum deflection can be clearly seen by vertical lines in the blurred image occurring on the SEM screen. This is due to the repetitive and reproducible character of the vibration. Thus, the deflection amplitude can be measured with the SEM cursors. This method is a very straightforward approach to measuring in wafer-plane movement without great instrumental complexity as would be required by interference techniques [137].

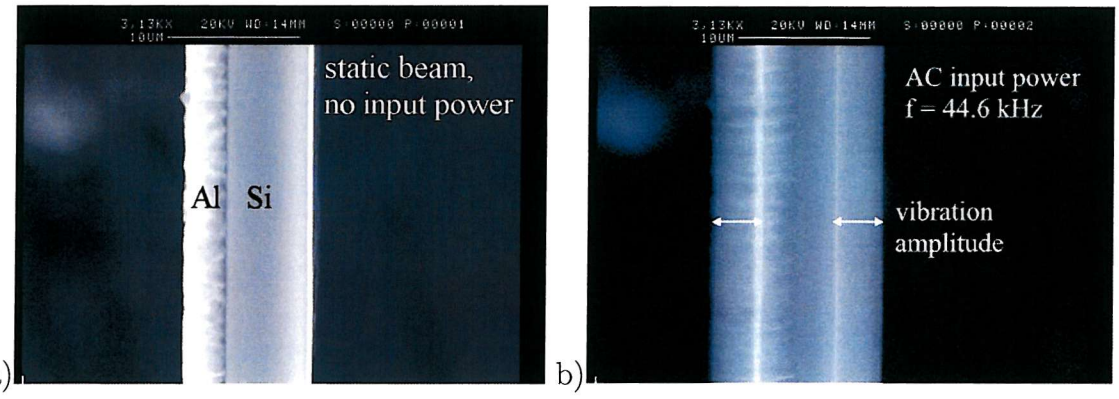

a) b)

Figure 7.10: SEM images of a bimorph actuator (top view) a) stationary, b) vibrating at resonance (l = 1000 μm, h = 6 μm, w_{Si} = 5.1 μm, w_{Al} = 2.8 μm).

Figure 7.11 shows an amplitude versus frequency plot for the same bimorph ac-

tuator as depicted in figure 7.10. The input voltage is 10 V, the resistance of the actuator is 39 kΩ. The resonant frequency is found to be 44.6 kHz, which is in reasonable agreement with the analytical calculation of 49.6 kHz for the first mode of a straight composite beam (see chapter 4.2.5). According to chapter 4.3.5, an ANSYS modal simulation was carried out using the measured dimensions of the actuator. It also takes the static deflection and the aluminium reference temperature into account. The static deflection is caused by the rms-value of the ac-input power which is 1.3 mW. The aluminium reference temperature is set to 314 K. A resonant frequency of 44.8 kHz is obtained, which is in good agreement with the measurement. The shape of the measured curve suggests a slightly non-linear resonance with a hard spring characteristic [120]. The static deflection of the beam is measured to be 2.9 μm.

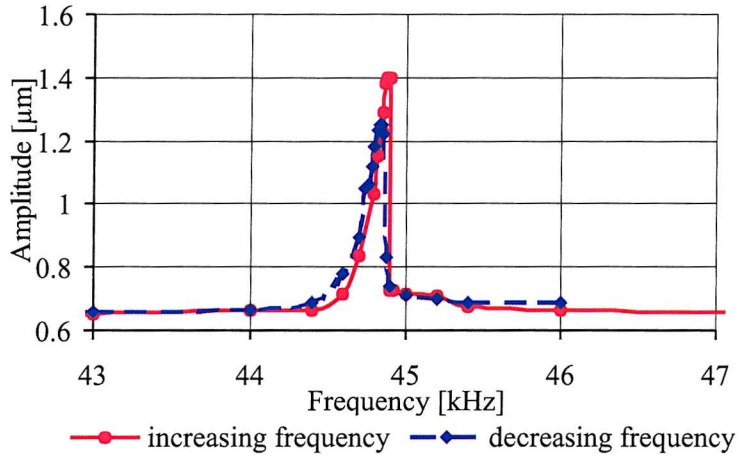

Figure 7.11: Vibration amplitude versus frequency (l = 1000 μm, h = 6 μm, w_{Si} = 5.1 μm, w_{Al} = 2.8 μm, rms-value of the ac-input power: 1.3 mW).

For a 1400 μm long actuator (h = 6 μm, w_{Si} = 5.6 μm, w_{Al} = 2.7 μm), we have measured the first (20.9 kHz) and second lateral mode (56.1 kHz). The input voltage is 10 V, the resistance of the actuator is 57 kΩ. To confirm the mode shape we measured the vibration amplitude along the length of the bimorph beam. These measurements only give the magnitude for the displacement, not the direction. Figure 7.12 gives plots of the deflection amplitude as a function of the position along the beam. To compare the curves with the calculated mode shape curves (see chapter 4.2.5), the absolute values for the calculated curves are taken. The measured and the calculated curves follow the same trend. The discrepancy between the measured and the calculated curves is due to the limited measurement accuracy using the SEM cursor tools for submicron deflections and due to noise in the SEM image.

Table 7.2 gives the calculated and measured values for the lateral resonant frequencies of actuators with different dimensions. The discrepancy between measured and analytical values results from the static deflection, which means there is an initial curvature, which tends to decrease the resonant frequency [138]. The static deflection

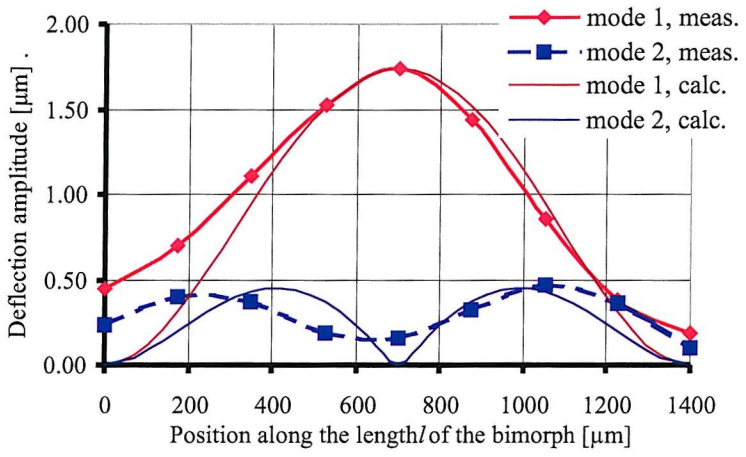

Figure 7.12: Vibration amplitude along the bimorph beam ($l = 1400$ μm, $h = 6$ μm, $w_{Si} = 5.6$ μm, $w_{Al} = 2.7$ μm) for the 1st (20.9 kHz) and the 2nd lateral mode (56.1 kHz), rms-value of ac-input power: 1.0 mW).

has been accounted for in a modal analysis using ANSYS, where the rms-value of the AC input power was used to obtain the static deflection as described in chapter 4.3.5. The values for the power P used in the simulation, are also given in the table. An aluminium reference temperature of 314 K was used. The temperature of the bulk silicon T_0 was set to 300 K. The simulation results are in good agreement with the measurements. Note, a fairly large amplitude for the ac-signal resulting in rms-values of 1 mW to 3.8 mW was used since this power level is required to obtain resonant vibrations that can easily be detected in the SEM.

l [μm]	600	1000	1000	1400
w_{Si} [μm]	3.3	2.8	5.1	5.6
w_{Al} [μm]	3.2	3.2	2.8	2.7
P [mW]	3.2	1.4	1.0	3.8
f_r [kHz] (calculated)	109.1	36.6	49.6	26.6
f_r [kHz] (simulated)	87.1	32.9	44.8	20.5
f_r [kHz] (measured)	84.8	33.1	44.6	20.9

Table 7.2: Calculated, simulated and measured resonant frequencies (mode 1) for actuators of different dimensions.

7.2.5 Summary

The static displacement of clamped-clamped beam actuators was measured in an SEM. With a 1000 μm long beam a displacement of about 4.5 μm was obtained at an input power of 3 mW. A 1400 μm long beam produced a deflection of 4 μm at 1 mW input power. The bimorph displacement was found to be about an order of

magnitude larger than the buckling deflection of silicon beams without aluminium coating.

The time constants for the response of vertical bimorph actuators to input pulses has been measured. From these measurements the maximum frequency of full thermal response was calculated to be between 26 Hz and 200 Hz depending on the actuator size. Lateral modes were excited thermally and found to be between 20 and 85 kHz, significantly above the maximum frequency of full thermal response.

7.3 One-Dimensional Meander Type Actuator

7.3.1 Test Setup

A similar test setup as for measurements on the clamped-clamped beam actuator is used (section 7.2.1). A power-supply, pulse generator and signal generator individually provide the electrical input for static deflection, time constant and resonance measurements respectively. Input voltage and current are measured to obtain the electrical input power, whilst displacement measurements are carried out with the SEM cursor tools. The actuator chips are packaged onto a 28-pin dual in-line (DIL) package as shown in figure 7.13.

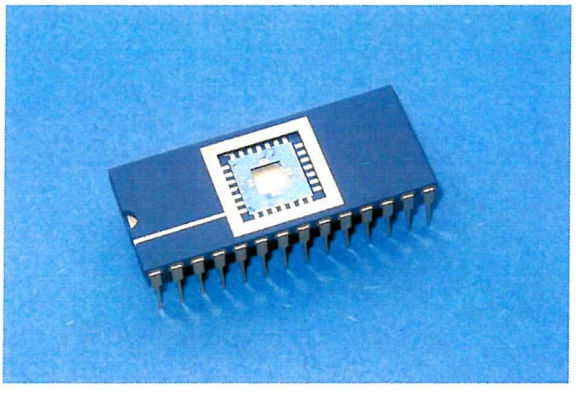

Figure 7.13: Actuator chip packaged into a 28-pin DIL package.

7.3.2 Static Deflection

A DC input is applied to the actuator placed in the SEM chamber and the displacement of the front plate is measured with the cursors. Upon applying an input power, the front plate of the actuator moves towards the contact pads, which agrees with the simulated direction of movement. Figure 7.14 shows a plot of displacement versus input power. The diagram shows three measured graphs, which have an al-

most linear rise with a small hysteresis between the increasing and decreasing power branches (when decreasing the power, a slightly higher displacement is observed for the same input power when increasing). For an input power of 6 mW, a displacement of 13.2 μm is observed. The three measurements were carried out within a time interval of about 30 minutes and are quite identical within the measurement tolerance, confirming the reproducibility of the experiment.

The two dashed lines represent simulated graphs based on thermal and structural simulations performed in ANSYS as described in chapter 4.4.2 and 4.4.3. The measured dimensions of the actuator have been used in the simulations, too. The simulated graphs are linear rise functions, where the steeper of the two is based on a thermal expansion coefficient of aluminium of $\alpha_{Al} = 2.5 \cdot 10^{-5}$ which is the standard value for bulk aluminium and has been used in previous simulations. This simulated displacement is noticeably higher than that of the measurements, but is of the same order of magnitude. The discrepancy may be due to slightly different material properties, especially α_{Al}. Therefore a simulated graph has been added for $\alpha_{Al} = 1.5 \cdot 10^{-5}$. Measurements on cantilever devices showed that α_{Al} can vary between $1.5 \cdot 10^{-5}$ and $2.5 \cdot 10^{-5}$ for aluminium sidewall deposits [136]. This implies the two simulated graphs give a range of expected deflection values. The measurements lie at the lower end of this range suggesting that α_{Al} is roughly $1.5 \cdot 10^{-5}$ for the measured actuator.

Possible reasons for the hysteresis between increasing and decreasing power branches are thermal loading beyond the elastic range of the bimorph materials (aluminium and silicon) or a change in the temperature distribution of the whole chip. The electrical resistance of the actuator is measured to be 5.8 kΩ, which agrees well with the calculated 5.4 kΩ from the resistivity specification.

Another displacement measurement has been carried out using an optical microscope where the actuator operates in ambient conditions. For each measurement point, a photo is taken with a digital camera fitted onto the microscope. From the photos, the displacement could be measured and scaled to the actual deflection. The displacement is significantly smaller than in the vacuum of the SEM due to convection heat losses. With an input power of 30 mW, a deflection of 5.3 μm has been obtained. Figure 7.15 shows the displacement plot, again showing the curve to denote a linear response. The reason for the significantly smaller deflections is that heat conduction through air becomes a second mechanism for heat loss. Therefore, the bimorph beams reach a significantly lower temperature for the same input power. The ANSYS model presented in chapter 4.4 does not account for convection losses. The temperature of the bimorphs has not been measured, neither in vacuum nor in ambient conditions. However, failure experiments have shown, that the silicon beams of the actuator break when an input power of roughly 30 mW is applied under the vacuum conditions in the SEM. With the same input power of 30 mW, the deflection

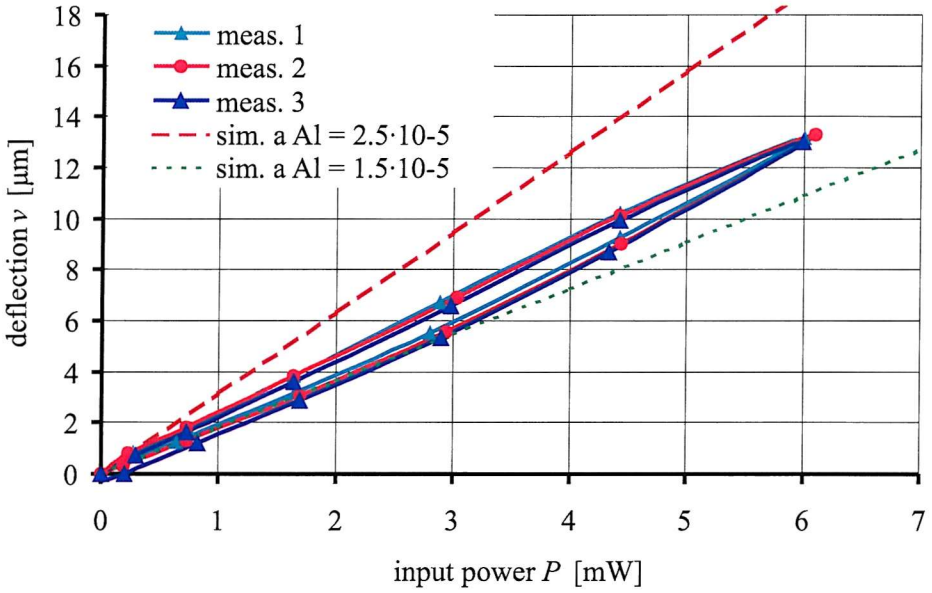

Figure 7.14: Deflection v against input power P for a one-dimensional meander actuator, measurement in the SEM, $l_b = 1000$ μm, $w_{Si} = 8$ μm, $w_{Al} = 1.5$ μm, $l_1 = 300$ μm, $l_2 = 300$ μm, $l_3 = 300$ μm, $l_4 = 200$ μm.

of the actuator in ambient conditions is a moderate 5.3 μm, suggesting a much lower temperature than in vacuum conditions. No hysteresis could be observed for this measurement, also suggesting a significantly lower temperature.

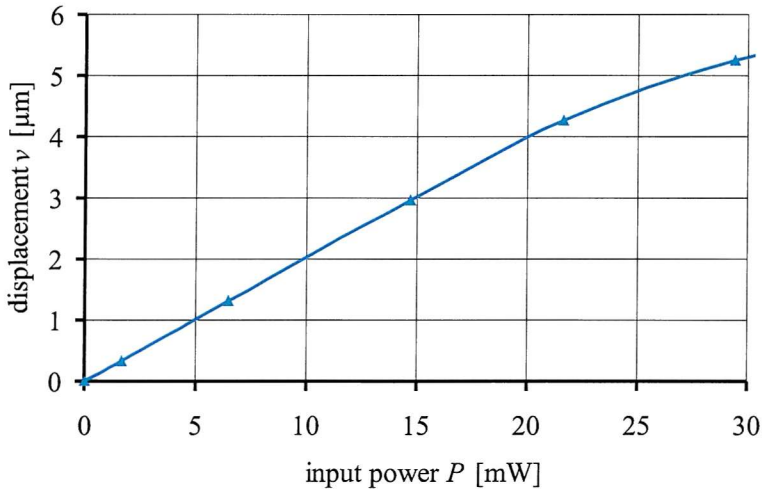

Figure 7.15: Deflection v against input power P for a one-dimensional meander actuator, measurement on an optical microscope in ambient conditions, dimensions see figure 7.14.

7.3.3 Thermal Time Constant

Using the new LEO SEM [139] allows capturing screen images at any time, which is highly beneficial for time constant measurements. A pulsed input is applied to the actuator, where both the pulse time and the pause time are 250 ms. The peak input power P is 6 mW. Figure 7.16 shows SEM images of the actuator: a) the whole actuator (no input power applied, b) the front plate (input pulses applied), c) a magnified view of the front plate allowing measurement of displacement versus time for a positive edge (switching on the power), d) a magnified view of the front plate for displacement versus time measurements after a negative edge of the signal.

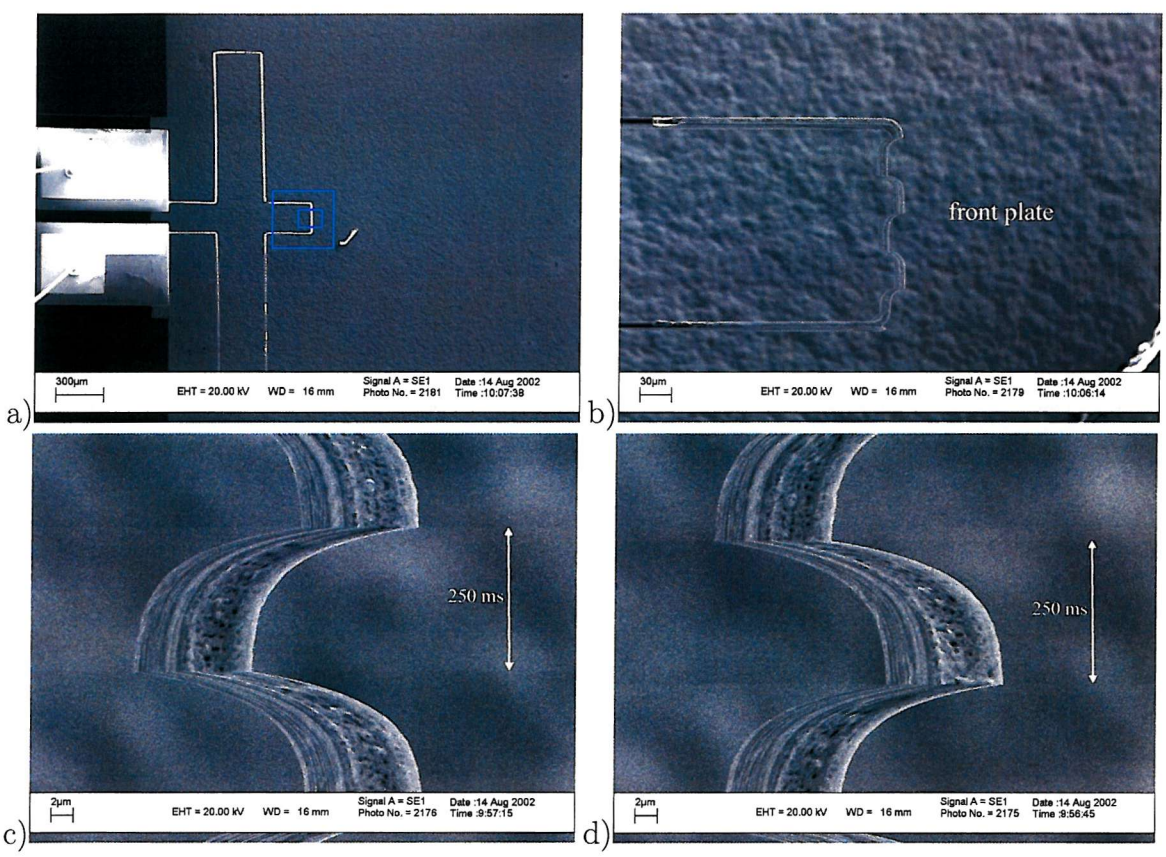

Figure 7.16: SEM images of the one-dimensional meander actuator a) the whole actuator (no input power applied, b) the front plate (input pulses applied), c) magnified view of the front plate, for measurement of displacement versus time for a positive edge, d) magnified view of the front plate, for measurement of displacement versus time for a negative edge, dimensions see figure 7.14, peak input power: 6 mW .

The images in figure 7.16 c,d are taken at scan rate 4, which means it takes 640 ms to scan the whole screen area. While the SEM scans the image line by line, the input pulse gradually heats up the actuator making it move to the left (figure 7.16d), making the resulting SEM image a plot of position versus time, where the time axis is the vertical axis. In figure 7.16c, the input pulse is switched off and the actuator cools down and moves to the right while the image is scanned. From the

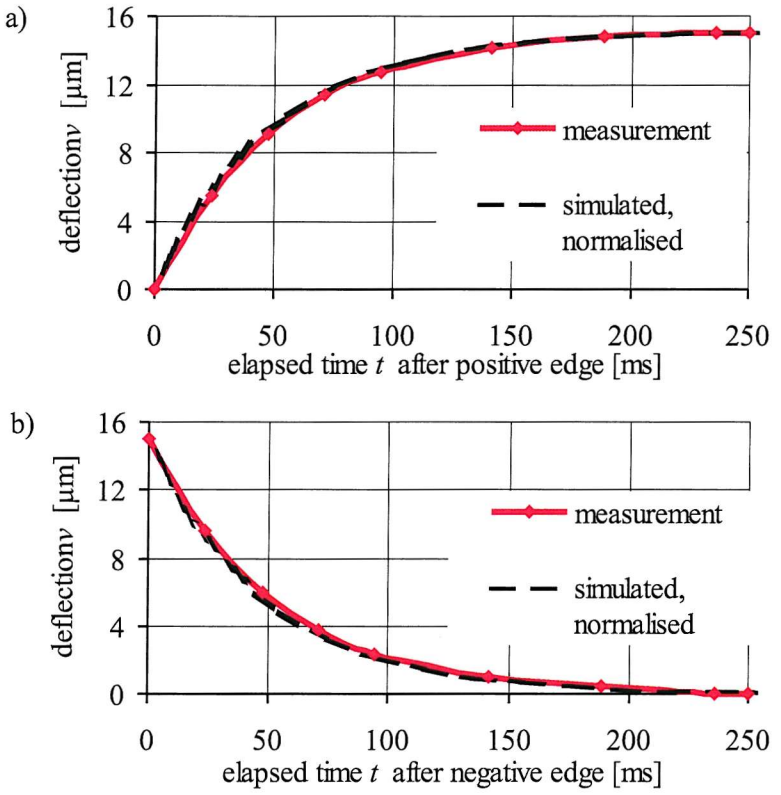

Figure 7.17: Deflection v against time, a) after positive edge, b) after negative edge, dimensions see figure 7.14.

two images, displacement versus time plots both for the positive and the negative edge have been extracted. The plots are shown in figure 7.17. The dashed curves are the results of the transient ANSYS simulation (temperature against time, see chapter 4.4.4), normalised to the measured displacement. The simulation is based on the dimensions of the measured device and the same peak input power of 6 mW. The measured graphs are almost identical to the simulated ones. The method described in chapter 4.3.4 was used to prove that the graphs are exponential rise functions and to determine the time constant. For the measurement, a time constant τ of 49 ms was obtained (compared to $\tau = 48$ ms for the simulation).

7.3.4 Lateral Resonances

The actuator is driven with an AC input whose frequency is significantly above the maximum frequency for full thermal response, meaning there is a static deflection upon which a vibration is superimposed. The rms value of the AC input is 5 mW. This fairly high input power is necessary to obtain vibration amplitudes that can easily be detected in the SEM. Since both the negative and the positive half cycles of the input signal heat up the beam, the temperature changes at double its frequency. The

driving frequency is manually swept from a value below half the calculated resonant frequency to a value above and then decreased again. The vibration amplitude is measured with the SEM cursor tool at the front plate of the actuator by measuring the total width of the vibration image of the beam and subtracting the width of the static beam. Figure 7.18 shows SEM images of the front plate of the actuator in its static (a) and vibrating state (c,d).

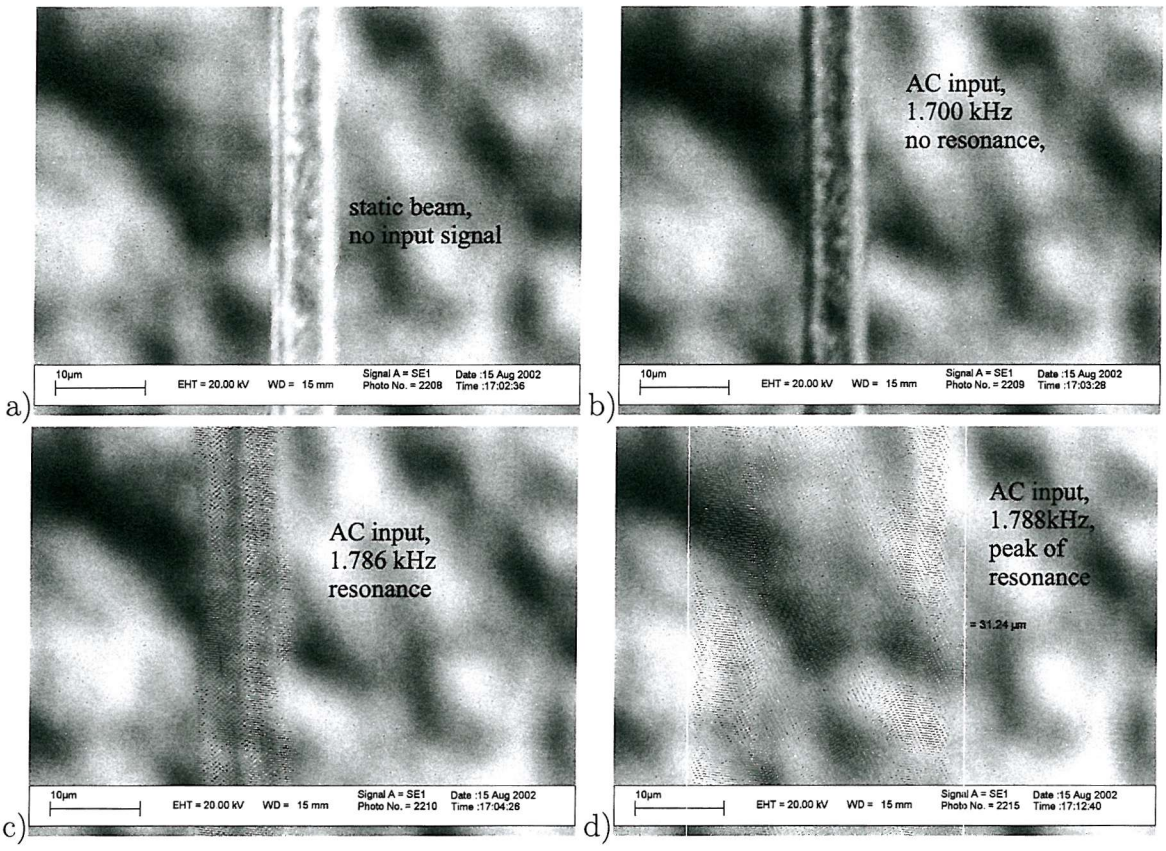

Figure 7.18: SEM images of the front plate a) static, no input power, b) AC input at 1.700 kHz, no resonance, c) AC input at 1.786 kHz, vibrating at resonance, d) AC input at 1.788 kHz, maximium vibration amplitude at the peak of the resonance, dimensions see figure 7.14, rms-value of input power: 5 mW.

Figure 7.19 shows vibration amplitude versus frequency plots for the first and second harmonic of the lateral mode. The curve is symmetric and is identical for increasing and decreasing frequency. The fact that no axial forces can build up in the meander geometry is the likely reason for the symmetrical shape of the resonance curve [140] (for the clamped-clamped beam actuator, a hard spring characteristic was observed, section 7.2.4). The vibration peak is found to be at 3576 Hz for the first harmonic and 7148 Hz for the second harmonic. The modal ANSYS simulation finds the first harmonic at 3899 Hz (see chapter 4.4.5). Figure 7.20 shows SEM images of half the actuator in its resonant state both for the first (a) and the second harmonic (b). The zigzag shape of the beams, caused by the vibration along the bimorphs

and the front plate of the actuator, gives a qualitative image of the mode shape, by distinguishing the areas of small and large vibration. The vibration pattern is qualitatively consistent with the mode shape of the simulation (see chapter 4.4.5, figure 4.25), which also shows the highest vibration amplitude at the bimorphs and the front plate.

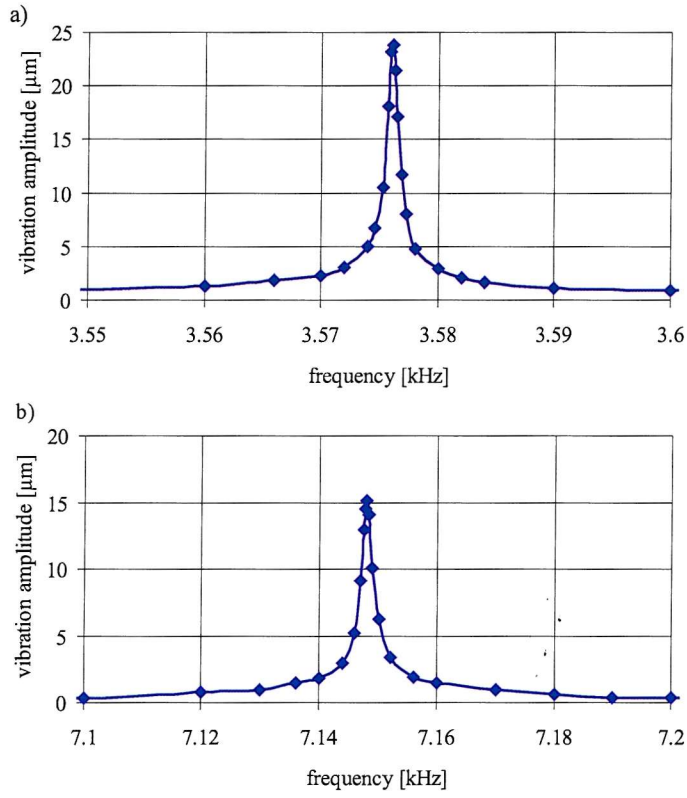

Figure 7.19: Vibration amplitude against frequency for the first lateral mode a) first harmonic, b) second harmonic, dimensions see figure 7.14, rms-value of input power: 5 mW.

7.3.5 Summary

The static displacement of the one-dimensional meander actuator has been measured both in an SEM and with an optical microscope. In the SEM, a displacement of 13.2 μm was obtained at 6 mW input power. In ambient conditions, 30 mW are necessary to produce a displacement of 5.3 μm. A linear relation between input power and deflection has been observed, which is consistent with FEA simulations.

The thermal time constant was measured to be 49 ms. From this measurement, a maximum frequency for full thermal response of 2.1 Hz was calculated. Lateral resonances were excited thermally and found to be at 3576 Hz (first harmonic) and 7148 Hz (second harmonic). Both frequencies are significantly above the frequency

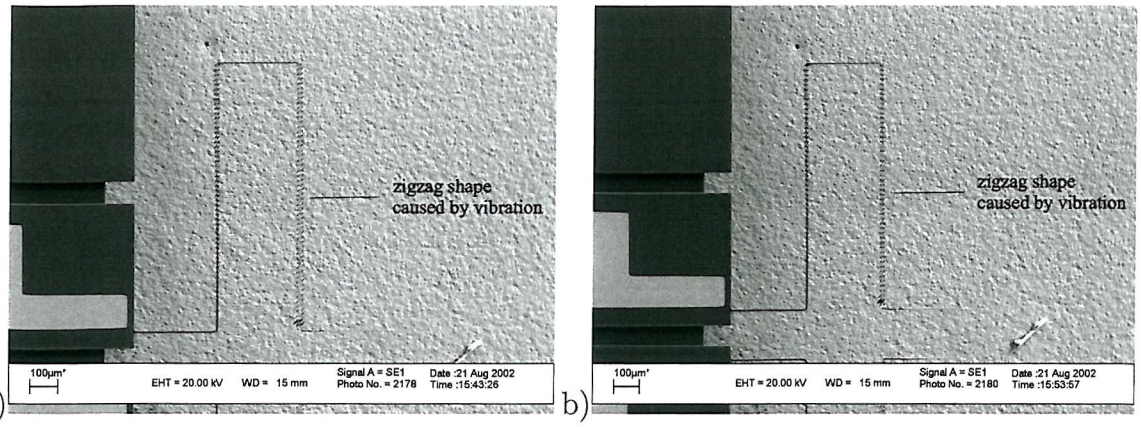

Figure 7.20: SEM images of the one-dimensional meander actuator a) resonating at 3576 Hz (first harmonic) b) resonating at 7148 Hz (second harmonic) dimensions see figure 7.14, rms-value of input power: 5 mW.

for full thermal response.

7.4 Two-Dimensional Meander Type Actuator

Due to the problems of the fabrication process, particulary the release etching (see chapter 5.5) and the complex geometry of the two-dimensional meander actuator, only one device with fully intact silicon beams was left after completion of the batch process. Preliminary measurements on this actuator showed that movement can be achieved when an actuation voltage is applied. However, the motion was always in the same direction, no matter which of the four actuators was powered. The amount of movement was different for the different actuators. We believe, the reason for this behaviour is residual gold, which forms bridges connecting the silicon beams and hence has a significant influence on the mechanical compliance of the whole actuator (see figure 7.21). Measurements on devices, where parts of the silicon beams have been broken off during the fabrication process indicate that actuators without gold bridges move in the expected direction (see chapter 3.5). However, due to the asymmetrical character of the break, there was always a small component of the movement which is perpendicular to the expected direction. More work on these actuators is planned in the future.

7.5 Micro-relays

All preliminary tests were carried out on micro-relays fabricated from a wafer, which had undergone tests with Cool Grease (see chapter 5.5.3). An optical microscope was used as inspection tool. In order to apply the electrical input power, the devices were

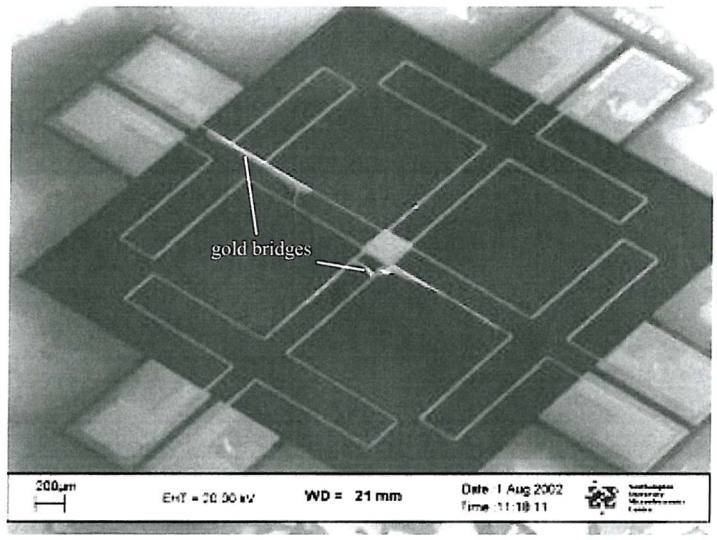

Figure 7.21: SEM image of the two-dimensional meander actuator, showing bridges of gold residues.

packaged into a DIL package as shown in figure 7.13. After completion of the release etch, the following observations were made:

- For most of the normally closed micro-switches, the moveable contact was firmly pressed against the fixed contact pair. When an input power was applied to the actuator (20 mW), the moveable contact moved away from the fixed contact pair by about 3 μm. This behaviour is consistent with the desired switching movement.

- For most normally open micro-switches the moveable contact had moved away from the fixed contact pair. When an input power was applied to the actuator, the moveable contact moved towards the fixed contact pair until it touched (at about 25 mW). This behaviour is also consistent with the desired switching movement.

However, even when they were firmly pressed against each other, there was no electrical contact between the fixed and the movable contacts, not even when a voltage of 30 V was applied to the contact pads of the contact circuit. Possible reasons are:

- Contamination of the contact area prevented an electrical contact between the moveable and the fixed contacts. Cool Grease residues may be responsible for this contamination.

- It was observed that the adhesion of the chrome/gold layer used for the contacts was poor in parts of the wafer. Missing metal patches could be the reason for not getting electrical contact.

More work needs to be done on the fabrication and measurement of micro-switches in the future focussing on improved contact deposition and more quantitative measurements.

7.6 Conclusion

The clamped-clamped beam actuator and the one-dimensional meander type actuator were characterised. With a 1000 μm long clamped-clamped beam actuator, a displacement of approximately 4.5 μm was achieved with an input power of 3 mW. The displacement versus power plot is close to the linear behaviour predicted by the simulation. The thermal time constant ranges from 0.5 ms to 3.8 ms depending on the size of the actuator. The lateral resonant frequencies were found to be between 20 and 85 kHz.

The one-dimensional meander actuator produced a displacement of 13.2 μm at 6 mW input power. The thermal time constant was measured to be 49 ms. The first lateral resonant mode was measured to be 3576 Hz for the first harmonic and 7148 Hz for the second harmonic. Both for the clamped-clamped beam actuator and the one-dimensional meander type actuator, reasonable and at times a good agreement of the measurements with the analytical calculations or the simulations was observed.

Due to the lack of fully operational devices, the two-dimensional meander actuators and the micro-switches could not be quantitatively characterised. However, preliminary experiments suggest that the actuators work in principle. More work will be required on fabricating working devices before any thorough characterisation can commence.

Chapter 8

Conclusion and Suggestions for Further Work

8.1 Conclusion

Micropositioning stages for application in integrated scanning probe devices require micro actuators that enable large displacements with a low input power and low actuation voltages. Piezoelectric and electrostatic implementations cannot fulfill these requirements whereas thermal bimorph actuators are suitable candidates to meet these goals. Up to now, only planar bimorphs have been realised, where a metal layer is deposited on top of a silicon bridge. When heated, the bridge performs a movement perpendicular to the wafer plane. For micropositioning applications, movement parallel to the wafer plane is required. To fulfil this goal, we have developed vertical bimorphs, consisting of silicon beams, side-coated with aluminium. When heated they produce lateral movement.

A clamped-clamped silicon beam with an aluminium sidewall deposition is the simplest implementation of a vertical bimorph actuator. It is heated by a current through the silicon. With a 1000 μm long beam, a displacement of 4.5 μm was obtained at an input power of 3 mW. A 1400 μm long beam produced a deflection of 4 μm at 1 mW input power. At low input power, the deflection versus input power plot follows a linear function as predicted by analytical calculations and ANSYS simulations. The thermal time constant was measured to be between 0.5 ms to 3.8 ms depending on the dimensions of the actuator. Good agreement with transient ANSYS simulations was achieved. The first lateral mode was excited thermally and was found to be between 20 and 85 kHz, also depending on the device dimensions. A modal analysis in ANSYS taking static deflection and intrinsic stress in the aluminium layer into account confirmed the measurement results.

To increase the actuation range with still a comparable level of input power, an advanced actuator design was devised based on a meander shaped silicon beam, also heated by an electrical current through the silicon. The one-dimensional meander actuator consists of four bimorphs, 1000 μm long. The symmetrical design ensures linear displacement. A displacement of 13.2 μm was achieved with an input power of 6 mW. The deflection versus power plot shows a linear characteristic agreeing with the ANSYS simulation. The thermal time constant was measured to be 49 ms as compared with 48 ms obtained by a transient ANSYS simulation. Measurements for the first lateral mode are at 3576 Hz for the first harmonic and 7148 Hz for the second harmonic.

By combining 4 meander type actuators, a two-dimensional positioning stage is obtained. To move its central table in the x-direction, the x-actuator is powered whilst the three passive actuators merely act as compliant suspensions. The symmetrical design ensures linear movement. Preliminary measurements confirm the functionality of the device in principle. ANSYS simulations predict a static deflection of 4.2 μm with 8 mW of input power, a thermal time constant of 31 ms and the first lateral mode at 2926 kHz.

As an example for a practical application of vertical bimorph actuators, normally open and normally closed micro-switches have been designed. They are based on a one-dimensional meander type actuator that moves a gold contact towards or away from a fixed contact pair closing or opening the electrical contact on the contact circuit. The contact electrodes are gold patches on the sidewall of the contact trench. Preliminary results show that the actuators are capable of moving the movable contact as required, however no electrical contact could be achieved between the movable and the fixed electrodes.

In order to fabricate vertical bimorph devices, a number of non-standard fabrication processes had to be developed. Most importantly, a process to deposit aluminium onto the sidewalls of silicon beams was implemented. Aluminium sputtering and angled evaporation of aluminium combined with dry- and wet-etching was investigated. Angled evaporation followed by an isotropic aluminium wet-etch yields the best results. An optimised aluminium wet etch accounts for non-uniformities in the aluminium thickness across the wafer introduced by an inhomogeneous distance of the different wafer parts from the aluminium crucible during the evaporation process.

For the contacts of the micro-relays, chrome/gold depositions are required on opposite sidewalls of the narrow contact trench as well as for gold conductors on the horizontal wafer surface. These requirements could be met with two consecutive chrome/gold evaporation stages at a steep angle of incidence from either side of the contact trench. A chrome/gold wet-etch defines the pattern of the gold conductors

on the wafer surface.

After the definition of the silicon beams by a DRIE process, 30 μm deep trenches become a challenge for all photolithography steps. A lithography procedure based on a viscous Shipley SPR220-7 resist was developed which is capable of covering areas on the horizontal wafer surface, in the trenches and even on the silicon beams. On the other hand exposed areas can be cleanly developed regardless of whether they are on the wafer surface, in trenches or on silicon beams. We used a double coating at 800 rpm spin speed.

To make the bimorph beams free to move, the handle silicon and the buried oxide layer has to be removed from the back. We have investigated different approaches for this release etch including KOH etching and dry-etching in an SF_6 plasma. The dry-etch from the back requires the front of the wafer to be protected from reactive species. Different protection methods were investigated including different protection photoresists and gluing of a backing wafer. It turns out that dry-etching with a backing wafer glued on using SPR220-7 photoresist is the best alternative for etching the handle silicon wafer. To etch the buried oxide, a standard dry-etch in CHF_3 and Ar was used.

The batch fabrication process is based on SOI substrates with a 6 μm or 30 μm thick device silicon layer. The patterns of the silicon beams are defined by a DRIE process. For the contacts, gold is evaporated and patterned. In the case of the micro-relays, the double evaporation process is used. To deposit the aluminium sidewall coatings for the bimorphs, the angled evaporation and aluminium wet-etching is carried out up to 4 times from different directions. A thick resist pattern used for lift-off makes the sidewall evaporation selective. Lastly, the release etch from the back makes the actuators free to move.

Using the above processes and designs we have shown that thermally actuated vertical bimorphs are a versatile alternative for in-wafer plane actuation.

8.2 Suggestions for Further Work

8.2.1 Two-Dimensional Meander Actuators

More work is required on the current design of the two-dimensional meander type actuators. There are three wafers left at the stage where the silicon beams and the gold contacts have been defined. Completing the remaining stages, mainly aluminium sidewall deposition and the release etch, should give a number of working devices. Furthermore, to increase the process yield, the use of DRIE, which offers a helium cooling system for the wafer, for the release etch should be investigated. Quantitative

measurements should be carried out, including static deflection, thermal time constant and lateral resonances. A mask redesign should include thicker silicon beams to increase the yield of the fabrication process.

8.2.2 Micro-Relays

For the micro-relays, there are four more wafers left, where the silicon beams have been defined. By completing the contact evaporation, the aluminium sidewall deposition and the release etch, more devices could be obtained. Most importantly, the release has to be carried out using a backing wafer glued onto the device wafer with SPR220-7 photoresist, thereby avoiding contact contamination as introduced by Cool Grease. To improve the adhesion of the chrome/gold contacts, a test batch could be carried out, further investigating different layer thicknesses and evaporation angles. A mask redesign should aim at increasing the contact area. Also, a thicker device silicon layer would help to increase the contact area.

8.2.3 Different Actuator Metals and Sidewall Deposition Approach

To construct the actuator bimorphs we have used aluminium, mainly because both an aluminium evaporation and sputtering process was available. Although aluminium is ranked as a fairly good material for thermal actuators [141] it has the disadvantage of a low melting point at 660 $^{\circ}$C. Nickel, copper and manganese would be worth investigating, since they have the best properties in terms of achievable work, displacement and blocking force [141]. Chrome/gold may be an alternative because of their well known deposition techniques, even though their properties are not ranked very high. Although, the aluminium sidewall deposition process is a reproducible way of obtaining vertical bimorph devices, a process that yields a better uniformity across the wafer would be desirable for mass fabrication. Even though initial experiments ruled out sputtering and dry-etching, more profound experiments might lead to an alternative process sequence.

8.2.4 Integrated Scanning Probe devices

Based on the two-dimensional meander actuators, micro scanning probe devices could be designed. A tip needs to be integrated onto the central table of the device. This could be done by mounting a separately fabricated tip or by using tip-etching techniques to define a tip on the central table before the definition of the silicon beams.

For the required displacement in the z-direction (due to the topography of the sample) the compliance of the actuator should be sufficient for initial tests. A more advanced design should have an integrated z-actuator, which could be a thermally actuated planar bimorph. Furthermore, control circuitry for the scanning movement and a sensor for the z-displacement would be required.

8.2.5 Further Applications

As mentioned above, thermal vertical bimorph actuators are versatile devices and their application is not restricted to micro-positioning tasks.

Microgripper

Figure 8.1 depicts the layout of a micro-gripper, based on thermally actuated bimorphs arranged similarly to the meander actuator design. Applying a driving voltage between both bondpad sets (marked A and B) heats up the bimorphs and pushes the tweezer-like ends of the gripper together.

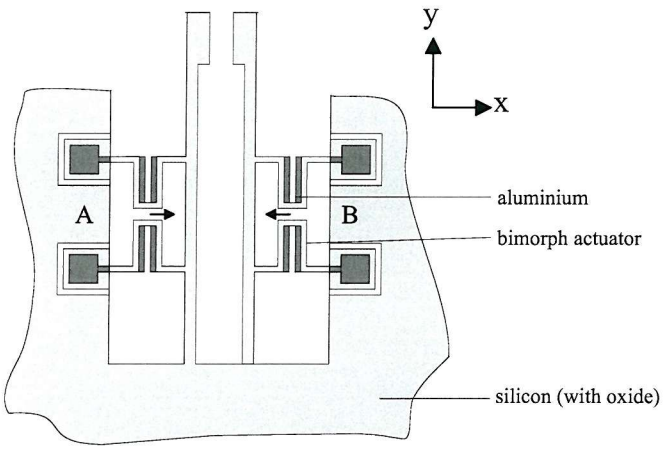

Figure 8.1: Micro-gripper based on thermally actuated vertical bimorphs.

Micro-Fluidic Valve

In Figure 8.2, a microfluidic valve based on a clamped-clamped vertical bimorph is depicted. The valve consists of two wafers, a silicon wafer with a recess and an SOI wafer with the bimorph. The fabrication process requires wafer-bonding of two silicon wafers. The oxide layer of the SOI-wafer is used as a sacrificial layer to release the bimorph. Details of the process sequence would need further work. In figure 8.2a, the valve is closed. Applying a driving voltage between the bondpads A1 and A2, the bimorph is heated up moving the shutter away from the left fluid channel enabling

a liquid to pass from the left fluid channel through the valve chamber into the right fluid channel. Achieving a proper sealing characteristic may be difficult.

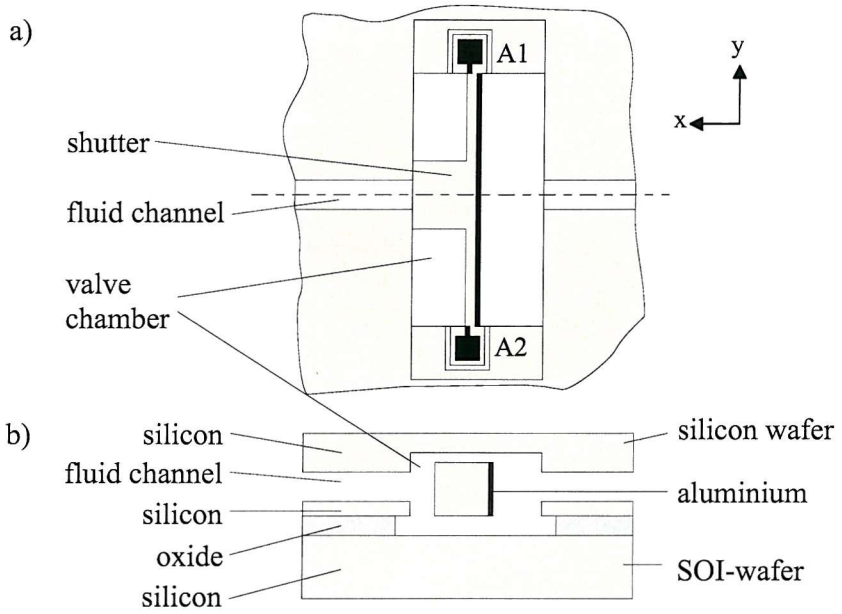

Figure 8.2: Micro-fluidic valve based on a thermally actuated vertical bimorph, a) plan view, b) cross-section.

Appendix A

Analytical Analysis on the Clamped-Clamped Beam Actuator Accounting for Axial Forces

This appendix gives an analytical calculation to obtain the equation of the deflection curve for a clamped-clamped beam actuator. The calculation presented in chapter 4.2.2 does not account for axial reaction forces at the ends of the beam. In the calculation below we account for these axial reactions as illustrated in figure A.1a. The axial reaction forces R_{Aa} and R_{Ba}, the lateral reaction forces R_A and R_B as well as the reaction couples M_A and M_B at the supports of the beam are shown.

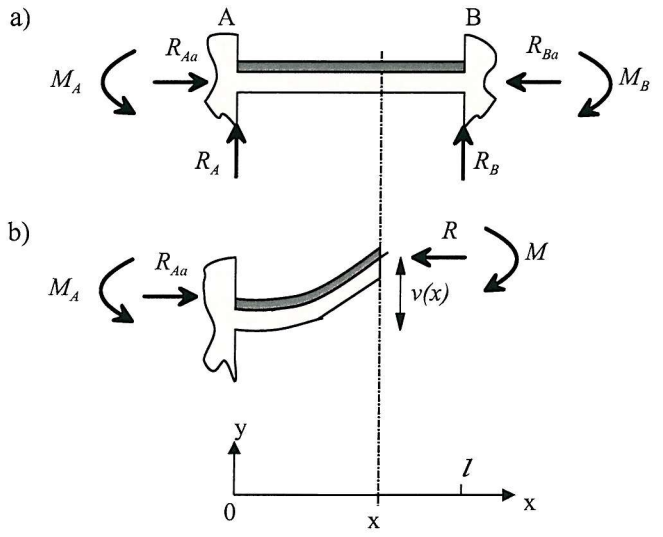

Figure A.1: a) Reaction forces and reaction couples at the supports of the beam, b) free body diagram.

From the free body diagram (figure A.1b), the equilibrium of moments is obtained

$$M = M_A + Rv(x) \tag{A.1}$$

Note that the lateral reaction forces R_A and R_B have been omitted in equation A.1, because in previous calculations and simulations it was shown that they are zero (see chapter 4.2.2).

Analogously to chapter 4.2.2, we get the differential equation of the deflection curve (the temperature distribution, chapter 4.2.1, equations 4.6, 4.7, is substituted)

$$\frac{d^2v}{dx^2} - \frac{R}{EI}v(x) = \frac{M_A}{EI} + \frac{BC}{l}x^2 - BCx \tag{A.2}$$

Equation A.2 is an inhomogeneous second order linear differential equation with constant coefficients. It can be solved by solving the homogeneous differential equation and superposing this solution with a particular solution of the inhomogeneous differential equation, which can be found using a trial function [142]. The homogeneous differential equation is

$$\frac{d^2v}{dx^2} - \frac{R}{EI}v(x) = 0 \tag{A.3}$$

Its general solution is given by

$$v_h(x) = C_1 e^{\sqrt{\frac{R}{EI}}x} + C_2 e^{-\sqrt{\frac{R}{EI}}x} \tag{A.4}$$

where C_1 and C_2 are constants, which have to be determined using the boundary conditions. To find a particular solution $v_p(x)$ for the inhomogeneous differential equation, we use a trial function, which is of the same form as the term on the right of the differential equation.

$$v_p(x) = A_2x^2 + A_1x + A_0 \tag{A.5}$$

where A_2, A_1 and A_0 are constants. By substituting the trial function A.5 into the differential equation A.2, the constants can be determined and the particular solution becomes

$$v_p(x) = \frac{BCEI}{lR}x^2 - \frac{BCEI}{R}x + \frac{M_A}{R} - \frac{2BC(EI)^2}{lR^2} \tag{A.6}$$

Superposing the solution of the homogeneous differential equation $v_h(x)$ and the particular solution of the inhomogeneous equation $v_p(x)$, we get the general solution of the differential equation

$$v(x) = C_1 e^{\sqrt{\frac{R}{EI}}x} + C_2 e^{-\sqrt{\frac{R}{EI}}x} + \frac{BCEI}{lR}x^2 - \frac{BCEI}{R}x + \frac{M_A}{R} - \frac{2BC(EI)^2}{lR^2} \quad \text{(A.7)}$$

The first derivative of the general solution is

$$\frac{dv}{dx} = C_1\sqrt{\frac{R}{EI}}e^{\sqrt{\frac{R}{EI}}x} - C_2\sqrt{\frac{R}{EI}}e^{-\sqrt{\frac{R}{EI}}x} + \frac{2BCEI}{lR}x - \frac{BCEI}{R} \quad \text{(A.8)}$$

The unknowns, C_1, C_2, M_A and R, have to be determined from the boundary conditions

$$v(x=0) = 0 \quad \text{(A.9)}$$

$$v(x=l) = 0 \quad \text{(A.10)}$$

$$\frac{dv}{dx}(x=0) = 0 \quad \text{(A.11)}$$

$$\frac{dv}{dx}(x=l) = 0 \quad \text{(A.12)}$$

$$\frac{dv}{dx}\left(x=\frac{l}{2}\right) = 0 \quad \text{(A.13)}$$

These boundary conditions give a system of five nonlinear equations with four unknowns, C_1, C_2, M_A and R. Even though there are five equations for four unknowns, the system is indeterminate. Three of the four unknowns, C_1, C_2, M_A, can be expressed in terms of the fourth unknown, R. From equation A.13, we get

$$C_1 = C_2\, e^{-\sqrt{\frac{R}{EI}}l} \quad \text{(A.14)}$$

Using equation A.14 in equation A.12 gives

$$C_2 = -\frac{BCEI}{R\sqrt{\frac{R}{EI}}\left(1 - e^{-\sqrt{\frac{R}{EI}}l}\right)} \quad \text{(A.15)}$$

Substituting equation A.15 into equation A.14 gives

$$C_1 = -\frac{BCEI}{R\sqrt{\frac{R}{EI}}\left(1 - e^{-\sqrt{\frac{R}{EI}}l}\right)}\, e^{-\sqrt{\frac{R}{EI}}l} \quad \text{(A.16)}$$

Using equations A.15 and A.16 in equation A.11 gives identity, but no further information is obtained. Substituting equations A.15 and A.16 into equation A.9, we

obtain

$$M_A = \frac{BCEI\left(1+e^{-\sqrt{\frac{R}{EI}}l}\right)}{R\sqrt{\frac{R}{EI}}\left(1-e^{-\sqrt{\frac{R}{EI}}l}\right)} + \frac{2BC(EI)^2}{lR} \tag{A.17}$$

Substituting equations A.15, A.16 and A.17 into equation A.10 gives identity and again no further information is obtained.

With equations A.15, A.16 and A.17, equation A.7 gives a function in x with the axial force R as a parameter.

Using the simulated axial reaction, $R = 7.1 \cdot 10^{-4}$ N, the deflection curve can be plotted based on equation A.7. Figure A.2 shows the deflection curve according to equation A.7 compared with the simulated deflection curve and the analytical curve calculated according to chapter 4.2.2. The centre deflection is 1.1 μm for the analysis taking the axial forces into account, whereas the simple analytical calculation and the structural ANSYS simulation given in chapter 4.3.3 give a centre deflection of 2.1 μm. The reaction couple M_A is $-1.81 \cdot 10^{-9}$ Nm (equation A.17). The couple resulting from the axial reaction force and the centre deflection of the beam Rv_c is $8.2 \cdot 10^{-10}$ Nm. The fact that both values are on the same order of magnitude means that the axial reaction forces cannot be neglected. Therefore it is surprising, that the simple calculation neglecting the axial reactions gives the same result as the ANSYS simulation.

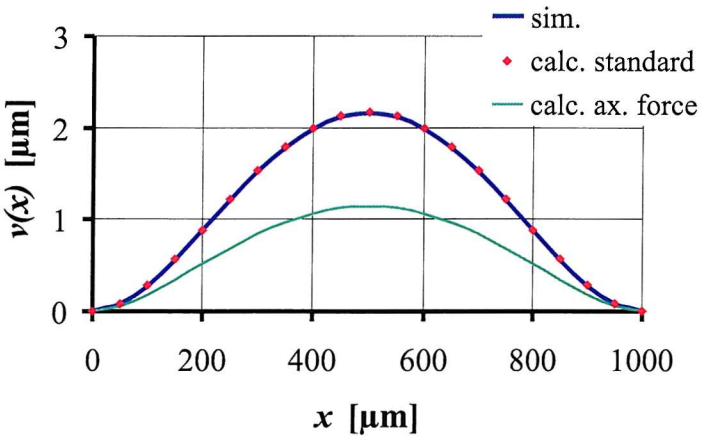

Figure A.2: Calculated deflection curve according to equation A.7 (marked calc. ax. force), compared with the simulated deflection curve (marked sim.) and calculated curve (marked calc. standard, see chapter 4.2.2), ($P = 2\ mW$, $l = 1000\ \mu m$, $w_{Si} = 5\ \mu m$, $w_{Al} = 2.5\ \mu m$, $h = 6\ \mu m$, $T_0 = 300K$).

Varying the parameter R in equation A.7, the following observations have been made.

- With very small reaction forces R ($R \rightarrow 0$), the deflection curve approaches the deflection curve found with the simple analysis neglecting the axial reactions (chapter 4.2.2). The centre deflection becomes 2.1 μm for the above dimensions of the actuator.
- With a positive reaction force R (compressive stress), the centre deflection is smaller than the centre deflection found with the simple analysis neglecting the axial reactions (chapter 4.2.2).
- With a negative reaction force R (tensile stress), the centre deflection is greater than the centre deflection found with the simple analysis neglecting the axial reactions (chapter 4.2.2).

It is surprising that a compressive stress causes a smaller centre deflection than a tensile stress. Therefore, the expansion of the beam caused by the thermal expansion is compared with the elongation of the beam because of the shape of the deflection curve.

In both analytical models and in the ANSYS model, the distance l between the supports of the beam is constant. At the reference temperature T_0, when the beam is straight, the length of the beam is also l. When the beam heats up and assumes the shape of the deflection curve, the beam expands to a length $l + \Delta l_i$. This elongation due to the shape of the deflection curve is given by [142]

$$\Delta l_i = \int_0^l \sqrt{1 + \left(\frac{dv}{dx}\right)^2}\, dx - l \tag{A.18}$$

With the above dimensions (see figure A.2) and the deflection curve for a very small force ($R = 1 \cdot 10^{-8}$ N, $v_c = 2.1$ μm) we get an elongation Δl_i of $1.14 \cdot 10^{-2}$ μm.

Now, we consider a bimorph that is free to move at either end but does not bend. Heating up the bimorph causes an elongation Δl_t of the beam due to thermal expansion. Aluminium has a higher thermal expansion coefficient than silicon, hence aluminium expands more than silicon. Since both material are bonded together in bimorph actuators, the elongation at the bearing surface of the two material has to be equal. Hence, the aluminium experiences a compressive stress and the silicon a tensile stress. Similar to [7] we get

$$\Delta l_t = l \Delta T_{av} \left(\alpha_{Al} - \frac{\alpha_{Al} - \alpha_{Si}}{\frac{1}{E_{Si} w_{Si}} + \frac{1}{E_{Al} w_{Al}}} \right) \tag{A.19}$$

where ΔT_{av} is the average temperature difference of the bimorph actuator with respect to the reference temperature T_0. It can be calculated from the temperature

distribution $\Delta T(x)$ (chapter 4.2.1, equation 4.6) according to [142]

$$\Delta T_{av} = \frac{1}{l} \int_0^l \Delta T(x) dx \tag{A.20}$$

Using equations A.19 and A.20 for a bimorph of the above dimensions (see figure A.2), we get an elongation Δl_t due to thermal expansion of 0.89 μm, which is two orders of magnitude greater than the elongation Δl_i due to the shape of the deflection curve. This confirms that the thermal expansion causes compressive reaction forces at the supports of the clamped-clamped bimorph beam. The question, why a compressive axial stress causes a smaller deflection than a tensile stress remains unanswered.

Appendix B

LMS Process Listings

In this appendix, the LMS process listings are given for the fabrication batches associated with this work. For a detailed description of the fabrication processes refer to chapters 5 and 6. LMS is a library system which allows to create a fabrication batch file from a large variety of standard and nonstandard process steps.

B.1 Process Development Batches

B.1.1 Aluminium Sidewall Deposition (K1789)

The LMS-file for the test-batch into aluminium sidewall deposition is listed. Chapter 5.2 describes the work in detail.

			r1
			g1
1	x	G-S12	Title page 9 wafers: p-type ¡100¿ checks
2	x	G-1P	Lithography Notes k599m
3	x	G-1	Notebook page
		g2	silicon dry etch
4	x	W-C1	RCA clean
5	x	F4-00	Wet oxidation: 1.1 micron, 1100degC:
			l,rO2,x'wO2,30'dO2, x'wO2,uN2
6	x	P-G2	Photolith mask K599M AA, DF Field: nom. 2.2um resist
7	x	P-RHBD	Hardbake for dry etch
8	x	D-O1S	Etch SiO2 Anisot. OPT80+ CHF3+Ar
9	x	P-RS	Resist strip asher 50 min
10	x	W-C2	Fuming Nitric acid clean, 2nd pot only
11	x	D-S5	Trench etch Si. 5 microns SYS90 HBr process
12	x	WH-7E1	Wet etch oxide, 7:1 BHF 25degC. To hydrophobic Si + 20secs.

13	x	W-C1	RCA clean
14	x	F4-0	Wet oxidation 200nm+-10nm, 1000degC, 10'O2,x'wetO2,30'N2.
		g3	Al deposition/patterning
	++++++		
15	x————	MS-AS10	Sputter 1000nm Al/Si 1% in TRIKON SIGMA see engineer, wafer 1
16	x————	MS-0	Sputter 2000nm Al/Si 1% in TRIKON SIGMA see engineer, wafer 2
17	x————	MS-0	Sputter 3000nm Al/Si 1% in TRIKON SIGMA see engineer, wafer 3
18	———x——	ME-AL0	Evaporate pure Aluminium: 1000 nm, angled evaporation, no rotation WAFERS COULD BE Au CONTAMINATED. see engineer, wafer 4
19	————x—	ME-AL0	Evaporate pure Aluminium: 1500 nm, angled evaporation, no rotation WAFERS COULD BE Au CONTAMINATED. see engineer, wafer 5
20	————x	ME-AL0	Evaporate pure Aluminium: 2000 nm, angled evaporation, no rotation WAFERS COULD BE Au CONTAMINATED. see engineer, wafer 6
	++++++		
21	x	D-MAT1	Etch Al . SRS SS1C Cl2+SiCl4+Ar (wafer 1,2,3,4,5,6)
		g4	Repeat aluminum depositions as required, depending on results above (wafer 7,8,9)
	++++++		
22	x————	MS-AS10	Sputter 1000nm Al/Si 1% in TRIKON SIGMA see engineer, 1 wafer
23	—x————	MS-0	Sputter 2000nm Al/Si 1% in TRIKON SIGMA see engineer, 1 wafer
24	——x———	MS-0	Sputter 3000nm Al/Si 1% in TRIKON SIGMA see engineer, 1 wafer
25	———x——	ME-AL0	Evaporate pure Aluminium: 1000 nm, angled evaporation, no rotation WAFERS COULD BE Au CONTAMINATED. see engineer, 1 wafer
26	————x—	ME-AL0	Evaporate pure Aluminium: 1500 nm, angled evaporation, no rotation WAFERS COULD BE Au CONTAMINATED. see engineer, 1 wafer
27	————	xME-AL0	Evaporate pure Aluminium: 2000 nm, angled evaporation, no rotation WAFERS COULD BE Au CONTAMINATED. see engineer, 1 wafer
	++++++		
28	x	D-MAT1	Etch Al SRS SS1C Cl2+SiCl4+Ar (wafer 7,8,9)

B.1.2 Thick Photoresist Lithography (R2033)

The LMS-file for the test-batch on thick photoresist lithography is listed. Chapter 5.4 describes the work in detail. Please note, the batch was carried out using Shipley SPR220-7 photoresist instead of STR 1075 as written in the listing.

		r1	
		g1	
1	x	P-EM	E-BEAM Mask/Reticle Writing
2	x	G-S12	Title Page: 5 wafers, MATERIAL: p-type (100)
3	x	G-1P	Lithography Notes
4	x	G-1	Notebook page
		evaporation	
5	x	ME-AL0	Evaporate pure Aluminium thickness: 1000 nm
6	x	P-G0	Photolith mask K988M AE, LF Field: STR 1075)
7	x	P-RHBW	Hardbake for wet etch
8	x	WM-A2	Wet etch Al, Orthophosphoric acid, 37degC, till clear.
9	x	P-RS	Resist strip
		evapangl1	
10	x	P-G0	Photolith mask K988M A1, DF Field: STR 1075
11	x	P-RHBW	Hardbake for wet etch
12	x	ME-0	Angled evaporation of pure aluminium using wafer jig, monitor reading 600 nm, flat up, see engineer
13	x	WM-0	Wet etch Al, Orthophosphoric acid, 37degC, till clear on horizontal surfaces
14	x	P-RS	Resist strip
		evapangl2	
15	x	P-G0	Photolith mask K988M A2, DF Field: STR 1075
16	x	P-RHBW	Hardbake for wet etch
17	x	ME-0	Angled evaporation of pure aluminium using wafer jig, monitor reading 600 nm, flat down, see engineer
18	x	WM-0	Wet etch Al, Orthophosphoric acid, 37degC, till clear on horizontal surfaces
19	x	P-RS	Resist strip

B.1.3 Chrome/Gold Contact Deposition (R2072)

The LMS-file for the test-batch on chrome/gold contact deposition is listed. Chapter 5.3 describes the work in detail.

		r1	
		g1	

1	x	P-EM	E-BEAM Mask/Reticle Writing
2	x	G-S12	Title Page: 6 wafers: 4 from r1819r and 2 from r1942r
3	x	G-1P	Lithography Notes
4	x	G-1	Notebook page
	+++++		
5	x————	G-3	Special Instructions Wafer 1
6	x————	ME-0	Evaporate Chrome-Gold: Angled Evaporation, Use special jig. chrome: 40 nm, gold 200 nm
7	x————	ME-0	Evaporate Chrome-Gold: Angled Evaporation, Use special jig. chrome: 40 nm, gold 200 nm, rotate wafer 180 deg
8	x————	G-3	Special Instructions CLEAVE WAFER AND MEASURE Au THICKNESS ON SEM
9	—x———	G-3	* Special Instructions Wafer 2
10	—x———	ME-0	Evaporate Chrome-Gold: Angled Evaporation, Use special jig. chrome: 40 nm, gold 300 nm
11	—x———	ME-0	Evaporate Chrome-Gold: Angled Evaporation, Use special jig. chrome: 40 nm, gold 300 nm, rotate wafer 180 deg
12	—x———	G-3	Special Instructions CLEAVE WAFER AND MEASURE Au THICKNESS ON SEM
13	——x——	G-3	Special Instructions Wafer 3
14	——x——	ME-0	Evaporate Chrome-Gold: Angled Evaporation, Use special jig. chrome: 40 nm, gold 400 nm
15	——x——	ME-0	Evaporate Chrome-Gold: Angled Evaporation, Use special jig. chrome: 40 nm, gold 400 nm, rotate wafer 180 deg
16	——x——	G-3	Special Instructions CLEAVE WAFER AND MEASURE Au THICKNESS ON SEM
17	———x—	G-3	Special Instructions Wafer 4
18	———x—	ME-0	Evaporate Chrome-Gold: Angled Evaporation, Use special jig. chrome: 40 nm, gold 500 nm
19	———x—	ME-0	Evaporate Chrome-Gold: Angled Evaporation, Use special jig. chrome: 40 nm, gold 500 nm,rotate wafer 180 deg
20	———x—	G-3	Special Instructions CLEAVE WAFER AND MEASURE Au THICKNESS ON SEM
21	————	x G-3	Special Instructions Wafer 5 and 6
22	————	x W-C1	RCA clean
23	————x	F4-W0010	Wet oxidation 200nm+-10nm, 1000degC, 10'O2,x'wetO2,30'N2.
24	————x	ME-0	Evaporate Chrome-Gold: Angled Evaporation, Use special jig. chrome: 40 nm, gold 300 nm
25	————x	ME-0	Evaporate Chrome-Gold: Angled Evaporation, Use special jig. chrome: 40 nm, gold 300 nm, Rotate wafer 180 deg
26	————x	P-G0X	Photolith mask K988M AE, Light Field: Sprt220 (for wafers with GOLD)

27	———x	P-RHBX	Hardbake for wet etch (for wafers with GOLD)
28	———x	WM-0X	Wet etch gold, (Wafers with GOLD)
29	———x	WM-0X	Wet etch Chrome, (Wafers with GOLD)
30	———x	P-RSX	Resist strip (for wafers with GOLD)
31	———x	G-3	Special Instructions CLEAVE WAFER AND MEASURE Au THICKNESS ON SEM

B.1.4 Through Wafer Etching Using SF_6 (D2166)

The LMS-file for the test-batch on through wafer etching using the SF_6 process is listed. The process is needed for releasing the actuator beams by silicon dry-etching Chapter 5.5 describes the work in detail.

		r1	
		g1	
1	x	P-EM	E-BEAM Mask/Reticle Writing
2	x	G-S12	Title Page: 12 wafers, MATERIAL: p-type checks
3	x	G-1P	Lithography Notes
4	x	G-1	Notebook page
		sf6etch	
	++		
5	—x	G-3	Special Instructions: wafer1 to 6
6	—x	W-C2	Fuming Nitric acid clean, 2nd pot only
7	—x	P-G2	Photolith mask KA25M, BE Dark Field: nom. 2.2um resist
8	—x	P-RHBD	Hardbake for dry etch
9	—x	D-S2S	Deep etch Si Partially anisot. on fronts OPT80+ SF6 1 um
10	—x	P-RS	Resist strip
11	—x	ME-AL10D	Evaporate pure Al 1000nm +- 100nm WITHOUT dip etch, fronts
12	—x	P-G0X	Photlith mask KA25M BE, Dark Field: nom: 2.2 um resist for Au contam. wafers, fronts
13	—x	P-RHBX	Hardbake (for wafers with GOLD)
14	—x	WM-0X	Wet etch Al, Othophosphoric acid, 37 degC, till clear, for Au contam. wafers
15	—x	P-RSX	Resist strip (for wafers with GOLD)
16	—x	D-0X	Dry etch: Deep etch Si. Partially anisotrop Au contam PT RIE80 SF6, 450 um
17	—x	G-3	Special Instructions: Cleave wafer and view in the SEM
18	x—	G-3	Special Instructions: wafer 7 to 12
19	x—	W-C1	RCA clean
20	x—	F4-W1000	Wet oxidation: 1.0micron, 1100degC:

			l,rO2,x'wO2,30'dO2, x'wO2,uN2
21	x—	P-RF	Frontspin resist S1818
22	x—	P-RHBW	Hardbake for wet etch
23	x—	WH-7E1	Wet etch oxide, 7:1 BHF 25degC. To hydrophobic Si + 20secs. (on backs)
24	x—	P-RS	Resist strip
25	x—	ME-AL10B	Evaporate pure Al 1000nm onto BACKS.no dip etch
26	x—	P-G0X	Photlith mask KA25M BE, Dark Field: nom: 2.2 um resist for Au contam. wafers, backs
27	x—	P-RHBX	Hardbake (for wafers with GOLD)
28	x—	WM-0X	Wet etch Al, Othophosphoric acid, 37 degC, till clear (backs), for Au contam. wafers
29	x—	P-RSX	Resist strip (for wafers with GOLD)
30	x—	D-0X	Dry etch: Deep etch Si. Partially anisotrop Au contam PT RIE80 SF6, from backs, to oxide layer
31	x—	G-3	Special Instructions: Cleave wafer and view in the SEM

B.2 Device Fabrication Batches

B.2.1 Clamped-Clamped Beam Actuator(K1859)

The LMS-file for the fabrication batch of the clamped-clamped beam actuator is listed. Chapter 6.2.1 describes the fabrication batch in detail.

		r1	
		g1	
1	x	G-S6	Title Page: 6 wafers, MATERIAL: SOI STHM007, 6 um Si, 2 um SiO2, 525 um handle
2	x	G-1P	Lithography Notes
3	x	G-1	Notebook page
		g2	double sided alignment
4	x	W-C2	Fuming Nitric acid clean, 2nd pot only
5	x	P-GF	Photolith mask K927M, layer S2, Dark Field on BACKS (fronts protected), 1.1um,
6	x	P-RHBD	Hardbake for dry etch, 30 min, 115 deg
7	x	D-S7	Etch Si: Alignment marks backs. For OPTICAL resist OPT80+ SF6, 5 um deep
8	x	P-RS	Resist strip
9	x	W-C2	Fuming Nitric acid clean, 2nd pot only
10	x	P-GDB	Photolith mask K927M,layer S1, Dark Field on FRONTS, DoubleSided Alignment 1.1 um, (backs protected)
11	x	G-2	See Engineer: Inspect

12 x	P-RHBD	Hardbake for dry etch, 30 min, 115 deg
13 x	D-S7	Etch Si: Alignment marks Fronts. For OPTICAL resist OPT80+ SF6, 1 um deep
14 x	P-RS	Resist strip
	g3	KOH back etch
15 x	W-C1	RCA clean
16 x	F4-W0060	Wet oxidation: 600nm, 1000degC: l,rO2,x'wO2,uN2
17 x	LN-160	Deposit Si3N4 160nm+-20nm @ 740degC DCS:NH4 1:4, 2.3nm/m.
18 x	P-GB	Photolith mask K927M layer BE, Dark Field on BACKS (fronts protected) 1.1um
19 x	P-RG	Spin resist on edges
20 x	G-2	See Engineer: Inspect
21 x	P-RHBD	Hardbake for dry etch, 30 min, 115 deg
22 x	D-NO1S	Etch Si3N4 or Si3N4+PadSiO2. Anisot. OPTICAL resist OPT80+ CHF3+Ar
23 x	P-RS	Resist strip
24 x	WH-2D1	Dip etch, 20:1 BHF 25degC. Until just hydrophobic
25 x	WS-3	Etch silicon in KOH, 500 um deep
26 x	WN-1	Strip/Wet etch Si3N4, Orthophosphoric acid 160degC
27 x	WH-7C1	Strip all SiO2 from wafer: 7:1 BHF 25degC
	h1	silicon trench etch
28 x	W-C1	RCA clean
29 x	LO-0	Blank sheet for LPCVD LTO. 1.3 microns
30 x	P-GF	Photolith mask K927M layer TE, Dark Field on FRONTS (backs protected), 1.1um
31 x	G-2	See Engineer: Inspect
32 x	P-RHBD	Hardbake for dry etch, 30 min, 115 deg
33 x	D-O1S	Etch SiO2 . Anisot. OPT80+ CHF3+Ar
34 x	P-RS	Resist strip
35 x	W-C2	Fuming Nitric acid clean, 2nd pot only
36 x	D-S5	Trench etch Si. Anisot. 5.5 microns, SYS90, HBr process, etch to buried oxide layer
37 x	WH-7C1	Strip all SiO2 from wafer: 7:1 BHF 25degC
	h3	oxidation
38 x	W-C1	RCA clean
39 x	F4-0	*Furnace 4: wet oxidation, 200 nm, 950 degC, 5degC ramp up/down
40 x	P-GF	Photolith mask K927M, layer OE, Dark Field on FRONTS (backs protected) 1.1 um resist
41 x	G-2	See Engineer: Inspect
42 x	P-RHBW	Hardbake for wet etch
43 x	WH-2E1	Wet etch oxide, 20:1 BHF 25degC. To hydrophobic

		Si + 40secs., open contact pads
44 x	P-RS	Resist strip
+-+		
45 x —	ME-AL0	Evaporate FRONTS pure Aluminium: 2000 nm, monitor reading 600 nm, angled evaporation, no rotation, see engineer, see special instructions
46 x —	P-GF	Photolith mask K927M, layer AE, Light Field on FRONTS (backs protected), 1.1 um
47 x —	G-2	See Engineer: Inspect
48 x —	P-RHBW	Hardbake for wet etch
49 x —	WM-A2	Wet etch Al, Orthophosphoric acid, 37degC, till clear on top, stop and rinse immediately
50 x —	P-RS	Resist strip
51 x —	W-C3	Fuming Nitric Acid clean, metallised wafers
52 x —	F9-H45	Alloy/ Anneal: 30mins H2/N2 450degC 5'N2,30'H2/N2,5'N2.
	h7	bimorph release wafer (1 and 2)
53 x —	P-RF	Frontspin resist 2.2 um
54 x —	P-RHBD	Hardbake for dry etch
55 x —	D-S2S	Deep etch Si. Partially anisot. For OPTICAL resist OPT80+ SF6, from back
56 x —	D-O1S	Etch SiO2 Anisot. For OPTICAL resist OPT80+ CHF3+Ar
	h8	sawing (wafer 1 and 2)
57 x —	G-3	saw chips
58 x —	G-3	remove resist in Aceton on a single chip basis
	h2	Al deposition/patterning (wafers 3,4,5,6)
59 — x	ME-AL0	Evaporate FRONTS pure Aluminium: 2000 nm, monitor reading 600 nm, angled evaporation, no rotation, see engineer, see special instructions
60 — x	P-GF	Photolith mask K927M, layer AE, Light Field on FRONTS (backs protected), 1.1 um
61 — x	G-2	See Engineer: Inspect
62 — x	P-RHBW	Hardbake for wet etch
63 — x	WM-A2	Wet etch Al, Orthophosphoric acid, 37degC, till clear on top, stop and rinse immediately
64 — x	P-RS	Resist strip
65 — x	W-C3	Fuming Nitric Acid clean, metallised wafers
66 — x	F9-H45	Alloy/ Anneal: 30mins H2/N2 450degC 5'N2,30'H2/N2,5'N2.
	h4	bimorph release (wafers 3,4,5,6)
67 — x	P-RF	Frontspin resist 2.2 um
68 — x	P-RHBD	Hardbake for dry etch
69 — x	D-S2S	Deep etch Si. Partially anisot. For OPTICAL resist OPT80+ SF6, from back
70 — x	D-O1S	Etch SiO2 Anisot. For OPTICAL resist OPT80+ CHF3+Ar

		h5	sawing (wafers 3,4,5,6)
71	— x	G-3	saw chips
72	— x	G-3	remove resist in Aceton on a single chip basis

B.2.2 Meander Actuators (K2136)

The LMS-file for the fabrication batch of the meander actuators is listed. Chapter 6.2.2 describes the fabrication batch in detail.

		r1	
		g1	
1	x	P-EM	E-BEAM Mask/Reticle Writing
2	x	G-S6	Title Page: 6 wafers, MATERIAL: SOI STHM007, 30 um Si, 2 um SiO2, polished on both sides + 6 check wafers 100
3	x	G-1P	Lithography Notes
4	x	G-1	Notebook page
		g2	trench etch
5	x	W-C2	Fuming Nitric acid clean, 2nd pot only, + 6 check wafers
6	x	P-GF	Photolith mask KA25M, layer TE , Dark Field on fronts, 1.1um, + 6 check wafers
7	x	G-2	See Engineer: Inspect + 6 check wafers
8	x	P-RHBD	Hardbake for dry etch, 30 min, 115 deg + 6 check wafers
9	x	G-3	Dry etch: DRIE to buried oxide External RAL + 6 check wafers
10	x	P-RS	Resist strip + 6 check wafers
		h2	backside alignment
11	x	P-GDB	Photolith mask KA25M, S2 Dark Field on BACKS: DoubleSided Alignment For DOUBLE-POLISHED wafers only 1.1 um resist
12	x	P-RHBD	Hardbake for dry etch
13	x	D-S2S	Deep etch Si Partially anisot. For ANY resist OPT80+ SF6, 5 um, on Backs
14	x	P-RS	Resist strip
		h9	oxidation and contact window etch
15	x	W-C1	RCA clean
16	x	F4-W0060	Wet oxidation: 300nm, 1000degC: l,rO2,x'wO2,uN2
17	x	P-0	Photolith mask KA25M, layer OE, DF, on Fronts, SPRT 220-7
18	x	G-2	See Engineer: Inspect
19	x	P-RHBD	Hardbake for dry etch
20	x	D-O1F	Etch SiO2 Anisot. For D/F EBMF/OPTICAL

		resist OPT80+ CHF3+Ar 300nm
21 x	P-RS	Resist strip
	h1	planar gold evaporation
22 x	WH-2D5	Dip etch, 20:1 BHF 25degC. For 10secs ONLY
23 x	ME-CRAU0	Evaporate Chrome-Gold: gold thickness 400 nm
24 x	P-0X	Photolith mask K25M, layer GE,LF, on Fronts, SPRT 220-7 (for wafers with GOLD)
25 x	G-2	See Engineer: Inspect
26 x	P-RHBX	Hardbake (for wafers with GOLD)
27 x	WM-0	Wet etch gold
28 x	WM-0	Wet etch chrome
29 x	P-RSX	Resist strip (for wafers with GOLD)
	h611	angled evaporation 1
30 x	P-0X	Photolith mask KA25M, layer A1, LF, SPRT 220-7, 30 um (for wafers with GOLD)
31 x	G-2	See Engineer: Inspect
32 x	P-RHBX	Hardbake (for wafers with GOLD)
33 x	ME-AL0	Evaporate FRONTS pure Aluminium: monitor reading 450 nm, angled evaporation in special jig, flat position in jig 0 deg
34 x	WM-0X	Wet etch Al, Orthophosphoric acid, 37 degC, until clear on horizontal surfaces, stop and rinse immediately (for wafers with GOLD)
35 x	P-RSX	Resist strip (for wafers with GOLD)
		h612 angled evaporation 2
36 x	P-0X	Photolith mask KA25M, layer A2, LF, SPRT 220-7, 30 um (for wafers with GOLD)
37 x	G-2	See Engineer: Inspect
38 x	P-RHBX	Hardbake (for wafers with GOLD)
39 x	ME-AL0	Evaporate FRONTS pure Aluminium: monitor reading 450 nm, angled evaporation in special jig, flat position in jig 180 deg
40 x	WM-0X	Wet etch Al, Orthophosphoric acid, 37 degC, until clear on horizontal surfaces, stop and rinse immediately (for wafers with GOLD)
41 x	P-RSX	Resist strip (for wafers with GOLD)
	h613	angled evaporation 3
42 x	P-0X	Photolith mask KA25M, layer A3, LF, SPRT 220-7, 30 um (for wafers with GOLD)
43 x	G-2	See Engineer: Inspect
44 x	P-RHBX	Hardbake (for wafers with GOLD)
45 x	ME-AL0	Evaporate FRONTS pure Aluminium: monitor reading 450 nm, angled evaporation in special jig, flat position in jig 90 deg
46 x	WM-0X	Wet etch Al, Orthophosphoric acid, 37 degC, until clear on horizontal surfaces, stop and rinse

		immediately (for wafers with GOLD)
47 x	P-RSX	Resist strip (for wafers with GOLD)
	h614	angled evaporation 4
48 x	P-0X	Photolith mask KA25M, layer A4, LF, SPRT 220-7, 30 um (for wafers with GOLD)
49 x	G-2	See Engineer: Inspect
50 x	P-RHBX	Hardbake (for wafers with GOLD)
51 x	ME-AL0	Evaporate FRONTS pure Aluminium: monitor reading 450 nm, angled evaporation in special jig, flat position in jig 270 deg
52 x	WM-0X	Wet etch Al, Orthophosphoric acid, 37 degC, until clear on horizontal surfaces, stop and rinse immediately (for wafers with GOLD)
53 x	P-RSX	Resist strip (for wafers with GOLD)
54 x	G-2	See Engineer for instructions
55 x	F7-0	Alloy/Anneal according to requirements NOTE: Wafers have Cr/Au on them
	h7	bimorph release
56 x	ME-AL10B	Evaporate pure Al 1000nm onto BACKS. WAFERS COULD BE Au CONTAMINATED
57 x	P-G0X	Photolith mask KA25M RE, Dark Field: SPRT 518, 1,1 um, on backs (for wafers with GOLD)
58 x	P-RGX	Frontpin resist SPRT 220-7 (for wafers with GOLD)
59 x	P-RHBX	Hardbake (for wafers with GOLD)
60 x	WM-0X	Wet etch aluminium, orthophosphoric acid, 37 degC, until clear on back, wafers with gold
61 x	P-RSX	Resist strip (for wafers with GOLD)
62 x	P-0X	Glue backing wafer, using SPR220-7
63 x	P-RHBX	Hardbake on programmable hotplate, ramp to 105 degC at 60 degC/hr, soak 120 min
64 x	D-S2X	+ Deep etch Si. Partially anisot. Au CONTAM PT RIE80 SF6 from BACK (photoresist will be removed during etch)
65 x	P-RSX	separate wafers in acetone and resist strip in FNA
66 x	WM-0X	Wet etch aluminium, orthophosphoric acid, 37 degC, strip all Al from back, wafers with gold
67 x	D-O1X	Etch SiO2 Anisot. Au CONTAM PT RIE80 CHF3+Ar from BACK
	h8	sawing
68 x	P-0X	Glue backing wafer, using SPR220-7
69 x	P-RGX	Backspin resist SPRT 220-7 (for wafers with GOLD)
70 x	P-RHBX	Hardbake in oven 50 degC
71 x	G-3	saw chips
72 x	G-3	remove resist on a single chip basis

B.2.3 Micro-Relays (K2135)

The LMS-file for the fabrication batch of the micro-relays is listed. Chapter 6.2.3 describes the fabrication batch in detail.

		r1	
		g1	
1	x	P-EM	E-BEAM Mask/Reticle Writing
2	x	G-S6	Title Page: 6 wafers, MATERIAL: SOI STHM007, 30 um Si, 2 um SiO2, polished on both sides + 6 check wafers 100
3	x	G-1P	Lithography Notes
4	x	G-1	Notebook page
		g22	trench etch
5	x	W-C2	Fuming Nitric acid clean, 2nd pot only, +6 check wafers
6	x	P-GF	Photolith mask KA26M, TE , Dark Field on fronts, 1.1um, + 6 check wafers
7	x	G-2	See Engineer: Inspect +6 check wafers
8	x	P-RHBD	Hardbake for dry etch, 30 min, 115 deg, +6 check wafers
9	x	G-3	Dry etch: DRIE to buried oxide External RAL + 6 check wafers
10	x	P-RS	Resist strip + 6 check wafers
		h23	backside alignment
11	x	P-GDB	Photolith mask KA26M, S2 Dark Field on BACKS: DoubleSided Alignment For DOUBLE-POLISHED wafers only 1.1 um resist
12	x	P-RHBD	Hardbake for dry etch
13	x	D-S2S	Deep etch Si Partially anisot. OPT80+ SF6, 5 um, on Backs
14	x	P-RS	Resist strip
		h99	oxidation and contact window etch
15	x	W-C1	RCA clean
16	x	F4-W0060	Wet oxidation: 300nm, 1000degC: l,rO2,x'wO2,uN2
17	x	P-0	Photolith mask KA26M, layer OE, DF, on Fronts, SPRT 220-7
18	x	G-2	See Engineer: Inspect
19	x	P-RHBW	Hardbake for wet etch
20	x	D-O1F	Etch SiO2 Anisot. For D/F EBMF/OPTICAL resist OPT80+ CHF3+Ar
21	x	P-RS	Resist strip
		h	gold evaporation
22	x	WH-2D5	Dip etch, 20:1 BHF 25degC. For 10secs ONLY
23	x	ME-CRAU0	Evaporate Chrome-Gold: angled evaporation in special jig, Cr 40 nm, Au 300 nm, flat position 0 deg FRONTS

24 x	ME-CRAU0	Evaporate Chrome-Gold: angled evaporation in special jig, Cr 40 nm, Au 300 nm, flat position 180 deg FRONTS
25 x	P-0X	Photolith mask KA26M, layer GE, LF, SPRT 220-7, 30 um (for wafers with GOLD)
26 x	G-2	See Engineer: Inspect
27 x	P-RHBX	Hardbake (for wafers with GOLD)
28 x	WM-0	Wet etch gold
29 x	WM-0	Wet etch chrome
30 x	WM-0	Wet etch gold
31 x	WM-0	Wet etch chrome
32 x	P-RSX	Resist strip (for wafers with GOLD)
	h621	angled evaporation 1
33 x	P-0X	Photolith mask KA26M, layer A1, LF, SPRT 220-7, 30 um (for wafers with GOLD)
34 x	G-2	See Engineer: Inspect
35 x	P-RHBX	Hardbake (for wafers with GOLD)
36 x	ME-AL0	Evaporate FRONTS pure Aluminium: monitor reading 450 nm, angled evaporation in special jig, flat position in jig 0 deg
37 x	WM-0X	Wet etch Al, Orthophosphoric acid, 37 degC, until clear on horizontal surfaces, stop and rinse immediately (for wafers with GOLD)
38 x	P-RSX	Resist strip (for wafers with GOLD)
	h612	angled evaporation 2
		um (for wafers with GOLD)
40 x	G-2	See Engineer: Inspect
41 x	P-RHBX	Hardbake (for wafers with GOLD)
42 x	ME-AL0	Evaporate FRONTS pure Aluminium: monitor reading 450 nm, angled evaporation in special jig, flat position in jig 180 deg
43 x	WM-0X	Wet etch Al, Orthophosphoric acid, 37 degC, until clear on horizontal surfaces, stop and rinse immediately (for wafers with GOLD)
44 x	P-RSX	Resist strip (for wafers with GOLD)
45 x	G-2	See Engineer for instructions
46 x	F7-0	Alloy/Anneal according to requirements
	h7	bimorph release
47 x	ME-AL10B	Evaporate pure Al 1000nm onto BACKS. WAFERS COULD BE Au CONTAMINATED
48 x	P-G0X	Photolith mask KA26M RE, Dark Field: SPRT 518, 1,1 um, on backs (for wafers with GOLD)
49 x	P-RGX	Frontpin resist SPRT 220-7 (for wafers with GOLD)
50 x	P-RHBX	Hardbake (for wafers with GOLD)
51 x	WM-0X	Wet etch aluminium, orthophosphoric acid, 37 degC, until clear on back, wafers with gold

52 x	D-S2X	Deep etch Si Partially anisot. Au CONTAM PT RIE80 SF6 from BACK (photoresist will be removed during etch)
53 x	WM-0X	Wet etch aluminium, orthophosphoric acid, 37 degC, strip all Al from back, wafers with gold
54 x	D-O1X	Etch SiO2 Anisot. Au CONTAM PT RIE80 CHF3+Ar from BACK
55 x	WM-0X	Wet etch aluminium, orthophosphoric acid, 37 degC, remove Al residues from sidewall evaporation, for gold wafers
56 x	WM-0X	Wet etch chrome/gold
	h8	sawing
57 x	G-3	saw chips
58 x	G-3	remove resist on a single chip basis

Appendix C

Mask Layout Details

In this appendix, details of the mask layout for the three device fabrication batches are given. The mask layouts were created in Tanner EDA L-Edit version 8.20 [143]. The different designs are saved as different cells. A cell can include another cell as an instance. The highest level cell, called 'topcell', shows the distribution of the different design across the wafer. It includes the cells for all different designs. The following sections describe the mask design for the clamped-clamped beam actuator, meander actuators and micro-relays. The description is easy to follow on a computer with the corresponding L-edit file, opening the cells according to the description. Only a few images of the mask layout are given since capturing significant information on a screen shot is difficult. It is most efficient to view the design on a computer screen, where zooming in and out is easily possible.

C.1 Clamped-Clamped Beam Actuator, Mask K927m

The file 'k927m.tdb' is the L-edit layout file for the clamped-clamped beam actuator. It can be found in $\backslash\backslash hisalpha\backslash users\backslash cad\backslash masks\backslash k927m$. It contains the following layers:

- S1: Alignment, dark field, front, etching of alignment marks on the front of the wafer.
- S2: Alignment, dark field, back, etching of alignment marks on the back of the wafer.
- BE: Backside etch, dark field, back, KOH etching for device release.
- TE: Trench etch, dark field, front, trench etch to define beam geometry.
- OE: Oxide etch, dark field, front, etch contact windows for pads.

- AE: Aluminium etch, light field, front, etch aluminium.

Figure C.1 shows sketches of the layouts of clamped-clamped beam actuators with and without a central platform. The characteristic dimensions are marked. The central platform is a square of length $l_c = 170$ μm. The contact pads are squares of length $l_p = 500$ μm. The other dimensions vary with the different designs.

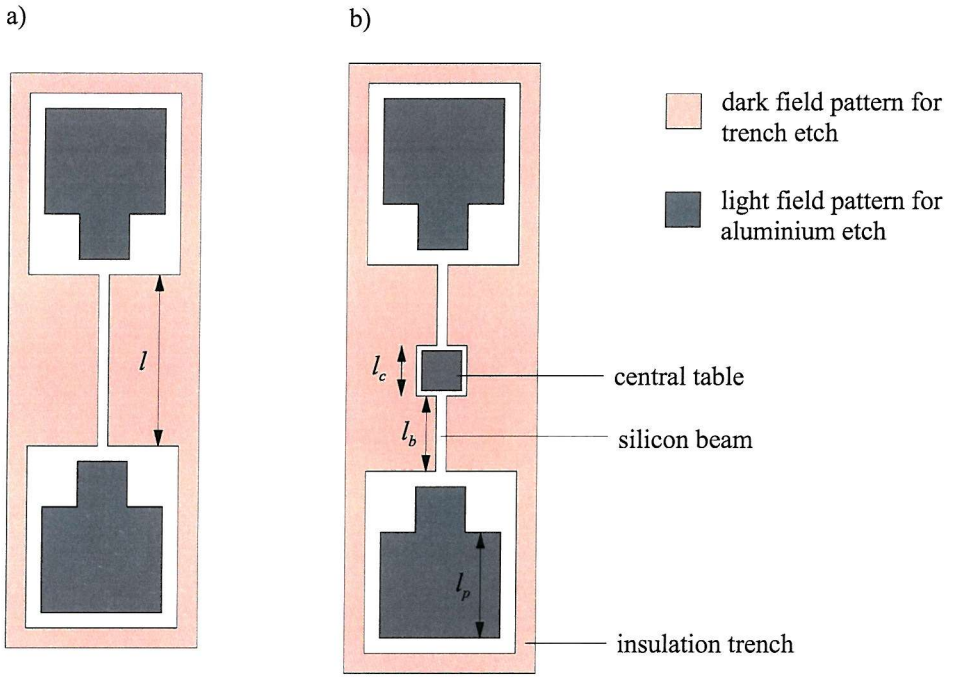

Figure C.1: Layout of double-clamped actuators, a) without central platform, b) with central platform, trench etch pattern and aluminium etch pattern shown.

Table C.1 gives the cell names and characteristic dimensions of the different designs. The cells are all instances in the topcell.

C.2 Meander Actuators (Mask KA25m) and Micro-Relays (Mask KA26m).

The file 'ka25_26m.tdb' is the L-edit layout file for the meander actuators (and the micro-relays. It can be found in $\backslash\backslash hisalpha\backslash users\backslash cad\backslash masks\backslash ka25m\_26m$. KA25m is the mask set for the meander actuators, KA26m is the mask set for the micro relays. The following layers are included in the design file:

- S2: Alignment, dark field, back, etching of alignment marks on the back of the wafer.

Cell name	central platform	l [μm]	l_b [μm]	w_{Si} [μm]
mainl200tSi2	yes	-	200	2
mainl200tSi3	yes	-	200	3
mainl200tSi5	yes	-	200	5
mainl300tSi2	yes	-	300	2
mainl300tSi3	yes	-	300	3
mainl300tSi5	yes	-	300	5
mainl500tSi2	yes	-	500	2
mainl500tSi3	yes	-	500	3
mainl500tSi5	yes	-	500	5
mainl700tSi2	yes	-	700	2
mainl700tSi3	yes	-	700	3
mainl700tSi5	yes	-	700	5
whole_l200tSi2	no	400	-	2
whole_l200tSi3	no	400	-	3
whole_l200tSi5	no	400	-	5
whole_l300tSi2	no	600	-	2
whole_l300tSi3	no	600	-	3
whole_l300tSi5	no	600	-	5
whole_l500tSi2	no	1000	-	2
whole_l500tSi3	no	1000	-	3
whole_l500tSi5	no	1000	-	5
whole_l700tSi2	no	1400	-	2
whole_l700tSi3	no	1400	-	3
whole_l700tSi5	no	1400	-	5

Table C.1: Cell names for clamped-clamped beam actuators and the characteristic device dimensions.

- BE: Backside etch, dark field, back, RIE for device release.
- TE: Trench etch, course patterns, dark field, front, trench etch to define beam geometry.
- TE2: Trench etch, fine patterns, dark field, front, trench etch to define beam geometry (note: the trench etch layer was split in course and fine to reduce time for e-beam writing of the mask).
- OE: Oxide etch, dark field, front, etch contact windows for pads.
- GE: Gold etch, light field, front, etch gold for contact pads.
- A1: Aluminium 1, light field, front, lift-off pattern for aluminium sidewall evaporation 1.
- A2: Aluminium 2, light field, front, lift-off pattern for aluminium sidewall evaporation 2.

- A3: Aluminium 3, light field, front, lift-off pattern for aluminium sidewall evaporation 3.
- A4: Aluminium 4, light field, front, lift-off pattern for aluminium sidewall evaporation 4.

C.2.1 Meander Actuators (Mask KA25m)

Figure C.2 depicts a part of a one-dimensional meander type actuator. It shows the characteristic dimensions of the one-dimensional meander actuator. The length of the bimorphs l_b is 1000 μm, the width of the silicon w_{Si} is either 5 μm or 8 μm. The other dimensions are: $l_1 = 300$ μm, $l_2 = 300$ μm, $l_3 = 300$ μm, $l_4 = 200$ μm. The insulation trench is 80 μm wide.

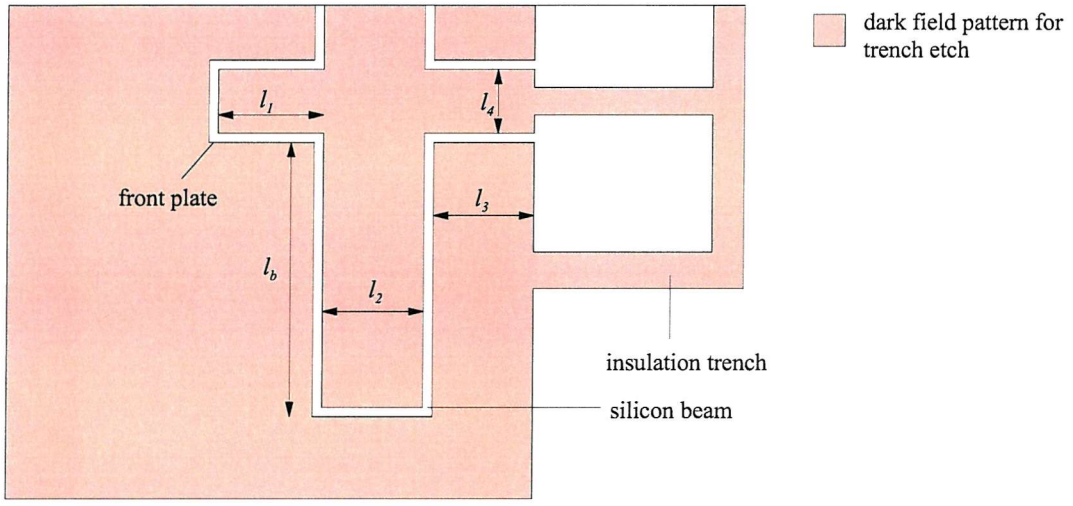

Figure C.2: Layout of a one-dimensional meander type actuator, trench-etch layer shown.

Figure C.3 depicts a part of a two-dimensional meander type actuator. The length of the bimorphs l_b is either 800 or 1000 μm, the width of the silicon is either 5 μm or 8 μm. The other dimensions are: $l_1 = 900$ or 1100 μm , $l_2 = 300$ μm, $l_3 = 300$ μm, $l_4 = 200$ μm, $l_c = 255$ μm. The insulation trench is 80 μm wide.

The topcell for KA25m is called 'topcell_2d'. It includes the following cells:

- 2d_805_main: Two-dimensional meander actuator, $l_b = 800$ μm, $l_1 = 900$ μm, $w_{Si} = 5$ μm.
- 2d_1008_main: Two-dimensional meander actuator, $l_b = 1000$ μm, $l_1 = 1100$ μm, $w_{Si} = 8$ μm.
- 1d_main: Four one-dimensional actuators, two of them with $w_{Si} = 5$ μm and two of them with $w_{Si} = 8$ μm.

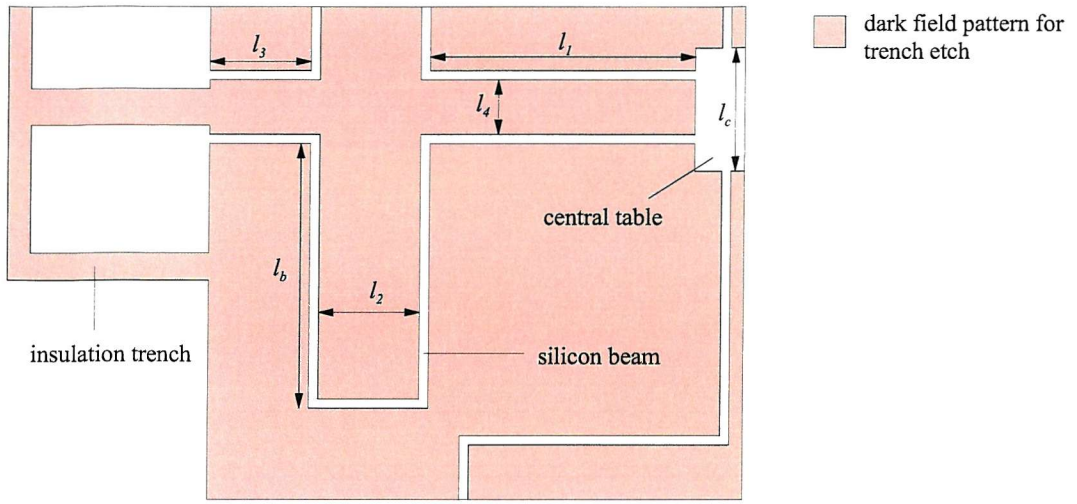

Figure C.3: Layout of a two-dimensional meander type actuator, trench-etch pattern shown.

- ac_main: Actuated Cantilevers, 1000 μm and 1500 μm long, w_{Si} is 5 μm and 8 μm.
- sc_main: Simple test cantilevers, 1000 μm and 1500 μm long, w_{Si} is 5 μm and 8 μm.

C.2.2 Micro Relays (Mask KA26m)

Figure C.4 depicts the layout for a micro-relay. The length of the bimorphs l_b is 1000 μm, the width of the silicon w_{Si} is either 5 μm or 8 μm. The other dimensions are: $l_1 = 300$ μm, $l_2 = 300$ μm, $l_3 = 300$ μm, $l_4 = 200$ μm. The insulation trench is 80 μm wide. The contact gap is either 6 μm, 12 μm or 20 μm wide.

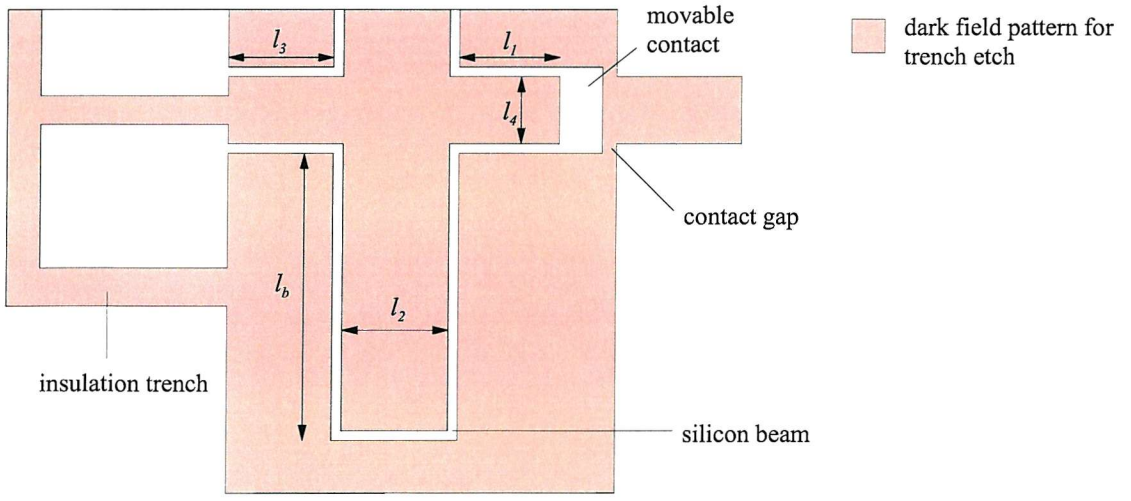

Figure C.4: Layout of a normally-closed micro relay, trench-etch pattern shown.

The topcell for KA25m is called 'topcell_ms'. It includes the following cells:

- ms_1005_main_612: Two normally open micro-relays with a contact gap of 6 μm and 12 μm, two normally closed micro-relays with a contact gap of 6 μm and 12 μm, $w_{Si} = 5$ μm for all four relays.
- ms_1008_main_612: Two normally open micro-relays with a contact gap of 6 μm and 12 μm, two normally closed micro-relays with a contact gap of 6 μm and 12 μm, $w_{Si} = 8$ μm for all four relays.
- ms_1005_main_620: Two normally open micro-relays with a contact gap of 6 μm and 12 μm, two normally closed micro-relays with a contact gap of 6 μm and 20 μm, $w_{Si} = 5$ μm for all four relays.
- ms_1008_main_620: Two normally open micro-relays with a contact gap of 6 μm and 12 μm, two normally closed micro-relays with a contact gap of 6 μm and 20 μm, $w_{Si} = 8$ μm for all four relays.
- ms_ac_main: Actuated Cantilevers, 1000 μm and 1500 μm long, w_{Si} is 5 μm and 8 μm.
- ms_mc_main: Test structures for laterally vibrating cantilevers.

Appendix D

ANSYS Log-Files

In this appendix, the ANSYS log-files are listed for the simulations described in chapter 4 and chapter 7, including simulations on the clamped-clamped beam (D.1), the one-dimensional meander actuator (D.2) and the two-dimensional meander actuator (D.3). For each actuator, the model is defined first, followed by thermal, structural, transient and modal analyses. The ANSYS log-files include a list of ANSYS commands and are read into the ANSYS Multi Physics software.

D.1 Clamped-Clamped Beam

The ANSYS-files for the clamped-clamped beam actuator are listed in this section, starting with the model, which is needed for all other simulations. The simulations are described in chapter 4.3.

D.1.1 Model for the Clamped-Clamped Beam

```
**********************************************
/pnum,volu,1
/prep7
emunit,mks
**********************************************
!dimensions
l=1000e-6
h=6e-6
wSi=5e-6
wAl=2.5e-6
t=0.01
volSi=l*wSi*h
pwr=2e-3
pwrden=pwr/volSi
**********************************************
!material properties
nu=0.3
```

```
ESI=1.3e11
aSi=2.6e-6
kSi=1.49e2
denSi=2.38e3
cSi=702.24
trefSi=300
EAl=6.5e10
aAl=2.5e-5
kAl=2.37e2
denAl=2.7e3
cAl=898.7
trefAl=300
*************************************************
!set material properties
!material 1 = silicon
mp,ex,1,ESi
mp,alpx,1,aSi
mp,kxx,1,kSi
mp,prxy,1,nu
mp,dens,1,denSi
mp,reft,1,trefSi
mp,c,1,cSi
!material 2 = aluminium
mp,ex,2,EAl
mp,alpx,2,aAl
mp,kxx,2,kAl
mp,prxy,2,nu
mp,dens,2,denAl
mp,reft,2,trefAl
mp,c,2,cAl
*************************************************
element type
et,1,70 ! element type
boptn,keep,no
*************************************************
!define geometry
block,0,l,0,wSi,0,h
block,0,l,wSi, wSi+wAl,0,h
*************************************************
!assign materials
vsel,s,volu,,1
vatt,1,,1
allsel
vsel,s,volu,,2
vatt,2,,1
allsel
*************************************************
!determine mesh density
```

```
lsel,s,length,,h
lesize,all,,,1
allsel
lsel,s,length,,wSi
lesize,all,,,1
allsel
lsel,s,length,,wAl
lesize,all,,,1
allsel
lsel,s,length,,l
lesize,all,,,80
allsel
*********************************************
!mesh the model
vmesh,all
allsel
*********************************************
!merge the two materials
nummrg,node,1e-7
nummrg,kp,1e-7
save
```

D.1.2 Temperature Distribution (Clamped-Clamped Beam)

```
*********************************************
!apply thermal boundary conditions
/solu
asel,s,loc,x,0 ! select areas at x=0, right terminal face
da,all,temp,300
allsel
asel,s,loc,x,l ! select areas at x=l, left terminal face
da,all,temp,300
allsel
vsel,s,mat,,1
bfv,all,hgen,pwrden
allsel
*********************************************
!obtain thermal solution
solve
```

D.1.3 Deflection Curve (Clamped-Clamped Beam)

```
*********************************************
!apply structural boundary conditions
/prep7
et,1,45
nsel,s,loc,x,0 ! select all nodes at x=0
d,all,all
```

```
allsel
nsel,s,loc,x,l ! select all nodes at x=l
d,all,all
allsel
**********************************************
!read results of thermal simulation
ldread,temp,,,,,,rth ! read temperature load
**********************************************
!obtain structural solution
/solve
antype,static
pstres,on
solve
finish
**********************************************
!plot deflection shape
/post1
plnsol,u,y,0
```

D.1.4 Thermal Time Constant (Clamped-Clamped Beam)

```
**********************************************
! set up transient solution
/solu
antype,trans,new
solcontrol,on,0
tunif,300 ! initial condition, temperature for all nodes = tref
allsel
asel,s,loc,x,0 ! select areas at x=0, right terminal face
da,all,temp,300
allsel
asel,s,loc,x,l ! select areas at x=l, left terminal face
da,all,temp,300
allsel
save
time,t
allsel
autots,on
DELTIM,0.01*t,0.01*t,0.1*t,1
kbc,1
vsel,s,mat,,1
bfv,all,hgen,pwrden
allsel
outres,all,all
save
**********************************************
! obtain transient solution
solve
```

```
**********************************************
! plot temperature versus time
/post26
nsol,2,43,temp
/yrange,300,340
/xrange,0,1e-2
/gropt,axnsc,1.6
/gropt,ltyp,0
/axlab,x,time[s]
/axlab,y,temperature[K]
/gropt,divx,5
/gropt,divy,4
plvar,2
prvar,2
```

D.1.5 Lateral Resonances (Clamped-Clamped Beam)

Standard Analysis (Lateral Resonances, Clamped-Clamped Beam)

```
**********************************************
! setup modal analysis
antype,modal
modopt,lanb,6
allsel
asel,s,loc,x,0 ! select areas at x=0
da,all,ux,0 ! constraints
da,all,uy,0
da,all,uz,0
allsel
asel,s,loc,x,l ! select areas at x=l
da,all,ux,0 ! constraints
da,all,uy,0
da,all,uz,0
allsel
mxpand,5
**********************************************
! obtain modal solution
solve
**********************************************
! print displacement along x-axis
/post1
set,list
set,1,4
pldisp,0
!anmode,10,0
path,p1,2
ppath,1,,0,0,0
ppath,2,,l,0,0
pdef,disp,u,y
```

```
prpath,disp
```

Analysis Varying the Static Deflection (Lateral Resonances, Clamped-Clamped Beam)

```
**********************************************
!number of points
rep=10
!multiplier power=counter*multiplier*1e-3
mult=0.2
**********************************************
! loop thermal solution
*do,counter,0,rep,1
/prep7
pwr=counter*mult*1e-3
pwrden=pwr/volSi
et,1,70
asel,s,loc,x,0
da,all,temp,300
allsel
asel,s,loc,x,l
da,all,temp,300
allsel
allsel
vsel,s,mat,,1
bfv,all,hgen,pwrden
allsel
/solu
antype,static
outres,nsol
lswrite,counter+1
*enddo
**********************************************
! obtain thermal solution
lssolve,1,counter+1
save
finish
**********************************************
! loop structural and modal solution
*do,counter,0,rep,1
/prep7
et,1,45
nsel,s,loc,x,0 ! select all nodes at x=0
d,all,all
allsel
nsel,s,loc,x,l ! select all nodes at x=l
d,all,all
allsel
```

```
/solu
ldread,temp,counter+1,,,,,rth
bfedele,all,hgen
antype,static
*********************************************
! obtain structural solution
solve
finish
*********************************************
! write output file
/post1
nsort,u,y,1
*get,vc,sort,,max
finish
/solu
antype,modal
pstres,on
modopt,subsp,4
allsel
nsel,s,loc,x,0 ! select all nodes at x=0
d,all,all
allsel
nsel,s,loc,x,l ! select all nodes at x=l
d,all,all
allsel
mxpand,4
outres,all,all
solve
/post1
set,1,1
*get,frmod1,active,,set,freq
nsort,u,y,1
*get,max_uy1,sort,,max
nsort,u,z,1
*get,max_uz1,sort,,max
set,1,2
*get,frmod2,active,,set,freq
nsort,u,y,1
*get,max_uy2,sort,,max
nsort,u,z,1
*get,max_uz2,sort,,max
set,1,3
*get,frmod3,active,,set,freq
nsort,u,y,1
*get,max_uy3,sort,,max
nsort,u,z,1
*get,max_uz3,sort,,max
set,1,4
```

```
*get,frmod4,active,,set,freq
nsort,u,y,1
*get,max_uy4,sort,,max
nsort,u,z,1
*get,max_uz4,sort,,max
pwr_mW=counter*mult
*cfopen,resdata,txt,,append
*vwrite,trefAl,pwr_mW,vc,frmod1,max_uy1,max_uz1,frmod2,max_uy2,max_uz2,
frmod3,max_uy3,max_uz3,frmod4,max_uy4,max_uz4
(f5.1,2x,f4.2,2x,e9.4,,4x,f8.1,1x,e7.2,1x,e7.2,4x,f8.1,1x,e7.2,1x,e7.2,4x,
f8.1,1x,e7.2,1x,e7.2,4x,f8.1,1x,e7.2,1x,e7.2)
*cfclos,resdata,txt
finish
*enddo
```

Analysis Varying the Aluminium Reference Temperature (Lateral Resonances, Clamped-Clamped Beam)

```
**********************************************
!number of points
rep=10
!temperature range, trefAl=300+trange
trange=40
**********************************************
!loop aluminium reference temperature
*do,counter,0,trange,trange/rep
**********************************************
!structural analysis
/prep7
et,1,45
tunif,300
trefAl=300+counter
mp,reft,2,trefAl
nsel,s,loc,x,0 ! select all nodes at x=0
d,all,all
allsel
nsel,s,loc,x,l ! select all nodes at x=l
d,all,all
allsel
/solve
antype,static
pstres,on
**********************************************
!obtain structural solution
solve
finish
**********************************************
!modal analysis
```

```
/solu
antype,modal
pstres,on
modopt,subsp,4
allsel
nsel,s,loc,x,0 ! select all nodes at x=0
d,all,all
allsel
nsel,s,loc,x,l ! select all nodes at x=l
d,all,all
allsel
mxpand,5
solve
*********************************************
!write data to output file
/post1
set,1,1
*get,frmod1,active,,set,freq
nsort,u,y,1
*get,max_uy1,sort,,max
nsort,u,z,1
*get,max_uz1,sort,,max
set,1,2
*get,frmod2,active,,set,freq
nsort,u,y,1
*get,max_uy2,sort,,max
nsort,u,z,1
*get,max_uz2,sort,,max
set,1,3
*get,frmod3,active,,set,freq
nsort,u,y,1
*get,max_uy3,sort,,max
nsort,u,z,1
*get,max_uz3,sort,,max
set,1,4
*get,frmod4,active,,set,freq
nsort,u,y,1
*get,max_uy4,sort,,max
nsort,u,z,1
*get,max_uz4,sort,,max
pwr_mW=0
*cfopen,resdata,txt,,append
*vwrite,trefAl,pwr_mW,frmod1,max_uy1,max_uz1,frmod2,max_uy2,max_uz2,
frmod3,max_uy3,max_uz3,frmod4,max_uy4,max_uz4
(f6.2,2x,f4.2,4x,e12.6,1x,e7.2,1x,e7.2,4x,e12.6,1x,e7.2,1x,
e7.2,4xe12.6,1x,e7.2,1x,e7.2,4xe12.6,1x,e7.2,1x,e7.2)
*cfclos,resdata,txt
finish
```

```
*enddo
```

D.2 One-Dimensional Meander Actuator

The ANSYS-files for the one-dimensional meander actuator are listed in this section, starting with the model, which is needed for all other simulations. The simulations are described in chapter 4.4.

D.2.1 Model for the One-Dimensional Meander Actuator

```
**********************************************
!model
/pnum,volu,1
/prep7
emunit,mks
**********************************************
!dimensions
l=1000e-6
h=30e-6
wSi=8e-6
b=300e-6
l1=100e-6
wAl=1.5e-6
wcr=8e-6
w1=8e-6
w2=8e-6
vol1=4*l*wSi*h
vol2=2*b*w1*h
vol3=4*b*w2*h
volSi=vol1+vol2+vol3
**********************************************
!material properties
nu=0.3
tref=300
ESI=1.3e11
aSi=2.6e-6
kSi=1.49e2
denSi=2.38e3
cSi=702.24
EAl=6.5e10
aAl=2.5e-5
kAl=2.37e2
denAl=2.7e3
cAl=898.7
**********************************************
!set material properties
!material 1 = silicon
```

```
mp,ex,1,ESi
mp,alpx,1,aSi
mp,kxx,1,kSi
mp,prxy,1,nu
mp,dens,1,denSi
mp,reft,1,tref
mp,c,1,cSi
!material 2 = aluminium
mp,ex,2,EAl
mp,alpx,2,aAl
mp,kxx,2,kAl
mp,prxy,2,nu
mp,dens,2,denAl
mp,reft,2,tref
mp,c,2,cAl
**********************************************
!element type, thermal
et,1,70
**********************************************
!define geometry
boptn,keep,no
block,0,b-wAl,l,l+w2,0,h
block,b-wAl,b,l,l+w2,0,h
block,b,b+wSi,l,l+w2,0,h
block,b,b+wSi,w1,l,0,h
block,b,b+wSi,0,w1,0,h
block,b+wSi,b+wSi+wAl,0,w1,0,h
block,b+wSi+wAl,2*b-wSi-wAl,0,w1,0,h
block,2*b-wSi-wAl,2*b-wSi,0,w1,0,h
block,2*b-wSi,2*b,0,w1,0,h
block,2*b-wSi,2*b,w1,l,0,h
block,2*b-wSi,2*b,l,l+w2,0,h
block,2*b,2*b+wAl,l,l+w2,0,h
block,2*b+wAl,3*b,l,l+w2,0,h
block,3*b,3*b+wcr,l,l+w2,0,h
block,3*b,3*b+wcr,l+w2,l+w2+l1,0,h
block,b-wAl,b,0,w1,0,h
block,b-wAl,b,w1,l,0,h
block,2*b,2*b+wAl,0,w1,0,h
block,2*b,2*b+wAl,w1,l,0,h
allsel
**********************************************
!assign materials to geometry
vsel,all
vatt,1,,1
allsel
vsel,s,loc,x,b-wAl,b
vsel,u,loc,y,l,l+w2
```

```
vatt,2,,1
allsel
vsel,s,loc,x,2*b,2*b+wAl
vsel,u,loc,y,l,l+w2
vatt,2,,1
allsel
*********************************************
!define mesh density
lsel,s,length,,h
lesize,all,,,1
allsel
lsel,s,length,,wSi
lesize,all,,,1
allsel
lsel,s,length,,h
lesize,all,,,1
allsel
lsel,s,length,,wSi
lesize,all,,,1
allsel
lsel,s,length,,wAl
lesize,all,,,1
allsel
lsel,s,length,,wcr
lesize,all,,,1
allsel
lsel,s,length,,w1
lesize,all,,,1
allsel
lsel,s,length,,w2
lesize,all,,,1
allsel
lsel,s,length,,l-2*wSi,l+wSi
lesize,all,,,80
allsel
lsel,s,length,,l1-wSi,l1+wSi
lesize,all,,,10
allsel
lsel,s,length,,b-2*wSi,b+2*wSi
lesize,all,,,20
allsel
lsel,s,length,,l-2*wSi,l+wSi
lesize,all,,,80
allsel
lsel,s,length,,l1-wSi,l1+wSi
lesize,all,,,5
allsel
lsel,s,length,,b-2*wSi,b+2*wSi
```

```
lesize,all,,,20
allsel
*********************************************
!mesh the model
vmesh,all
vsel,all
*********************************************
!mirror half structure
local,11,0,0,l+w2+l1,0
vsymm,y,all
allsel
*********************************************
!merge the two materials
nummrg,node,1e-7
nummrg,kp,1e-7
finish
```

D.2.2 Temperature Distribution (One-Dimensional Meander Actuator)

```
*********************************************
!define volumes and input power
/prep7
et,1,70 ! element type
vol1=4*l*wSi*h
vol2=2*b*w1*h
vol3=4*b*w2*h
volSi=vol1+vol2+vol3
pwr=6e-3
pwrden=pwr/volSi
asel,s,loc,x,0 ! select areas at x=0
*********************************************
!apply thermal boundary conditions and loads
da,all,temp,300
allsel
vsel,s,mat,,1
vsel,u,loc,x,3*b,3*b+wcr
bfv,all,hgen,pwrden
allsel
*********************************************
!obtain thermal solution
/solve
solve
```

D.2.3 Static Deflection (One-Dimensional Meander Actuator)

Simple Analysis (Static Deflection, One-Dimensional Meander Actuator)

```
**********************************************
!apply structural boundary conditions
/prep7
et,1,45
nsel,s,loc,x,0 ! select all nodes at x=0
d,all,all
allsel
**********************************************
!read results of thermal analysis
ldread,temp,,,,,,rth ! read temperature load
finish
**********************************************
!apply thermal boundary conditions
/solve
antype,static
solve
finish
```

Analysis Varying the Input Power (Static Deflection, One-Dimensional Meander Actuator)

```
**********************************************
!set maximum power
maxpower=2
**********************************************
! loop for thermal analysis
*do,counter,1,maxpower,1
pwr=counter*1e-3
pwrden=pwr/volSi
/prep7
**********************************************
! thermal analysis
et,1,70 ! element type
asel,s,loc,x,0 ! select areas at x=0
da,all,temp,300
allsel vsel,s,mat,,1 !vsel,u,loc,x,3*b,3*b+wcr bfv,all,hgen,pwrden
allsel
/solu antype,static outres,nsol lswrite,counter *enddo
**********************************************
!obtain thermal solution
lssolve,1,maxpower
save
finish
**********************************************
```

```
!loop for structural analysis
*do,counter,1,maxpower,6
/prep7
et,1,45
nsel,s,loc,x,0 ! select all nodes at x=0
*********************************************
!structural boundary conditions
d,all,all
allsel
ldread,temp,counter,,,,,rth ! read temperature load
bfedele,all,hgen
finish
/solu
antype,static
*********************************************
!obtain structural solution
solve
finish
*********************************************
!write data to output file
/post1
pwr_mW=counter
*get,defl,node,953,u,x
*cfopen,meald_stat_1,txt,,append
*vwrite,pwr_mW,defl
(f5.1,2x,e15.7)
*cfclos,meald_stat_1,txt
finish
*enddo
```

D.2.4 Thermal Time Constant (One-Dimensional Meander Actuator)

```
*********************************************
! specify transient analysis
/solu
antype,trans,new
solcontrol,on,0
*********************************************
!define thermal boundary condtions
tunif,300 ! initial condition, temperature for all nodes = tref
allsel
asel,s,loc,x,0 ! select areas at x=0
da,all,temp,300
allsel
save
*********************************************
!setup transient analysis
```

```
time,t
allsel
autots,on
DELTIM,0.01*t,0.01*t,0.1*t,1
kbc,1
vsel,s,mat,,1
!vsel,u,loc,x,3*b,3*b+wcr
bfv,all,hgen,pwrden
allsel
outres,all,all
save
**********************************************
!obtain transient solution
solve
**********************************************
!plot temperature versus time
/post26
nsol,2,953,temp
/yrange,300,420
/xrange,0,t
/gropt,axnsc,1.6
/gropt,ltyp,0
/axlab,x,time[s]
/axlab,y,temperature[K]
/gropt,divx,5
/gropt,divy,4
plvar,2
prvar,2
```

D.2.5 Lateral Resonances (One-Dimensional Meander Actuator)

```
**********************************************
! thermal analysis
/solu
asel,s,loc,x,0 ! select areas at x=0
da,all,temp,300
allsel
vsel,s,mat,,1
!vsel,u,loc,x,3*b,3*b+wcr
bfv,all,hgen,pwrden
allsel
solve
/prep7
et,1,45
nsel,s,loc,x,0 ! select all nodes at x=0
d,all,all
allsel
```

```
ldread,temp,,,,,,rth ! read temperature load
*********************************************
! obtain thermal solution
/solve
antype,static
pstres,on
solve
finish
*********************************************
! modal analysis
/solu
antype,modal
pstres,on
modopt,lanb,10
allsel
asel,s,loc,x,0 ! select areas at x=0
da,all,ux,0 ! constraints
da,all,uy,0
da,all,uz,0
allsel
mxpand,10
solve
/post1
set,list
set,1,2
pldisp,0
!anmode,10,0
```

D.3 Two-Dimensional Meander Actuator

The ANSYS-files for the two-dimensional meander actuator are listed in this section, starting with the model, which is needed for all other simulations. The simulations are described in chapter 4.5.

D.3.1 Model for the Two-Dimensional Meander Actuator

```
*********************************************
/pnum,volu,1
/prep7
emunit,mks
*********************************************
!dimensions
l=1000e-6
h=30e-6
wSi=8e-6
a=300e-6
b=300e-6
```

```
c=100e-6
m=100e-6
n=100e-6
wAl=1.5e-6
wa=8e-6
wb=8e-6
wc=8e-6
wm=10e-6
d=l+wb+n-c-wm-wc
************************************************
!material properties
nu=0.3
tref=300
ESI=1.3e11
aSi=2.6e-6
kSi=1.49e2
denSi=2.38e3
EAl=6.5e10
aAl=2.5e-5
kAl=2.37e2
denAl=2.7e3
************************************************
!set material properties
!material 1 = silicon
mp,ex,1,ESi
mp,alpx,1,aSi
mp,kxx,1,kSi
mp,prxy,1,nu
mp,dens,1,denSi
mp,reft,1,tref
!material 2 = aluminium
mp,ex,2,EAl
mp,alpx,2,aAl
mp,kxx,2,kAl
mp,prxy,2,nu
mp,dens,2,denAl
mp,reft,2,tref
************************************************
! silicon geometry
local,12,0,-m-wc-d-wm-c-2*wSi-b-a,-m-wc-l-wb,0,0
wpcsys
block,0,a-wAl,l+wb,l+wb+wa,0,h
block,a-wAl,a,l+wb,l+wb+wa,0,h
block,a,a+wSi,l+wb,l+wb+wa,0,h
block,a,a+wSi,wb,l+wb,0,h
block,a,a+wSi,0,wb,0,h
block,a+wSi,a+wSi+wAl,0,wb,0,h
block,a+wSi+wAl,a+wSi+b-wAl,0,wb,0,h
```

```
block,a+wSi+b-wAl,a+wSi+b,0,wb,0,h
block,a+wSi+b,a+2*wSi+b,0,wb,0,h
block,a+wSi+b,a+2*wSi+b,wb,wb+l,0,h
block,a+wSi+b,a+2*wSi+b,wb+l,wb+l+wc,0,h
block,a+2*wSi+b,a+2*wSi+b+wAl,wb+l,wb+l+wc,0,h
block,a+2*wSi+b+wAl,a+2*wSi+b+c,wb+l,wb+l+wc,0,h
block,a+2*wSi+b+c,a+2*wSi+b+c+wm,wb+l,wb+l+wc,0,h
!block,a+2*wSi+b+c,a+2*wSi+b+c+wm,wb+l+wa,wb+l+wc+m,0,h
block,a+2*wSi+b+c+wm,a+2*wSi+b+c+wm+d,wb+l,wb+l+wc,0,h
block,a+2*wSi+b+c+wm+d,a+2*wSi+b+c+wm+d+wc,wb+l+wc,wb+l+wc+m,0,h
**********************************************
! settings for meshing
et,1,70
vatt,1,,1
lsel,s,length,,h
lesize,all,,,1
lsel,s,length,,wSi
lesize,all,,,1
lsel,s,length,,wAl
lesize,all,,,1
lsel,s,length,,wa
lesize,all,,,1
lsel,s,length,,wb
lesize,all,,,1
lsel,s,length,,wc
lesize,all,,,1
lsel,s,length,,wm
lesize,all,,,1
lsel,s,length,,l
lesize,all,,,40
lsel,s,length,,m
lesize,all,,,4
lsel,s,length,,a
lesize,all,,,10
lsel,s,length,,b
lesize,all,,,10
lsel,s,length,,c
lesize,all,,,10
lsel,s,length,,d
lesize,all,,,30
vmesh,all
local,13,0,0,0,0,45
vsymm,y,all
csys,12
wpcsys
block,a+2*wSi+b+c+wm+d,a+2*wSi+b+c+wm+d+wc,wb+l,wb+l+wc,0,h
vatt,1,,1
lsel,s,length,,wc
```

```
lesize,all,,,1
vmesh,all
csys,0
wpcsys
vsymm,y,all
vsymm,x,all
*********************************************
! aluminium geometry (x-act.)
vsel,none
csys,12
wpcsys
block,a-wAl,a,0,wb,0,h
block,a-wAl,a,wb,wb+l,0,h
block,a+2*wSi+b,a+2*wSi+b+wAl,0,wb,0,h
block,a+2*wSi+b,a+2*wSi+b+wAl,wb,wb+l,0,h
vatt,2,,1
lsel,s,length,,wAl
lesize,all,,,1
lsel,s,length,,l,
lesize,all,,,40
vmesh,all
*********************************************
! create the whole model
csys,13
vsymm,y,all
csys,0
vsymm,y,all
vsymm,x,all
*********************************************
! merge materials
allsel
nummrg,node,1e-7
nummrg,kp,1e-7
```

D.3.2 Temperature Distribution (Two-Dimensional Meander Actuator)

```
*********************************************
!thermal analysis
/prep7
csys,0
et,1,70 ! element type
vol1=4*l*wSi*h
vol2=2*a*wa*h
vol3=2*b*wb*h
vol4=2*c*wc*h
vol5=2*wa*wSi*h+4*wb*wSi*h
vol6=2*wc*wSi*h
```

```
volSi=vol1+vol2+vol3+vol4+vol5+vol6
pwr=6e-3
pwrden=pwr/volSi
*********************************************
!thermal boundary conditions
asel,s,loc,x,-m-wc-d-wm-c-2*wSi-b-a
asel,a,loc,x,m+wc+d+wm+c+2*wSi+b+a
asel,a,loc,y,-m-wc-d-wm-c-2*wSi-b-a
asel,a,loc,y,m+wc+d+wm+c+2*wSi+b+a
da,all,temp,300
allsel
vsel,s,loc,x,-m-wc-d-wm-c-2*wSi-b-a,-m-wc-d
vsel,u,loc,y,m+wc+l+wb+n,m+wc+d+wm+c+2*wSi+b+a
vsel,u,loc,y,-m-wc-l-wb-n,-m-wc-d-wm-c-2*wSi-b-a
vsel,u,mat,,2
*********************************************
!apply heat generation
bfv,all,hgen,pwrden
allsel
*********************************************
!obtain thermal solution
/solve
solve
*********************************************
!plot temperature distribution
/post1
plnsol,temp
```

D.3.3 Static Deflection (Two-Dimensional Meander Actuator)

```
*********************************************
! structural analysis
/prep7
csys,0
et,1,45
*********************************************
! structural boundary conditions
asel,s,loc,x,-m-wc-d-wm-c-2*wSi-b-a
asel,a,loc,x,m+wc+d+wm+c+2*wSi+b+a
asel,a,loc,y,-m-wc-d-wm-c-2*wSi-b-a
asel,a,loc,y,m+wc+d+wm+c+2*wSi+b+a
da,all,all
allsel
*********************************************
!read results of thermal analysis
ldread,temp,,,,,,rth ! read temperature load
*********************************************
```

```
!obtain structural solution
/solve
solve
*********************************************
! plot deflection results
/post1
plnsol,u,x
/dscale,all,5
nsel,s,,,693
prnsol,u,s
allsel
```

D.3.4 Thermal Time Constant (Two-Dimensional Meander Actuator)

```
*********************************************
! transient analysis
/solu
antype,trans,new
solcontrol,on,0
*********************************************
!apply thermal boundary conditions
tunif,300 ! initial condition, temperature for all nodes 300 K
allsel
asel,s,loc,x,-m-wc-d-wm-c-2*wSi-b-a
asel,a,loc,x,m+wc+d+wm+c+2*wSi+b+a
asel,a,loc,y,-m-wc-d-wm-c-2*wSi-b-a
asel,a,loc,y,m+wc+d+wm+c+2*wSi+b+a
da,all,temp,300
save
time,t
allsel
autots,on
DELTIM,0.01*t,0.01*t,0.1*t,1
kbc,1
allsel
vsel,s,loc,x,-m-wc-d-wm-c-2*wSi-b-a,-m-wc-d
vsel,u,loc,y,m+wc+l+wb+n,m+wc+d+wm+c+2*wSi+b+a
vsel,u,loc,y,-m-wc-l-wb-n,-m-wc-d-wm-c-2*wSi-b-a
vsel,u,mat,,2
bfv,all,hgen,pwrden
allsel
outres,all,all
save
*********************************************
!obtain transient solution
solve
*********************************************
```

```
!plot temperature versus time
/post26
nsol,2,350,temp
/yrange,300,360
/xrange,0,t
/gropt,axnsc,1.6
/gropt,ltyp,0
/axlab,x,time[s]
/axlab,y,temperature[K]
/gropt,divx,5
/gropt,divy,4
plvar,2
prvar,2
```

D.3.5 Lateral Resonances (Two-Dimensional Meander Actuator)

```
**********************************************
! modal analysis
/solu
antype,modal
modopt,lanb,10
allsel
**********************************************
!apply boundary conditions
asel,s,loc,x,-m-wc-d-wm-c-2*wSi-b-a
asel,a,loc,x,m+wc+d+wm+c+2*wSi+b+a
asel,a,loc,y,-m-wc-d-wm-c-2*wSi-b-a
asel,a,loc,y,m+wc+d+wm+c+2*wSi+b+a
da,all,all
mxpand,5
solve
**********************************************
! plot mode shape
/post1
set,list
set,1,2
pldisp,0
```

Appendix E

Publications

E.1 Journal Publications

- H. Sehr, A. G. R. Evans, A. Brunnschweiler, G. J. Ensell, and T. E. G. Niblock, "Fabrication and test of thermal vertical bimorph actuators for movement in the wafer plane," *Journal of Micromechanics and Microengineering*, vol. 11, pp. 306 – 310, 2001.

- H. Sehr, I. S. Tomlin, B. Huang, S. P. Beeby, A. G. R. Evans, A. Brunnschweiler, G. J. Ensell, C. G. J. Schabmueller, and T. E. G. Niblock, "Time constant and lateral resonaces of thermal vertical bimorph actuators," *Journal of Micromechanics and Microengineering*, vol. 12, pp. 410 – 413, 2002.

- C. G. J. Schabmueller, M. Koch, M. E. Mokhtari, A. G. R. Evans, A. Brunnschweiler, and H. Sehr, "Self-aligning gas/liquid micropump," *Journal of Micromechanics and Microengineering*, vol. 12, pp. 420 – 424, 2002.

E.2 Conference Publications

- H. Sehr, A. G. R. Evans, A. Brunnschweiler, and G. J. Ensell, "Design and fabrication of a novel thermally actuated vertical bimorph scanner for an integrated afm," Design, Test and Integration of MEMS and MOEMS, Paris, France, SPIE Vol. 4019, 2000.

- H. Sehr, A. G. R. Evans, A. Brunnschweiler, G. J. Ensell, and M. Kraft, "A 3-dimensional actuator based on a novel combination of thermally actuated planar and vertical bimorphs," International Conference on New Actuators, ACTUATOR, Bremen, Germany, 2000.

- H. Sehr, A. G. R. Evans, A. Brunnschweiler, and M. Kraft, "Theoretical analyses on a novel actuator based on thermally actuated vertical bimorphs," Euro-

pean Conference on Solid-State Transducers, Eurosensors, Copenhagen, Denmark, 2000.

- H. Sehr, A. G. R. Evans, A. Brunnschweiler, and G. J. Ensell, "Novel process for deposition of aluminium onto sidewalls of silicon trenches," Microfabrication Process Technology VI, SPIE Vol. 4174, 2000.

- H. Sehr, I. S. Tomlin, S. P. Beeby, A. G. R. Evans, A. Brunnschweiler, G. J. Ensell, C. G. J. Schabmueller, and T. E. G. Niblock, "Dynamic characterisation of thermal vertical bimorph actuators," Micromechanics Europe, MME, Cork, Ireland, 2001.

- C. G. J. Schabmueller, M. Koch, M. E. Mokthari, A. G. R. Evans, A. Brunnschweiler, and H. Sehr, "Mass-producible, bubble tolerant gas/liquid micropump with self-aligning feature," Micromechanics Europe, MME, Cork, Ireland, 2001.

- T. Niblock, M. Kraft, and H. Sehr, "Design criteria for a hybrid nano photolithography system," Micromechanics Europe, MME, Cork, Ireland, 2001.

- T. Niblock, A. Brunnschweiler, A. G. R. Evans, and H. Sehr, "Temperature sensing using cmos p-n diodes for mems fabricated thermally actuated bimorhs," Micromechanics Europe, MME, Cork, Ireland, 2001.

- H. Sehr, A. G. R. Evans, A. Brunnschweiler, G. J. Ensell, and C. G. J. Schabmueller, "Design and fabrication of a thermally actuated microrelay based on vertical bimorphs," European Conference on Solid-State Transducers, Eurosensors XVI, Prague, Czech Republic, 2002.

- H. Sehr, A. G. R. Evans, G. J. Ensell, A. Brunnschweiler, C. G. J. Schabmueller, and T. E. G. Niblock, "Design and fabrication of a advanced thermal vertical bimorph actuators for micropositioning," Micromechanics Europe, MME, Sinaia, Romania, 2002.

- C. G. J. Schabmueller, A. G. R. Evans, G. J. Ensell, A. Brunnschweiler, H. Sehr, T. E. G. Niblock, V. D. Kunz, and M. Bu, "Thermal evaluation of a micromachined pcr chip," Micromechanics Europe, MME, Sinaia, Romania, 2002.

- C. G. J. Schabmueller, A. G. R. Evans, G. J. Ensell, A. Brunnschweiler, H. Sehr, and M. Bu, "Towards an electrostatically closable reaction chamber," Micromechanics Europe, MME, Sinaia, Romania, 2002.

References

[1] S. D. Senturia, *Microsystem Design*, Kluwer Academic Publishers, Norwell, Massachusetts, 2001.

[2] G. T. A. Kovacs, *Micromachined Transducers Sourcebook*, WCB/McGraw-Hill, New York, 1998.

[3] M. J. Madou, *Fundamentals of Microfabrication, second edition*, CRC Press, Boca Raton, Florida, 2002.

[4] O. N. Tufte, P. W. Chapman, and D. Long, "Silicon diffused-element piezoresistive diaphragms," *Journal of Applied Physics*, vol. 33, pp. 3322 – 3327, 1962.

[5] S. Akamine, T. R. Albrecht, M. J. Zdeblick, and C. F. Quate, "A planar process for microfabrication of a scanning tunneling mircroscope," *Sensors and Actuators*, vol. A21-A23, pp. 3386–3396, 1990.

[6] P.-F. Indermuehle, V. P. Jaecklin, J. Brugger, N. F. Linder, N. F. de Rooij, and M. Bingelli, "Afm imaging with an xy-micropositioner with integrated tip," *Sensors and Actuators*, vol. A46-A47, pp. 562–565, 1995.

[7] S. P. Timoshenko, "Analysis of bi-metal thermostats," *Journal of the Optical Society of America*, vol. 11, pp. 233–255, 1925.

[8] W. Riethmueller and W. Benecke, "Thermally excited silicon microactuators," *IEEE Transactions on Electron Devices*, vol. 35, no. 6, pp. 758–763, 1988.

[9] W. S. N. Trimmer and K. J. Gabriel, "Design considerations for a practical electrostatic micro-motor," *Sensors and Actuators*, vol. 11, pp. 189 – 206, 1987.

[10] W. C. Tang, T-C. H. Nguyen, and R. T. Howe, "Laterally driven polysilicon resonant microstructures," *Sensors and Actuators*, vol. 20, pp. 25–32, 1989.

[11] V. P. Jaecklin, C. Linder, N. F. de Rooij, and J. M. Mooret, "Micromechanical comb actuators with low driving voltage," *Journal of Micromechanics Microengineering*, vol. 2, no. 6, pp. 2538–2543, Nov/Dec 1992.

[12] Z. L. Zhang and N. C. MacDonald, "Integrated silicon process for microdynamic vacuum field emission cathodes," *Journal of Vacuum Science and Technology*, vol. B11, no. 6, pp. 2538–2543, Nov/Dec 1993.

[13] S. Buettgenbach, *Mikromechanik*, Teubner, Stuttgart, 2 edition, 1994.

[14] S. Fatikov and U. Rembold, *Microsystem Technology and Microrobotics*, Springer, Berlin, 1997.

[15] R. Bindig and G. Helke, "Application of piezoceramic multilayer actuators, experiences and solutions," International Conference on New Actuators, ACTUATOR, Bremen, Germany, June 2000.

[16] A. Bauer and F. Moeller, "Piezo actuator special design," International Conference on New Actuators, ACTUATOR, Bremen, Germany, June 1994.

[17] U. Dibbern, "Piezoelectric actuators in multilayer technique," International Conference on New Actuators, ACTUATOR, Bremen, Germany, June 1994.

[18] J. M. Gere and S. P. Timoshenko, *Mechanics of Materials*, Stanley Thornes, Cheltenham, 4 edition, 1999.

[19] R. Cragun and L. L. Howell, "A constrained thermal expansion microactuator," DSC-Vol. 66, Micro-Electro-Mechanical Systems (MEMS), ASME, 1998.

[20] C. Doering, T. Grauer, J. Marek, M. S. Mettner, H.-P. Trah, and M. William, "Micromachined thermoelectrically driven cantilever structures for fluid jet deflection," Micro Electromechanical Systems'92, Travemuende, Germany, 1992.

[21] X.-Q. Sun, K. R. Farmer, and W. N. Carr, "A bistable microrelay based on two-segment multimorph cantilever actuators," Micro Electromechanical Systems'98, Heidelberg, Germany, 1998.

[22] J. Buehler, J. Funk, O. Paul, F. P. Steiner, and H. Baltes, "Thermally actuated cmos micromirrors," *Sensors and Actuators*, vol. A46-47, pp. 572 – 575, 1995.

[23] S. Schweizer, P. Cousseau, and P. Calmes, S. Renaud, "Two-dimensional thermally actuated optical microscanner," Eurosensors XIII, The Hague, Netherlands, 1999.

[24] H. Guckel, J. Klein, T. Christenson, and K. Skrobis, "Thermo-magnetic metal flexure actuator," Solid State Sensors and Actuators Workshop, Hilton Head SC, 1992.

[25] J. H. Comtois, M. A. Michaelicek, and C. C. Barron, "Characterization of electrothermal actuators and arrays fabricated in a four-level, planarized surface-micromachined polycrystalline silicon process," International Conference on Solid State Sensors and Actuators (Transducers'97), Chicago, 1997.

[26] C. S. Pan and w. Hsu, "An electro-thermally and laterally driven polysilicon microactuator," *Journal of Micromechanics and Microengineering*, vol. 7, pp. 7–13, 1997.

[27] P. B. Allen, N. C. Boydston, J. T. Howard, S. Y. Ko, E. S. Kolesar, Ruff, J. M. Wilken, and R. J. Wilks, "Theoretical and experimental characterization of the in-plane tip force and deflection achieved with asymmetrical polysilicon electrothermal microactuators," Micromachined Devices and Components VI, Proceedings of SPIE Vol. 4176, 2000.

[28] T. Moulton and G. K. Anathasuresh, "Micromechanical devices with embedded electro-thermal-compliant actuation," *Sensors and Actuators*, vol. A 90, pp. 38–48, 2001.

[29] C. G. Keller and R. T. Howe, "Nickel-filled hexsil thermally actuated tweezers," International Conference on Solid State Sensors and Actuators (Transducers'95), Stockholm, Sweden, 1995.

[30] C. Keller and M. Ferrari, "Milli-scale polysilicon structures," Solid State Sensors and Actuators Workshop, Hilton Head SC, 1994.

[31] J. Li and G. K. Anathasuresh, "A quality study on the eximer laser micromachining of electro-thermal compliant micro devices," *Journal of Micromechanics and Microengineering*, vol. 11, pp. 38–47, 2001.

[32] J. Jonsmann, O. Sigmund, and S. Bouwstra, "Compliant electro-thermal microactuators," International Conference on Micro Electromechanical Systems (MEMS'99), Orlando FL, 1999.

[33] G. K. Ananthasuresh, S. Kota, and Y. Gianchandani, "A methodical approach to the design of compliant micromechanisms," Solid State Sensors and Actuators Workshop, Hilton Head SC, 1994.

[34] A. Saxena and G. K. Ananthasuresh, "Topology synthesis of compliant mechanisms for nonlinear force-deflection and curved path specifications," *Journal of Mechanical Design*, vol. 123, pp. 33–42, 2001.

[35] G. Thornell, M. Bexell, J.-A. Schweitz, and S. Johansson, "The design and fabrication of a gripping tool for micromanipulation," The 6th International

Conference on Solid-State Sensor and Actuators and Eurosensors IX, Stockholm, Sweden, 1995.

[36] M. Chiao and L. Liwei, "Self-buckling of micromachined beams under resistive heating," *Journal of Microelectromechanical Systems*, vol. 9, no. 1, pp. 146 – 151, 2000.

[37] M. Chiao and L. Lin, "Microactuators based on electrothermal expansion of clamped-clamped beams," Microelectromechanical Systems '97, 1997.

[38] L. Que, J.-S Park, and Y. B. Gianchandani, "Bent-beam electrothermal actuators - part i: Single beam and cascaded devices," *Journal of Microelectromechanical Systems*, vol. 10, no. 2, pp. 247 – 254, 2001.

[39] J.-S Park, L. L. Chu, and Y. B. Oliver, A. D. Gianchandani, "Bent-beam electrothermal actuators - part ii: Linear and rotary microengines," *Journal of Microelectromechanical Systems*, vol. 10, no. 2, pp. 255 – 262, 2001.

[40] G. B. Lee, H. Il Tsai, C. S. Shey, Y. H. Lin, R. S. Chan, and C. J. Kung, "Analysis of micromachined electro-thermal bent-beam actuators and their applications on micro-grippers/micro-optics," International Conference on New Actuators, ACTUATOR, Bremen, Germany, 2000.

[41] S. Buetefisch, G. Pokar, S. Buettgenbach, and J. Hesselbach, "A new sma actuated miniature silicon gripper for micro assembly," 7th International Conference on New Actuators, ACTUATOR, Bremen, Germany, 2000.

[42] N. Lhermet and F. Claeyssen, "Actuator based on biased magnetostrictive rare earth-iron alloys," International Conference on New Actuators, ACTUATOR, Bremen, Germany, 1992.

[43] G. Flik, "Giant magnetostrictive thin film transducers for microsystems," International Conference on New Actuators, ACTUATOR, Bremen, Germany, 1994.

[44] H. Lehr, "Application of the liga-technique for the development of microactuators based on electromagnetic principles," International Conference on New Actuators, ACTUATOR, Bremen, Germany, 1992.

[45] C. H. Ahn and Allen M. G., "A fully integrated micromagnetic actuator with a multilevel meander magnetic core," Solid State Sensors and Actuators Workshop, Hilton Head SC, 1992.

[46] G. Binnig, H. Rohrer, C. Gerber, and E. Weibel, "Surface studies by scanning tunneling microscopy," *Physical Review Letters*, vol. 49, no. 1, pp. 57–61, 1982.

[47] G. Binnig and C. F. Quate, "Atomic force microscope," *Physical Review Letters*, vol. 56, no. 9, pp. 930–933, 1986.

[48] E. S. Snow, P. M. Campell, and F. K. Perkins, "Nanofabrication with proximal probes," *Proceedings of the IEEE*, vol. 85, no. 4, pp. 601–611, 1997.

[49] J. A. Dagata, J. Schneir, H. H. Harary, C. J. Evans, M. T. Postek, and J. Bennett, "Modification of hydrogen passivated silicon by a scanning tunneling microscope operating in air," *Applied Physics Letters*, vol. 56, no. 20, pp. 2001–2003, 1990.

[50] S. C. Minne, H. T. Soh, P. Flueckiger, and C. F. Quate, "Fabrication of 0.1 μm metal oxide semiconductor field-effect transistor with the atomic force microscope," *Applied Physics Letters*, vol. 66, no. 6, pp. 703–705, 1995.

[51] K Matsumoto, "Stm/afm nano-oxidation process to room temperature operated single-electron transistor and other devices," *Proceedings of the IEEE*, vol. 85, no. 4, pp. 612–628, 1997.

[52] J. W. Lyding, T. C. Shen, J. S. Hubacek, J. R. Tucker, and G. C. Abeln, "Nanoscale patterning and oxidation of h-passivated si(100)-2x1 surfaces with an ultrahigh vacuum scanning tunneling microscope," *Applied Physics Letters*, vol. 64, no. 15, pp. 2010–2012, 1994.

[53] C. R. K. Marrian and R. J. Colton, "Low-voltage electron lithography with a scanning tunneling microscope," *Applied Physics Letters*, vol. 56, no. 8, pp. 755–757, 1990.

[54] C. Van Haesendonck, L. Stockman, G. Neuttiens, C. Strunk, and Y. Bruynseraede, "Nanolithographic pattering of au films with a scanning tunneling microscope," *Journal of Vacuum Science and Technology*, vol. B13, no. 3, pp. 1290–1293, 1995.

[55] U. Demir, K. K. Balasubramanian, V. Cammarata, and C. Shannon, "Scanning probe lithograph of novel langmuir-schaefer films: Electrochemical applications," *Journal of Vacuum Science and Technology*, vol. B13, no. 3, pp. 1294–1299, 1995.

[56] M. A. McCord, D. P. Kern, and T. H. P. Chang, "Direct deposition of 10 nm metallic feature with the scanning tunneling microscope," *Journal of Vacuum Science and Technology*, vol. B6, no. 6, pp. 1877–1880, 1988.

[57] S. Rubel, X. D. Wang, and A. L. de Lozanne, "Nanofabrication with a scanning tunneling microscope using chemical vapor deposition," *Journal of Vacuum Science and Technology*, vol. B13, no. 3, pp. 1332–1336, 1995.

[58] H. J. Mamin, S. Chiamg, H. Birk, P. H. Guenther, and D. Rugar, "Gold deposition from a scanning tunneling microscope tip," *Journal of Vacuum Science and Technology*, vol. B9, no. 2, pp. 1398–1402, 1991.

[59] S. Hosaka, H. Koyanagani, A. Kikukawa, M. Miayamoto, and R. Imura, "Fabrication of nanometer-scale structures on insulator and in magnetic materials using a scanning probe microscope," *Journal of Vacuum Science and Technology*, vol. B13, no. 3, pp. 1307–1311, 1995.

[60] D. M. Eigler and E. K. Schweizer, "Positioning single atoms with a scanning tunneling microscope," *Nature*, vol. 344, pp. 524–526, 1990.

[61] Z. L. Zhang and N. C. MacDonald, "A rie process for submicron silicon electromechanical structures," *Journal of Micromechanics and Microengineering*, vol. 2, pp. 31–38, 1992.

[62] Y. Xu and N. C. MacDonald, "Integrated micro-scanning tunneling microscope," *Applied Physics Letters*, vol. 67, no. 16, pp. 2305–2307, 1995.

[63] J. J. Yao, S. C. Arney, and N. C. MacDonald, "Fabrication of high frequency two-dimensional nanoactuators for scanned probe devices," *Journal of Microelectromechanical Systems*, vol. 1, no. 1, pp. 14–22, 1992.

[64] T. E. G. Niblock, *Micro Scanning Probe*, Ph.D. thesis, University of Southampton, 2001.

[65] K. E. Peterson, "Michromechanical membrane switches on silicon," *IBM Journal of Research and Development*, vol. 23, no. 4, pp. 376 – 385, 1979.

[66] R. Wood, M. Ramaswamy, D. Vijay, B. Dudley, C. Allen, E. Hill, and K. Markus, "Mems microrelays," *Mechatronics*, vol. 8, pp. 535–547, 1998.

[67] H. Hosaka, H. Kuwano, and K.; Yanagisawa, "Electromagnetic microrelays: Concepts and fundamental characteristics," *Sensors and Actuators*, vol. A40, pp. 41–47, 1994.

[68] J. Schimkat, "Contact material for microrelays," Micro Electromechanical Systems'98, Heidelberg, Germany, 1998.

[69] I. Schiele, J. Huber, C. Evers, B. Hillerich, and F. Kozlowski, "Micromechanical relay with electrostatic actuation," International Conference on Solid-State Sensors and Actuators, Transducers, Chicago, 1997.

[70] J. J. Yao and M. F. Chang, "A surface micromachined miniature switch for telecomunications applications with signal frequencies from dc up to 4 ghz,"

International Conference on Solid-State Sensors and Actuators, Transducers, Stockholm, Sweden, 1995.

[71] F. Ploetz, S. Michaelis, R. Aigner, H.-J. Timme, J. Binder, and R. Noe, "A low-voltage torsional actuator for application in rf-microswiches," *Sensor and Actuators*, vol. A92, pp. 312–317, 2001.

[72] M.-A. Gretillat, P. Thiebaud, C. Linder, and N. F. de Rooij, "Integrated circuit compatible electrostatic polysilicon microrelays," *Journal of Micromechanics and Microengineering*, vol. A, pp. 40–43, 1995.

[73] J. Drake, H. Jerman, B. Lutze, and M. Stuber, "An electrostatically actuated micro-relay," International Conference on Solid-State Sensors and Actuators, Transducers, Stockholm, Sweden, 1995.

[74] W. P Taylor and M. G. Allen, "Integrated magnetic microrelays: Normally open, normally closed, and multiple-pole devices," International Conference on Solid-State Sensors and Actuators, Transducers, Chicago, 1997.

[75] A. B. Frazier, C. H. Ahn, and M. G. Allen, ," *Sensors and Actuators*, vol. A45, pp. 47–55, 1994.

[76] T. Seki, M. Sakata, T. Nakajima, and M. Matsumoto, "Thermal buckling actuators for micro relays," International Conference on Solid-State Sensors and Actuators, Transducers, Chicago, 1997.

[77] M. Koch, A. Evans, and A. Brunnschweiler, *Microfluidic Technology and Applications*, Research Study Press Ltd., Baldock, Hertfordshire, England, 2000.

[78] R. Zengerle and M. Richter, "Simulation of microfluidic systems," *Journal of Micromechanics and Microengineering*, vol. 4, no. 4, 1994.

[79] R. Zengerle, J. Ulrich, S. Kluge, M. Richter, and A. Richter, "Bidirectional silcon micropump," *Sensors and Actuators*, vol. A50, pp. 81 – 86, 1995.

[80] M. Koch, N. Harris, A. G. R. Evans, N. M. White, and A. Brunnschweiler, "A novel micromachined pump based on thick-film piezoelectric actuation," *Sensors and Actuators*, vol. A70, pp. 980 – 103, 1998.

[81] M. Koch, A. G. R. Evans, and A. Brunnschweiler, "The dynamic micropump driven with a screen printed pzt actuator," *Journal of Micromechanics and Microengineering*, vol. 8, no. 2, 1998.

[82] A. Olsson, P. Enoksen, G. Stemme, and E. Stemme, "A valveless planar pump isotropically etched in silicon," Micromechanics Europe, Copenhagen, Denmark, 1995.

[83] Q. Gong and Z. Zhou, "Design optimization and simulation of micro electromagnetic pump," International Conference on Solid-State Sensors and Actuators, Transducers, Sendai, Japan, 1999.

[84] G. Zhan, T. Lo, L. Liu, and P. Tsien, "A silicon membrane micropump with integrated bimetallic actuator," *Chinese Journal of Electronics*, vol. 5, no. 2, 1996.

[85] C. G. J. Schabmueller, M. Koch, M. E. Mokhtari, A. G. R. Evans, A. Brunnschweiler, and H. Sehr, "Mass-producible, bubble tolerant gas/liquid micropump with self-aligning feature," Micromechanics Europe, Cork Ireland, 2001.

[86] C. G. J. Schabmueller, *Microfluidic Devices for Integrated Bio/Chemical Systems*, Ph.D. thesis, University of Southampton, 2001.

[87] R. S. Muller, "Microdynamics," *Sensors and Actuators*, vol. A21-23, pp. 1 – 8, 1990.

[88] R. T. Howe, "Resoanant microsensors," International Conference on Solid-State Sensors and Actuators, Transducers, 1987.

[89] W. C. Tang, T-C. H. Nguyen, M. W. Judy, and R. T. Howe, "Electrostatic-comb drive of lateral polysilicon resonators," *Sensors and Actuators*, vol. A21-23, pp. 328–331, 1990.

[90] S. P. Beeby and N. M. White, "Silicon micromachined resonator with thick-film printed vibration excitation and detection mechanisms," *Sensors and Actuators*, vol. A88, pp. 189 – 197, 2001.

[91] D. B. Hicks, S.-C. Chang, M. W. Putty, and D. S. Eddy, "Piezoelectrically activated resonant bridge microaccelerometer," Solid-State Sensor and Actuator Workshop, Hilton Head, 1994.

[92] T. S. J. Lammerink, M. Elwenspoek, R. H. Van Ouwerkerk, S. Bouwstra, and J. H. I. Fluitman, "Performance of thermally excited resonantors," *Sensors and Actuators*, vol. A21-23, pp. 352 – 356, 1990.

[93] M. W. Putty and K. Najafi, "A micromachined vibrating ring gyroscope," Solid-State Sensor and Actuator Workshop, Hilton Head, 1994.

[94] D. W. Burns, J. D. Zook, R. D. Horning, W. R. Herb, and H. Guckel, "A digital pressure sensor basend on resonant microbeams," Solid-State Sensor and Actuator Workshop, Hilton Head, 1994.

[95] J. r. Vig, r. L Filler, and Y. Kim, "Chemical sensor based on quartz microresonantors," *Journal of Microelectromechanical Systems*, vol. 5, no. 2, 1996.

[96] L. J. Hornbeck, "Digital light processing for high-brightness, high resolution applications," Electronic Imaging, EI, San Jose, California, 1997.

[97] J. Kraenert, C. Deter, T. Gessner, and W. Doetzel, "Laser display technology," Micro Electromechanical Systems (MEMS), 1998.

[98] M.-H. Kiang, O. Solgaard, R. S. Muller, and K. Y. Lau, "Micromachined microscanners for optical scanning," *Proceedings of SPIE*, vol. 3008, pp. 82 – 90, 1997.

[99] T. Gessner, "Recent progress in microactuators," International Conference on New Actuators, ACTUATOR, Bremen, Germany, 2000.

[100] H. Lakner, W. Doleschal, P Duerr, A. Gehner, H. Schenk, A. Wolter, and G. Zimmer, "Micromirrors for direct writing systems and scanners," *Proceedings of SPIE*, vol. 3878, pp. 217 – 227, 1999.

[101] J.-W. Shin, S.-W. Chung, Y.-K. Kim, and B. K. Choi, "Design and fabrication of micromirror array supported by vertical springs," *Sensors and Actuators*, vol. A66, pp. 144 – 149, 1998.

[102] S.-G. Kim and K.-H. Hwang, "Thin film micromirror array for information display system," EuroDisplay '99, 1999.

[103] H. Miyajima, N. Asaoka, Y. Arima, and K. Minamoto, "An electromagnetic optical scanner with polyimide-based hinges," International Conference on Solid-State Sensors and Actuators, Transducers, Senday, Japan, 1999.

[104] W. D. Cowan and V. M. Bright, "Thermally actuated piston micromirror arrays," *Proceedings of SPIE*, vol. 3131, pp. 260 – 271, 1997.

[105] R. A. Buser, N. F. de Rooij, H. Tischhauser, A. Dommann, and G. Staufert, "Biaxial scanning mirror activated by bimorph structures for medical applications," *Sensors and Actuators*, vol. A31, pp. 29 – 34, 1992.

[106] E. Westkamper, R. D. Schraft, C. Bark, G. Vogele, and T. Weisener, "Adhesive gripper - a new approach to handling mems," International Conference on New Actuators, ACTUATOR, Bremen, Germany, 1996.

[107] A. Menciassi, B. Hannaford, M. C. Carazzo, and P. Dario, "4-axis electromagnetic gripper," IEEE International Conference on Robotics and Automation, Detroit, Michigan, 1999.

[108] C. Kim, A. P. Pisano, and R. S. Muller, "Silicon-processed overhanging microgripper," *Journal of Microelectromechanical Systems*, vol. 1, no. 1, pp. 31 – 36, 1992.

[109] S. Linzhi, C. Jianyu, and S. Pin, "The design of milli grippers using piezoelectric actuator as well as electromagnetic force," International Symposium on Micro Machine and Human Science, 1995.

[110] R. Salim, H. Wurmus, A. Harnisch, and D. Huelsenberg, "Microgrippers created in microstructurable glass," *Microsystem Technologies*, vol. 4, no. 1, pp. 32 – 34, 1997.

[111] G. Greitmann and R. A. Buser, "Tactile microgripper for automated handling of microparts," *Sensors and Actuators*, vol. A53, pp. 410 – 415, 1996.

[112] Y. Suzuki, "Flexible microgripper," *International Journal of the Japanese Society for precision engineering*, vol. 29, pp. 10 – 13, 1995.

[113] E. Just, M. Kohl, W. Pflegig, and S. Miyazaki, "Sma microgripper with integrated antagonism," *Sensors and Actuators*, vol. A83, pp. 208 – 213, 2000.

[114] A. P. Lee, D. R. Ciarlo, P. A. Krulevitch, S. Lehew, J. Trevino, and M. A. Northrup, "A practical microgripper by fine alignment, eutectic bonding and sma actuation," *Sensors and Actuators*, vol. A54, pp. 755 – 759, 1996.

[115] H. Sehr, A. G. R. Evans, A. Brunnschweiler, and G. J. Ensell, "Design and fabrication of a novel thermally actuated vertical bimorph scanner for an integrated afm," Design, Test and Integration of MEMS and MOEMS, Paris, France, SPIE Vol. 4019, 2000.

[116] H. Sehr, A. G. R. Evans, A. Brunnschweiler, G. J. Ensell, and M. Kraft, "A 3-dimensional actuator based on a novel combination of thermally actuated planar and vertical bimorphs," International Conference on New Actuators, ACTUATOR, Bremen, Germany, 2000.

[117] H. Sehr, A. G. R. Evans, A. Brunnschweiler, G. J. Ensell, and T. E. G. Niblock, "Fabrication and test of thermal vertical bimorph actuators for movement in the wafer plane," *Journal of Micromechanics and Microengineering*, vol. 11, pp. 306 – 310, 2001.

[118] F. P. Incropera and D. P. De Witt, *Introduction to Heat Transfer*, Wiley, New York, 1985.

[119] W. T. Thomson, *Theory of Vibration with Applications*, George Allen & Unwin, 1983.

[120] R. D. Blevins, *Formulas for Natural Frequency and Mode Shape*, Van Nostrand Reinhold Company, Inc., New York, 1979.

[121] ANSYS Inc. Southpointe 275 Technology Drive Canonsburg PA 15317 www.ansys.com, "Ansys multiphysics," .

[122] L. C. Thomas, *Heat Transfer - Professional Version*, Prentice-Hall, Englewood Cliffs, New Jersey, 1993.

[123] H. Sehr, A. G. R. Evans, A. Brunnschweiler, and G. J. Ensell, "Novel process for deposition of aluminium onto sidewalls of silicon trenches," Microfabrication Process Technology VI, SPIE Vol. 4174, 2000.

[124] S. M. Sze, *VLSI Technology, second edition*, McGraw-Hill, New York, 1988.

[125] W. Menz and J. Mohr, *Mikrosystemtechink fuer Ingenieure*, VCH, Weinheim, Germany, 1997.

[126] Shipley Comp. L. L. C. Marborough MA www.ansys.com, "I-line photoresist, megaposit spr 220 series," .

[127] Microlithography Chemical Corp. 1254 Chestnut STreet Newton MA, "Nano su-8 resists," .

[128] J. M. Shaw, J. D. Gelorme, N. C. LaBianca, W. E. Conley, and S. J. Holmes, "Negative photoresists for optical lithography," *IBM Journal of Research and Development*, vol. 41, no. 1/2, 1997.

[129] H. Lorenz, M. Despont, N. Fahrni, J. Brugger, P. Vettiger, and P. Renaud, "High-aspect-ratio, ultrathick, negative-tone near-uv photoresist and its applications for mems," *Sensors and Actuators*, vol. A64, pp. 33 – 39, 1998.

[130] Microlithography Chemical Carp. 1254 Chestnut Street Newton MA, "Nano pmgi resists," .

[131] AI Technology Inc. 70 Washington Road Princton NJ 08550, "Cool-grease cgr7018, none silicone compound, non curing, very high thermal conductivity," .

[132] F. Laermer and A. Schilp, "Method of anisotropically etching silicon," US Patent, No. 55001893, 1996.

[133] H. Sehr, I. S. Tomlin, S. P. Beeby, A. G. R. Evans, A. Brunnschweiler, G. J. Ensell, C. G. J. Schabmueller, and T. E. G. Niblock, "Dynamic characterisation of thermal vertical bimorph actuators," Micromechanics Europe, MME, Cork, Ireland, 2001.

[134] H. Sehr, I. S. Tomlin, B. Huang, S. P. Beeby, A. G. R. Evans, A. Brunnschweiler, G. J. Ensell, C. G. J. Schabmueller, and T. E. G. Niblock, "Time constant and lateral resonaces of thermal vertical bimorph actuators," *Journal of Micromechanics and Microengineering*, vol. 12, pp. 410 – 413, 2002.

[135] I. S. Tomlin, "Vertical thermal bimorph actuators," Project report, bachelor of engineering, University of Southampton, 2001.

[136] B. Huang, "Test and charactersiation of vertical thermal bimorph actuator," Project report, bachelor of engineering, University of Southampton, 2002.

[137] M. R. Hart, R. A. Conant, K. Y. Lau, and R. S. Muller, ," *Journal of Microelectromechanical Systems*, vol. 9, no. 4, 2000.

[138] P. Chidamparam and A. W. Leissa, "Vibration of planar curved beams, rings, and arches," *Applied Mechanics Reviews*, vol. 46, no. 9, 1993.

[139] LEO Electron Microscopy Ltd Cambridge England, "Leo 1400 series scanning electron microscopes," .

[140] S. S. Rao, *Mechanical Vibrations*, Addison-Wesley, New York, 1986.

[141] J. Jonsmann and S. Bouwstra, "Material considerations for topology optimised thermal microactuators," Eurosensors XIV, Copenhagen, Denmark, 2000.

[142] L Papula, *Mathematische Formelsammlung fuer Ingenieure und Naturwissenschaftler*, Vieweg, Braunschweig, Wiesbaden, 1994.

[143] Tanner EDA 2650 East Foothill Boulevard Pasadena CA 91107, "L-edit pro version 8.20," .